

DOCTORAL THESIS

**Nonlinear modeling of reinforced dowel joints in timber
structures – a combined experimental-numerical study**

submitted in satisfaction of the requirements for the degree
Doctor of Science in Civil Engineering
of the Vienna University of Technology, Faculty of Civil Engineering

DISSERTATION

**Nichtlineare Modellierung von querzugverstärkten
Stabdübelverbindungen in Holzkonstruktionen – eine
kombiniert experimentell-numerische Studie**

ausgeführt zum Zwecke der Erlangung des akademischen Grades eines
Doktors der technischen Wissenschaften
eingereicht an der Technischen Universität Wien, Fakultät für Bauingenieurwesen

von

Dipl.-Ing. **Michael Schweigler**
Matrikelnr.: 00728165

Betreuer:

Univ.-Prof. Dipl.-Ing. Dr. techn. Dr. h.c.mult. **Josef Eberhardsteiner**
Institut für Mechanik der Werkstoffe und Strukturen
Technische Universität Wien

Gutachter:

Assoc. Prof. Dipl.-Ing. Dr. techn. **Thomas K. Bader**
Department of Building Technology
Linnæus University Växjö

Assoc. Prof. **Thierry Descamps** PhD
Department of Structural Mechanics and Civil Engineering
Faculty of Engineering, University of Mons

Wien, im Jänner 2018

.....

"Look deep into nature, and then you will understand everything better"

Albert Einstein

Acknowledgements

This thesis is the scientific outcome of my research activity at the Institute for Mechanics of Materials and Structures (IMWS) at the Vienna University of Technology (TU Wien). That is thanks to a large number of people of whom I would like to address the most important ones in the following.

I would like to express my deepest gratitude to my advisor Thomas K. Bader, for his amazing support throughout my Ph.D. research, and setting an example with his immense knowledge on the "beautiful complicated" material wood and his dedication to science in general. I would like to thank him for introducing me to the world of science, for guiding me, for motivating and restraining me, when necessary, and also for serving as examiner of this thesis. I am truly grateful for all the valuable scientific discussions, for the uncountable e-mails and hours on the phone, which proved his unbowed support after he resumed his scientific career at Linnæus University in Växjö, Sweden. In the last few years, he became an example in scientific and human matters to me.

I would like to thank Georg Hochreiner for so many insightful discussions, especially on topics related to engineering practice. He always impressed me with his broad knowledge, and his inexhaustible dedication to the building material wood. I would like to thank him for sharing the passion for knowledge transfer to our students within the lectures of Timber Engineering 1 and 2. In this regard, our student assistants and tutors are thanked as well.

I am indebted to Josef Eberhardsteiner, Vice Rector of TU Wien, and former head of the IMWS for taking me on board, for his support and help in strategic decisions, for always having an open door when needed. Furthermore, my deepest thanks go to Dr. Thierry Descamps (University of Mons) for agreeing to be co-examiner of this thesis.

I would like to thank Christian Hellmich, current head of the institute, for his dedication to science, and for creating a positive and encouraging work environment, to which each and every colleague has contributed as well. Therefore, I am thankful for my current and former colleagues Maximilian Autengruber, Guiseppe Balduzzi, Eva Binder, Josef Füssl, Pedro Godinho, Herwig Hengl, Georg Kandler, Hawraa Kariem, Thomas Kiefer, Olaf Lahayne, Wolfgang Lederer, Mingjing Li, Markus Lukacevic, Sebastian Pech, Bernhard Pichler, Vítězslav Štembera, Victoria Vass, Leopold Wagner, Hui Wang, Luis Zelaya-Lainez and Jiaolong Zhang. My special thanks go to Markus Königsberger and Thomas Schlappal, for interesting scientific and non-scientific discussions.

Furthermore, I like to gratefully acknowledge the support of the staff at the laboratory, namely Wolfgang Dörner, Dominic Hassan, Marcel Meyer, Roland Reihnsner and the former student assistant Gerhard Unger. Special thanks go to Gabriele Ostrowski, Martina Pöll and Astrid Schuh for the smooth handling of administrative issues, David Kaufmann for his great job as system administrator, and Christine Mascha (Dean's Office) for her administrative support during this thesis and teaching-related tasks.

Colleagues from Linnæus University, namely Michael Dorn, Bertil Enquist and Johan Vessby are thanked for their hospitality and support during my research stay in Växjö. Furthermore, Jean-Francois Boçquet, Romain Lemaître and Carmen Sandhaas are thanked for the fruitful discussions during working meetings in the frame of COST FP1402.

I would like to thank my friends and family for their support during the last couple of years. Especially, I would like to express my deepest gratitude to my parents Maria and Kurt for their restless support, for giving me the opportunity to receive an academic education – an opportunity they never got.

Abstract

Steel dowels are indispensable elements for the design of joints in modern timber structures. Dowels are broadly used because of their flexibility in design and easy assembling on-site, as well as due to their advantageous mechanical behavior. Recent developments in reinforcement techniques allow for designing ductile dowel joints, which exhibit nonlinear slip behavior. However, currently applied limit state approaches for calculation of connection strength are not able to fully exploit the potential of dowel joints. This calls for development of more advanced calculation methods, which was aimed for in this thesis.

For thorough understanding of the complex mechanical behavior of dowel connections, application of a so-called multiscale approach is advantageous. Thereby, nonlinear load-deformation behavior of dowel connections is studied on different length scales, from the scale of connection components, up to the joint level. The aim of this thesis was to exploit knowledge from lower scales in models that finally allow for nonlinear analysis of timber structures. In the work at hand, this was achieved by a combined experimental-numerical analysis.

Experimental studies on the nonlinear embedment slip of ductile dowel connections, and its relation to the orthotropic material behavior of wood, was one of the objectives of this work. Breaking new ground by testing up to large dowel displacements, at various angles to the grain, for unconstrained and constrained lateral displacement conditions, required development of new testing procedures and test setups. Test results gave access to nonlinear embedment slip curves and showed their dependence on loading direction and lateral displacement conditions.

In the next step, embedment slip data were exploited in modeling of single-dowel connections. Beam-on-nonlinear foundation modeling was applied for this purpose. Validation of connection tests and a parameter study not only highlighted suitability of the calculation method, but allowed for gaining insight into limit states. Thus, beam-on-foundation modeling was found to be an attractive alternative to advanced 3D FEM models for engineering design.

Parameterized equations for regression analysis of nonlinear slip curves, and interaction curves describing the grain angle dependence of mechanical parameters, were summarized in a literature review. With these equations at hand, a multi-dimensional parameterization method for the nonlinear slip as a function of the load-to-grain angle was developed. This method was applied to experimental data derived in embedment and single-dowel connection tests as well as in simulations. Analytical equations for connection slip are expected to facilitate engineering modeling at the single-dowel connection and joint level, respectively.

Joint modeling aimed at establishing a calculation method suitable for engineering design with an attractive trade-off between modeling effort, calculation time and accuracy. This was tackled by a semi-analytical model based on nonlinear elastic springs for the dowel slip and rigid connection members. Thereby, global joint slip, and thus stiffness and strength of joints, as well as local load distribution within joints can be predicted. This model proved to be suitable for single-dowel-based and joint-based design concepts. Calculation examples showed pronounced influence of loading direction dependence and nonlinearity of dowel slip on local load distribution, as well as on global joint slip. Influence of interaction between internal forces on the joint stiffness became obvious from structural analysis with nonlinear joint slip.

This work covers a combined experimental-numerical analysis of the slip behavior of ductile dowel joints, from the wood embedment and steel dowel bending behavior, the single-dowel slip, to the joint behavior, with final application in nonlinear structural analysis. Presented models predicted nonlinear slip with suitable accuracy and efficiency. Application of nonlinear joint slip in structural analysis showed the potential of ductile dowel joints, which could be exploited in engineering design by the herein presented multiscale modeling strategy.

Kurzfassung

Im modernen Ingenieurholzbau werden Stabdübelverbindungen aufgrund ihres vorteilhaften mechanischen Verhaltens und ihrer Flexibilität in Entwurf und Herstellung weitverbreitet eingesetzt. Neu- und Weiterentwicklungen von Verstärkungsmaßnahmen erlauben einen wirtschaftlichen Einsatz von querzugverstärkten Verbindungen, welche durch ein duktiles, nicht-lineares Last-Verformungsverhalten gekennzeichnet sind. Mit traditionellen, meist auf Grenzwertbetrachtungen basierenden Bemessungsmethoden, kann jedoch das volle Potenzial dieser Verbindungen nicht ausgeschöpft werden. Dies war die Motivation für die Entwicklung von erweiterten Berechnungsmethoden für Stabdübelverbindungen.

Für ein weitreichendes Verständnis des komplexen mechanischen Verhaltens von Dübelverbindungen ist die Anwendung einer Mehrskalenmodellierung von Vorteil. Bei diesem Ansatz wird das nichtlineare Last-Verformungsverhalten, ausgehend von den Verbindungskomponenten, hin zur Verbindungsmittelgruppe, auf unterschiedlichen Längenskalen untersucht. Das Ziel dieser Arbeit war es, mittels Modellen auf kleinen Längenskalen, Wissen über das mechanische Verhalten zu generieren, welches schlussendlich eine nichtlineare Analyse von Holzkonstruktionen ermöglicht. Dafür wurde ein kombiniert experimentell-numerischer Ansatz gewählt.

Als Grundlage für die Modellierung wurde eine experimentelle Untersuchung des nicht-linearen Lochleibungsverhaltens von duktilen Dübelverbindungen, unter Berücksichtigung des orthotropen Materialverhaltens von Holz, durchgeführt. Mit der Untersuchung des Lochleibungsverhaltens bis zu großen Dübelverschiebungen, in Kombination mit verschiedenen Kraft-Faserwinkeln und für unerzwungene und erzwungene Verschiebungsrandbedingungen, wurden neue Wege beschritten, welche die Entwicklung von neuen Versuchsaufbauten und Versuchsprogrammen erforderlich machten. Die Versuchsergebnisse zeigten eine starke Abhängigkeit der nichtlinearen Last-Verschiebungskurven von den Verschiebungsrandbedingungen des Dübels sowie von dessen Belastungsrichtung in Bezug auf die Faserorientierung des Holzes.

Im nächsten Schritt wurde das Last-Verschiebungsverhalten von Einzeldübelverbindungen, basierend auf den experimentellen Lochleibungsdaten, mittels eines nichtlinear gebetteten Balkenmodells bestimmt. Die Eignung dieser Modellierungsstrategie wurde durch Validierung des Modells anhand von Einzelverbindungsversuchen, sowie durch eine Parameterstudie unterstrichen. Es konnte gezeigt werden, dass mit dem Balkenmodell, neben der Vorhersage des nichtlinearen Last-Verschiebungsverhaltens, auch die Untersuchung von Grenzfällen möglich ist. Somit kann dieses Ingenieurmodell als attraktive Alternative zu aufwändigen 3D FEM Modellierungen von Einzeldübelverbindungen angesehen werden.

Des Weiteren wurden Regressionsgleichungen zur Parameterisierung des nichtlinearen Last-Verformungsverhaltens von Verbindungen, sowie von Interaktionskurven für mechanische Eigenschaften über den Kraft-Faserwinkel, in einem Literaturstudium zusammengefasst. Diese Methoden dienten als Grundlage für die Entwicklung eines mehrdimensionalen Ansatzes zur parameterisierten Beschreibung des Last-Verformungsverhaltens in Abhängigkeit des Kraft-Faserwinkels. Der mehrdimensionale Ansatz wurde anschließend auf Last-Verschiebungskurven aus Lochleibungs- sowie Einzeldübelversuchen und Einzeldübelmodellierungen angewandt. Die analytische Definition des Last-Verschiebungsverhaltens von Verbindungselementen erleichtert die Modellierung des Einzeldübel- bzw. Dübelgruppenverhaltens, und somit die Weiterentwicklung und Verbreitung dieser Modelle in der Ingenieurpraxis.

Die Modellierung von Dübelgruppen zielte auf die Entwicklung eines Ingenieurmodells ab, welches eine Ausgewogenheit zwischen Modellierungsaufwand, Berechnungszeit und Vorhersagegenauigkeit aufweist. Dies wurde mit einem semi-analytischen Modell ermöglicht, welches

das lokale Last-Verschiebungsverhalten der einzelnen Dübel durch nichtlineare Federn, eingebettet in starren Anschlussbauteilen, berücksichtigt. Mit diesem Modellierungsansatz kann sowohl das globale Last-Verformungsverhalten der Verbindung, als auch die lokale Lastverteilung innerhalb der Dübelgruppe vorhergesagt werden. Es wurde gezeigt, dass dieses Modell sowohl als Grundlage für Bemessungskonzepte basierend auf der Einzeldübeltragfähigkeit, als auch basierend auf Dübelgruppentragfähigkeit geeignet ist. Mittels Berechnungsbeispielen wurde der erhebliche Einfluss des nichtlinearen, belastungsrichtungsabhängigen Einzeldübelverhaltens auf die lokale Lastverteilung und das globale Dübelgruppenverhalten gezeigt. Die Anwendung des Dübelgruppenmodells in nichtlinearen Strukturmodellierungen von Holzkonstruktionen machte den Einfluss der Schnittgrößeninteraktion auf die Verbindungssteifigkeit, und somit auf die Lastverteilung in der Struktur sichtbar.

In dieser Arbeit wurde eine kombiniert experimentell-numerische Studie über das Last-Verformungsverhalten von duktilen Dübelverbindungen vorgestellt. Diese Studie spannt einen Bogen vom Lochleibungs- und Dübelbiegeverhalten, über das Last-Verschiebungsverhalten von Einzeldübelverbindungen, hin zu Dübelgruppen, mit anschließender Anwendung in nichtlinearer Strukturberechnung von Holzkonstruktionen. Es konnte gezeigt werden, dass die präsentierten Modelle eine effiziente und ausreichend präzise Vorhersage des Last-Verformungsverhaltens von Dübelverbindungen ermöglichen. Deren Anwendung in nichtlinearen Strukturmodellierungen unterstrich das Potenzial von duktilen Dübelverbindungen, welches durch den Einsatz der vorgestellten Mehrskalenmodellierung ausgeschöpft werden kann.

Contents

Introduction	1
Motivation	1
Field of investigations	3
Research objectives	3
Outline of the thesis	4
Contribution by the author	6
Experimental and computational analysis of the load-deformation behavior of joints and their components	7
Wood embedment and steel dowel bending resistance	7
Single-dowel behavior	11
Parameterization of slip curves	13
Joint behavior	14
Structural analysis with nonlinear semi-rigid joints	16
1 Load-to-grain angle dependence of the embedment behavior of dowel-type fasteners in laminated veneer lumber (Schweigler et al., 2016b)	18
1.1 Introduction	19
1.2 Materials and methods	21
1.2.1 Laminated veneer lumber specimens and steel dowels	21
1.2.2 Test setup	22
1.2.3 Load and deformation measurement techniques	23
1.2.4 Evaluation methods	24
1.3 Results and discussion	26
1.3.1 Displacement behavior	26
1.3.2 Embedment stress vs. dowel displacement	29
1.3.3 Stiffness behavior	32
1.3.4 Embedment strength	34
1.3.5 Surface strains and visual inspection of test specimens	36
1.4 Conclusions	38
Notation	39
2 Constrained displacement boundary condition in embedment testing of dowel-type fasteners in LVL (Schweigler et al., 2017)	41
2.1 Introduction	42
2.2 Materials and methods	43

2.2.1	Wood specimens and steel dowels	43
2.2.2	Test setup and loading protocol	45
2.2.3	Load and deformation measurement techniques	46
2.2.4	Evaluation methods	46
2.3	Results and discussion	48
2.3.1	Constrained lateral dowel displacement behavior	48
2.3.2	Load-displacement behavior	49
2.3.3	Embedment stiffness	51
2.3.4	Embedment strength	54
2.3.5	Influence of lateral displacement boundary conditions	56
2.4	Conclusions	59
	Notation	62
3	An engineering modeling approach for the nonlinear load-displacement behavior of single dowel connections – parameter study (Schweigler et al., 2016a)	63
3.1	Introduction	64
3.2	Engineering model	64
3.3	Experiments	65
3.3.1	Bending tests on steel dowels	66
3.3.2	Embedment tests of LVL	66
3.3.3	Single dowel connection tests	67
3.4	Model validation	68
3.5	Parameter study	70
3.5.1	Side member thickness	70
3.5.1.1	Connection strength and dowel failure modes	70
3.5.1.2	Comparison to EC 5 and DIN 1052:2008	72
3.5.1.3	Plastic deformations in the steel dowel	73
3.5.2	Load-to-grain angle	74
3.5.2.1	Connection slip behavior	74
3.5.2.2	Comparison to EC 5	75
3.5.2.3	Plastic deformations in the steel dowel	76
3.6	Conclusions	78
	Notation	79
4	Parameterization equations for the nonlinear connection slip applied to the anisotropic embedment behavior of wood (Schweigler et al., 2018b)	80
4.1	Introduction	81
4.2	General strategy for parameterization	83
4.2.1	Parameterization of slip curves (<i>Step01</i>)	86
4.2.1.1	Foschi (1974)	86
4.2.1.2	Yee and Melchers (1986)	86
4.2.1.3	Richard and Abbott (1975)	87
4.2.1.4	Jensen (1994)	87
4.2.1.5	Glos (1978)	88
4.2.1.6	Sauvat (2001)	88
4.2.2	Regression over the load-to-grain angle (<i>Step02</i>)	89

4.2.2.1	Hankinson (1921)	89
4.2.2.2	Root-mean-square (RMS) (Gupta and Sinha, 2012)	90
4.2.2.3	Sin-function / Cos-function for S-shaped trends	90
4.2.2.4	Adapted Gompertz function	90
4.2.2.5	Sin-function for bell-type trends	91
4.2.2.6	Adapted Gaussian function	92
4.2.2.7	Adapted Gumbel function	92
4.3	Application of parameterized regression equations to the embedment behavior of Laminated Veneer Lumber	92
4.3.1	Comparison of regression equations for parameterization of slip curves (<i>Step01</i>)	92
4.3.2	Comparison of regression equations for parameterization over the load-to-grain angle (<i>Step02</i>)	94
4.3.3	Parameterization of embedment test data for Laminated Veneer Lumber (<i>Step01–03</i>)	96
4.3.3.1	Parameterized vertical embedment stress, f_{hv}	97
4.3.3.2	Parameterized horizontal embedment stress, f_{hh}	100
4.4	Discussion of further influences	104
4.4.1	Initial slip	104
4.4.2	Influence of the displacement range of the embedment slip curve on regression parameters	104
4.4.3	Impact of the work on practical application	106
4.5	Conclusions	107
	Notation	108
5	Engineering modeling of semi-rigid joints for nonlinear analysis of timber structures (Schweigler et al., 2018a)	111
5.1	Introduction	112
5.2	Joint modeling approach	113
5.2.1	Modeling strategy and assumptions	113
5.2.2	Calculation procedure	115
5.2.3	Material models for single-dowel connection and joint behavior	119
5.2.3.1	Anisotropic nonlinear elastic joint model	119
5.2.3.2	Anisotropic linear elastic joint model	120
5.2.3.3	Isotropic linear elastic joint model	122
5.2.3.4	Other types of fastener behavior including contact	123
5.3	Joint model validation	123
5.3.1	Single-dowel connection slip for validation	123
5.3.2	Dowel joint under moment loading	124
5.4	Model applications for studying joint behavior	126
5.4.1	Input data for calculation examples	126
5.4.2	Joint slip	127
5.4.3	Joint limit surface – interaction of internal forces	130
5.4.4	Load distribution and load redistribution	132
5.5	Application in engineering design	135
5.6	Joint-based design of semi-rigid joints with nonlinear structural analysis	139
5.7	Conclusion	141

Notation	142
Conclusions and outlook	146
Summary of the combined experimental and computational study	146
Research contribution and main findings	147
Proposals for the next generation of design and test standards	150
Perspectives and future research studies	151
Bibliography	153
Personal information	161
Curriculum Vitae	161
Scientific Dissemination	163

Introduction

Motivation

Wood as building material has long history, going several thousand years back to the time when first humans became sedentary. The currently oldest known and still existing timber structure, namely a wooden well, is dated back to an age of more than 7000 years (Lisner and Rug, 2013). Timber was the prevalent construction material until the industrial revolution. During this time, the portion of timber related to the total volume of construction materials reduced from 80% in 1850 to about 30% in 1900 (Lisner and Rug, 2013). The importance of wood as building material further decreased in the 20th century to about 3–10%.

However, in the last decades wood is experiencing a renaissance as economic and sustainable building material. Keeping in mind that the building sector, including the energy consumed during the life time of buildings, is responsible for more than 30% of the global energy consumption (Berardi, 2017), highlights the potential of wood as building material to substantially contribute to reduction in CO₂ emissions. Beside ecological aspects, in recent years wood as building material got attractive from an economic point of view as well. Development of high-performance engineered wood based products in combination with new connection techniques allow for novel building systems for the design of modern timber structures. As a consequence, timber engineering is approaching the field of wide-spanning and high-rising buildings. Thus, going from traditional, workmanship designed structures to advanced, industrially produced structures, new modeling and design strategies are required. The complexity of modern timber structures makes the use of software including numerical methods indispensable. This is especially important for the design of connections, which play a key role in the design of modern timber buildings. Connections are costly in terms of labor, and thus, an efficient connection design influences substantially the competitiveness of timber structures.

Dowel-type fasteners, like nails, clamps, screws, rods, bolts and dowels, are characterized by their flexibility in application, and thus, dowel-type fasteners are probably one of the most important connection types in timber structures. Like timber structures themselves, dowel-type fasteners exhibit a long history. First types appeared by means of wooden nails in the 10th century (Gerner, 2000). Later iron, and consecutively steel was used as fastener material. In recent times new developments, by means of glued-in rods and self-tapping screws entered the market. With improvement of connection techniques, modeling strategies for dowel-type fasteners improved as well. At the very beginning, design of connections was purely based on experience and later on experimentally-based empirical models. From the first half of the 20th century on, analytical models, like the limit state approach by Johansen (1949) for laterally loaded dowel-type fasteners have been applied in engineering design. However, recent developments in the design of timber structures, and thus also in the complexity of their

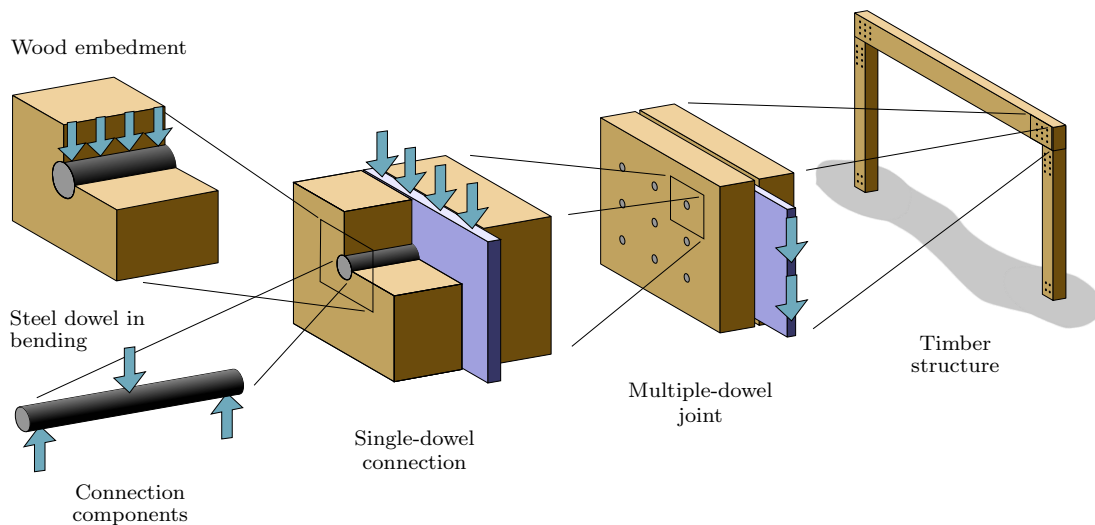


Figure 1: Scales of dowel-type connections in multiscale analysis.

connections, did not lead to advances in their engineering design. The state-of-the-art design of connections, see e.g. the European timber engineering design standard EC 5 (EN 1995-1-1, 2004), is still the limit state calculation of *Johansen*.

The complex mechanical nature of wood with its inherent anisotropic behavior, strongly influences the load-deformation behavior of dowel-type connections. Experimental investigations on different length scales, i.e., wood embedment and steel fastener bending, single-fastener, and joint level, showed pronounced nonlinear, loading direction dependent slip behavior (e.g. Bléron and Duchanois, 2006; Schoenmakers and Svensson, 2011; Dorn et al., 2013; Bouchaïr et al., 2007). However, this complex mechanical behavior is strongly simplified in current design standards. To fully exploit the potential of wood, more advanced calculation methods are required. Adaptability plays an important role in such methods, since dowel-type connections are characterized by their manifoldness in application. This calls for numerical methods, like for example models based on the finite element method (e.g. Schoenmakers et al., 2010; Franke and Quenneville, 2011; Resch and Kaliske, 2010). However, for engineering practice a trade-off between accuracy and modeling effort has to be found. One possibility would be to use semi-analytical or semi-numerical models, respectively, based on spring elements with rheological models representing the load-deformation behavior of connection elements.

For a thorough understanding of the load-deformation behavior of dowel-type connections, it is advantageous to use a so-called multiscale approach (see Figure 1). From a practical engineering point of view, the goal is the design of reliable and economic *structures*. Simply speaking, timber structures consist of two main elements, namely the timber members themselves and connections linking these members. Herein, joints are defined as a group of multiple *fasteners*, embedded in the surrounding wood matrix. On the scale of the *single-fastener*, wood and dowel properties, namely the *wood embedment* and the *steel fastener bending behavior*, are decisive.

Thus, for description of the load-deformation behavior of connections, a bottom-up approach could be used. In this case, load-deformation behavior of the lower scale is used as input to the next higher scale. This could be done for example by nonlinear springs, accounting for the loading direction dependent nature of wood. Such an approach is followed for

dowel connections in this contribution, where a combination of experimental and numerical methods is used at the length scales of wood embedment and steel dowel bending behavior, as well as at the scale of single-dowel behavior, which consequently serves as input to a semi-analytical joint model. The joint model finally gives access to the joint slip, implemented in structural analysis.

Field of investigations

This work is dedicated to a combination of selected materials and dowel-types, design and loading situations, as well as environmental conditions, being consistently applied to experimental and computational studies within a multiscale approach, from the scale of connection components up to the joint, for application in structural analysis. Experimental investigations for validation of models were limited to steel dowels, with three different diameters, embedded in laminated veneer lumber (LVL) made of spruce, with parallel orientated veneers. LVL was chosen for reason of its similar mechanical behavior to solid timber, taking advantage of its comparably low variability in mechanical properties, and thus, allowing for comparably small sample-size in experimental investigations. Experiments and simulations were dedicated to ductile connection behavior, which was ensured by screw-reinforcement of specimens in experimental investigations. Commonly used steel-to-LVL dowel connections in double-shear have been studied in this work, consistently over all length-scales. Standard climatic conditions, typical for timber in indoor applications, were chosen for experiments and mechanical properties in simulations. Furthermore, studies were limited to monotonic, static loading, for in-plane loading situations. From a structural analysis point of view, this includes loading by bending moment, axial and transverse forces, as well as combinations of these internal forces.

Research objectives

The main objective of the thesis has been a thorough study of the loading direction dependent global slip behavior of dowel joints and their components, beyond the quasi-elastic regime, including development of a semi-analytical joint model for nonlinear analysis of timber structures in engineering applications. Therefore, the following tasks have been defined:

- (a) Studying experimentally the nonlinear, loading direction dependent embedment behavior of steel dowels embedded in a clear-wood like engineered wood-based product, namely LVL, up to large dowel displacements (Publications 1 and 2).
- (b) Experimental analysis of global and local effects of unconstrained and constrained lateral displacement boundary conditions on the wood embedment and single-dowel behavior, by applying contactless optical measurement systems (Publications 1, 2 and 3).
- (c) Application and validation of a beam-on-nonlinear elastic foundation model for prediction of the nonlinear load-displacement slip of single-dowel connections (Publication 3).
- (d) Reviewing regression functions for parameterization of fastener slip and interaction curves, and development of a multi-dimensional parameterization method for nonlinear slip curves as a function of the loading direction (Publication 4).
- (e) Development, validation and application of an engineering model for semi-rigid joints for prediction of global joint slip and local load distribution within the joint (Publication 5).

- (f) Application of the engineering joint model to nonlinear structural analysis of timber structures (Publication 5).

These tasks were addressed in five peer-reviewed publications, outlined in the following.

Outline of the thesis

In the following, the outline of this thesis is summarized according to the publications.

In **Publication 1**, an extensive experimental program for the embedment behavior of steel dowels embedded in laminated veneer lumber was carried out. Full-hole embedment tests, based on recommendations of the related testing standard EN 383 (2007), on screw-reinforced LVL-specimens, for two different dowel diameters, and at seven different load-to-grain angles were tested. Loading was applied up to large dowel displacements, i.e., displacements of two times the dowel diameter, and thus representative for ductile joints. Unconstrained lateral dowel displacement boundary conditions were applied. Thus, the dowel was able to freely move perpendicular to the loading direction. A novel test setup was developed for this purpose. It uses a pendulum for unconstrained displacement loading. Furthermore, different loading directions were investigated by rotation of the base construction of the testing device. Global dowel displacement, as well as the local strains on the specimen surface, were measured by means of a contactless optical measurement system, based on digital image correlation (DIC). DIC allowed for recording of the nonlinear displacement path of the steel dowel, as a result of the anisotropic mechanical behavior of wood, when loading at an angle to the grain. Ductile, nonlinear embedment slip with a substantial influence of the loading direction was found. Pronounced displacement hardening got obvious for load-to-grain angles larger than 45° , when loading beyond the quasi-elastic regime. Furthermore, the local mechanical behavior of wood below the dowel, could be identified by strain fields quantified by DIC measurements.

Publication 2 is dedicated to experimental investigations of the embedment behavior under constrained lateral dowel displacement condition. The same testing conditions, i.e., same materials, same climatic conditions and same loading procedure, as for unconstrained embedment tests in Publication 1 were used. Thus, results from unconstrained and constrained experiments could be interpreted as a single dataset, which allowed for direct assessment of the influence of displacement boundary conditions. Constrained loading was achieved by using a biaxial test setup, which gave, in addition to vertical loading forces, access to laterally evoked forces as a result of the anisotropic nature of wood when loaded at an angle to the grain. DIC was applied, in order to capture the global dowel displacement, as well as the local strain distribution below the dowel. Unconstrained and constrained loading conditions could be related to a lower and upper limit of the embedment slip, respectively. A good correlation between lateral dowel displacement in unconstrained condition and lateral dowel forces in constrained condition was found. In addition, constrained loading resulted in considerably higher embedment forces in loading direction, than for unconstrained condition, when loaded different from principal material directions.

In **Publication 3**, the nonlinear load-displacement behavior of single-dowel connections, which depends on a variety of geometrical parameters, such as timber side member thickness and dowel diameter, as well as on mechanical parameters, such as load-to-grain angle, was studied. Experimentally determined embedment slip and steel dowel bending were applied to a numerical beam-on-nonlinear elastic foundation model for single-dowel connections. Model validation was based on a consistent experimental dataset, which encompassed connection

component as well as single-dowel connection tests. Good agreement of model predictions with experiments was found. A parameter study by adjusting the aforementioned parameters was conducted, and thus, the influence of these parameters on single-dowel connection strength and stiffness could be shown. In addition, elastic single-dowel connection limit was assessed by identification of the onset of plastic deformations in the steel dowel. Finally, numerical model predictions were compared to analytical results from design equations of the European design standard, EC 5. This highlighted a kinematical incompatibility of the current design model in EC 5, as well as a considerable overestimation of dowel connection stiffness when subjected to ultimate limit loads. From the parameter study it was seen that single-dowel connection strength and failure mode depend not only on geometrical and strength properties of the connection components, but also on the size of dowel displacement. Furthermore, the elastic single-dowel connection limit was found at comparable low dowel displacements.

In **Publication 4**, a literature study on regression functions for mathematical description of connection slip and interaction curves was carried out. This covered approaches from different scientific fields. Exponential, polynomial or power-functions, including, e.g., the approach by Foschi (1974), were identified to be promising for description of the connection slip in timber engineering. In contrast, combinations of exponential as well as trigonometric functions, e.g., the *Hankinson formula* (Hankinson, 1921), were found to be suitable for interaction curves. Suitability and flexibility were assessed by applying these functions to slip curves and interaction curves, typically found for dowel connections in timber engineering practice. Based on these functions, a multi-dimensional approach for parameterized equations of connection force as a function of connection displacement and load-to-grain angle was developed. This was realized by a three-step approach, where firstly, regression analysis of the slip behavior in various directions to the grain was performed before, in a second step, a parametric equation for the regression parameters over the load-to-grain angle was derived. These two regression steps were combined in a third step. Finally, the three-step approach was applied to parameterization of the dataset from embedment tests presented in **Publication 2**. Furthermore, the influence of various parameters, such as displacement range and initial slip, on the parameterized slip definition was discussed.

Publication 5 is dedicated to presentation and application of a semi-analytical joint model for determination of the nonlinear joint behavior. This joint model is based on kinematic and equilibrium considerations with the assumption of rigid members and nonlinear springs for dowel slip. It allows for determination of the global joint slip, as well as for local load distribution within the joint, and thus is suitable for single-dowel-based as well as for joint-based design methods. Validation of the model showed good correlation between results from joint experiments and model predictions, where joints were subjected to in-plane bending moments. The parameterization technique presented in **Publication 4** was applied on results from numerical simulations on single-dowel connections presented in **Publication 3**, and consequently used as input to nonlinear springs of the joint model. Subsequently, model capability was demonstrated by application to different joint design situations, and investigation of global and local joint behavior. In addition, the influence of model simplifications by means of using linear and loading direction independent, instead of nonlinear loading direction dependent single-dowel models, on the load distribution as well as joint slip, was discussed. Furthermore, predicted nonlinear joint stiffness was used as input to nonlinear analysis of timber structures, which gave access to load distribution and redistribution between joints and structural members. Finally, principles for a joint-based design approach with semi-rigid joints using nonlinear structural analysis were proposed.

Contribution by the author

This thesis is a cumulative work consisting of four publications in peer-reviewed scientific journals, and one peer-reviewed conference paper. The authors contributions to the corresponding publications are listed below:

- **Publication 1:** *Load-to-grain angle dependence of the embedment behavior of dowel-type fasteners in laminated veneer lumber* (Schweigler et al., 2016b)

The author contributed to the design of the experimental program, performed all experiments in the laboratory and their analysis, substantially contributed to interpretation of test data and prepared most of the manuscript.

- **Publication 2:** *Constrained displacement boundary condition in embedment testing of dowel-type fasteners in LVL* (Schweigler et al., 2017)

The author substantially contributed to the design of the experimental program, performed all experiments in the laboratory and their analysis, substantially contributed to interpretation of test data and prepared most of the manuscript.

- **Publication 3:** *An engineering modeling approach for the nonlinear load-displacement behavior of single dowel connections – parameter study* (Schweigler et al., 2016a)

The author performed most of the numerical study, substantially contributed to analysis and interpretation of simulation results and prepared most of the manuscript.

- **Publication 4:** *Parameterization equations for the nonlinear connection slip applied to the anisotropic embedment behavior of wood* (Schweigler et al., 2018b)

The author performed the literature study, greatly contributed to the concept and development of the parameterization method, performed the numerical study and prepared most of the manuscript.

- **Publication 5:** *Engineering modeling of semi-rigid joints for nonlinear analysis of timber structures* (Schweigler et al., 2018a)

The author substantially contributed to the concept and development of the semi-analytical model, performed main parts of the numerical study and prepared most of the manuscript.

Experimental and computational analysis of the load-deformation behavior of joints and their components

Methods for experimental and computational multiscale analysis of joint slip, from the load-deformation behavior of connection components up to the joint level, are described in the following (see Figure 2).

Wood embedment and steel dowel bending resistance

Loading single-dowel connections perpendicular to the dowel axis can cause bending of the nonlinear elastic embedded steel dowel. Thus, the *embedment behavior* of wood, by means of force-displacement curves, and the *steel dowel* under bending, described by moment-rotation relationships, need to be quantified.

Most of previous work related to the *embedment behavior* focused on experimental investigations. By reason of the anisotropic mechanical nature of wood and wood products, a complex stress state in the wood below the interface with the steel dowel is evoked. This makes numerical modeling of the embedment behavior challenging, and thus experimental investigations are indispensable.

In line with commonly used limit state models for the design of dowel connections (cf. EC 5), *experimental* investigations predominately focused on determination of single mechanical parameters, like embedment strength or stiffness, and less on documentation of the embedment slip curve.

Comprehensive experimental programs on the embedment strength were, e.g., performed by Whale and Smith (1986), who studied the embedment behavior of various softwood and hardwood species loaded parallel and perpendicular to the grain. Only a limited number of embedment tests were conducted at load-to-grain angles in between the principal material directions. Among others, Ehlbeck and Werner (1992), and Bléron and Duchanois (2006) carried out experiments for hardwood and softwood loaded by an angle to the grain, respectively. However, embedment strength is typically determined at comparable small dowel displacements, and thus pronounced displacement hardening effects for loading at an angle close to 90° , e.g., reported in Bléron and Duchanois (2006); Sawata and Yasumura (2002), have been rarely considered.

Less effort was invested on stiffness properties of embedment tests. Variability in experimental results showed that stiffness is sensitive to many parameters and these relationships are

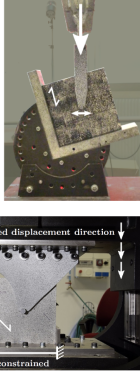
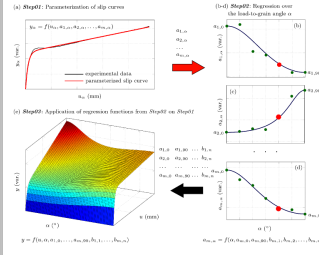
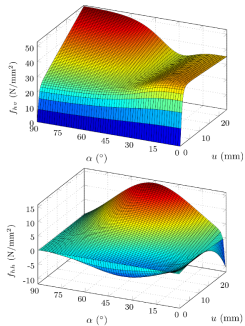
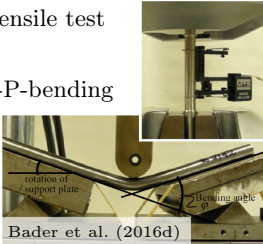
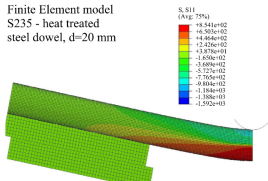
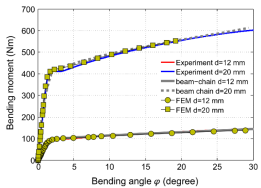
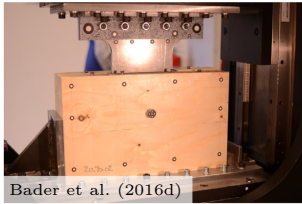
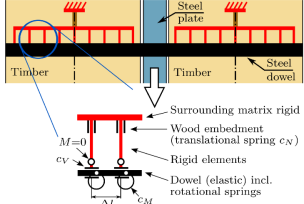
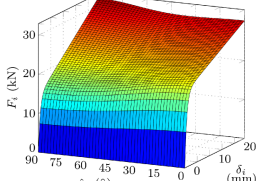
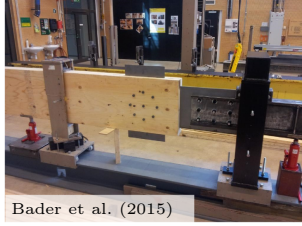
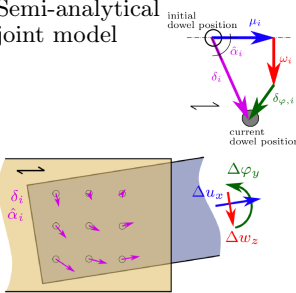
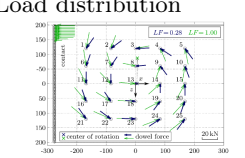
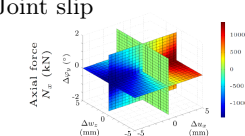
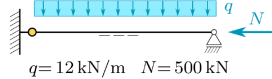
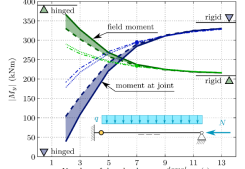
	Experimental investigations	Computational analysis	Output												
<p>Wood embedment</p> <p>Publication 1 Publication 2 Publication 4</p>	<p>Embedment tests:</p> <p>Unconstrained Constrained</p> 	<p>Parameterization</p> 	<p>Embedment slip (parameterized)</p> 												
<p>Steel dowel in bending</p> <p>Publication 3</p>	<p>Tensile test 3-P-bending</p>  <p>Bader et al. (2016d)</p>	<p>3D Finite Element model</p> <p>Finite Element model S235 - heat treated steel dowel, d=20 mm</p>  <p>Bader et al. (2016d)</p>	<p>Moment-rotation curve</p>  <p>Bader et al. (2016d)</p>												
<p>Single-dowel connection</p> <p>Publication 3 Publication 4</p>	<p>Single-dowel connection test</p>  <p>Bader et al. (2016d)</p>	<p>Beam-on-foundation model</p> 	<p>Single-dowel slip (parameterized)</p> 												
<p>Multiple-dowel joint</p> <p>Publication 5</p>	<p>Multiple-dowel joint test</p>  <p>Bader et al. (2015)</p>	<p>Semi-analytical joint model</p> 	<p>Load distribution</p>  <p>Joint slip</p> 												
<p>Timber structure</p> <p>Publication 5</p>	<p>Design concepts for timber structures</p> <table border="1" data-bbox="419 1753 738 1910"> <thead> <tr> <th>Type of structural analysis</th> <th>Type of resistance</th> <th>Type of failure criterion</th> </tr> </thead> <tbody> <tr> <td>linear elastic</td> <td>elastic</td> <td>local, fastener strength</td> </tr> <tr> <td>linear elastic</td> <td>nonlinear (elasto-plastic)</td> <td>local, fastener strength</td> </tr> <tr> <td>nonlinear</td> <td>nonlinear (elasto-plastic)</td> <td>global, joint strength</td> </tr> </tbody> </table>	Type of structural analysis	Type of resistance	Type of failure criterion	linear elastic	elastic	local, fastener strength	linear elastic	nonlinear (elasto-plastic)	local, fastener strength	nonlinear	nonlinear (elasto-plastic)	global, joint strength	<p>Nonlinear analysis</p> <p>Load case 02 (LC02)</p>  <p>$q = 12 \text{ kN/m}$ $N = 500 \text{ kN}$</p>	<p>Load distribution</p> 
Type of structural analysis	Type of resistance	Type of failure criterion													
linear elastic	elastic	local, fastener strength													
linear elastic	nonlinear (elasto-plastic)	local, fastener strength													
nonlinear	nonlinear (elasto-plastic)	global, joint strength													

Figure 2: Combined experimental-numerical study of dowel joints in multiscale analysis.

not obvious from experiments (Awaludin et al., 2007; Hwang and Komatsu, 2002). Stiffness parameters are considerably influenced by the applied test method, i.e., half-hole or full-hole tests (Awaludin et al., 2007; Franke and Magnière, 2014), as well as by the measurement technique for measuring the dowel displacement.

Only few tests beyond small dowel displacements are reported in literature, which however predominately focused on load application parallel or perpendicular to the grain. Bléron and Duchanois (2006), Sandhaas et al. (2013), and Sawata and Yasumura (2002) carried out embedment tests with steel dowels of 8–24 mm in diameter, up to dowel displacements of 12, 15 and 20 mm, respectively. Corresponding embedment properties are of importance for the engineering design, since recent developments related to reinforcement techniques, allow for a pronounced ductile behavior of dowel connections, and thus, for dowel displacements beyond the quasi-elastic regime.

As regards *standards for embedment tests*, most of previous work followed the regulations of the European test standard EN 383 (2007), or the American standard ASTM D5764-97a (2002). The latter allows for half-hole and full-hole test specimens, while EN 383 gives regulations only for full-hole tests. Testing standards define the specimen preparation, loading protocol, load and force measurement principles, documentation and evaluation of experimental data. Test standards regulate the definition of single mechanical parameters, like the embedment strength and stiffness, but documentation of the load-displacement curve is not intended. In addition, embedment experiments according to test standards are limited to small dowel displacements, i.e., up to a 5 mm displacement limit as specified in EN 383. However, no regulations are defined for loading at an angle in between the principal material directions. As a consequence, there is only limited data on embedment stresses beyond the displacement limit, as well as for loading at an angle to the grain.

The current version of the *European design standard for timber structures*, EC 5, uses only the embedment strength to describe the embedment behavior. For loading at an angle between the principal material directions, the *Hankinson formula* (Hankinson, 1921) is used as interaction criterion, which defines a reduction of the embedment strength with increasing load-to-grain angle.

In order to tackle the aim of studying the embedment behavior up to large dowel displacements, including loading at angles between the principal material directions, new experimental approaches had to be found. This included the development of novel test setups, and testing procedures (see Figure 2, and Publications 1 and 2). To allow for testing beyond the quasi-elastic displacement limit, timber specimens have to be reinforced, which was done in this study by inserting self-tapping screws. Dowel displacements and corresponding reaction forces have to be documented continuously, to give access to the nonlinear embedment slip, which is an indispensable input to numerical modeling of ductile single-dowel connections. Furthermore, unloading-reloading sequences should be included. This allows for determination of the unloading stiffness, which gives access to the elastic response of the embedment behavior.

For loading at an angle to the grain, beyond the quasi-elastic regime, the lateral displacement boundary condition, namely *unconstrained* (Publication 1) and *constrained* loading (Publication 2), respectively, substantially influences the embedment behavior. For such loading conditions, lateral displacements or lateral reaction forces are caused as a reason of unconstrained or constrained loading conditions, respectively. In order to quantify these parameters, alternative embedment test setups have to be used, as for example proposed herein. For the unconstrained condition, load was applied via a pendulum, allowing the dowel to freely move lateral to the applied loading direction, while for constrained condition, lateral dowel displacement was prevented in a biaxial test setup, which allowed to quantify corresponding

lateral reaction forces. To allow for quantification of the nonlinear dowel displacement path, when loading with unconstrained lateral displacement conditions, the use of contactless measurement systems is advantageous. This is why an optical deformation measurement system, based on digital image correlation (DIC) technique, was applied (Publications 1 and 2). One pair of cameras was placed at the front- and backside of the embedment test setup, respectively. By such a setting, a three-dimensional displacement field of the wooden specimen, as well as loading and bearing device can be recorded, which consequently allows for calculation of strains on the wood surface. Furthermore, DIC allows for determination of the dowel displacement relative to the unloaded wood surface, which is especially important for stiffness calculation. In addition, DIC gives insight into the deformation behavior of the wood below the dowels, which especially aims at a deeper understanding of the embedment behavior when loading at an angle to the grain. Thereby, with DIC it is possible to identify zones of densified wood, as well as local and global cracks.

Experimental and numerical methods can be used to describe the moment-rotation relationship of *steel dowels in bending*. When using numerical methods, the challenging task is to correctly identify the basic mechanical properties of steel dowels.

Numerous researchers, e.g., Sandhaas and van de Kuilen (2017); Bader et al. (2016d), identified higher steel grades as indicated by product specification. This is a result of defining only minimum and no maximum values regarding the mechanical properties of steel in the related product standard (cf. EN 14592, 2012). However, the steel quality substantially influences the bending resistance of the steel dowel, and thus the force required for development of plastic hinges in connections. Consequently, using mechanical properties from product specifications might lead to misprediction of the single-dowel failure mode, which might cause undesired brittle failure, instead of desired ductile failure. Thus, for numerical simulation of the moment-rotation behavior of the steel dowel in bending, tensile tests for identification of the basic mechanical properties of the steel are required.

Furthermore, investigations on steel dowels showed considerable difference in the behavior of dowels of different diameters (Bader et al., 2016d). As a possible reason, the authors mentioned the presence of a thin zone, with higher strength, close to the dowel surface, as a consequence of the manufacturing process. Thus, assuming a homogeneous material behavior over the cross-section of the dowel, naturally result in higher mechanical properties for smaller dowel diameters, since the outer layer of higher strength is probably of almost constant thickness, independent from the dowel diameter, and thus more dominant for smaller diameters. However, when using dog-bone shaped specimens for tensile tests, only the inner, i.e., softer, layer is tested.

Numerical modeling of the moment-rotation relationship of the steel dowel in bending can be done, e.g., by using solid elements in 3D FEM simulations, or by beam elements with 1D plasticity. For an accurate simulation of the moment-rotation behavior, numerical modeling calls for: (i) reliable mechanical parameters of the steel, ideally based on tensile tests, (ii) nonlinear elastic or even plastic material models, (iii) models being able to account for large displacements, which are present in dowel connections with plastic hinges, and (iv) models allowing for multiple layers over the cross-section of the dowel, in order to tackle possible outer layers of higher strength.

Alternatively, the moment-rotation relationship can be determined directly from *bending tests* on steel dowels. However, as a reason of inhomogeneous mechanical properties over the cross-section of the dowel, simple up- or down-scaling to other dowel diameters leads to erroneous results.

Similar to *testing standards* for wood embedment behavior, the testing standard for description of steel dowels in bending (EN 409, 2009) aims at definition of a single mechanical property, namely the yield moment of the fastener. According to EN 409, the yield moment of the dowel has to be determined for a bending angle as a function of the dowel diameter. Consequently, in the *design standard* EC 5, the yield moment of the dowel is used as input to the calculation of the single-dowel connection strength.

In this work, information on the steel dowel bending behavior were taken from Bader et al. (2016d). Therein, the authors used both, experimental investigations and numerical simulations (see Figure 2). To overcome the problem of heterogeneous mechanical properties over the dowel cross-section, a heat treatment process was used to guarantee homogeneous conditions. Experimental investigations using 3-point-bending tests on dowels with two different diameters were performed. On both ends, dowels rested on line-supported steel plates, which allowed for free inclination around the horizontal support axis. Furthermore a roller bearing was introduced at the support plates, allowing for unconstrained horizontal movement of the supports, which emerges at large dowel deformations. In addition, tensile tests on dog-bone shaped dowel specimens were carried out. For both experiments, forces from the testing machine, and displacements from LVDTs were continuously recorded. Subsequently, results from tensile tests were used as input to 3D FEM simulations of the 3-point bending tests. Calculations were based on large displacement theory and a nonlinear elastic material model. For simulations, constant mechanical properties over the cross-section were applied. A good correlation between simulated and experimentally determined moment-rotation relationships verified the assumption of homogeneous material behavior. Results from 3-point bending tests were subsequently used in Publication 3 for numerical modeling of the single-dowel slip behavior, by description of the steel dowel as beam chain including the nonlinear moment-rotation behavior from experiments in rotational springs.

Single-dowel behavior

Load-displacement behavior of single-dowel connections is influenced by numerous factors, like (i) mechanical properties of the components, i.e., wood embedment behavior of the single connection members, and steel dowel in bending, (ii) the geometry of the connection, i.e., number and location of shear planes, as well as side member thickness, and (iii) loading direction with respect to the grain orientation. Experimental, numerical as well as analytical methods can be applied to identify the single-dowel slip behavior.

In engineering practice, predominately *analytical* limit state analyses are used. Ideal plastic material properties of steel dowels in bending and of wood under embedment stresses are assumed. Consequently, only limit loads but no deformations are obtained. Thus, with these approaches only the strength of single-dowel connections, but not their associated displacement can be predicted, i.e., no information on the connection stiffness can be given. Each design situation, i.e., each connection layout, requires derivation of a design equation. Design equations in literature and design standards are given only for a limited number of connection layouts. Further design equations could be derived, however, this is time consuming. Their combination must fulfill compatibility, which might be difficult to establish in case of multiple shear planes.

Numerical simulations are used to overcome limitations of analytical approaches and for predicting the nonlinear load-displacement behavior of dowel connections. Furthermore, numerical models are characterized by their flexibility and adaptability in the connection layout, and thus, are not limited to specific design examples. Three-dimensional finite element method

(FEM) simulations of connections with elasto-plastic and brittle material models for wood might be used (Dias et al., 2010; Franke and Quenneville, 2011; Resch and Kaliske, 2010; Santos et al., 2009). These simulations allow gaining insight into the development of plastic deformations in steel dowels and the distribution of stresses in the timber members (Fueyo et al., 2009). However, up to now, most models were based on small strain theory, which limits maximum strains in the timber and, consequently, maximum dowel deformations in case of plastic hinges in steel dowels. In addition, modeling of single-dowel connections loaded at an angle to the grain was shown to be challenging, as a result of the complex mechanical behavior of wood. In such loading situations, shear stresses interacting with normal stresses substantially contribute to the wood embedment behavior, which is not fully understood yet. Furthermore, as a reason of considerable calculation time, as well as extensive effort for pre- and postprocessing, 3D FEM simulations are uneconomic for the daily use by engineers.

Alternatively, beam-on-foundation models are used for predicting slip curves of single-dowel connections. Compared to 3D FEM models, modeling and calculation effort substantially reduces. Linear foundation moduli might be used for simulating the embedment stiffness (Hager, 1930; Hirai, 1983), or more advanced approaches could be applied by considering the nonlinear embedment slip, as it was, e.g., proposed by Hochreiner et al. (2013).

Similar to numerical simulations, *experiments* on single-dowel connections allow for documentation of the nonlinear load-displacement curve. Experiments are used to get a deeper understanding of the mechanical behavior of single-dowel connections, regarding their global load-displacement behavior as well as local effects in the surrounding timber matrix. However, experimental approaches are cumbersome and costly in engineering design, and results from experiments are only valid for the specific tested connection setup. Thus, experimental design is limited to exceptional situations.

For experimental investigations of single-dowel connections, testing standard EN 26 891 (1991) is applied. Regulations in EN 26 891 are similar to the standard for embedment testing, EN 383. However, the strength of the single-dowel connection is defined for a displacement limit of 15 mm, instead of 5 mm, as it is used for embedment tests.

The current design approach for single-dowel connections in EC 5 (European yield model, EYM), is based on the limit state analysis proposed by Johansen (1949), Möller (1950), Meyer (1957). This allows for prediction of the single-dowel connection strength. However, kinematical compatibility between the dowel displacement at embedment strength (EN 383) and the bending angle for the yield moment of the dowel (EN 409) is not verified. Since the limit state approach does not give deformations, an empirical equation for their elastic stiffness in the serviceability limit state (SLS) is given. However, the stiffness is assumed to be isotropic, and thus, the single-dowel connection stiffness does not depend on the loading direction with respect to the grain. For calculation of the stiffness in the ultimate limit state (ULS), a constant factor of two-third is used for calculating a reduced secant stiffness.

In this work a numerical approach by means of the beam-on-nonlinear elastic foundation model proposed by Hochreiner et al. (2013) to predict the direction dependent nonlinear single-dowel slip behavior is followed (see Figure 2 and Publication 3). In addition, experimental results on single-dowel connections presented in Bader et al. (2016d) were used to validate this numerical approach. The beam-on-nonlinear elastic foundation model builds upon beam and spring elements. The steel dowel is discretized by a beam-chain, where the elastic behavior of the dowel is covered by the beam element itself, and the in general nonlinear plastic characteristics by rotational springs connecting the single beam elements. This beam-chain rests on rigid beam elements, including translational springs for the nonlinear embedment behavior. In addition, translational springs might be located along the steel dowel axis to account for

reaction forces, e.g., caused by friction forces, parallel to its axis. Several elements of one connection member are combined by another rigid element giving access to the reaction force of this member for a specific applied displacement. By summation of connection member forces, the single-dowel connection reaction force can be calculated. Finally, incremental load application yields a nonlinear slip curve for the single-dowel connection.

Parameterization of slip curves

Analytical or numerical models for single-dowel connections or joints, respectively, require input data of mechanical properties, such as the nonlinear elastic embedment or single-dowel connection slip. These data are determined either experimentally or numerically. In both cases, data are – by means of load-displacement curves – defined numerically, i.e., pointwise. However, for modeling purposes a closed mathematical description of slip curves would be desirable. This calls for parameterization techniques to transform numerically defined, into mathematically described slip curves.

Numerous researchers, from different scientific fields, proposed parameterization methods for slip curves. Exponential or power functions could be used, as it was, e.g., done by Foschi (1974), Yee and Melchers (1986), as well as by Richard and Abbott (1975). As an alternative, polynomial functions, see, e.g., Jensen (1994) or Glos (1978), or combinations of functions Sauvat (2001), might be applied.

Other types of functions were proposed to mathematically describe mechanical parameters over the load-to-grain angle. This includes the well-known *Hankinson formula* (Hankinson, 1921), which is currently used in EC 5 to calculate embedment strength of wood at an angle to the grain. A similar approach, was used by Gupta and Sinha (2012) for the shear strength of Douglas-fir at an angle to the grain.

Regression analysis, like the least square method, can be used to determine parameters for mathematical description of slip curves or interaction curves over the load-to-grain angle. Alternatively, some parameterization equations allow for physical interpretation of its parameters. In these cases, predefined parameters, e.g., from embedment or single-dowel experiments, can be applied directly in parameterization equations.

In this work it is the aim to develop a method, which allows for definition of the nonlinear slip behavior as function of the anisotropy. Therefore, a combination of parameterization methods for the description of the slip behavior with methods for the description over the load-to-grain angle is used (Publication 4).

A three-dimensional problem has to be solved, which is tackled by a three-step approach. Firstly, regression analysis of the slip behavior in various directions to the grain is performed before, in a second step, a parametric equation for the regression parameters over the load-to-grain angle is derived. These two regression steps are combined in a third step, resulting in a single mathematical equation of the force parameter as a function of the displacement parameter and the load-to-grain angle.

Parameterized definition of slip curves, as a function of the load-to-grain angle, were used on the level of the embedment behavior, as well as on the level of single-dowel connections (see Figure 2). Parameterized embedment slip definition served as input to the numerical beam-on-nonlinear foundation single-dowel model. Results from single-dowel model were parameterized as well, in order to serve as input to the joint model (Publication 5).

Joint behavior

In this work, a joint is defined as a group of at least two single-dowels. Thus, the joint behavior is driven by (i) the single-dowel load-displacement behavior, (ii) the interaction between the single-dowels, when acting as a group of dowels, (iii) the elastic, as well as possible brittle failure of the surrounding timber matrix, and (iv) the applied global loading by means of internal forces.

When describing joint behavior, it has to be distinguished between the *local* behavior, i.e., the load distribution over the single-dowels within the joint, and *global* behavior, i.e., the stiffness and strength of the joint as a whole. The latter is of importance, when using a *joint-based* design, as well as when addressing joint stiffness in structural analysis, to account for the prevalent case of semi-rigid behavior of dowel joints. The local load distribution is decisive for *single-dowel-based* design, as it is used in the current version of EC 5, since single-dowel forces are used for verification of the joint bearing capacity. However, load distribution is crucial for joint-based design as well. Joint-based design requires ductile behavior of the joint. This has to be ensured by verification against brittle failure modes, and thus, thorough knowledge on the load distribution among the dowels and stresses in the timber matrix are essential. Joint behavior can be studied by applying experimental, numerical or analytical methods.

In engineering practice, mainly *analytical* approaches are used. Commonly, calculation based on the so-called polar moment of inertia is applied for determination of the load distribution and joint stiffness. This approach assumes, and thus is limited to, linear elastic single-dowel behavior, neglecting the loading direction dependent dowel slip. However, it was shown by, e.g., Bader et al. (2017), that the nonlinear direction dependent single-dowel behavior substantially influences load distribution within the connection, and consequently the global joint behavior. Furthermore, elastic deformations of the connection members, namely wood or steel, are neglected. Thus, uniform load distribution is assumed when loaded by axial and/or transverse force. Nevertheless, a substantial influence of elastic deformations of the timber matrix was shown by Jorissen (1998) and Bader et al. (2017), for small, i.e., quasi-elastic dowel displacements when loaded by a transverse force. Furthermore, it is assumed, that dowel forces are linearly related to the distance from the center of rotation, when loaded by a bending moment, as well as that no interaction between internal forces exists. However, both is only true for the herein assumed linear elastic, loading direction independent single-dowel behavior. Racher (1995) extended this analytical approach by introducing loading direction dependent, but still linear-elastic, single-dowel slip behavior.

Coupled formulation, i.e., considering interaction between internal forces is required when loading joints by a combination of bending moment with axial and/or transverse force. This is however neglected in most practical designs.

Numerical models are used to overcome aforementioned simplifications and limitations of analytical models. Three-dimensional discretization of the joint components with solid elements in FEM software could be used (e.g. Ormarsson and Blond, 2012; Avez et al., 2017). This approach requires appropriate material models for wood and steel, which must at least account for elasticity and plasticity. Definition of such constitutive models for wood might be challenging, as a reason of large strains close to the dowel-wood interface. In addition, a contact criterion (Dorn, 2012; Iraola et al., 2016), to account for the interaction between dowel and timber, has to be defined. 3D FEM models allow for deep insight into the local stresses and deformations in the joint. However, the modeling and computational effort is demanding, which makes 3D models inappropriate for engineering practice. As regards

practical design, 3D models could be reduced to 2D FEM models of joints (Bader et al., 2017), or even to a combination of beam-on-foundation model for single-dowel connections (e.g. Hochreiner et al., 2013) and a three dimensional discretization of the timber (Bader et al., 2017). As an advantage, these models allow to consider effects of elastic deformations of timber between the dowels, as well as give access to the stress distribution over the timber thickness. However, computational efforts are still considerable, and thus, these models are unsuitable for integration in structural analysis for engineering design.

An attractive alternative related to the accuracy calculation time trade-off, are semi-analytical joint models. However, these models do not allow for considering the influence of the elastic deformation of timber in the joint area on the load distribution, as well as stress distribution over the timber thickness, as a reason of assuming rigid, two dimensional elements for the connection members. Corresponding models with rigid members and springs have been presented by Descamps et al. (2011) and Jensen (1994). These models allow for coupled formulation of the joint slip, i.e., the influence of interaction between internal forces can be considered. As a result, realistic nonlinear joint stiffness and load distribution within the joint can be determined (Publication 5). Compared to 3D or 2D FEM models, pre- and post-processing effort, as well as calculation time decreases substantially, which allow for integration in engineering structural analysis.

Experiments on dowel joints allow for documentation of the nonlinear load-displacement curve. Experiments are used to get a deeper understanding of the mechanics of the global joint behavior, by means of load-displacement curves or moment-rotation curves (Bader et al., 2015, 2016c; Bouchair et al., 2007; Sandhaas and van de Kuilen, 2017). Furthermore, application of advanced measurement techniques, like, e.g., contactless DIC-technique, give access to local dowel deformations and strains in the timber matrix, and thus, to the load distribution within the joint (Bader et al., 2015, 2016c; Sjödin et al., 2006). Nevertheless, experimental investigations are cumbersome and unhandy for engineering design applications, since results from experiments are valid only for the specific tested joint setup and loading situation, and thus, the required flexibility for engineering design is not given. General principles for experimental investigations on joints are specified in the same *testing standard* as for single-dowel connections, i.e., EN 26 891 (1991).

As regards the engineering design of dowel joints, the *European standard for design of timber structures*, EC 5, is applied. As mentioned earlier, the current version of EC 5 follows a single-dowel-based design. Hardly any regulations regarding the stiffness and strength of joints is given. Information on the load distribution in the joint are missing as well, which however is required for verification of the single-dowel strength, limiting the joint strength in EC 5. In engineering practice, the aforementioned analytical approach, based on the polar moment of inertia, is commonly used to distribute loads within the joint, in order to get single-dowel forces for verification.

In this work a semi-analytical model for engineering design of dowel joints was proposed (see Figure 2 and Publication 5). This joint model has proven to be a promising alternative to simplified analytical models, and complex numerical models for description of the mechanical behavior of dowel joints. On the one hand, this model allows for calculation of load distribution within the joint, which gives access to realistic, and thus, more reliable prediction of single-dowel forces. On the other hand, the herein proposed model allows for prediction of the nonlinear load-deformation behavior of joints, which can be used for nonlinear analysis of timber structures with ductile semi-rigid joints. The modeling strategy proposed by Jensen (1994) was taken up. In this semi-analytical approach, load distribution and joint stiffness is determined based on nonlinear, loading direction dependent springs for the load-displacement

behavior of dowels embedded in rigid connection members. Based on a set of relative joint deformations, i.e., relative axial and transverse displacement and relative rotation, size and orientation of single-dowel displacements are calculated. Load distribution, i.e., single-dowel forces, is determined by considering the load-slip behavior of the single-dowels. Applying equilibrium conditions gives a set of internal forces for the input set of relative joint deformations. For numerical determination of the joint stiffness, incremental loading is required. An iterative procedure is necessary, when calculating load distribution based on a set of internal forces. This approach allows for uncoupled as well as coupled formulation of the joint behavior (Publication 5). Advantageous is application of parameterized single-dowel slip definition, as proposed in Publication 4.

The joint model was applied to different engineering design situations (Publication 5). Furthermore, the modeling strategy was validated by experiments on dowel joints loaded by a bending moment (Bader et al., 2015).

Structural analysis with nonlinear semi-rigid joints

Many modern timber structures are characterized by a complex, often statically indetermined structural system. In such structures, joint stiffness affects load distribution within and deformation of the structure (Brühl et al., 2011; Racher, 1995). Thus, loading of the joint and structural members depend on the stiffness of the joint and timber members. At the same time, the stiffness of the joint depends on the loading of the joint, especially when taking nonlinear joint slip into account. Thus, in statically indetermined structures it is of special importance to take the interaction between joints and timber members into account.

In structural analysis, joint stiffness can be considered by springs connecting structural members. Linear or nonlinear, uncoupled or coupled springs, representing the joint slip might be used (Publication 5). Most commonly, *uncoupled* linear joint stiffness is applied in structural analysis (Racher, 1995). Linear spring definition allows only for studying the structural response in the quasi-elastic regime, representing serviceability load cases. In uncoupled approaches, the influence of simultaneously acting internal forces on the joint stiffness is neglected. For small, i.e., quasi-elastic joint slip, uncoupled linear joint definitions are a good approximation as it is shown in Publication 5. Thus, for studying SLS load cases or for joint stiffness sensitivity analysis of a structural system, definition of uncoupled linear joint stiffness is sufficient.

In contrast, *coupled* nonlinear joint stiffness allow to describe the joint, and thus, the structural behavior beyond quasi-elastic deformations. Thus, this approach is appropriate for structural analysis of ULS loading situations. Load redistribution between joints and timber members can be studied (Publication 5). When applying coupled springs, the influence of simultaneously acting internal forces on the joint stiffness is considered. Application of a coupled and possibly nonlinear joint slip in structural analysis can be realized in two ways: (i) the predefined nonlinear coupled joint behavior is considered as input to the structural analysis, or (ii) numerical or semi-analytical joint models are directly implemented in the structural analysis software.

Herein, the approach of predefined joint slip is followed (see Figure 2 and Publication 5). In the case of coupled description, each internal force at the joint is a function of all relative deformations at the joint. Thus, e.g., for in-plane loading, each of the three internal forces, namely axial force, transverse force and bending moment, depend on all three relative joint deformations, namely, relative axial and transverse displacement and relative rotation. These coupled nonlinear joint definitions are predefined based on the aforementioned semi-analytical

joint model. A three-dimensional grid of relative joint deformations is created, where each grid point accommodates a unique set of relative joint deformations. Each of this relative joint deformation sets is applied to the semi-analytical joint model, resulting in a set of internal forces, describing the stiffness of the coupled springs. These coupled springs are implemented for structural analysis, with nonlinear coupled joint behavior.

Chapter 1

Load-to-grain angle dependence of the embedment behavior of dowel-type fasteners in laminated veneer lumber (Schweigler et al., 2016b)

Authored by Michael Schweigler, Thomas K. Bader, Georg Hochreiner,
Gerhard Unger & Josef Eberhardsteiner

Published in *Construction and Building Materials*, 126:1020–1033, 2016

The final publication is available at:

<http://www.sciencedirect.com/science/article/pii/S0950061816314891>

Abstract: Load-to-grain angle dependence of the embedment behavior of steel dowels in laminated veneer lumber, as a consequence of the anisotropic material behavior of wood, is experimentally investigated in this study. As a novel issue, in addition to the stress dependence, the displacement path of the dowel depending on the load-to-grain angle, is discussed. Full-hole embedment tests of screw-reinforced LVL specimens up to dowel displacements of two times the dowel diameter and thus, representative for highly ductile dowel connections were conducted. Tests were performed with unconstrained lateral displacement boundary conditions of steel dowels with a diameter of 12 mm and 16 mm. Surface deformations were monitored with a full-field deformation measurement system. Increasing the load-to-grain angle caused reduced quasi-elastic limits and loading stiffness. However, for load-to-grain angles of 60° and higher, a pronounced displacement-hardening effect, leading to high embedment stresses at large dowel displacements, was observed. For the investigated dowel diameters, surface strains and plastic deformations around the dowel indicate an almost dowel diameter independent load bearing area, which might explain higher nominal embedment stresses and consequently a more pronounced hardening effect of the smaller dowel diameter. Dowel displacements perpendicular to the initial loading direction, i.e., nonlinear displacement paths of the dowel, were related to the anisotropic stiffness of wood and densification effects close to the dowel. The established experimental dataset was compared to current European timber engineering design equations and could serve as input to analytical and numerical models of dowel connections.

Keywords: full-hole embedment tests, anisotropy, laminated veneer lumber, ductility, displacement boundary conditions, digital image correlation

1.1 Introduction

The embedment behavior of steel dowels in wood and engineered wood based products, as an essential characteristic in the design of dowel connections, is investigated in this experimental study. Due to the inherent anisotropic mechanical nature of wood and wood products, a complex stress state in the wood below the interface with the steel dowel is evoked. This complex stress state is commonly simplified in engineering applications by using a fictitious uniform embedment stress distribution over the diameter of the dowel (EN 383, 2007).

In previous studies, embedment testing of wood and wood products predominantly focused on loading in the principal material directions, i.e., parallel (0°) and perpendicular to the grain (90°). Extensive experimental programs, serving as input to current timber engineering design standards, were performed by Whale and Smith (1986), who investigated the embedment behavior parallel and perpendicular to the grain for various softwood and hardwood species.

Knowledge about the embedment stress at load-to-grain angles in between the principal material directions is essential, since in engineering applications, the individual dowels of dowel connections are typically loaded at arbitrary angles to the grain. Loading at arbitrary load-to-grain angles is particularly the case for dowel groups transferring bending moments (Bader et al., 2015, 2016c). Only a limited number of experiments have been conducted at load-to-grain angles in between the principal material directions. Ehlbeck and Werner (1992) investigated three intermediate load-to-grain angles on hardwood species and proposed using the so-called *Hankinson* formula (Hankinson, 1921) as an interaction criterion. The latter is used in the current version of the European design standard for timber structures, EN 1995-1-1 (Eurocode 5) (EN 1995-1-1, 2004) in order to account for the influence of the load-to-grain angle on the embedment strength. Further experimental investigations on the load-to-grain angle dependence, and proposals for adjustments of the interaction criterion, were carried out for softwood by Bléron and Duchanois (2006), for European hardwood by Hübner et al. (2008), for tropical hardwood by Awaludin et al. (2007) and for solid timber and laminated veneer lumber (LVL) from radiata pine by Franke and Quenneville (2010). However, proposals for design equations have been limited to the assumptions of the European yield model (EN 383, 2007; Johansen, 1949), i.e., an assumed ideal plastic material behavior of wood, while pronounced hardening effects for load-to-grain angles close to 90° have rarely been considered for the engineering design of connections (Hochreiner et al., 2013; Pedersen, 2002).

Compared to embedment strength properties, less data are reported as regards stiffness properties of embedment tests and their dependence on wood and steel dowel characteristics. Full-hole embedment tests were shown to yield lower stiffness values compared to half-hole embedment tests, since unpreventable bending deformations of the dowels increase the displacements measured in full-hole tests (Franke and Magnière, 2014; Santos et al., 2010). Contradictory data were presented regarding the influence of the dowel diameter on the initial stiffness. An increase in stiffness would be suggested by test results of Karagiannis et al. (2016), while in Hwang and Komatsu (2002) and Stamato and Calil Jr (2000) a decrease with increased dowel diameter is reported. Viscoelastic effects on the stiffness of dowel connections under serviceability conditions were investigated in Reynolds et al. (2013).

Embedment stresses change nonlinearly with the size of the prescribed dowel displacement. The majority of embedment experiments has been limited to small dowel displacements,

i.e., up to a 5 mm displacement limit as specified in the European testing standard EN 383 (2007). Particularly embedment tests parallel to the grain are dominated by a brittle splitting failure at even smaller displacements (Sandhaas et al., 2013). Only few tests beyond this limit are reported in literature. Sandhaas et al. (2013) studied the embedment behavior parallel to the grain for various softwood and hardwood species up to a maximum dowel displacement of 15 mm. Bléron and Duchanois (2006) and Sawata and Yasumura (2002) carried out embedment tests on softwood species up to dowel displacements of 12 and 20 mm, respectively. Corresponding embedment properties are of importance for the engineering design, since recent developments related to reinforcement techniques (Lathuilière et al., 2015; Santos et al., 2013, see e.g.), allow for a pronounced ductile behavior of dowel connections (Brühl et al., 2011), and thus, for single dowel displacements beyond the displacement limit defined in test standards (Bader et al., 2015, 2016c). Several further influences, such as the material quality (Sandhaas et al., 2013) and the surface characteristics (Rodd, 1973; Sjödin et al., 2008) of the steel dowel, on the embedment stresses and the ductility of dowel connections have been revealed.

Finally, embedment stresses are influenced by the lateral displacement boundary conditions of the steel dowel during loading. To the best of our knowledge, this effect has hardly been investigated (Bader et al., 2016d) and is again a consequence of the anisotropic material characteristics of wood. For load-to-grain angles in between the principal material directions of wood, a lateral displacement (Bléron and Duchanois, 2006) or a reaction force (Bader et al., 2016d) is encountered for unconstrained or constrained displacement boundary conditions, respectively. The corresponding effects can be related to dowels in timber-to-timber and steel-to-timber connections, respectively. Regarding the latter, the displacement direction is prescribed by a steel plate, typically connecting several dowels, while the dowels are unconstrained in the lateral direction in case of timber-to-timber connections. Increasing the embedment testing displacement limit is expected to amplify the corresponding displacement and load effects on the overall embedment stress-displacement relationship.

The aim of this study was to establish a complete experimental dataset for specific combinations of a wood based product and steel dowels, which could serve as input to analytical and numerical models of dowel connections (Bader et al., 2016d; Hochreiner et al., 2013) as well as for a revision of corresponding engineering testing (EN 383, 2007) and design standards (EN 1995-1-1, 2004).

Derived from the above described characteristics of the embedment behavior, the particular objective of this study was a thorough experimental characterization of the embedment behavior of steel dowels in LVL at various load-to-grain angles up to large dowel displacements, representative for ductile dowel connections. Special emphasis was laid on the lateral displacement of the dowel. In addition, the surface strain distribution was recorded. The latter objectives were tackled using a full-field deformation measurement system for monitoring of surface displacements of wood as well as of the steel dowel and the loading device. This technique has proven to support the evaluation of embedment (Reynolds et al., 2016; Schoenmakers and Svensson, 2011) and connection tests (Bader et al., 2015, 2016c,d; Karagiannis et al., 2016; Sjödin et al., 2006; Stelmokas et al., 1997) by giving access to three-dimensional deformation and strain fields over a predefined field of view. It facilitates the interpretation and identification of load transfer mechanisms and of the development of cracks.

Herein, full-hole embedment tests were carried out following the principles of EN 383 (2007). The test setup allowed for an unconstrained lateral displacement of the dowel by using a pendulum loading device in a uniaxial test machine. LVL was chosen by reason of its comparably homogeneous but still anisotropic material behavior. This was expected to

reduce the variation in test results, and thus to give access to causal relationships between the investigated material characteristics and the embedment stress-displacement behavior. Also, the number of test repetitions for a specific test configuration could be reduced due to the reduced variation in material properties. Tests were performed for load-to-grain angles from parallel (0°) to perpendicular to the grain (90°) with a step size of 15° . The influence of the dowel diameter on the test results was investigated by using dowels with a diameter of 12 mm and 16 mm. LVL test specimens were reinforced with self-tapping screws in order to avoid extensive premature splitting of the LVL and to allow for testing up to dowel displacements of at least two times the dowel diameter. Test results will be compared to mean values suggested by Eurocode 5 (EN 1995-1-1, 2004).

1.2 Materials and methods

1.2.1 Laminated veneer lumber specimens and steel dowels

In total, 85 embedment tests were performed with free (i.e., unconstrained) lateral dowel displacements. Tests with two different dowel diameters (d), 12 mm and 16 mm, loaded under $\alpha_{initial} = 0^\circ, 15^\circ, 30^\circ, 45^\circ, 60^\circ, 75^\circ, \text{ and } 90^\circ$ to the grain were carried out.

Test specimens were manufactured of LVL with parallel oriented veneers from spruce (Kerto-S[®], Metsä, Finland). LVL with a thickness of 51 mm was chosen and only for a small number of tests with 12 mm dowels, LVL with a thickness of 45 mm was used. Specimen width and height were 200 mm, see Fig. 1.1 and Table 1.1. A reinforcement of the LVL specimens by means of self-tapping screws (SPAX T-STAR plus, SPAX International GmbH & Co.KG, Germany), with a diameter of 8 mm and a length of 180 mm was inserted into predrilled holes below and above the dowel, see Fig. 1.1. In order to avoid influences of the reinforcement on the embedment behavior, screws were located as far away from the loaded dowel as possible (Fig. 1.1). For tests perpendicular to the grain, which were not reinforced, the width was increased to 400 mm. Specimen dimensions, reinforcement measures, the number of tests per load-to-grain angle and dowel diameter are summarized in Table 1.1.

As far as possible, specimens for a certain test series and a certain dowel diameter were cut from the same LVL board. Consequently, low variation in the density of the specimens was found. Test specimens had a mean density of 510.3 kg/m^3 (stdv = 9.15 kg/m^3) and 501.9 kg/m^3 (stdv = 8.26 kg/m^3) for dowels with 12 mm and 16 mm diameter, respectively.

Before testing, specimens were stored in a climate chamber at standard climate conditions of 20°C and 65% relative humidity, until mass equilibrium was reached. The corresponding moisture content (MC) was determined on small, kiln-dried LVL specimens and amounted to 11.45% (stdv = 0.548%, n = 11).

Special attention was paid to the steel grade and surface quality of the dowels. In order to ensure only elastic bending deformations of the dowel and therefore quasi uniform loading over the thickness of the specimen, dowels of high steel quality were used. In this study, dowels were made of two different steel qualities, i.e., conventional galvanized steel dowels (steel quality S 235) and parallel pins of hardened steel with smoothed surface. Parallel pins did not have any surface coating, as it was the case for galvanized steel dowels.

In order to describe the surface quality of the different dowels, the surface texture of each dowel was recorded by means of a contact-free characterization technique based on the principle of chromatic distance measurement (FRT MicroProf[®], FRT GmbH, Germany). The arithmetic average of the surface roughness, R_a , measured at four different positions on the dowel surfaces, was used to describe the surface quality. A cutoff wavelength of 0.8 mm was

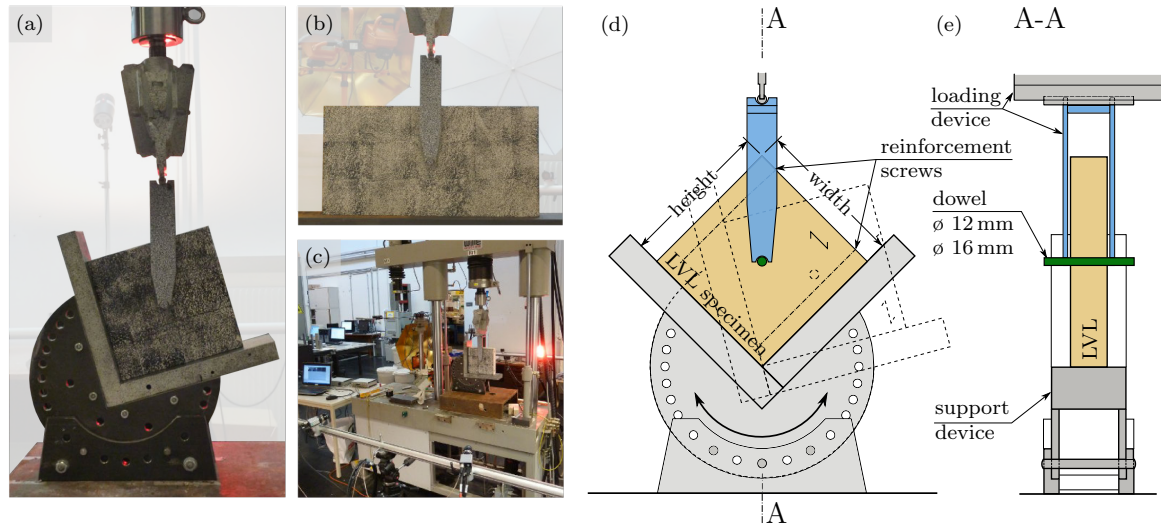


Figure 1.1: Test setup for full-hole embedment tests: (a) $\alpha=15^\circ$, (b) $\alpha=90^\circ$, (c) DIC-measurement system, (d) sketch of the test setup for loading under 45° and (e) cross section through the test setup.

applied for determination of R_a , as recommended in EN ISO 4288 (1997). The mean value of R_a amounted to $0.90 \mu\text{m}$ ($\text{stdv}=0.014 \mu\text{m}$) and $1.11 \mu\text{m}$ ($\text{stdv}=0.034 \mu\text{m}$) for galvanized steel dowels with 12 mm and 16 mm diameter, respectively. For the parallel pins of hardened steel with smoothed surface, R_a values of $1.14 \mu\text{m}$ ($\text{stdv}=0.029 \mu\text{m}$) and $0.68 \mu\text{m}$ ($\text{stdv}=0.007 \mu\text{m}$) were measured for dowels with a diameter of 12 mm and 16 mm, respectively. Based on these results, no significant influence of the surface quality on the embedment behavior was expected.

1.2.2 Test setup

Tests were carried out as full-hole embedment tests under compression following the principles of EN 383 (2007). A special support device was designed for testing at various load-to-grain angles. It consisted of a rectangular V-shaped steel structure, which rested on a circular support construction (Fig. 1.1). The latter could be rotated in 5° steps relative to each other allowing testing between 0° and 90° to the grain. This support device allowed for an economic production of the test specimens, since they could be cut in a rectangular shape parallel and perpendicular to the grain direction of the LVL, independent of the applied load-to-grain angle. The initial load-to-grain angle was set by rotation of the support device in the corresponding position before testing.

Specimens were loaded via the steel dowel, located at the center of the LVL specimen. Steel elements on both sides of the specimen constituted the loading device, which acted as a pendulum with the center of rotation at the contact point fixed to the cross head of the testing machine. It was loaded via vertical displacements of the testing machine, see Fig. 1.1. The fillet radii at the top and the bottom of the steel loading elements were slightly larger than half of the dowel diameter, in order to avoid frictional effects. Due to the pendulum, the dowel was not constrained perpendicular to the loading direction, and thus, able to follow the in general nonlinear displacement path, evoked by the orthotropic material behavior of LVL, or wood in general. Specimens loaded perpendicular to the grain were directly placed at the

Table 1.1: Dimensions of tested LVL specimens (cf. Fig. 1.1).

$\alpha_{initial}$ (°)	Width (mm)	Height (mm)	Thickness (mm)	Unreinforced, reinf. (-)	Number of tests (-)
<i>d</i> = 12 mm					
0	200	200	45/51	R	7
15	200	200	45/51	R	5
30	200	200	45/51	R	6
45	200	200	45/51	R	6
60	200	200	45/51	R	7
75	200	200	45/51	R	6
90	400	200	45/51	U	7
<i>d</i> = 16 mm					
0	200	200	51	R	6
15	200	200	51	R	7
30	200	200	51	R	6
45	200	200	51	R	6
60	200	200	51	R	6
75	200	200	51	R	6
90	400	200	51	U	4

foundation construction of the testing machine without support device.

Tests were partly performed in a uniaxial electro-mechanical testing machine of type LFM 150 and partly in a servo-hydraulic testing machine of type DLFV 250, both of manufacturer Walter and Bai. Loading was applied displacement controlled up to a displacement of at least two times the dowel diameter, i.e., 24 mm and 32 mm for 12 mm and 16 mm dowels, respectively. In addition, two unloading sequences, one in the quasi-elastic and one in the elasto-plastic domain were applied. The first unloading cycle was performed at an embedment stress of approximately half of the expected quasi-elastic stress limit. The second unloading cycle was applied only for a part of the tests, at a dowel displacement approximately equal to the dowel diameter. At the beginning and at the end of each unloading cycle, the force (for the first unloading cycle) or displacement (for the second unloading cycle) was kept constant for 5 sec, in order to reduce the influence of time dependent effects on the unloading stiffness (Bader et al., 2016a). Because of the control software of the testing machines, the holding criterion had to be equal to the stopping criterion. A displacement rate of 2 mm/min for loading, unloading and reloading sequences was chosen, with an exception for the second unloading and reloading sequence which was performed with a displacement rate of 6 mm/min in order to reduce test durations.

1.2.3 Load and deformation measurement techniques

Vertical reaction forces as a consequence of prescribed displacements were directly recorded by the load cell of the testing machine.

As regards the deformation behavior, a non-contact displacement measurement system, based on digital image correlation (DIC) technique (Q-400, Dantec Dynamics, Germany) was used. In total, two pairs of 5 mpx cameras, one on each side of the test setup, were applied.

Different fields of view for the front and back side of the test specimens were chosen in order to cover the entire test setup (field of view of approx. 55x47 cm) on the front, as well as the local strain field in the vicinity of the dowel with a high resolution (field of view: approx. 25x21 cm) on the back. A facet size of 15 px and grid spacing of 11 px for the total view, and a facet size of 21 px and grid spacing of 15 px for the detailed view have been chosen. For the smaller field of view, a spraying method and for the larger field of view a print method for the application of a speckle patterns on the surface of the test specimens was employed. A point size of about 2–3 px was aspired. Application of two cameras each, allowed for recording three-dimensional displacement fields on each side, where the in-plane displacement fields were of special interest. Application of a speckle pattern on several elements of the test setup, i.e., on the LVL specimen, dowel heads, loading device and support device, allowed to consistently record the displacements of all elements over the entire loading history. Therefore, the nonlinear displacement path of the steel dowel was recorded as well as the inclination of the pendulum, which gave access to the change of loading direction during loading.

Having at hand the displacement field of the LVL specimen and the dowel head, it was possible to calculate the dowel displacement relative to the unloaded zone of the specimen right above the dowel. Thus, several compliances of the testing device and specimen were excluded from the dowel displacement, which is especially important for stiffness determination, as also emphasized in the regulations specified in EN 383 (2007). This method of displacement measurement is different from the one used in ASTM D5764-97a (2002) and also in several other publications (e.g. Awaludin et al., 2007; Bléron and Duchanois, 2006), which measured the displacement relative to the support of the specimen. Moreover, DIC measurements gave access to the strain field on the surface of the LVL specimens, which facilitated identification of failure modes and cracks and allowed for visualization of the load distribution.

1.2.4 Evaluation methods

Several different displacement quantities describing the displacement path of the dowel head were evaluated from contactless three-dimensional deformation measurements and are defined in Fig. 1.2a. Relative displacements between the steel dowel and the wood were calculated in order to exclude compliances of the test setup (cf. EN 383, 2007). Since, in general, the dowel follows a nonlinear displacement path, the actual total dowel displacement (u_{tan}) differs from the vertical displacement of the cross-head of the testing machine. The corresponding dowel displacement was obtained as the sum of displacement increments between the recorded loading steps. Another way of quantifying the dowel displacement is to use the displacement between the initial and the current dowel position, indicated as secant dowel displacement (u_{sec}) in Fig. 1.2a. The initial slip at the very beginning of the loading was neglected by setting the secant dowel displacement (u_{sec}) at an embedment stress of 1 N/mm² equal to zero.

The definition of the displacement directions goes in line with the definition of the dowel displacements (see Fig. 1.2a). Thus, the tangential dowel displacement direction (β_{tan}) was determined as the current direction of displacement of the dowel with respect to the grain direction, while the secant dowel displacement direction (β_{sec}) was determined as the angle between the secant dowel displacement vector and the grain direction. Having at hand the secant dowel displacement (u_{sec}) and the secant dowel displacement direction (β_{sec}), it is straightforward to calculate the vertical and lateral displacement, as well as the dowel displacements parallel and perpendicular to the grain.

The initial load-to-grain angle ($\alpha_{initial}$) was defined as the angle between the initially

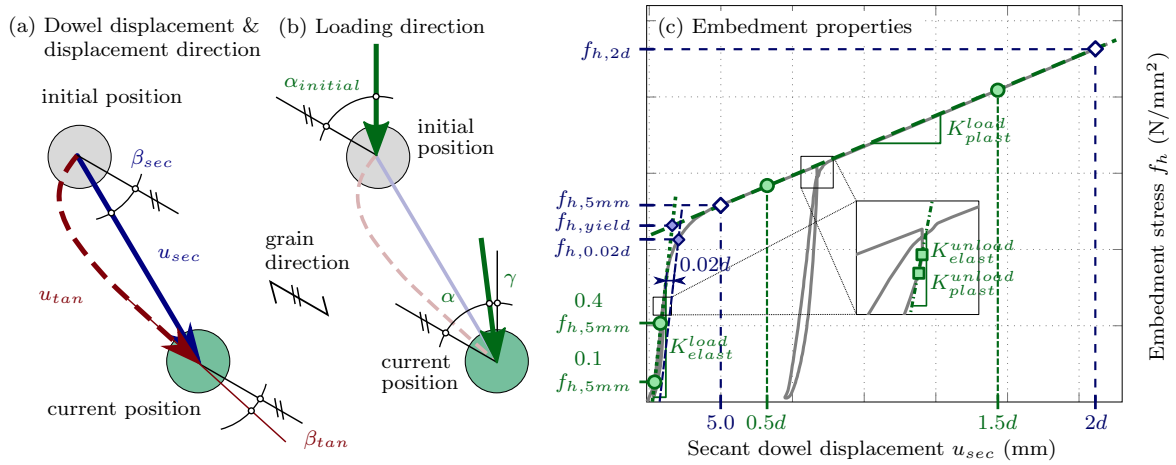


Figure 1.2: Definition of (a) dowel displacement and displacement direction, (b) loading direction and (c) embedment properties.

vertical load vector and the grain direction. Loading led, in general, to a lateral movement of the dowel, and consequently, to an inclination of the pendulum. Therefore a change in loading direction was observed, indicated as γ in Fig. 1.2b. The current load-to-grain angle is defined as α , which is equal to the initial angle $\alpha_{initial}$ minus the change in loading direction γ (Fig. 1.2b).

Embedment stresses (f_h) were determined as the vertical reaction force over the projected area of the dowel, i.e., the thickness of the LVL specimen times the dowel diameter (see also EN 383, 2007). Thus, embedment stresses are defined as nominal embedment stresses, since this definition assumes a uniform embedment stress distribution over the dowel diameter. The embedment stress multiplied by the dowel diameter gives the embedment force per unit length (f), which is another way to describe the embedment strength behavior. Subsequently, embedment stress-dowel displacement slip curves were generated, giving access to stiffness and strength properties. A point-wise stiffness and strength definition was used, in order to make test results comparable to other experiments. The corresponding parameters are visualized in Fig. 1.2c and described in the following.

The embedment strength was determined by two parameters. The first refers to the definition given by EN 383 (2007), $f_{h,5mm}$. This embedment strength is defined as the maximum embedment stress up to a secant dowel displacement of 5 mm. The second parameter describes the elasto-plastic embedment strength taken at a secant dowel displacement of two times the dowel diameter, $f_{h,2d}$. In addition, two parameters were used to define the quasi-elastic embedment limit. The first parameter refers to the 0.02d offset of the quasi-elastic loading stiffness (Hwang and Komatsu, 2002), $f_{h,0.02d}$, comparable to the 0.05d offset method used in ASTM D5764-97a (2002). The second property describes the yield stress of the embedment behavior ($f_{h,yield}$), and was determined as the intersection between the tangents defined by the quasi-elastic and elasto-plastic loading stiffness.

The loading stiffness (in terms of the embedment modulus) in the quasi-elastic part (K_{elast}^{load}), was calculated as the inclination of the line connecting the stress points on the loading path at 10% and 40% of the embedment strength $f_{h,5mm}$ (similar to the stress points suggested by EN 383 (2007)).

For the loading stiffness in the elasto-plastic part, the stiffness was determined between the stress points on the loading path at 0.5 and 1.5 times the dowel diameter. The unloading

stiffness parameters in the quasi-elastic domain (K_{elast}^{unload}) and in the elasto-plastic domain (K_{plast}^{unload}) were calculated from the first two recorded stress points immediately at the beginning of the unloading cycle, which referred to the stiffest part of the unloading sequence.

1.3 Results and discussion

In general, a pronounced ductile embedment behavior was observed for all tested dowel diameters and loading directions. Only for some experiments local cracking in the vicinity of the dowel, but no global splitting failure of the test specimens was detected, which indicates an appropriate combination of specimen geometry and reinforcement measures. Continuous integrity of the specimens over the entire loading history, in combination with the homogeneous material behavior of LVL, yielded meaningful results with low variation up to large dowel displacements.

No obvious influence of the specimen thickness and the dowel material, i.e., the steel quality and the surface coating, on the embedment behavior became evident in the analysis. Although minor plastic bending deformations in the steel dowel with a diameter of 12 mm and steel quality S 235 (only used for a limited number of tests) were observed, no apparent influence on the embedment stress-displacement relationship was obvious.

1.3.1 Displacement behavior

Loading the dowel via a steel pendulum allowed for unconstrained lateral dowel displacements transverse to the initial vertical loading direction. The corresponding displacements of the dowel with respect to the global orientation of the test setup are shown in Fig. 1.3. The tangential and the secant dowel displacement directions β_{tan} and β_{sec} (cf. Fig. 1.2a) are illustrated in Figs. 1.4c and 1.4d for 12 mm and 16 mm dowels, respectively. Both dowel diameters exhibited a similar behavior and therefore only general statements for both diameters are given in the following.

For loading parallel to the principal material directions, the response of the displacement behavior was almost symmetric, i.e., the dowel displacement path closely followed the initial loading direction $\alpha_{initial}$ of 0° and 90° , respectively. In contrast to loading parallel to the grain (0°), for loading perpendicular to the grain (90°) minor deviations of the displacement path from $\alpha_{initial}$ indicate an insignificant asymmetric load-bearing mechanism. For all other load-to-grain angles, lateral dowel displacements, with similar characteristics for all load-to-grain angles and dowel diameters, were measured. At the beginning, the dowel moved towards the initially softer material direction, i.e., perpendicular to the grain. Increasing the load induced a change of the displacement direction towards grain parallel loading (Figs. 1.3 and 1.4c,d). Due to the principle of minimum energy in a closed system, the displacement vector of the unconstrained dowel always tends to face the area of lowest stiffness in the embedding wood material. Since wood is an orthotropic material, exhibiting different stiffness properties in its different material directions, a nonlinear displacement path of the dowel was observed for loading directions deviating from the principal material directions (Fig. 1.3). Changes in the stiffness properties of the material due to densification of its cellular structure led to changes in the displacement path of the dowel. A similar trend for the displacement path was observed by Bléron and Duchanois (2006) in embedment tests. Constraining the lateral dowel displacement would naturally yield reaction forces perpendicular to the loading direction. Corresponding forces were quantified by Bader et al. (2016d) in single dowel tests.

The change in displacement direction correlated well with the transition from elastic to

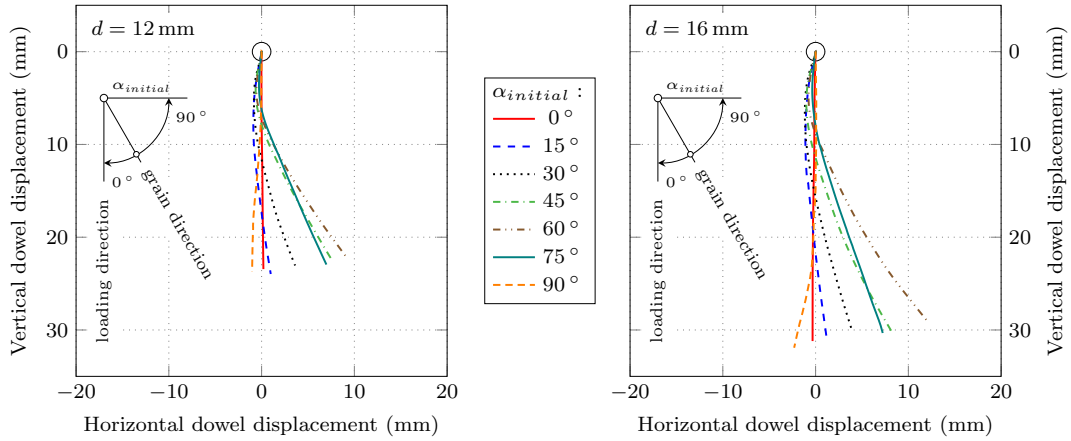


Figure 1.3: Displacement path of the vertically loaded dowel for $d=12$ mm (left) and $d=16$ mm (right).

plastic embedment behavior, which took place at a dowel displacement u_{sec} of approximately 1.2–1.8 mm (see Figs. 1.4c and d). For 12 mm dowels, the dowel displacement direction deviated about 5–16° from the initially applied displacement direction at the corresponding loading stage. For 16 mm dowels, slightly higher deviations up to 19° were found. At a secant dowel displacement of approximately 4–10 mm, the tangential displacement direction was equal to the initial displacement direction and further changed towards the grain parallel direction. A negative correlation between load-to-grain angle ($\alpha_{initial}$) and amplitude of the deviation became obvious, i.e., at small $\alpha_{initial}$ the change in β_{tan} developed slower than for large $\alpha_{initial}$. This could be explained by the smaller force component perpendicular to the grain for small $\alpha_{initial}$, which consequently requires larger dowel displacements for a similar densification of the material. Finally, at large displacements, β_{tan} ends up in a displacement direction of 8–38° smaller than the initially applied displacement direction. The highest deviation was found for loading under 60° with respect to the grain, where β_{tan} finally amounted to 22°. Apparently, the determination of β_{tan} is numerically quite sensitive, especially at small displacements, which also might be influenced by fitting quality of the loading device – dowel – borehole interfaces.

The secant dowel displacement direction β_{sec} (Figs. 1.4c and 1.4d) follows the same trend as β_{tan} and allowed calculating the transverse and longitudinal dowel displacement, as well as the applied vertical displacement of the dowel, at each loading stage. The vertical displacement was found to be up to 7.5% (for $\alpha_{initial}=60^\circ$ and both dowel diameters) smaller than the secant dowel displacement u_{sec} .

Fig. 1.4e and Fig. 1.4f show the difference between the initial loading direction $\alpha_{initial}$ and the current loading direction α with respect to the grain, indicated by γ . The trend of these curves is similar to the ones related to displacement directions. Maximum deviations of about 4° were found for loading under 60° to the grain. Therefore, a maximum transverse force of about 7% of the vertical load acted on the dowel, which slightly amplified the aforementioned effect of lateral dowel displacements since the specimen was loaded in compression. In contrast, loading in tension would lead to the opposite effect, i.e., a possible reduction of the transverse displacement component. However, due to a comparably long pendulum, only small transverse forces were induced, which are expected to be insignificant compared to the dowel displacement caused by the inhomogeneous stiffness conditions in the vicinity of the dowel.

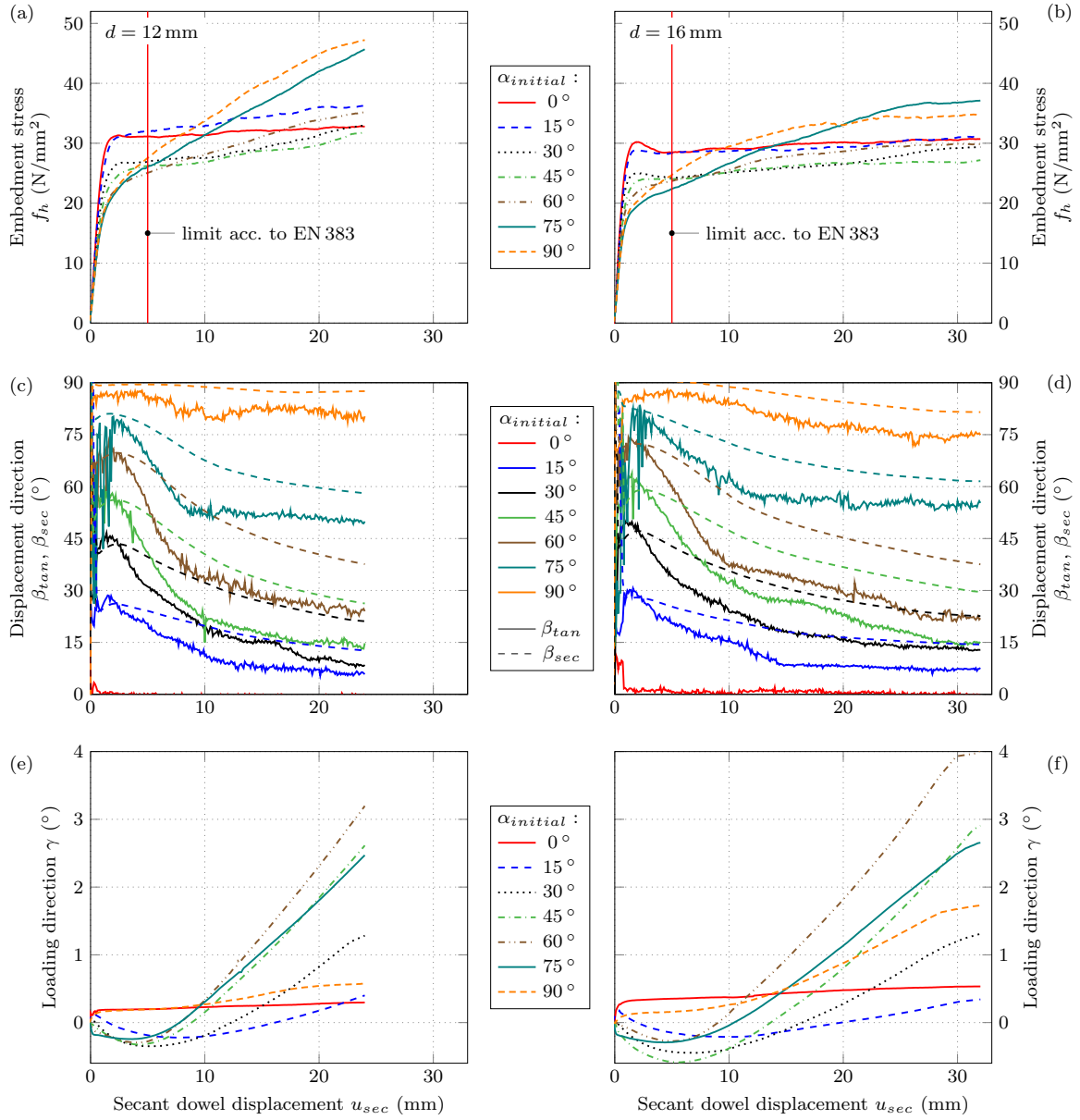


Figure 1.4: Embedment behavior for $d=12$ mm (left column) and $d=16$ mm (right column), (a)–(b) embedment stress f_h , (c)–(d) tangential β_{tan} and secant dowel displacement direction β_{sec} , and (e)–(f) change of loading direction γ plotted over secant dowel displacement u_{sec} .

1.3.2 Embedment stress vs. dowel displacement

The reaction of a steel dowel loaded under a certain angle to the grain of LVL is commonly described by its slip behavior, i.e., the nominal embedment stress plotted over the dowel displacement. Results are presented and discussed as embedment stresses f_h related to secant dowel displacements u_{sec} in dependence of the investigated initial load-to-grain angle $\alpha_{initial}$ (cf. Fig. 1.2c).

Figs. 1.4a and 1.4b visualize the experimentally determined slip curves and their dependence on the load-to-grain angle for dowels with a diameter of 12 mm and 16 mm, respectively. Therein, mean values of the nominal embedment stresses are shown. Fig. 1.5 additionally illustrates the variability of results. Three-dimensional illustrations of the slip behavior, i.e., slip curves plotted over the load-to-grain angle, are presented in Fig. 1.6. Linear interpolation has been used for the areas between the measured slip curves at 15° load-to-grain angle steps.

A general trend of the dependence of embedment stresses on dowel displacement and load-to-grain angle, independent of the dowel diameter, became obvious. In good approximation, the slip curves can be described by a quasi-linear elastic behavior, followed by a pronounced, almost linear plastic behavior for several load-to-grain angles studied in this contribution. The quasi-elastic loading stiffness (K_{elast}^{load}) decreased with increasing load-to-grain angle ($\alpha_{initial}$). Simultaneously, the quasi-elastic limit described by the 2% dowel diameter offset embedment strength ($f_{h,0.02d}$) decreased, while the loading stiffness of the elasto-plastic part (K_{plast}^{load}) increased. The quasi-elastic limit ($f_{h,0.02d}$) was reached at a secant dowel displacement of 1.0–1.3 mm, almost independent from the load-to-grain angle and dowel diameter. At large dowel displacements and large load-to-grain angles, hardening effects led to embedment stresses beyond the embedment stress parallel to the grain (Figs. 1.4 and 1.6).

The embedment stress-displacement behavior parallel and under 15° to the grain can be described by an almost linear-elastic, ideal plastic response. The level of the embedment stress is nearly identical for these two load-to-grain angles. Surprisingly, for a dowel with a diameter of 12 mm, slightly higher embedment stresses in the plastic region were found for $\alpha_{initial}=15^\circ$ compared to $\alpha_{initial}=0^\circ$. This could possibly have been caused by a reduced contact area for loading parallel to the grain, due to minor splitting in the center of the contact zone (see also DIC strain fields in Subsection 1.3.5), which consequently would reduce the nominal embedment stress. On the contrary, at a load-to-grain angle of 15°, smaller splitting forces led to less cracks, which in addition were located at the outer area of the embedment zone. Consequently, a more uniform load transition with slightly higher bearing capacity was possible. For 16 mm dowels, this effect might be reduced since the cracked area was considerably smaller in relation to the contact zone, than this was the case for 12 mm dowels.

The slip behavior at $\alpha_{initial}$ between 15° and 45° was characterized by a decrease of the quasi-elastic loading stiffness (K_{elast}^{load}), quasi-elastic embedment strength ($f_{h,0.02d}$) and maximum embedment strength ($f_{h,2d}$) for increasing $\alpha_{initial}$. The elasto-plastic loading stiffness (K_{plast}^{load}) slightly increased with increased load-to-grain angle.

The embedment behavior for $\alpha_{initial}$ of 60° and higher was dominated by a pronounced hardening behavior at large displacements. Interestingly, dowels with a diameter of 12 mm showed considerably stronger hardening behavior than dowels with a diameter of 16 mm (see Fig. 1.5). This observation is well in line with previous experimental findings of Sawata and Yasumura (2002) and Franke and Quenneville (2010).

The increase of the elasto-plastic loading stiffness (K_{plast}^{load}) is driven by hardening effects, namely by densification of the wood in the contact area below the dowel and by the so-

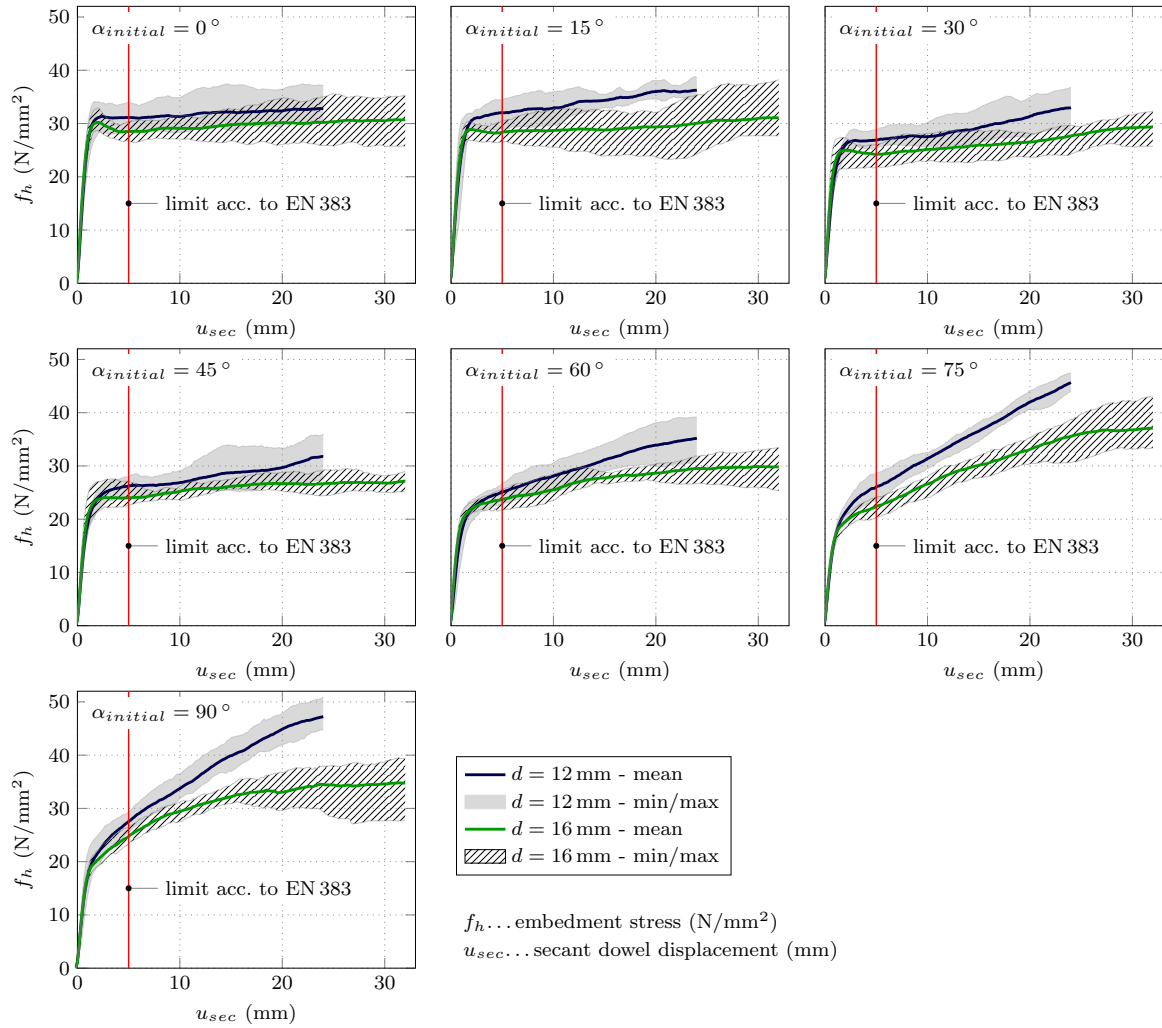


Figure 1.5: Embedment stress f_h vs. secant dowel displacement u_{sec} for $d=12$ mm and $d=16$ mm including the variability of the experimental data and the embedment stress limit according to EN 383 (2007).

called rope effect in wood fibers. The latter effect is related to tensile stresses parallel to the grain, which can arise for load components perpendicular to the grain, as a consequence of deviation forces gained from wood fibres in bending. Since both effects could be considered as almost independent from the dowel diameter, and at the same time, the embedment stress, defined as nominal embedment stress, is calculated as the load divided by the projected dowel area, a larger dowel diameter leads to an apparently lower embedment stress. For 16 mm dowels loaded at $\alpha_{initial}=90^\circ$, considerable delamination of the outer veneer layers of the LVL was observed for large dowel displacements. This led to a reduced embedment length, and consequently to lower nominal embedment stresses compared to 12 mm dowels.

The small variation of slip curves in Fig. 1.5, as well as small standard deviations given in Tab. 1.2, reflect the homogeneity of the applied materials, i.e., LVL and steel. The variation slightly increased with increased dowel displacement, which might be related to variability in the delamination of the outer veneer layers of the LVL.

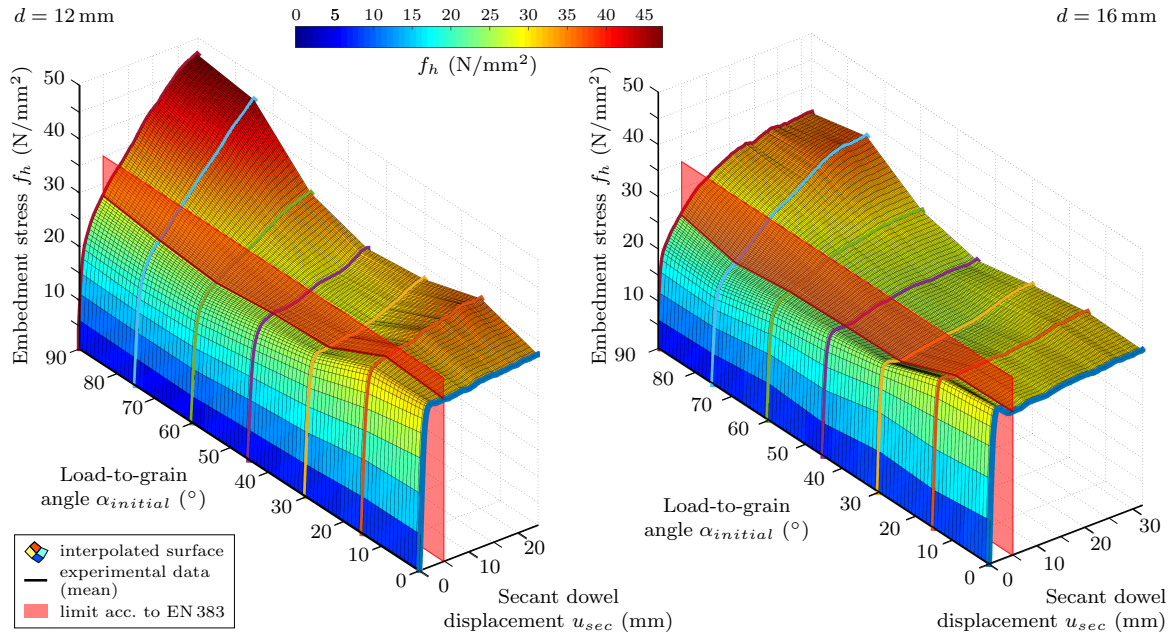


Figure 1.6: Embedment stress f_h plotted over the load-to-grain angle $\alpha_{initial}$ and the secant dowel displacement u_{sec} for dowel diameter 12 mm (left) and 16 mm (right), including the embedment stress limit according to EN 383 (2007).

Table 1.2: Embedment properties of LVL for $d=12$ mm and $d=16$ mm.

α (°)	K_{elast}^{load}		K_{plast}^{load}		K_{elast}^{unload}		K_{plast}^{unload}		$f_{h,0.02d}$		$f_{h,yield}$		$f_{h,5mm}$		$f_{h,2d}$		
	(initial)	Mean	Stdev	Mean	Stdev	Mean	Stdev	Mean	Stdev	Mean	Stdev	Mean	stdev	Mean	Stdv		
$d=12$ mm																	
0		29.8	4.12	0.107	0.112	57.4	5.78	54.2	0.50	28.0	3.20	30.5	2.09	31.8	1.76	33.5	2.15
15		29.7	10.3	0.239	0.124	53.9	8.58	49.7	-	27.7	3.42	31.1	3.19	32.1	2.28	36.9	1.35
30		23.9	2.24	0.279	0.167	46.9	4.97	42.0	0.04	22.1	1.53	25.8	1.42	27.3	0.95	33.0	2.68
45		22.7	3.08	0.235	0.154	40.9	3.34	37.9	1.61	19.7	0.75	25.2	1.64	26.3	1.56	32.2	3.10
60		20.7	4.95	0.595	0.185	37.0	5.06	28.7	2.60	18.7	0.91	22.9	1.96	25.1	1.24	35.4	2.79
75		19.3	1.64	1.068	0.164	31.9	2.63	28.9	0.15	17.6	0.87	21.6	2.49	26.1	1.60	45.7	1.47
90		20.3	4.91	1.157	0.207	34.7	5.08	25.5	1.14	18.3	1.74	23.5	1.88	27.5	1.46	47.3	2.73
$d=16$ mm																	
0		38.3	7.42	0.071	0.222	92.6	10.7	87.3	4.34	27.3	2.24	28.6	2.06	30.4	1.57	33.0	2.92
15		32.7	5.02	0.085	0.124	95.7	12.5	77.8	4.52	26.8	1.75	28.1	1.96	29.3	1.49	32.0	3.35
30		33.1	7.72	0.180	0.153	77.7	11.3	66.6	9.92	23.2	2.10	23.5	2.80	25.2	1.87	29.6	2.16
45		28.3	7.06	0.123	0.146	57.0	5.24	49.1	1.48	21.2	2.02	23.8	1.64	24.4	1.88	27.9	1.25
60		27.2	3.96	0.298	0.139	52.0	4.35	40.5	3.50	19.2	1.08	22.6	2.54	23.8	1.32	30.4	1.73
75		22.6	1.77	0.674	0.158	49.0	9.25	33.9	3.98	17.1	0.69	20.0	1.93	22.4	1.44	37.6	3.21
90		22.0	3.63	0.404	0.266	43.6	6.69	28.0	0.06	18.2	1.06	25.3	2.76	24.7	1.37	36.0	3.26

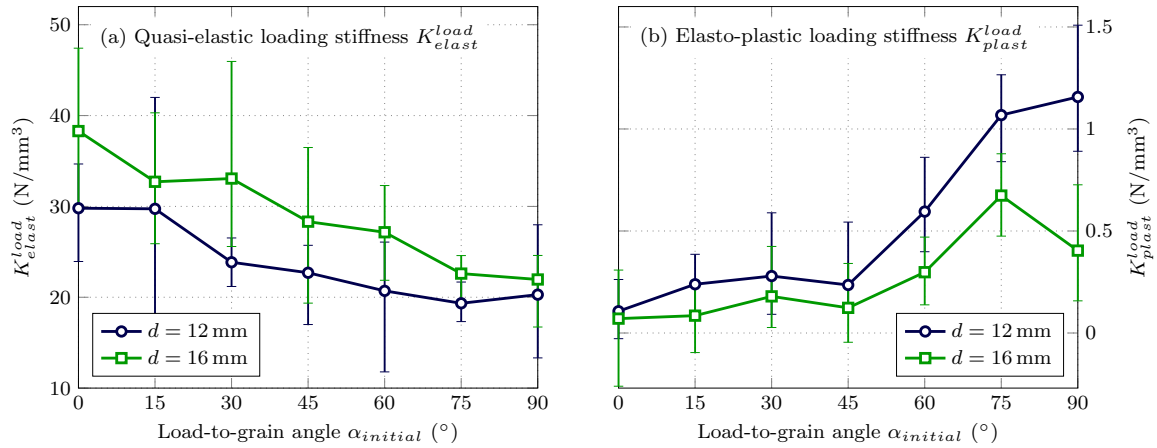


Figure 1.7: Loading stiffness plotted over the load-to-grain angle $\alpha_{initial}$ for 12 mm and 16 mm dowels, including the variability of the experimental data, (a) quasi-elastic loading stiffness K_{elast}^{load} and (b) elasto-plastic loading stiffness K_{plast}^{load} .

1.3.3 Stiffness behavior

Stiffness properties, in terms of embedment moduli (i.e., embedment stress per dowel displacement), were determined for loading and unloading situations in the quasi-elastic and elasto-plastic region of the slip curves. The corresponding parameters are summarized in Table 1.2 and visualized in Figs. 1.7 and 1.8 for the loading and unloading stiffness, respectively. Clear relationships between the stiffness properties and the load-to-grain angle $\alpha_{initial}$, as well as the dowel diameter, became obvious. The quasi-elastic loading stiffness K_{elast}^{load} decreased with increased load-to-grain angle as a reason of the anisotropic material behavior of LVL. The relationship between K_{elast}^{load} and $\alpha_{initial}$ roughly follows an S-shaped curve (Fig. 1.7a). A decrease in stiffness, between $\alpha_{initial}=0^\circ$ and 90° , of about 32% and 43% for 12 mm and 16 mm dowels, respectively, was found. This trend over the load-to-grain angle was also shown for tropical hardwood species by Awaludin et al. (2007).

In contrast to the quasi-elastic loading stiffness, the elasto-plastic embedment stiffness K_{plast}^{load} increased with increasing load-to-grain angle (Fig. 1.7b). Higher values were found for 12 mm than for 16 mm dowels. The trend over $\alpha_{initial}$ can be described by three characteristic regions (cf. Table 1.2), namely (i) $\alpha_{initial}=0-15^\circ$: K_{plast}^{load} was close to zero, relating to the more or less ideal plastic behavior; (ii) $\alpha_{initial}=15-45^\circ$: slightly increased K_{plast}^{load} ; (iii) $\alpha_{initial}=60-90^\circ$: strongly increased K_{plast}^{load} . The stiffness property for 16 mm dowels loaded perpendicular to the grain (Table 1.2) might not be representative, since considerable delamination of the outer veneers reduced the actual embedment length, and therefore also the nominal embedment stresses and the elasto-plastic stiffness.

Awaludin et al. (2007) reported rather constant elasto-plastic embedment stiffness however with experiments up to a maximum displacement of about 3 mm only. Nevertheless, a pronounced hardening, i.e., increased elasto-plastic stiffness, for load-to-grain angles close to 90° was previously shown by several contributions (Franke and Magnière, 2014; Santos et al., 2010; Sawata and Yasumura, 2002), in line with the data presented herein.

Differences between 12 mm and 16 mm dowels were higher for large $\alpha_{initial}$ than for small $\alpha_{initial}$ (Table 1.2 and Fig. 1.7b). This trend can be explained by the aforementioned hardening effects, which got more decisive for 12 mm than for 16 mm dowels at large load-to-grain angles.

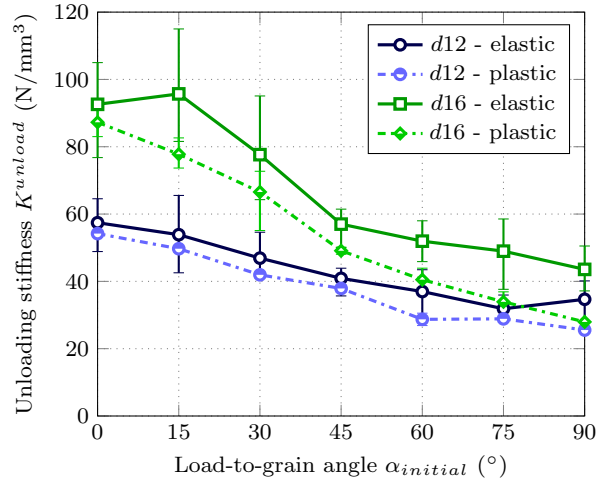


Figure 1.8: Unloading stiffness in the quasi-elastic part K_{elast}^{unload} and elasto-plastic part K_{plast}^{unload} vs. load-to-grain angle $\alpha_{initial}$ for the 12 mm and 16 mm dowel, including the variability of the experimental data.

Particularly interesting is the unloading stiffness, since it gives insight into elastic, i.e., recoverable, deformations in the embedment loading of the dowel. The corresponding parameters in the quasi-elastic (K_{elast}^{unload}) and elasto-plastic (K_{plast}^{unload}) region of the slip curves, showed a similar behavior as the quasi-elastic loading stiffness K_{elast}^{load} . That is, a decrease in stiffness for increasing load-to-grain angles, which can roughly be described by an S-shaped curve. The unloading stiffness amounted to about two times the quasi-elastic loading stiffness. It represents the elastic response of the structural system, while the quasi-elastic loading stiffness encompasses additional and also viscoelastic effects (Reynolds et al., 2013). Only minor differences between the unloading stiffness in the quasi-elastic and the elasto-plastic region were found, since only pronounced damage of the wood matrix is expected to reduce the elastic response. Higher stiffness values were observed for 16 mm than for 12 mm dowels, consistently for all load-to-grain angles. With increasing load-to-grain angle, this difference between the two dowel diameters decreased from 22% at $\alpha_{initial}=0^\circ$ to 8% at $\alpha_{initial}=90^\circ$.

A stiffer response of larger dowels is partly in contradiction to previously reported data, which indicated a reverse trend (Hwang and Komatsu, 2002; Stamato and Calil Jr, 2000). However, other publications showed the same trend as observed herein (Karagiannis et al., 2016). In the particular setup of full-hole embedment tests, the interpretation of this effect might be corrupted by elastic deformations of the steel dowel in bending (Franke and Magnière, 2014), which would be higher for 12 mm than for 16 mm dowels. A simple estimation of the elastic bending deformation of the dowel and correction of the stiffness properties of the LVL would more than double them. However, still 16 mm dowels would react stiffer than 12 mm dowels. High variability in initial stiffness properties (quasi-elastic loading stiffness) might negatively affect the interpretation of test data (cf. Fig. 1.7). Unloading stiffness was found less variable (cf. Fig. 1.8), and thus, is expected to be more reliable in the interpretation of test results.

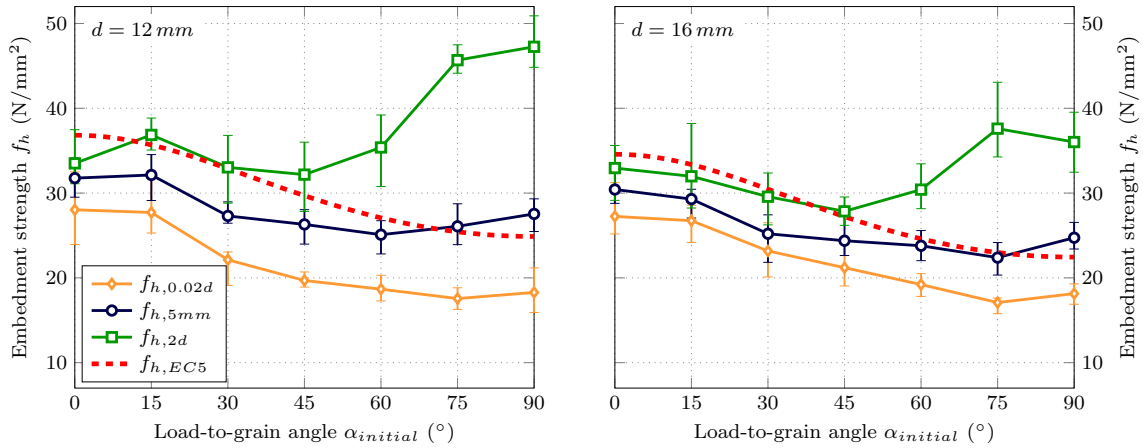


Figure 1.9: Embedment strength properties vs. load-to-grain angle $\alpha_{initial}$ for $d=12$ mm (left) and $d=16$ mm (right) including variability of the experimental data. Additional comparison of the experimentally determined embedment strength properties ($f_{h,0.02d}$, $f_{h,5mm}$ and $f_{h,2d}$) to Eurocode 5 (EN 1995-1-1, 2004) based calculation of the embedment strength ($f_{h,EC5}$).

1.3.4 Embedment strength

Embedment strength is commonly determined as the maximum nominal embedment stress up to a maximum dowel displacement of 5 mm (EN 383, 2007), $f_{h,5mm}$. The corresponding displacement limit is indicated by red lines in Figs. 1.4a and 1.4b, Fig. 1.5, and Fig. 1.10, as well as by the semi-transparent red surface in Fig. 1.6; see also Table 1.2. Additionally, the embedment strength was determined as the maximum nominal stress up to a secant dowel displacement of two times the dowel diameter, $f_{h,2d}$ (Table 1.2). Furthermore, the quasi-elastic embedment stress limit is described by the 2% offset limit, $f_{h,0.02d}$, and the yield stress by $f_{h,yield}$; see also Table 1.2. In Fig. 1.9, the two embedment strength parameters $f_{h,5mm}$ and $f_{h,2d}$, as well as the embedment stress at the quasi-elastic limit $f_{h,0.02d}$ are plotted over the load-to-grain angle. The diagrams include a comparison with the embedment strength determined according to Eqs. (8.31–8.33) of the European design code Eurocode 5 (EN 1995-1-1, 2004), $f_{h,EC5}$. For its calculation, experimentally determined mean densities of LVL were used. Thus, the corresponding embedment strength according to Eurocode 5 can be considered as mean value.

A clear correlation between embedment strength parameters and load-to-grain angle became obvious for both dowel diameters (Fig. 1.9). The experimentally determined embedment strength $f_{h,5mm}$, and quasi-elastic embedment strength $f_{h,0.02d}$ follow the S-shaped trend of the embedment strength determined according to Eurocode 5 (EN 1995-1-1, 2004), which results in a reduced embedment strength with increased load-to-grain angle. The mean value of $f_{h,5mm}$ parallel to the grain (0°) was 31.8 N/mm² and 30.4 N/mm² for 12 mm and 16 mm dowels, respectively. Larger differences between $f_{h,5mm}$ of these two dowel diameters were found for loading perpendicular to the grain (90°), where $f_{h,5mm}$ amounted to 27.5 N/mm² and 24.7 N/mm² for 12 mm and 16 mm dowels, respectively. The higher value for 12 mm dowels compared to 16 mm dowels might be explained by stronger hardening effects for 12 mm dowels. These effects get even more evident for $f_{h,2d}$ (Fig. 1.9). The corresponding embedment strength perpendicular to the grain (90°) was measured as 47.3 N/mm² and 36.0 N/mm², which means that the strength using 12 mm dowels was 31% higher than the strength using 16 mm dowels. Furthermore, these embedment strength values are 72% and 46% higher

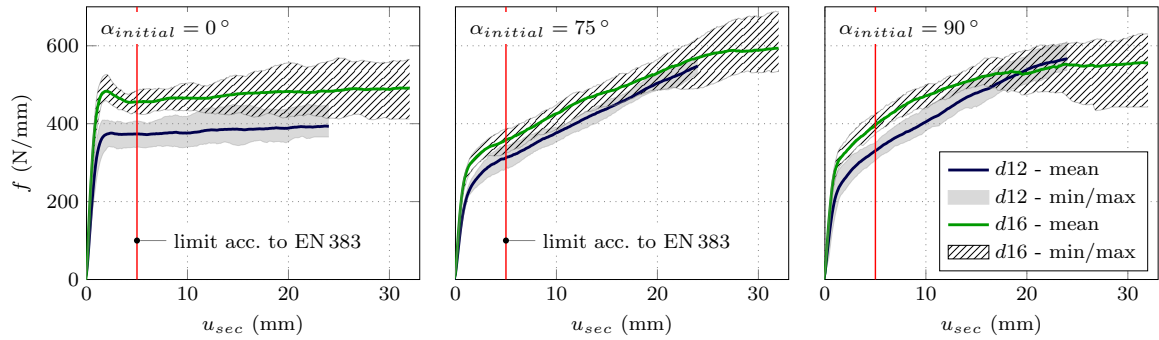


Figure 1.10: Embedment force per unit length f vs. secant dowel displacement u_{sec} for $d=12$ mm and $d=16$ mm including the variability of the experimental data and the embedment test limit according to EN 383 (2007).

than corresponding values at a maximum displacement of 5 mm, highlighting the large plastic resources for loading directions close to perpendicular to the grain. The embedment strength $f_{h,2d}$ for the 16 mm dowel loaded at 90° to the grain might not be representative, since considerable delamination of the outer veneers, led to a reduced embedment length, and consequently to lower nominal embedment stresses. However, the described findings are expected to be qualitatively reliable, since the same trends were also seen for loading at an angle of 75° . Almost identical embedment strengths $f_{h,5mm}$, at small $\alpha_{initial}$ for both dowel diameters, indicate a minor influence of the dowel diameter on the embedment strength for these loading situations.

In contrast, a huge difference of the embedment strength $f_{h,2d}$, between $d=12$ mm and 16 mm, for large $\alpha_{initial}$, was evident in the data. However, less difference between different dowel diameters was found in the embedment force per unit length f (Fig. 1.10), which has been found to be nearly the same for both dowel diameters, for $\alpha_{initial}$ of 75° and 90° , for a dowel displacement u_{sec} larger than 20 mm. This could be interpreted as the accumulated reaction force being almost independent from the dowel diameter, which would go in line with the hypothesis of an almost dowel-diameter independent rope effect in wood fibers, which causes tensile stresses along the grain, and densification effect on the load-carrying mechanisms, for the investigated range of dowel diameters, for large dowel displacements and large $\alpha_{initial}$. In addition, it should be kept in mind, that $f_{h,2d}$ refers to embedment stresses at $u_{sec}=24$ mm and 32 mm for 12 mm and 16 mm dowels, respectively. Comparing embedment stresses at the same absolute dowel displacement would lead to even higher differences in embedment stresses, and therefore the reaction forces, expressed as embedment force per unit length, for 12 mm and 16 mm dowels get even closer.

The quasi-elastic stress limit, $f_{h,0.02d}$, was found to be about 10–30 % below the embedment strength $f_{h,5mm}$, where an increase in deviation was found with increasing load-to-grain angle. The ratio between $f_{h,0.02d}$ at loading parallel (0°) and perpendicular to the grain (90°) showed a good correlation with the corresponding value k_{90} given by Eurocode 5 (EN 1995-1-1, 2004). The same trend for the quasi-elastic embedment strength, determined as the 5 % offset limit according to ASTM D5764-97a (2002), compared to $f_{h,0.02d}$ was found. However, the 5 % offset limit is not presented in this contribution, since the 2 % offset limit ($f_{h,0.02d}$) was found to be more suitable to describe the quasi-elastic limit. Experimentally determined embedment strength $f_{h,5mm}$ and the embedment strength calculated according to Eurocode 5 (EN 1995-1-1, 2004), $f_{h,EC5}$, were partly in good agreement. However, for load-to-grain angles up to

about 60° , Eurocode 5 (EN 1995-1-1, 2004) equation overestimates the embedment strength up to 17% in comparison to the experimentally gained data. The Eurocode 5 equation was developed for softwood and hardwood species (Ehlbeck and Werner, 1992). In LVL however, more than 10 mass percent of glue in the wood-based product increases the apparent density. Thus, using the apparent density of LVL might lead to an overestimation of the embedment strength.

1.3.5 Surface strains and visual inspection of test specimens

Deformations on the surface of the LVL test specimens, gained from DIC measurements, allowed following the load distribution and to assess the integrity of the specimens during loading. In addition, test specimens were visually inspected after testing. This included cutting of at least one specimen of each dowel diameter and load-to-grain angle along the center plane of the specimen, in order to identify plastic deformations and cracks. Specimens were cut in the center plane in order to exclude local surface effects. The corresponding permanent, plastic deformations are related to the unloaded condition after loading up to a dowel displacement of about 32 mm, for both dowel diameters. Combination of surface strains and visual inspection, allowed for identification of bearing mechanisms, cracks, strain distributions and differences between the applied dowel diameters.

Fig. 1.11 shows an overview of surface strains for one representative test of each load-to-grain angle using 12 mm dowels. Images are representing the loaded situation at a dowel displacement of about one time the dowel diameter, i.e., 12 mm. In addition, the last column in Fig. 1.11 contains an overlay of the surfaces of the cut specimens using 12 mm and 16 mm dowels. Green and red lines indicate areas of plastic deformations for 12 mm and 16 mm dowels, respectively. Basically, three different types of bearing mechanisms were found, which are similar in their appearance for both investigated dowel diameters.

For load-to-grain angles between 0° and 15° , the dowel pushed aside wood fibers, leading to a densification of the wood tissue on both lateral sides of the dowel. This deformation characteristic induced tensile stresses perpendicular to the grain, which led to splitting forces and a wedge action of the dowel. Strains parallel to the grain (ε_{xx}) admit a very local densification of the wood below the dowel, while strains perpendicular to the grain (ε_{yy}), show densified areas on both lateral sides of the dowel as well as local cracks on the LVL surface below the dowel. These local cracks were present at each test for $\alpha_{initial} = 0^\circ$ and 15° and for both dowel diameters. However, visual inspection after testing indicated these cracks to be only close to the specimen surface. For two tests only, cracks propagated throughout the specimen thickness. Additionally, these cracks were compensated by the reinforcement. Higher splitting forces were expected for 16 mm dowels than for 12 mm dowels and a more pronounced splitting of the specimens after removal of the reinforcement was evident.

For load-to-grain angles between 75° and 90° , the aforementioned rope effect in wood fibers, which causes tensile stresses along the grain, in combination with a pronounced densification below the dowel was highlighted by surface strains; particularly in terms of shear strains (ε_{xy}) and strains perpendicular to the grain (ε_{yy}). At the same time, failure of the wood fibers in tension became obvious from visual inspection. Due to the strong deformation of the fibers, and the evaluation of surface strains in the original coordinate system referring to the undeformed fibre direction, these cracks might have appeared as high tensile strains perpendicular to the grain ε_{yy} . The length of the specimens was obviously sufficient, since no global failure in shear was observed. A global failure was however observed for specimens with 12 mm dowels loaded at an angle of 75° to the grain. The corresponding dowel displace-

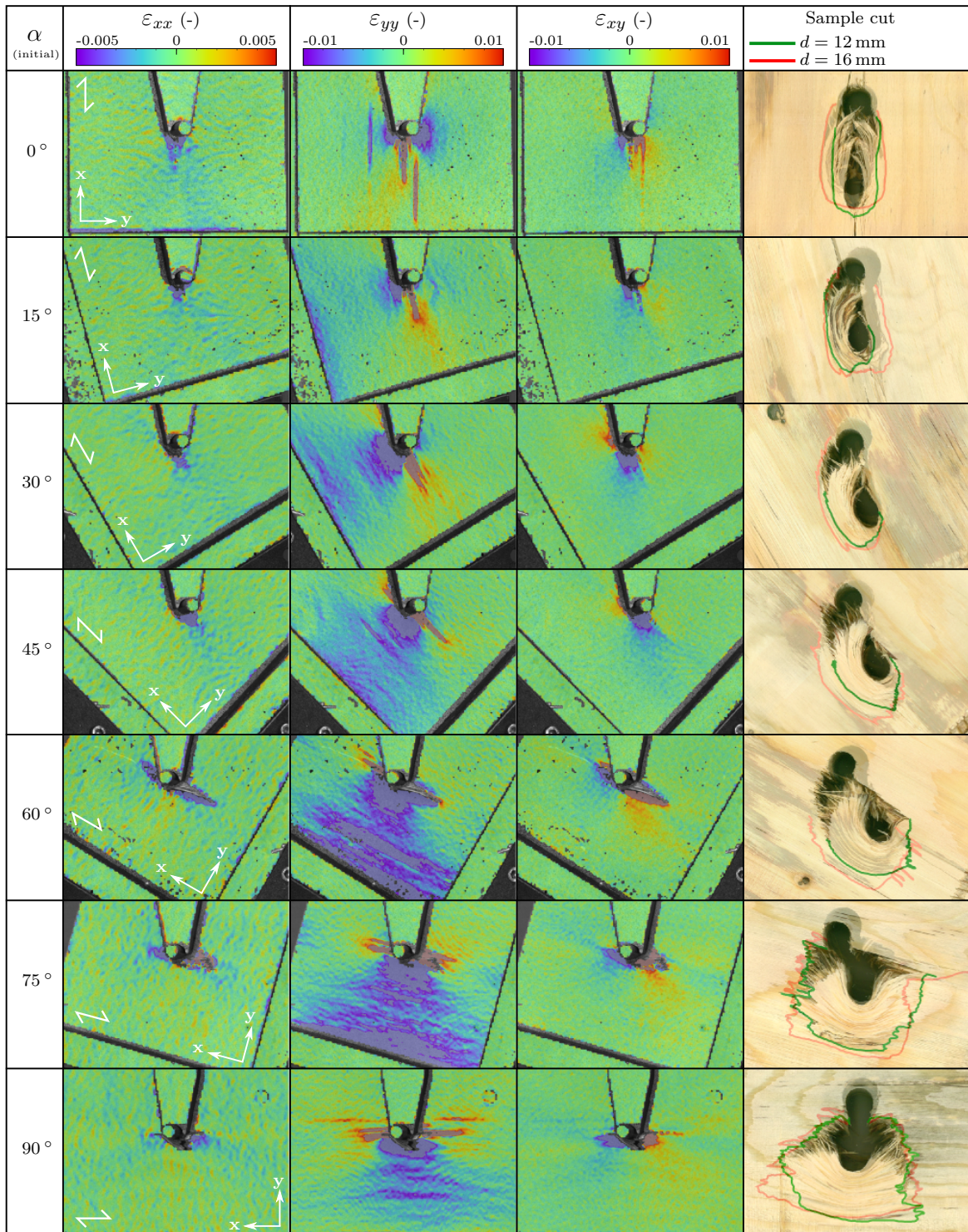


Figure 1.11: Surface strains (DIC) and visual inspection; (Column 1–3) Surface strains parallel to the grain ϵ_{xx} , perpendicular to the grain ϵ_{yy} and shear strains ϵ_{xy} for dowel diameter $d=12$ mm at a dowel displacement $u_{sec}=12$ mm for load-to-grain angles of 0° to 90° ; (Column 4) Designation of the visible plastic deformations as an overlay of $d=12$ mm and $d=16$ mm test specimens, cut along the center plane of the specimen, at approx. $u_{sec}=32$ mm for $\alpha_{initial}$ of 0° to 90° .

ment was about 30 mm, and thus, beyond the herein discussed limit of two times the dowel diameter. A minor load drop in the slip curve was followed by further increase in load due to the action of reinforcements ensuring the integrity of the test specimen.

The behavior at load-to-grain angles between 15° and 75° , was characterized by a transition and combination of the corresponding load transfer mechanisms discussed above. For $\alpha_{initial}$ between 30° and 45° the lateral displacement of the wood, typical for loading parallel to the grain, was dominant. The corresponding densified area however, was mainly on one side of the dowel, which induced a corresponding lateral dowel displacement and a shift of the loading direction towards parallel to the grain. Tensile strains perpendicular to the grain, as a result of splitting forces induced by the dowel, were visible up to $\alpha_{initial}$ of 30° and 45° for 12 mm and 16 mm dowels, respectively. However, no global splitting failure was detected. Up to these load-to-grain angles, a distinct development of a rope effect in wood fibers, which causes tensile stresses along the grain was not possible. In contrast, for load-to-grain angles of 60° , minor hardening effects in the embedment behavior were found, which might be explained by a greater extension of compressive strains perpendicular to the grain. Images of the cut specimens support this interpretation by the corresponding expansion of plastic deformations. These areas increased from an extension of about 3–5 mm for loading parallel to the grain (0°) to an extension of about 60 mm in width and 25 mm in thickness for 75° and 90° load-to-grain angles. Interestingly, for 75° and 90° almost the same plastic area for $d=12$ mm and $d=16$ mm, at the same absolute dowel displacement of about 32 mm was found, while for lower $\alpha_{initial}$ the size of plastic deformations was found to be larger for dowels with a diameter of 16 mm. The more or less equal area of plastic deformations for large load-to-grain angles explains the almost same size of loads for 12 mm and 16 mm dowels loaded under 75° and 90° to the grain. Consequently, embedment stresses had to be higher for 12 mm dowels than for 16 mm dowels.

1.4 Conclusions

A comprehensive dataset of embedment stress-dowel displacement relationships for two different dowel diameters embedded into laminated veneer lumber (LVL) made of spruce was established by conducting full-hole embedment tests in compression under free, i.e., unconstrained, lateral dowel displacement boundary conditions. The influence of the anisotropic material behavior of LVL and wood in general was revealed by tests at different load-to-grain angles. No global failure of the test specimens up to dowel displacements of at least two times the dowel diameter was observed. This confirmed a suitable combination of specimen size and reinforcement.

Monitoring of lateral dowel displacements revealed the effect of a deviation of the load-to-grain angle from principal material directions of wood.

- Dowels first moved towards the weaker material direction, i.e., perpendicular to the grain. After densification of the wood tissue below the dowel, it changed its lateral displacement orientation and moved towards parallel to the grain. This transition was found to correlate well with the quasi-elastic limit. Lateral displacements were most pronounced for load-to-grain angles between 30° and 75° with a maximum at 60° .

The following general conclusions can be drawn as regards the effect of increasing the load-to-grain angle:

- Decrease in the quasi-elastic limit, which was found at a displacement of 1.0–1.3 mm.

- Decrease in the quasi-elastic loading stiffness as well as in the unloading stiffness.
- Decrease in the maximum embedment stress up to 5 mm displacement.
- Increase in the elasto-plastic loading stiffness, i.e., increased hardening behavior of embedment stresses, which particularly increased for load-to-grain angles of 60° and higher. Corresponding DIC images showed the onset of the development of a rope effect in wood fibers, which causes tensile stresses along the grain.
- Stronger hardening effects for smaller dowel diameters, which was found to be related to the possibility of lateral load distribution below the dowel. DIC measurements as well as visual inspection revealed rather equally large stressed areas and plastic zones for the two different dowel diameters at load-to-grain angles close to 90° .

Determining stiffness properties from the initial part of the unloading paths was shown to considerably reduce the experimental variation.

For load-to-grain angles of less than 60° , Eurocode 5 (EN 1995-1-1, 2004) based embedment strength of LVL was up to 17% higher than experimental values up to a maximum displacement of 5 mm.

Due to pronounced hardening effects, embedment stresses increased with increased displacement. Thus, particularly for large load-to-grain angles, embedment strength considering the maximum displacement of two times the dowel diameter was found to be considerably (up to 90%) higher than values proposed by the design standard Eurocode 5.

The highly nonlinear relationship with potentially increased embedment stresses could be exploited by means of numerical modeling of single dowel connections (Bader et al., 2016d; Hochreiner et al., 2013). More realistic slip curves of single dowel connections would enhance the design of dowel connections, allowing for the calculation of a realistic load distribution within dowel groups.

Acknowledgements

The authors gratefully acknowledge the financial support of the Austrian Research Promotion Agency and the wood industry partnership Building with Wood within CEI-Bois for funding the research work within project *MechWood 2*. This work forms part of that project. The *MechWood 2* research partners are thanked for their cooperation and collaboration in this project.

Notation

d	dowel diameter
f	force per unit length
f_h	embedment stress
$f_{h,0.02d}$	embedment strength determined by 0.02d offset of the quasi-elastic loading stiffness K_{elast}^{load}
$f_{h,2d}$	embedment strength at a dowel displacement of two times the dowel diameter
$f_{h,5mm}$	embedment strength acc. to EN 383
$f_{h,EC5}$	embedment strength calculated acc. to EC 5, Eqs. (8.31–8.33)

$f_{h,yield}$	embedment yield strength
K_{elast}^{load}	quasi-elastic loading stiffness
K_{plast}^{load}	elasto-plastic loading stiffness
K^{unload}	unloading stiffness
K_{elast}^{unload}	quasi-elastic unloading stiffness
K_{plast}^{unload}	elasto-plastic unloading stiffness
R_a	arithmetic average of the surface roughness
u_{sec}	secant dowel displacement
u_{tan}	actual total dowel displacement
α	current load-to-grain angle
$\alpha_{initial}$	initial load-to-grain angle
β_{sec}	secant dowel displacement direction
β_{tan}	tangential dowel displacement direction
γ	change of loading direction
ε_{xx}	engineering strain in grain direction
ε_{xy}	engineering shear strain
ε_{yy}	engineering strain perpendicular to the grain

Constrained displacement boundary condition in embedment testing of dowel-type fasteners in LVL (Schweigler et al., 2017)

Authored by Michael Schweigler, Thomas K. Bader, Johann Vessby
& Josef Eberhardsteiner

Published in *Strain*, 53(6):e12238, pp. 17, DOI: 10.1111/str.12238, 2017

The final publication is available at:

<https://doi.org/10.1111/str.12238>

Abstract: The influence of the loading orientation with respect to the grain direction of wood and the influence of the lateral dowel displacement boundary conditions on the embedment behavior of steel dowels in laminated veneer lumber (LVL with parallel-laminated veneers) are investigated in this study. For limit states of the lateral boundary conditions, the load-displacement behavior was experimentally studied by means of full-hole embedment tests on screw-reinforced LVL, for two different dowel diameters and up to large dowel displacements. A novel biaxial test setup is proposed for embedment tests with constrained lateral dowel displacement boundary conditions, in order to quantify laterally evoked reaction forces. Corresponding forces were found to change orientation with increasing dowel displacement and amounted to about 20% and 40% of the vertical reaction force for dowel displacements of 5 mm and twice the dowel diameter, respectively. The influence of the lateral displacement boundary conditions was highlighted by comparison of the test data with a previously established dataset for unconstrained embedment testing. Constrained loading showed a stiffer response and higher nominal embedment stresses, as well as a more pronounced displacement hardening, compared to unconstrained loading.

Keywords: anisotropy, displacement boundary conditions, full-hole embedment tests, reinforced laminated veneer lumber, stiffness

2.1 Introduction

Profound knowledge on the embedment behavior of steel dowels in wood and engineered wood based products is essential for a reliable design of dowel connections and structural load-bearing elements where such mechanical connections are used. The experimental quantification of embedment characteristics, namely strength and stiffness properties, is however a challenging task not only due to the variability but also due to the complex mechanical properties of wood. With the experimental data presented in this contribution, a previously established dataset (Schweigler et al., 2016b) is extended and the discussion on the influence of various parameters as related to the material as well as to the testing setup is resumed.

Embedment characteristics are strongly affected by the anisotropic properties of the wood material. More specifically, the embedment stiffness and the embedment stresses reduce with increasing load-to-grain angle, i.e., from parallel to perpendicular to the grain loading (Schweigler et al., 2016b; Bléron and Duchanois, 2006; Ehlbeck and Werner, 1992; Hübner et al., 2008). For loading close to perpendicular to the grain, increasing the dowel displacement can however lead to strong displacement hardening effects, and consequently, to even higher embedment stresses than parallel to the grain (Schweigler et al., 2016b; Pedersen, 2002). This effect was shown to be stronger for smaller dowel diameters (Schweigler et al., 2016b; Franke and Quenneville, 2010; Sawata and Yasumura, 2002). Furthermore, a secondary effect of the anisotropy is encountered for load-to-grain angles deviating from the principal material directions. For such loading conditions, lateral displacements (Schweigler et al., 2016b) or reaction forces are caused due to unconstrained or constrained loading conditions, respectively. As a novel issue, we herein aim to quantify corresponding reaction forces in embedment tests.

The use of optical deformation measurement systems, based on digital image correlation technique in connection testing, has proven to give insight into the displacement behavior of the steel dowels as well as into the deformation behavior of the wood below the dowels (Bader et al., 2015; Sjödin et al., 2006). Recently, the combination of optical surface deformation measurement with micro-computed X-ray tomography gave unprecedented insight into the local deformation behavior of the porous wood microstructure under embedment loading (Lederer et al., 2016). This is particularly interesting for the interpretation of the global load-displacement behavior, as well as for the brittle failure of the wood, since the data obtained in this study show the densification of the cellular material and the development of cracks. Consequently, the nonlinear displacement path of dowels in unconstrained loading can be related to the densification of the wood cells perpendicular to the grain.

This contribution aims at a deeper understanding of the steel dowel embedment behavior under loading at an angle to the grain by means of a novel biaxial embedment test setup. The main difference to the previous test series (Schweigler et al., 2016b) are the lateral displacement boundary conditions during embedment testing. Beside discussing results from embedment tests presented herein, the objective of this contribution is to finally quantify the effect of different lateral dowel displacement conditions on the embedment stress-displacement relationship. From a mechanical point of view, results from embedment tests with unconstrained lateral loading conditions can be considered a lower limit, and those from embedment tests with constrained lateral boundary conditions can be considered an upper limit of the corresponding embedment stresses. From a practical, timber engineering point of view, constrained displacement loading of dowels is given in multiple steel-to-timber dowel connections loaded by an in-plane bending moment (cf. Bader et al., 2015).

Following-up the aim of the authors' previous works, embedment characteristics representative for ductile, i.e., reinforced dowel connections should be determined herein as well.

This is why reinforced embedment test specimens have been used in order to avoid premature brittle failure modes.

For reasons of comparability, embedment tests under constrained displacement conditions, were designed using the same materials and embedment testing conditions as used in the previous test series under unconstrained conditions (see Schweigler et al., 2016b). In both test series, laminated veneer lumber (LVL) loaded by 12 mm and 16 mm dowels, under standard moisture conditions, at the same load-to-grain angles and up to similar dowel displacements were investigated. Therefore, the data from both test series can be interpreted as a single dataset, representing an upper and lower limit of the embedment behavior in LVL, for two different displacement loading situations. Evaluation of test data includes the calculation of embedment stresses dependent on the dowel displacement and the load-to-grain angle, as well as embedment strength properties including definitions given in current testing and design standards. This facilitates the comparison with previous experimental data and design equations of the European timber engineering design standard EN 1995-1-1 (2004) (Eurocode 5). The output of these tests is also expected to support discussions related to testing regulations provided in embedment testing standards, as e.g. EN 383 (2007), ASTM D5764-97a (2002) or ISO/DIS 10984-2 (2009).

2.2 Materials and methods

2.2.1 Wood specimens and steel dowels

More than 50 embedment tests were carried out under constrained displacement boundary conditions, including two different dowel diameters, namely 12 mm and 16 mm, respectively. The load was applied in 15° steps, ranging from loading parallel (0°) to loading perpendicular (90°) to the grain.

Laminated veneer lumber (LVL) with 3 mm thick, parallel-laminated veneers, i.e., the grain orientations in all veneer layers show in the same direction, made of spruce (Kerto-S[®], Metsä, Finland), with a board thickness of 51 mm was chosen as wood material in the test setup. Wooden test specimens had a width and height of 200 x 200 mm, except for load-to-grain angles, α_{ini} , of 75° and 90°, where, due to the expected high shear stresses (cf. Fig. 11 in Schweigler et al. (2016b) and specimen dimensions in EN 383 (2007)), an increased specimen width of 400 mm was used (see Fig. 2.1 and Table 2.1). A reinforcement by means of self-tapping screws (SPAX T-STAR plus[®], SPAX International GmbH & Co.KG, Germany), with a diameter of 8 mm was inserted perpendicular to the grain direction into predrilled holes at a distance of 60 mm above and below the dowel axis in the fiber direction (see Fig. 2.1). A summary of the specimen geometry, the number of tests per load-to-grain angle and dowel diameter is given in Table 2.1.

Before testing, LVL specimens were stored under standard climatic conditions according to EN 383 (2007) at 20 °C and 65% relative humidity, until mass equilibrium was reached. The mean mass density of the LVL specimens amounted to 512.0 kg/m³ (stdv= 6.2 kg/m³, n= 27) and 509.0 kg/m³ (stdv= 6.1 kg/m³, n= 26) for dowels with 12 mm and 16 mm in diameter, respectively. Kiln-dried LVL specimens with dimensions of approximately 60 x 50 x 51 mm were used to determine the corresponding moisture content. The mean value of the moisture content amounted to 11.0% (stdv= 0.08%, n= 4).

Dowels of high steel quality, i.e., hardened steel of parallel pins with smoothed surface, were used for both dowel diameters. A high steel quality is essential in full-hole embedment test setups in order to ensure only elastic bending deformations of the dowel, and thus quasi-

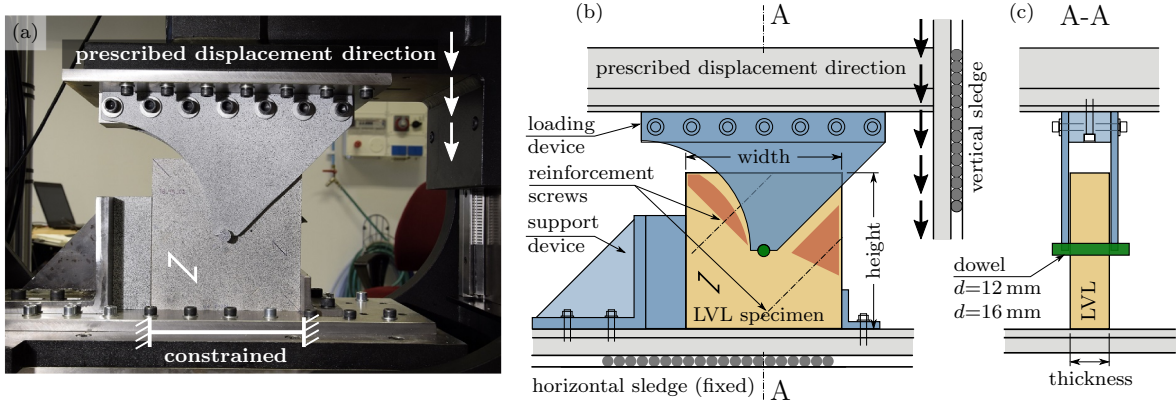


Figure 2.1: Test setup for full-hole embedment tests under constrained lateral displacement boundary conditions, (a) LVL specimen and steel parts with speckle pattern on a white base coat; vertical loading; horizontal displacement constrained; for a load-to-grain angle of 45° , (b) sketch of the test setup for loading under 45° to the grain, including the reference area (red-marked) used for calculation of the relative dowel displacement, and (c) cross section through the test setup.

Table 2.1: Dimensions of tested LVL specimens (cf. Fig. 2.1).

α_{ini} ($^\circ$)	Width (mm)	Height (mm)	Thickness (mm)	Number of tests (-)	
				$d=12$ mm	$d=16$ mm
0	200	200	51	3	3
15	200	200	51	4	4
30	200	200	51	4	4
45	200	200	51	5	4
60	200	200	51	4	4
75	400	200	51	4	4
90	400	200	51	3	3

uniform loading over the thickness of the specimen. This is especially important for the determination of stiffness parameters. The steel dowels were inserted into predrilled holes without any clearance.

The surface texture of the smoothed steel dowels was recorded for both applied dowel diameters by means of a contact-free characterization technique based on the principle of chromatic distance measurement (FRT MicroProf[®], FRT GmbH, Germany). In order to describe the surface quality, the arithmetic average of the surface roughness, R_a , measured at four different positions on the dowel surface was used. For calculation of R_a , a cutoff wavelength of 0.8 mm was applied, as recommended in EN ISO 4288 (1997). The mean value of R_a amounted to $1.14 \mu\text{m}$ ($\text{stdv}=0.029 \mu\text{m}$) and $0.68 \mu\text{m}$ ($\text{stdv}=0.007 \mu\text{m}$) for 12 mm and 16 mm dowels, respectively. Comparable R_a values were found for commercially galvanized steel dowels by Sandhaas et al. (2013). No significant influence of the surface quality on the embedment behavior was expected.

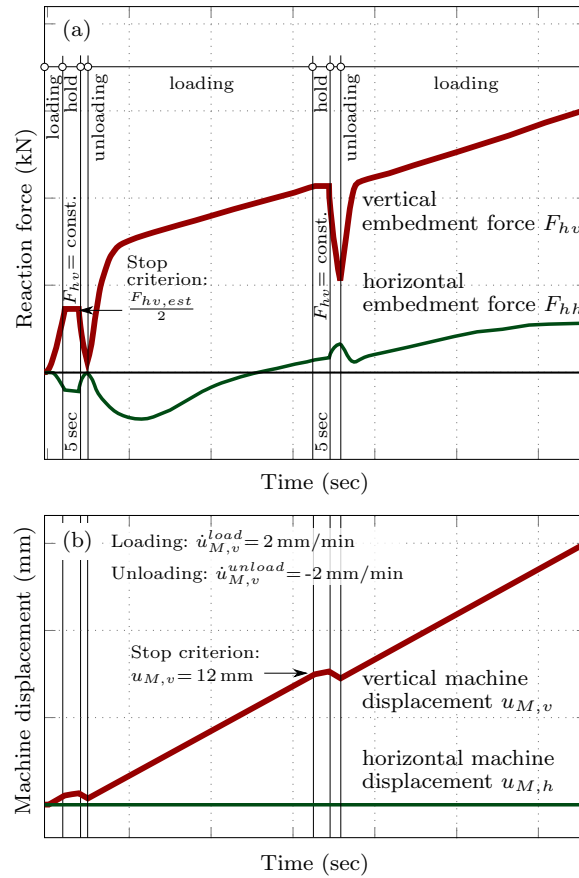


Figure 2.2: Loading protocol for embedment tests at constrained dowel displacement boundary conditions; (a) vertical F_{hv} and horizontal F_{hh} embedment forces vs. time, and (b) applied vertical $u_{M,v}$ and horizontal $u_{M,h}$ machine displacement vs. time.

2.2.2 Test setup and loading protocol

Embedment tests were carried out as full-hole embedment tests under compression following the principles of EN 383 (2007). A biaxial test setup allowed for recording vertical as well as horizontal reaction forces, caused by a prescribed vertical displacement of the piston (see Fig. 2.1). The testing machine (MTS Model 661.20F, MTS Systems Corporation, Sweden) consisted of a vertical and horizontal sledge, controlled independently from each other. The steel dowel, located in the center of the LVL specimen, was loaded in vertical direction by steel plates on both sides of the specimen. A curved shape of the steel plate on the left side from the steel dowel, i.e., the side with rising grain of the LVL specimen was chosen, in order to allow for recording surface deformations of an unloaded LVL specimen surface by means of an optical measurement system. The unloaded surface was used as a reference for the calculation of relative displacements between the LVL and the head of the steel dowel (cf. Fig. 2.1b and EN 383 (2007)). These steel plates were fixed to the vertical sledge of the testing machine (see Fig. 2.1). The LVL specimen was supported on the horizontal sledge, and the horizontal displacement of the sledge, $u_{M,h}$, was constrained, i.e., the displacement was set equal to zero during vertical load application (see Fig. 2.1). To achieve different load-to-grain angles for testing, the specimens were cut under a corresponding angle out of the LVL boards.

Loading was applied displacement controlled up to a vertical displacement of at least two

times the dowel diameter, i.e., 24 mm and 32 mm for 12 mm and 16 mm dowels, respectively. The loading protocol is illustrated in Fig. 2.2. The loading procedure included two unloading sequences, corresponding to the quasi-elastic and elasto-plastic range. The first unloading sequence was applied, by means of a stop criterion, when a vertical loading force of approximately half the estimated quasi-elastic load limit, $F_{hv,est}$, was reached. $F_{hv,est}$ was estimated based on results from previous embedment test at unconstrained loading conditions (Schweigler et al., 2016b), and was defined as the force at the end of the quasi-elastic part of the slip curve, which changed with load-to-grain angle and dowel diameter. Values of $F_{hv,est} = 10$ kN ($\alpha_{ini} = 0^\circ, 15^\circ$) and 7 kN ($\alpha_{ini} = 30^\circ - 90^\circ$) for dowel diameter of 12 mm, and $F_{hv,est} = 13$ kN ($\alpha_{ini} = 0^\circ, 15^\circ$) and 9 kN ($\alpha_{ini} = 30^\circ - 90^\circ$) for dowel diameter of 16 mm were estimated and used in the loading protocol (cf. Fig. 2.2). The second unloading sequence was performed at a vertical machine displacement, $u_{M,v}$, of approximately 12 mm (see Fig. 2.2b). At the beginning of each unloading cycle, the force F_{hv} was kept constant for 5 sec before unloading, in order to reduce the influence of time dependent effects on the unloading stiffness. A displacement rate, $\dot{u}_{M,v}$, of 2 mm/min for all sequences, i.e., loading, unloading and reloading cycle was chosen.

2.2.3 Load and deformation measurement techniques

The load cells of the biaxial testing machine directly recorded vertical and horizontal reaction forces as a result of the prescribed displacement of the vertical sledge. The deformation behavior of the steel dowel and the LVL specimen was measured separately by a non-contact displacement measurement system, based on digital image correlation (DIC) technique (Aramis[®], GOM, Braunschweig, Germany). Combination of two 12 mpx cameras allowed for recording a three-dimensional displacement field of the specimen surface, dowel head, loading and support device on one side of the test setup. For this purpose, after spraying of a white base coating, a fine speckle pattern was sprayed on each of these surfaces, with a desired point size of 2–3 pixels (see Fig. 2.1a). Thus, the DIC system gave access to the dowel displacement relative to the LVL surface, which was further used for the calculation of stiffness properties (EN 383, 2007). The field of view for the DIC was chosen to approximately 300 x 250 mm. A facet size of 19 px together with a grid spacing of 15 px (parameters have been set based on recommendations of the supplier and a preliminary study) resulted in a distance of approximately 1.2 mm between the measurement points. A noise study was carried out before each experiment, in order to check the suitability of the combination from speckle pattern, illumination and camera settings. For this purpose, a minimum of five DIC images have been taken of the specimen surface before mechanical loading. The maximum error, expressed as in-plane displacements amounted to $8 \cdot 10^{-3}$ mm, and expressed as resultant displacement including out-of-plane displacements, it amounted to $22 \cdot 10^{-3}$ mm, which is about 2% of the expected elastic embedment displacement. The maximum error of the measured strains amounted to $5 \cdot 10^{-4}$, which is less than 10% of the expected minimum strains in the vicinity of the dowel.

After testing, selected specimens were cut along the middle plane of the LVL for visual inspection of failure modes. Thus, residual permanent deformations and cracks in the final deformation state could be identified qualitatively, by means of obviously compressed wood cells and local grain deviations.

2.2.4 Evaluation methods

The dowel displacement, measured by DIC, was calculated as the displacement of the dowel head (green-marked in Fig. 2.1b) relative to an undeformed reference area of the LVL speci-

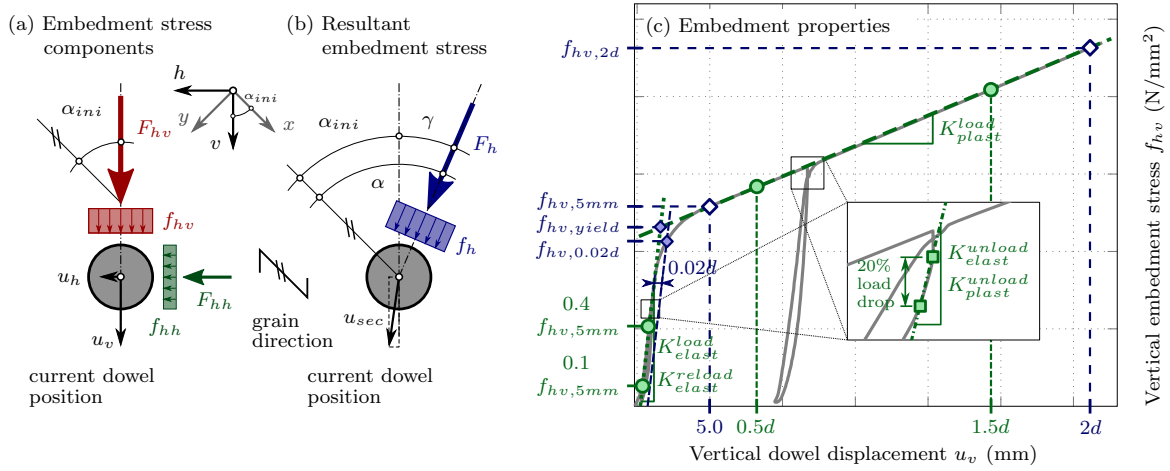


Figure 2.3: Definition of (a) embedment stress components, (b) resultant embedment stress and loading direction, and (c) embedment properties.

men (red-marked in Fig. 2.1b), following the recommendations of EN 383 (2007). For loading angles up to 30°, the reference area was set on the LVL surface, located at one side from the steel loading plate. For higher loading angles, reference areas on the LVL surface have been defined left and right from the steel loading plate (cf. Fig. 2.1b). As illustrated in Fig. 2.1b, reference areas were located in the upper half of the LVL specimen, defined by the area above a virtual line parallel to the grain direction crossing the steel dowel in the center of the LVL specimen. These parts of the specimen showed hardly any deformation, and thus, have been considered to behave as rigid body. Subsequently, the dowel displacement was divided into a vertical, u_v , and horizontal, u_h , displacement component (see Fig. 2.3a), with the vertical displacement component defined as the relative displacement parallel to the applied vertical loading direction (cf. coordinate system v, h in Fig. 2.3). The horizontal displacement component is a result of compliances in the contact surface between the horizontally constrained support device and the LVL specimen, as well as of the elastic reaction of the specimen itself during loading. In addition, the dowel displacement can be expressed as resultant displacement between the initial and current dowel position, indicated as secant dowel displacement, u_{sec} , in Fig. 2.3b. The initial slip at the very beginning of load application was excluded from the dowel displacement parameters by setting the dowel displacement at a vertical embedment stress of 1 N/mm² equal to zero.

Similar to the dowel displacements, vertical and horizontal embedment forces, which are reaction forces as a consequence of the applied vertical dowel displacement, were defined as vertical, f_{hv} , and horizontal embedment stress, f_{hh} , respectively (see Fig. 2.3a). In addition, the resultant embedment stress, f_h , was determined from the resultant embedment force, which was calculated by vector addition of the vertical and horizontal embedment force components (see Fig. 2.3b). For the calculation of embedment stresses, recorded vertical and horizontal reaction forces were divided by the projected area of the dowel, i.e., by the thickness of the LVL specimen times the dowel diameter. Thus, embedment stresses were defined as nominal embedment stress, assuming a uniform embedment stress distribution over the projected dowel area (see also definitions specified in EN 383 (2007)).

The initial load-to-grain angle, α_{ini} , was defined as the angle between the initial vertical loading direction and the grain direction. Loading of the orthotropic LVL led, in general, to a

horizontal reaction force, and thus, to an inclination of the initially vertical load vector. The observed change in the loading direction, γ , was calculated as the arctangent of the vertical, f_{hv} , and horizontal, f_{hh} , embedment stresses (see Fig. 2.3b). The loading direction, γ , depicts the orientation of the load vector since the embedment stresses are proportional to the directly measured load components F_{hv} and F_{hh} .

The embedment strength was defined by four different parameters. The first refers to the embedment strength definition given by EN 383 (2007), $f_{hv,5mm}$. This embedment strength was defined as the maximum nominal embedment stress up to a vertical dowel displacement of 5 mm (see Fig. 2.3c). The second parameter describes the elasto-plastic embedment strength taken at a vertical dowel displacement of two times the dowel diameter, $f_{hv,2d}$. In addition, two parameters were used to describe the quasi-elastic limit. One of this two parameters refers to the $0.02d$ offset of the quasi-elastic loading stiffness, $f_{hv,0.02d}$ (Hwang and Komatsu, 2002). This approach is comparable to the $0.05d$ offset method used in ASTM D5764-97a (2002). The second parameter describes the yield stress of the embedment behavior, $f_{h,yield}$, and was determined as the intersection between the lines defined by the quasi-elastic, K_{elast}^{load} , and elasto-plastic loading, K_{plast}^{load} , stiffness.

The loading stiffness (in terms of the embedment modulus) in the quasi-elastic part (K_{elast}^{load}), was calculated as the inclination of the line connecting the stress points on the loading path at 10% and 40% of the embedment strength $f_{hv,5mm}$ (similar to the stress points suggested by EN 383 (2007)). A similar definition was used for the reloading stiffness, K_{elast}^{reload} . For the reloading stiffness, the inclination of a line between the two stress points at 10% and 40% of the embedment strength $f_{hv,5mm}$ on the reloading path in the quasi-elastic range was used. The loading stiffness in the elasto-plastic part was determined between the stress points on the loading path at a vertical dowel displacement of 0.5 and 1.5 times the dowel diameter. The unloading stiffness parameters in the quasi-elastic domain (K_{elast}^{unload}) and in the elasto-plastic domain (K_{plast}^{unload}) were calculated as the inclination of the line connecting the first recorded stress point immediately at the beginning of the unloading cycle and the stress point at 20% load drop (see Fig. 2.3c).

2.3 Results and discussion

2.3.1 Constrained lateral dowel displacement behavior

Constraining the wooden test specimens in horizontal direction, i.e., lateral to the vertical loading direction, allowed for embedment tests at constrained lateral dowel displacement boundary conditions. Thus, the dowel could move only in vertical direction with respect to the testing machine setup. However, minor relative horizontal dowel displacements, u_h , with respect to the LVL specimen of less than 0.9 mm were measured by the DIC-system. The horizontal displacement corresponds to less than 3% of the applied vertical dowel displacement whereby the maximum was reached at $\alpha_{ini}=45^\circ$ for $d=16$ mm. This undesired horizontal displacement was caused by compliances in the contact area between the test specimen and the horizontal support device, as well as by horizontal elastic deformations of the LVL specimen itself. Thus, for practical reasons fully constrained dowel displacement conditions are difficult to establish. Nevertheless, the comparable small horizontal displacements, u_h , at constrained displacement boundary conditions are not expected to significantly influence the experimental results. In the following discussion, the vertical dowel displacement, u_v , is used, which was almost equal to the secant dowel displacement, u_{sec} , since the horizontal displacement component, u_h , was significantly smaller than the vertical displacement component, u_v .

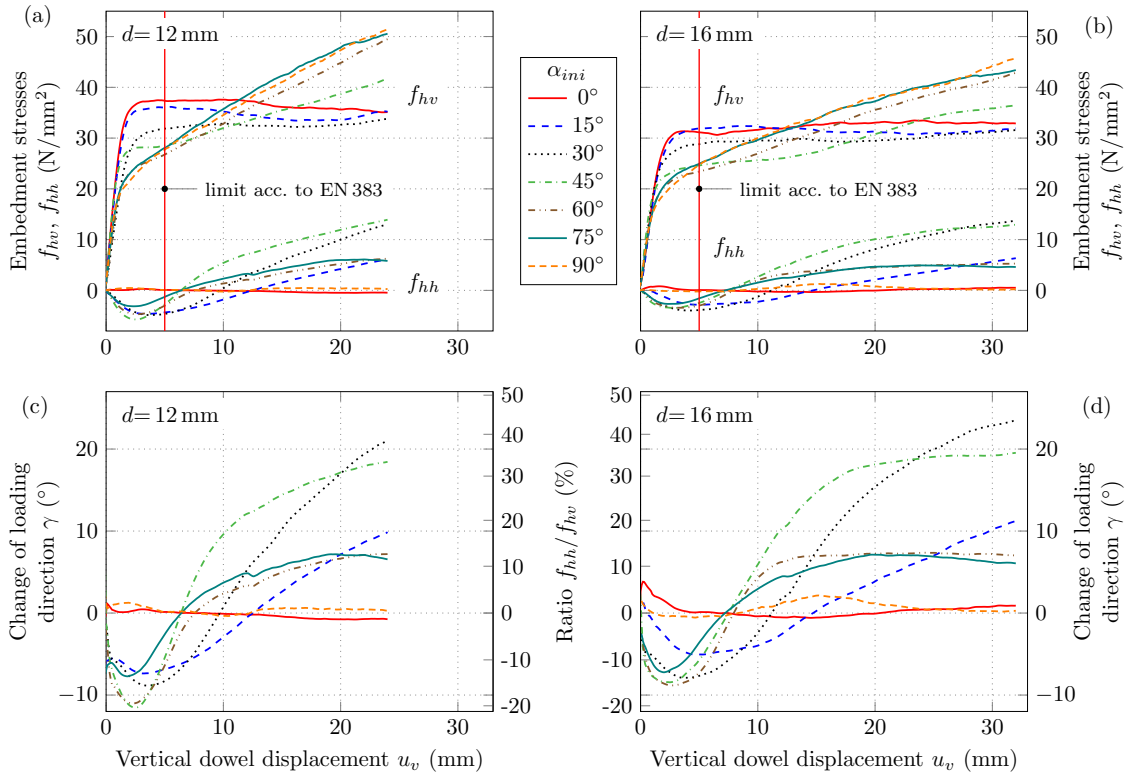


Figure 2.4: Embedment behavior for $d=12$ mm (left column) and $d=16$ mm (right column), (a)–(b) vertical embedment stress f_{hv} and horizontal embedment stress f_{hh} , (c)–(d) change of loading direction γ and ratio f_{hh}/f_{hv} , respectively, plotted over vertical dowel displacement u_v .

2.3.2 Load-displacement behavior

The load-displacement behavior of steel dowels embedded in wood or wood-based products, like LVL, is commonly described by its slip behavior, i.e., the vertical embedment stress, f_{hv} , plotted over the vertical dowel displacement, u_v . As a novel issue, the horizontal reaction force, caused by the constrained vertical load application of the anisotropic material, was quantified in this study. Fig. 2.4a and b visualizes the experimentally determined vertical and horizontal embedment stress (mean values) of the first-loading path and their dependence on the load-to-grain angle for dowels. Three-dimensional illustrations of the slip behavior are presented in Fig. 2.5. Linear interpolation has been used for the areas between the measured slip curves at 15° load-to-grain angle steps.

In general, a similar shape of the load-displacement curves has been found for both dowel diameters of 12 mm and 16 mm. However, differences in the magnitude of the nominal embedment stresses, dependent on the load-to-grain angle and dowel displacement, between these two dowels were observed.

For loading parallel to the grain (0°) up to loading at 30° to the grain, the load-displacement behavior can be characterized by an almost linear-elastic, ideal plastic response (cf. Fig. 2.4a and b). A decrease in the quasi-elastic stiffness, K_{elast}^{load} , and embedment strength, $f_{hv,0.02d}$, with increasing load-to-grain angle, α_{ini} , became obvious. The area for loading between 30° and 60° with respect to the grain, exhibits a further decrease in the quasi-elastic strength

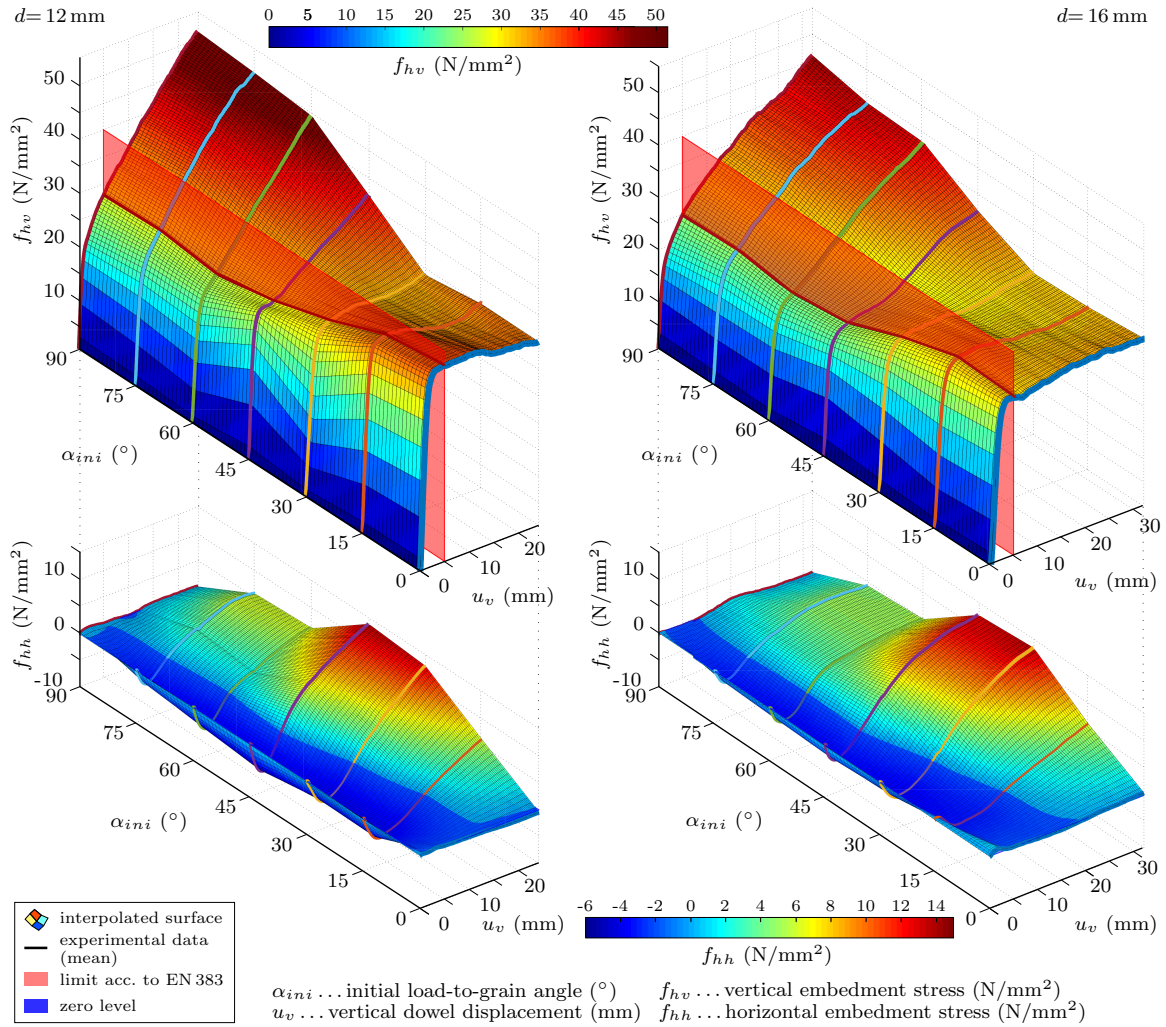


Figure 2.5: Vertical embedment stress f_{hv} (top), and horizontal embedment stress f_{hh} (bottom) plotted over the load-to-grain angle α_{ini} and the vertical dowel displacement u_v for dowel diameter 12 mm (left) and 16 mm (right), including the embedment stress limit according to EN 383 (2007).

limit, and additionally a pronounced increase of the elasto-plastic stiffness with increasing α_{ini} . For loading at 60° to the grain and higher, almost the same behavior regarding stiffness and strength for the quasi-elastic and elasto-plastic part was observed for all load-to-grain angles within this range. The corresponding increase of the elasto-plastic loading stiffness with increasing α_{ini} , could be explained by densification of the wood in the contact area below the dowel as well as by the so-called rope effect in wood fibers. In addition, the densification effect in the wood below the dowel is superimposed by strengthening effects caused by the constrained load application. This strengthening effect is expected to be strongest for load-to-grain angles, α_{ini} , with the highest lateral embedment stresses, which will be discussed next.

As obvious from Fig. 2.4a and b and Fig. 2.5, loading parallel to the principal material directions (0° and 90°), caused only negligible horizontal reaction forces, while for intermediate load-to-grain angles, pronounced horizontal embedment stresses were observed.

An interesting observation is that the horizontal embedment stress changes sign over the loading process Fig. 2.4c and d. This characteristic can be related to the anisotropic and porous wood microstructure and is well in-line with the change in sign of the horizontal dowel displacement from embedment test under unconstrained lateral dowel displacement conditions (Schweigler et al., 2016b). For unconstrained loading conditions, the dowel was found to move first towards the initial softer material direction, i.e., perpendicular to the grain. Consequently, constraining the dowel displacement to a vertical displacement path, caused an horizontal embedment stress facing the opposite direction. Further increasing the vertical dowel displacement led to densification of the wood in the contact area with the steel dowel (cf. Lederer et al., 2016), and thus, to a change of the stiffness conditions below the dowel. This causes a change in the horizontal embedment stress towards perpendicular to the grain. The point of transition in the direction of the lateral embedment stresses differed for different load-to-grain angles, and tends to be at a lower displacement for load-to-grain angles deviation most from the principal material directions.

The maximum absolute embedment stress, f_{hh} , was found for loading at 30° and 45° to the grain (see Fig. 2.4a and b). Considerably lower values were found for load-to-grain angles of 15° , 60° and 75° . However, the absolute horizontal embedment stress at the first peak, at a vertical dowel displacement of 2.3–5.3 mm, was found to be similar for all loading directions deviating from the principal material directions. These stresses amounted to 2.7–5.7 N/mm², with the highest values for load-to-grain angles of 30° and 45° .

The highest change in loading direction, γ , was found for loading at 30° to the grain, for both dowel diameters. At a vertical dowel displacement, u_v , of twice the dowel diameter, the direction of the resultant force vector deviated by 21.0° and 23.5° from the vertical displacement direction, for the dowel with 12 mm and 16 mm in diameter, respectively. In other words, the horizontal embedment stress amounted to about 40% of the vertical embedment stress (see Fig. 2.4c and d). A similar trend was seen for loading at 45° , while for other loading directions the maximum ratio horizontal/vertical embedment stress was less than 20%. However, at a comparable small vertical dowel displacement, u_v , of less than 5 mm, the horizontal embedment stress already amounted to 9%–20% of the vertical embedment stress for all loading directions deviating from the principal material directions.

2.3.3 Embedment stiffness

The stiffness of the embedment behavior is described by means of its embedment moduli, i.e., the vertical embedment stress per vertical dowel displacement. In total five parameters, two for unloading (Fig. 2.6), two for loading and one for reloading (Fig. 2.7), covering the quasi-elastic and elasto-plastic region, were determined. Mean values and standard deviations of stiffness properties are summarized in Table 2.2.

Unloading stiffness

The unloading stiffness is of special interest, since it gives insight into elastic, i.e., recoverable, deformations in the embedment loading of the dowel. Both unloading stiffness parameters (see Fig. 2.6) exhibit a similar trend, that is, a decrease in stiffness with an increase in the load-to-grain angle. The unloading stiffness in the elasto-plastic part, K_{plast}^{unload} , decreased between loading parallel (0°) and perpendicular to the grain (90°) by about 54% and 72% for the 12 mm and 16 mm dowel, respectively. Similar numbers were found for the unloading stiffness in the quasi-elastic part, K_{elast}^{unload} . Consistently, higher stiffness values were found for

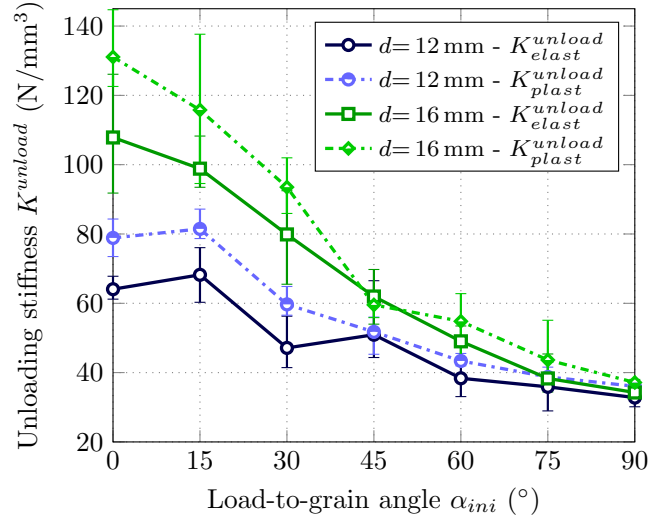


Figure 2.6: Unloading stiffness in the quasi-elastic part K_{elast}^{unload} and elasto-plastic part K_{plast}^{unload} vs. load-to-grain angle α_{ini} for the 12 mm and 16 mm dowel, including the variability of the experimental data.

Table 2.2: Embedment properties of LVL for $d=12$ mm and $d=16$ mm.

α_{ini} ($^{\circ}$)	K_{elast}^{load} (N/mm^3)		K_{plast}^{load} (N/mm^3)		K_{elast}^{reload} (N/mm^3)		K_{elast}^{unload} (N/mm^3)		K_{plast}^{unload} (N/mm^3)		$f_{h,0.02d}$ (N/mm^2)		$f_{h,yield}$ (N/mm^2)		$f_{h,5mm}$ (N/mm^2)		$f_{h,2d}$ (N/mm^2)		
	mean	stdv	mean	stdv	mean	stdv	mean	stdv	mean	stdv	mean	stdv	mean	stdv	mean	stdv	mean	stdv	
<i>d=12 mm</i>																			
0	27.6	8.58	-0.122	0.068	40.6	8.35	64.1	3.39	78.9	5.41	32.6	3.53	37.9	1.61	37.8	1.47	38.1	1.12	
15	26.1	7.67	-0.204	0.131	46.4	10.77	68.2	6.66	81.5	3.95	30.1	2.88	36.9	3.01	36.2	3.00	36.7	2.26	
30	16.3	2.85	0.017	0.079	29.9	3.89	47.1	6.38	59.7	3.75	26.8	2.94	32.0	1.81	31.9	1.84	34.2	1.69	
45	28.5	4.40	0.687	0.130	37.8	5.38	50.9	9.11	51.7	4.49	23.8	2.19	25.5	2.62	28.6	2.32	41.8	3.07	
60	18.4	1.34	1.207	0.097	28.4	1.46	38.4	4.57	43.4	1.70	19.7	0.70	22.2	1.75	26.8	1.20	49.5	2.42	
75	20.8	2.08	1.340	0.223	27.8	2.46	35.9	5.02	38.8	1.89	19.4	1.68	23.0	1.06	28.1	1.78	50.6	3.91	
90	21.4	2.77	1.298	0.063	27.8	3.72	32.8	2.43	36.1	1.74	18.1	0.53	22.9	0.42	27.7	0.40	51.4	3.83	
<i>d=16 mm</i>																			
0	17.2	1.43	0.135	0.066	54.6	6.92	107.9	17.25	131.1	11.93	27.6	1.95	30.4	1.10	31.5	1.32	33.9	1.03	
15	17.8	4.18	-0.092	0.038	50.3	8.44	98.8	6.52	115.8	17.78	26.8	1.60	32.9	1.44	31.9	1.10	32.7	1.39	
30	18.9	4.31	0.045	0.034	42.4	7.45	79.9	11.87	93.5	7.30	24.0	1.59	29.0	1.43	28.9	1.51	31.6	1.52	
45	22.6	2.41	0.518	0.105	43.0	3.11	62.0	6.53	59.5	2.72	19.3	1.01	21.7	1.30	24.6	1.02	36.5	1.21	
60	17.9	3.81	0.799	0.058	32.2	5.09	49.0	4.82	54.8	8.05	18.0	1.25	19.9	1.96	23.4	1.64	42.9	2.55	
75	18.7	8.00	0.749	0.069	28.0	8.27	38.3	5.10	43.6	9.00	18.0	1.21	23.1	1.02	24.9	1.12	43.9	2.14	
90	16.7	3.13	0.724	0.150	24.8	2.24	34.3	1.34	37.2	1.42	16.4	0.83	23.3	1.53	24.7	1.27	45.7	5.74	

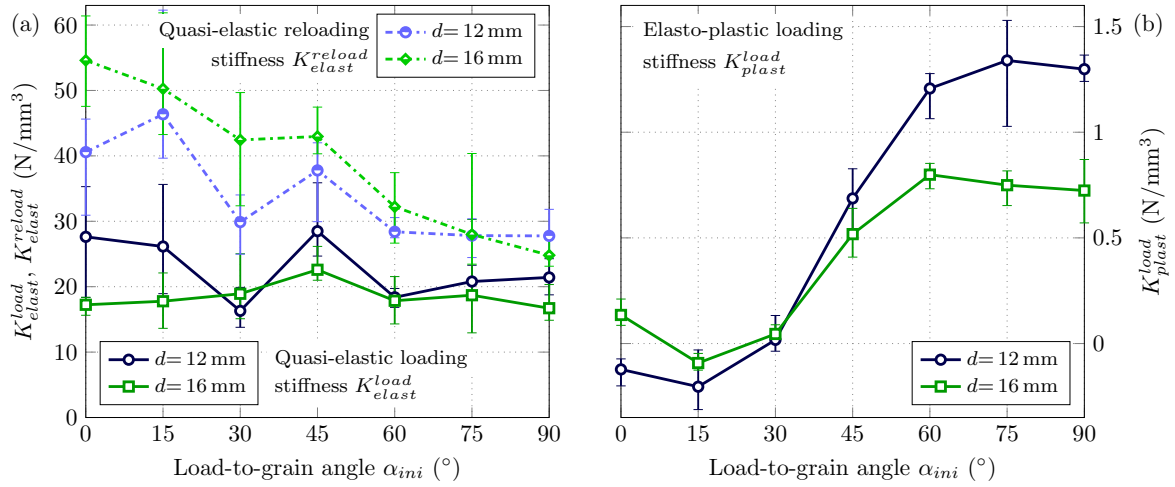


Figure 2.7: Loading and reloading stiffness plotted over the load-to-grain angle α_{ini} for 12 mm and 16 mm dowels, including the variability of the experimental data, (a) quasi-elastic loading stiffness K_{elast}^{load} and reloading stiffness K_{elast}^{reload} and (b) elasto-plastic loading stiffness K_{plast}^{load} .

16 mm than for 12 mm dowels. With increasing α_{ini} , this differences decreased from about 40% at $\alpha_{ini}=0^\circ$ to almost zero at $\alpha_{ini}=90^\circ$.

A stiffer response of larger dowels is partly in contradiction to previously reported data, which indicated a reverse trend (Hwang and Komatsu, 2002; Stamato and Calil Jr, 2000). However, other publications (Sandhaas et al., 2013; Karagiannis et al., 2016) and own tests (Schweigler et al., 2016b) showed the same trend as observed herein. In the particular setup of full-hole embedment tests, the interpretation of stiffness properties might be corrupted by elastic deformations of the steel dowel in bending (cf. Santos et al. (2010) and see also discussion in Schweigler et al. (2016b)).

The unloading stiffness was found to be 10%–20% higher for unloading in the elasto-plastic region compared to the quasi-elastic region. This might be explained by stiffening effects caused by constrained load application, which could be expected to be more pronounced for larger dowel displacements, since these constraining effects, expressed by a horizontal reaction force, increase with increasing vertical dowel displacement (cf. Fig. 2.4).

Loading and reloading stiffness

The quasi-elastic loading stiffness slightly decreased with increasing load-to-grain angle for the dowel with 12 mm in diameter (see Fig. 2.7a). In contrast, an almost load-to-grain angle independent behavior was found for 16 mm dowels. Both dowel diameters exhibited an increase in K_{elast}^{load} for loading at 45° to the grain, compared to the neighboring load-to-grain angles, i.e., 30° and 60° . Loading parallel (0°) and at 15° to the grain led to a similar stiffness behavior, which was found to be about 46%–60% stiffer for the 12 mm than the 16 mm dowel. For loading at 30° and 60° – 90° to the grain comparable stiffness properties were found for both investigated dowel diameters. Results describing the relationship between the quasi-elastic loading stiffness and load-to-grain angle (see Fig. 2.7a) could be questioned and are in contradiction to previous findings (Schweigler et al., 2016b), where a clear trend of decreasing quasi-elastic loading stiffness with increasing load-to-grain angle was found.

The quasi-elastic loading stiffness was found to be less than half of the unloading stiffness.

This can be explained by the fact of including additional softening effects, such as weak surface properties before full contact between the dowel and the wood is established. Furthermore, the loading stiffness in the quasi-elastic part is corrupted by unpreventable imperfections in the test setup, like small gaps between LVL specimen and support devices or slightly oversized boreholes. In addition, dowel displacement data from DIC measurements were only available for one side of the test specimen, since only one pair of cameras was disposable. Thus, the lack of data from both test specimen sides, in combination with the unstable displacement behavior for small dowel displacements, might have led to questionable results of the quasi-elastic stiffness, with largely high variability in the data.

A clearer trend over the load-to-grain angles was found for the quasi-elastic reloading stiffness, K_{elast}^{reload} (see Fig. 2.7a). However, the sensitivity of the loading procedure and test setup still seem to negatively influence the test results, as it became obvious for load-to-grain angles of 15° – 45° for the dowel with 12 mm in diameter. Nevertheless, consistently higher reloading stiffness values, K_{elast}^{reload} , were found for the 16 mm dowel than for the 12 mm dowel, well in line with the findings from the unloading stiffness (see Fig. 2.6).

In contrast to the quasi-elastic loading stiffness, the elasto-plastic loading stiffness K_{plast}^{load} exhibited less variable results and a clear relationship with the load-to-grain angle. An increase of K_{plast}^{load} with increasing α_{ini} can be seen from Fig. 2.7b, after K_{plast}^{load} was found to be almost constant for load-to-grain angles between 0° and 30° . The strongest increase in K_{plast}^{load} was found for $\alpha_{ini}=30^\circ$ to 60° . An up to 80% stiffer response was determined for the 12 mm than 16 mm dowel at large load-to-grain angles. This might be explained by the so-called rope effect of wood fibers in tension as one important factor for the displacement hardening behavior (cf. discussion Schweigler et al., 2016b).

Awaludin et al. (2007) reported rather constant elasto-plastic embedment stiffness however with experiments up to a maximum displacement of about 3 mm only. An increase of the elasto-plastic embedment stiffness, K_{plast}^{load} , for load-to-grain angles close to 90° was reported by several previous contributions (Schweigler et al., 2016b; Sawata and Yasumura, 2002; Santos et al., 2010; Franke and Magnière, 2014), in line with the results presented herein.

2.3.4 Embedment strength

Embedment strength is commonly determined as the maximum nominal embedment stress up to a dowel displacement of 5 mm (EN 383, 2007), $f_{hv,5mm}$. The corresponding displacement limit is indicated by red lines in Fig. 2.4a and b, as well as by the semi-transparent red surface in Fig. 2.5; see also Table 2.2. The diagrams of the embedment strength parameters in Fig. 2.8 include a comparison with the embedment strength determined according to Eqs. (8.31–8.33) of the European design code Eurocode 5 (EN 1995-1-1, 2004), $f_{hv,EC5}$. For its calculation, experimentally determined mean densities of LVL were used.

Independent from the type of the embedment strength property, discussed herein, a clear correlation between the embedment strength and load-to-grain angle became obvious for both dowel diameters (Fig. 2.8). The embedment strength properties $f_{hv,5mm}$ and $f_{hv,0.02d}$ followed the S-shaped trend of the embedment strength according to Eurocode 5, $f_{hv,EC5}$. In contrast, a strong increase of $f_{hv,2d}$ with an increase in α_{ini} , for large load-to-grain angles was found. Consistently higher embedment strength properties were found for the 12 mm than for the 16 mm dowel.

The mean value of $f_{hv,5mm}$ for loading parallel to the grain (0°) was found to be 37.8 N/mm^2 and 31.5 N/mm^2 for 12 mm and 16 mm dowels, respectively (see Fig. 2.8 and Table 2.2). For loading perpendicular to the grain (90°), $f_{hv,5mm}$ amounted to 27.7 N/mm^2 and 24.7 N/mm^2

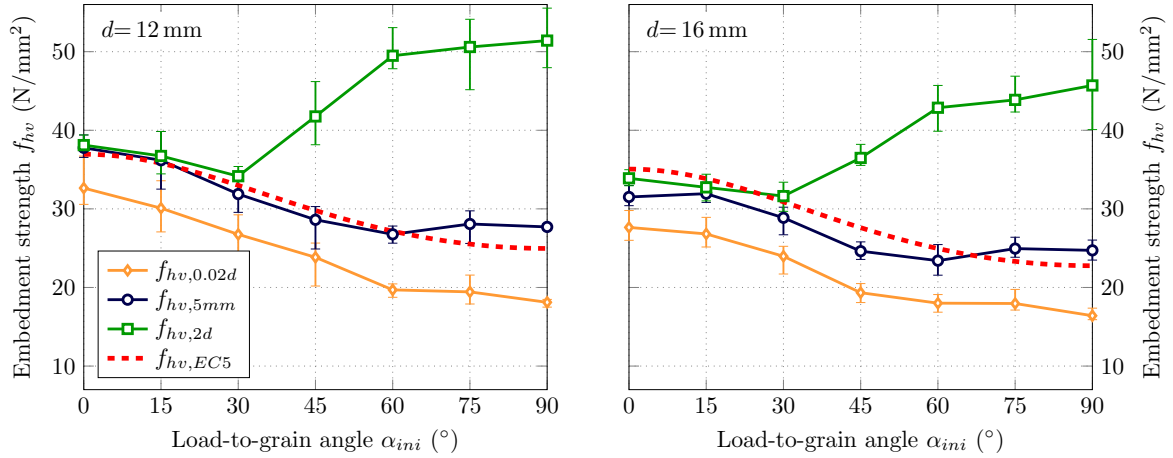


Figure 2.8: Embedment strength properties vs. load-to-grain angle α_{ini} for $d=12$ mm (left) and $d=16$ mm (right) including variability of the experimental data. Additional comparison of the experimentally determined embedment strength properties ($f_{hv,0.02d}$, $f_{hv,5mm}$ and $f_{hv,2d}$) to Eurocode 5 (EN 1995-1-1, 2004) based calculation of the embedment strength ($f_{hv,EC5}$).

for 12 mm and 16 mm dowels, respectively, which is 27% and 22% smaller than for loading parallel to the grain.

The embedment strength described by the 2% offset limit, $f_{hv,0.02d}$, was found to be consistently 12%–35% below $f_{hv,5mm}$, for both dowel diameters. The differences between these two parameters increased with increasing α_{ini} . This highlights the fact, that $f_{hv,5mm}$ already includes plastic deformations, and thus depends on the underlying dowel displacement limit.

Regarding the embedment strength at a dowel displacement of twice the dowel diameter, $f_{hv,2d}$, a strong increase of the embedment strength with increasing load-to-grain angle was seen for α_{ini} larger than 30° (see Fig. 2.8). While for load-to-grain angles between 0° and 30° almost identical values for $f_{hv,2d}$ and $f_{hv,5mm}$ were found. For loading perpendicular to the grain (90°), $f_{hv,2d}$ amounted to 51.4 N/mm^2 and 45.7 N/mm^2 for $d=12$ mm and $d=16$ mm, respectively. These embedment strength values are 86% and 85% higher than corresponding values at a vertical dowel displacement of 5 mm, $f_{hv,5mm}$, thus highlighting the huge plastic resources, gained from hardening effects.

Higher nominal embedment stresses were found for the dowel with 12 mm than with 16 mm in diameter, consistently for all three embedment strength parameters, i.e., $f_{hv,5mm}$, $f_{hv,0.02d}$ and $f_{hv,2d}$. Interestingly, almost constant differences between $f_{hv,2d}$ for the two investigated dowel diameters, with changing α_{ini} , namely approximately 10%–15%, were determined. This, is partly in contrast to findings from Schweigler et al. (2016b), which showed a considerable increase in the differences with increasing load-to-grain angle. However, it should be emphasized that the embedment strength, $f_{hv,2d}$, is calculated at two different absolute vertical dowel displacements, i.e., 24 mm and 32 mm for the 12 mm and 16 mm dowel respectively. Determination at the same absolute displacement, i.e., 24 mm, would give a considerable increase in the differences from approximately 10% for loading parallel to the grain (0°), to about 30% for loading perpendicular to the grain (90°), which is well in line with the data presented in Schweigler et al. (2016b).

Comparison of the embedment strength calculated from Eurocode 5, $f_{hv,EC5}$, showed a

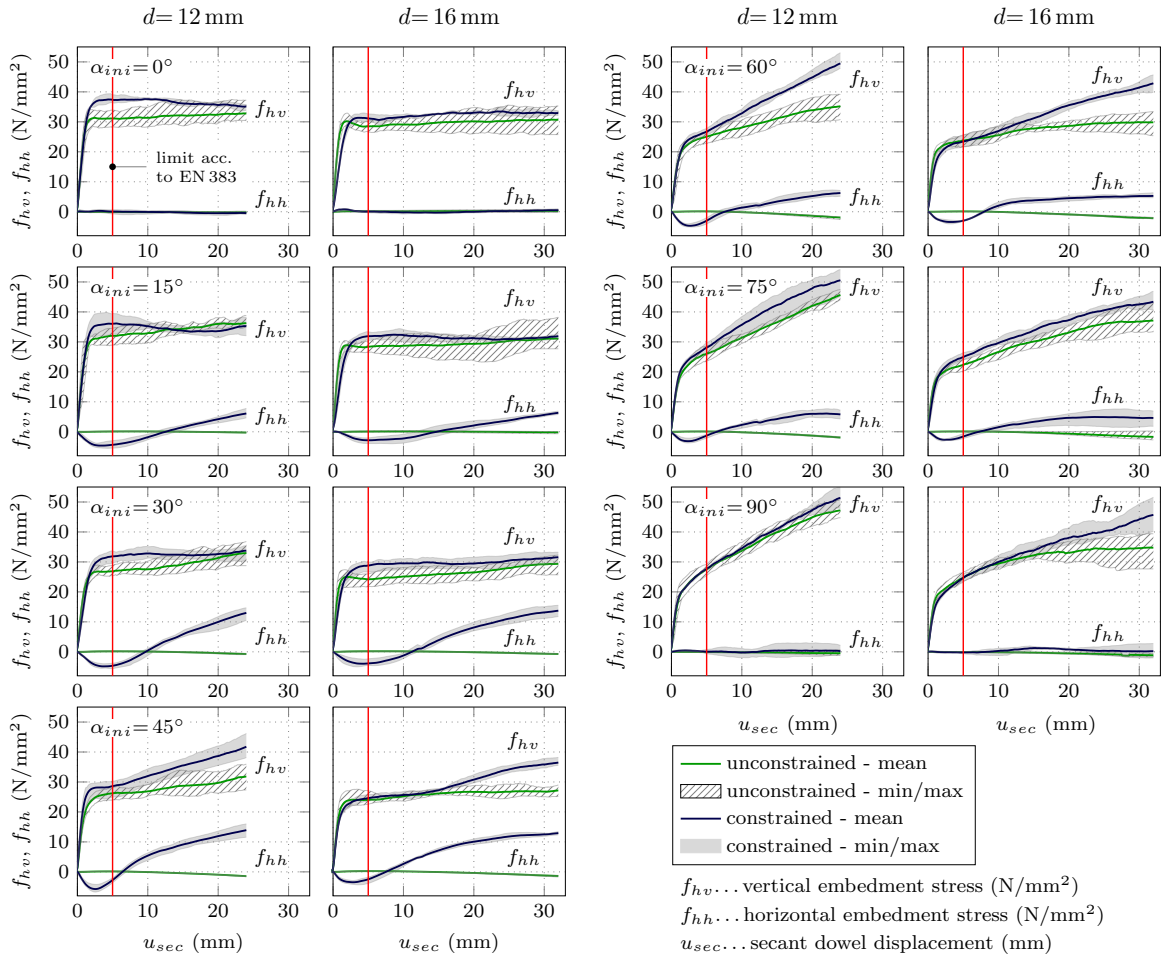


Figure 2.9: Comparison of the load-displacement behavior between unconstrained and constrained dowel displacement boundary conditions, for steel dowels with 12 mm and 16 mm in diameter embedded in LVL, loaded at different angles to the grain. Load components expressed as vertical embedment stress f_{hv} and horizontal embedment stress f_{hh} , plotted over the secant dowel displacement u_{sec} .

good correlation with the experimentally determined embedment strength, $f_{hv,5mm}$. However, $f_{hv,5mm}$ was slightly underestimated by Eurocode 5 for load-to-grain angles larger than 60° . A minor overestimation of the embedment strength, $f_{hv,5mm}$, by Eurocode 5 of about 10% was found for α_{ini} up to 60° for $d=16$ mm. These results are partly in conflict with findings in Schweigler et al. (2016b), where a more pronounced overestimation of the experimental strength by Eurocode 5 was found (see Schweigler et al., 2016b). Differences between the two embedment test series of LVL might be explained by differences in the loading situation, i.e., constrained vs. unconstrained dowel displacement boundary conditions.

2.3.5 Influence of lateral displacement boundary conditions

Finally, the embedment stress-dowel displacement behavior and its dependence on the lateral dowel displacement boundary conditions will be discussed by comparing the experimental dataset, for constrained loading, presented in this contribution with the dataset, for uncon-

strained loading, presented in Schweigler et al. (2016b).

For reason of comparability, the secant dowel displacement, u_{sec} , is used instead of the vertical dowel displacement, u_v , for the illustration of the slip curves from the two embedment test series (see Fig. 2.9). Regarding the slip behavior, negligible differences would be expected for loading parallel (0°) and perpendicular to the grain (90°), which should be independent of the lateral displacement boundary conditions. This was true for loading parallel to the grain for 16 mm dowels as well as for loading perpendicular to the grain for 12 mm dowels, where the difference is clearly within the variability of the data. However, for loading parallel to the grain, for 12 mm dowels, considerably higher stresses were measured for constrained than for unconstrained loading. This behavior cannot solely be explained by the variability of the test data. Instead, the local material response and the possibility to crack initiation and opening might be different in the two test setups. Similar observations were made for 16 mm dowels loaded perpendicular to the grain for dowel displacements larger than approximately 15 mm. Also in this case, constrained loading led to higher stresses, which however might be a result of an apparently more pronounced delamination of the outer veneer layers of the LVL specimen, reducing the actual embedment length for the test series at unconstrained loading. In addition, stiffening effects caused by the prescribed displacement path might positively influence the bearing capacity for loading perpendicular to the grain at constrained loading situations. The stiffening effect of the displacement constrained might also be supported by the fact of a slightly higher unloading stiffness in the elasto-plastic compared to the quasi-elastic region (see Fig. 2.10a and b), since a more pronounced stiffening can be expected for larger dowel displacements. In contrast, the opposite, i.e., slightly lower unloading stiffness in the elasto-plastic part, became obvious for unconstrained loading, where no stiffening effects can be expected (see Fig. 2.10a and b).

Obviously constraining the dowel displacement and enforcing a displacement path led to higher stresses and for the most part to a stiffer embedment behavior. The latter is well visible when comparing reloading or unloading stiffness (see Fig. 2.10a and b). Stiffness along the first loading path is however corrupted due to different displacement measurement setups applied in the two test series, in combination with unpreventable imperfections of the test setup, like slightly oversized boreholes or small gaps between test specimen and support construction. A decrease in the stiffness with increasing load-to-grain angle as well as higher stiffness properties for 16 mm than for 12 mm dowels were observed throughout both test series.

The most pronounced differences in the slip curves, i.e., the vertical embedment stress plotted over the secant dowel displacement, became obvious for loading under 45° and 60° to the grain (see Fig. 2.9). For these load-to-grain angles, constraining the lateral displacement led to about 31%–44% higher embedment stresses at a dowel displacement of two times the dowel diameter (Fig. 2.10c and d). These are moreover the load-to-grain angles where the highest lateral reaction forces have been measured in constrained testing conditions.

The lateral displacement condition of the dowel affects the embedment strength according to the test standard EN 383 (2007), $f_{hv,5mm}$, which suggest to measure the maximum stress up to a displacement of 5 mm. The differences of this strength property between unconstrained and constrained loading conditions are illustrated in Fig. 2.10c and d.

Instead of lateral, i.e., horizontal reaction forces in case of a prescribed linear displacement path, lateral dowel displacements and in general nonlinear displacement paths were found for unconstrained embedment testing (Schweigler et al., 2016b). The development of lateral displacements correspond well with the trend of lateral embedment stresses. Hence, stresses and displacements changed orientation over the loading path, which is a clear indication of changes in the microstructure of wood below the dowel as an origin of this behavior. Possible

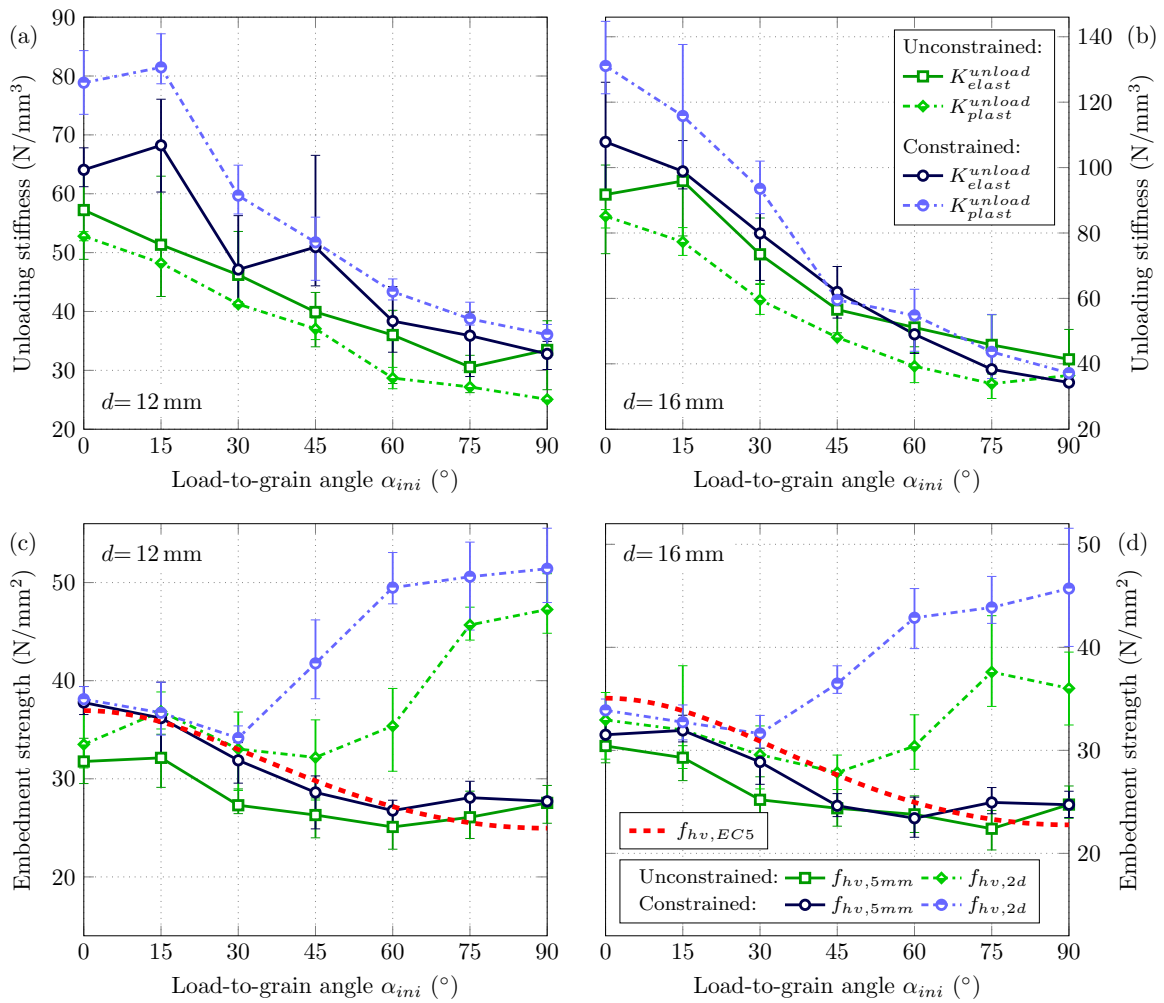


Figure 2.10: Comparison of embedment properties between unconstrained and constrained dowel displacement boundary conditions for $d = 12$ mm (left column) and $d = 16$ mm (right column), including the variability of the experimental data. (a)–(b) Unloading stiffness in the quasi-elastic K_{unload}^{elast} and elasto-plastic part K_{unload}^{plast} plotted over the load-to-grain angle α_{ini} . (c)–(d) Embedment strength properties $f_{hv,5mm}$ and $f_{hv,2d}$ vs. load-to-grain angle α_{ini} , including comparison to Eurocode 5 (EN 1995-1-1, 2004) based calculation of the embedment strength $f_{hv,EC5}$.

phenomena have already been discussed in this contribution and are also supported by surface strain images and visual inspection in Schweigler et al. (2016b), as well as by micro-computed X-ray tomography in Lederer et al. (2016).

Surface strain distributions, gained from DIC measurements, and permanent deformations, from specimen cuts, are illustrated for both loading conditions for the intermediate load-to-grain angles of 30°, 45° and 60° in Fig. 2.11. DIC images in combination with the permanent deformations after testing support the understanding for the local material behavior, and allow for interpretation of the differences in the slip curves between unconstrained and constrained loading conditions. It should be mentioned that different DIC measurement systems were used in the two test series. The systems use slightly different methods for strain determination. For reasons of comparability, deformations are presented as engineering strains in Fig. 2.11. Furthermore, the surface strain field might be corrupted by out-of-plane deformations and local inhomogeneities of the LVL. Corresponding effects are excluded when inspecting cut specimens.

DIC images showed qualitatively similar distributions of surface strains, expressed by ε_{xx} , ε_{yy} and ε_{xy} in the local material coordinate system, for unconstrained and constrained loading conditions.

For loading at an angle of 30° to the grain, a similar local material behavior becomes obvious from DIC images and specimen cuts (see Fig. 2.11). This confirms the almost identical load-displacement behavior for the vertical load component. However, from specimen cuts a considerable larger densified zone in lateral, i.e., horizontal direction was found. This might explain the comparable large horizontal embedment stress in constrained loading.

In contrast, constrained loading at 45° and 60° to the grain led to a significant change in the local material behavior compared to unconstrained loading, which is well visible in the slip curves of the vertical load component (cf. Fig. 2.9), and in the specimen cuts (see Fig. 2.11). As discussed above, unconstrained loading led to a lateral dowel displacement, which resulted in a horizontal dowel displacement facing the grain parallel direction for large vertical dowel displacements. Thus, the embedment behavior is closer to the one for loading parallel to the grain, especially for $\alpha_{ini}=45^\circ$ (see Schweigler et al., 2016b). Constraining the dowel displacement led to a more symmetric behavior with a more pronounced densified zone below the dowel, which is well visible from the specimen cuts (see Fig. 2.11). This behavior is close to the one found for loading perpendicular to the grain, i.e., displacement hardening based on the rope effect in wood fibers, which causes tensile stresses along the grain, in combination with an extensive densified zone below the dowel. Thus, the global load-displacement behavior is also close to the one for loading perpendicular to the grain.

2.4 Conclusions

A biaxial test setup for the quantification of vertical and horizontal reaction forces, for constrained full-hole embedment loading of steel dowels in LVL has been proposed in this work. It allowed to extend a previously initiated dataset for embedment stress-dowel displacement relationships for two different dowel diameters. Testing reinforced LVL specimens gave insight into the ductile load-displacement behavior up to dowel displacements of twice the dowel diameter. Loading under various angles to the grain, revealed the nonlinear development of a lateral reaction force for loading directions deviating from the principal material orientations. The lateral, i.e., horizontal reaction force even changed sign, i.e., changed its direction with increasing dowel displacement.

Anisotropic mechanical properties of wood, i.e., the dependence of the embedment behav-

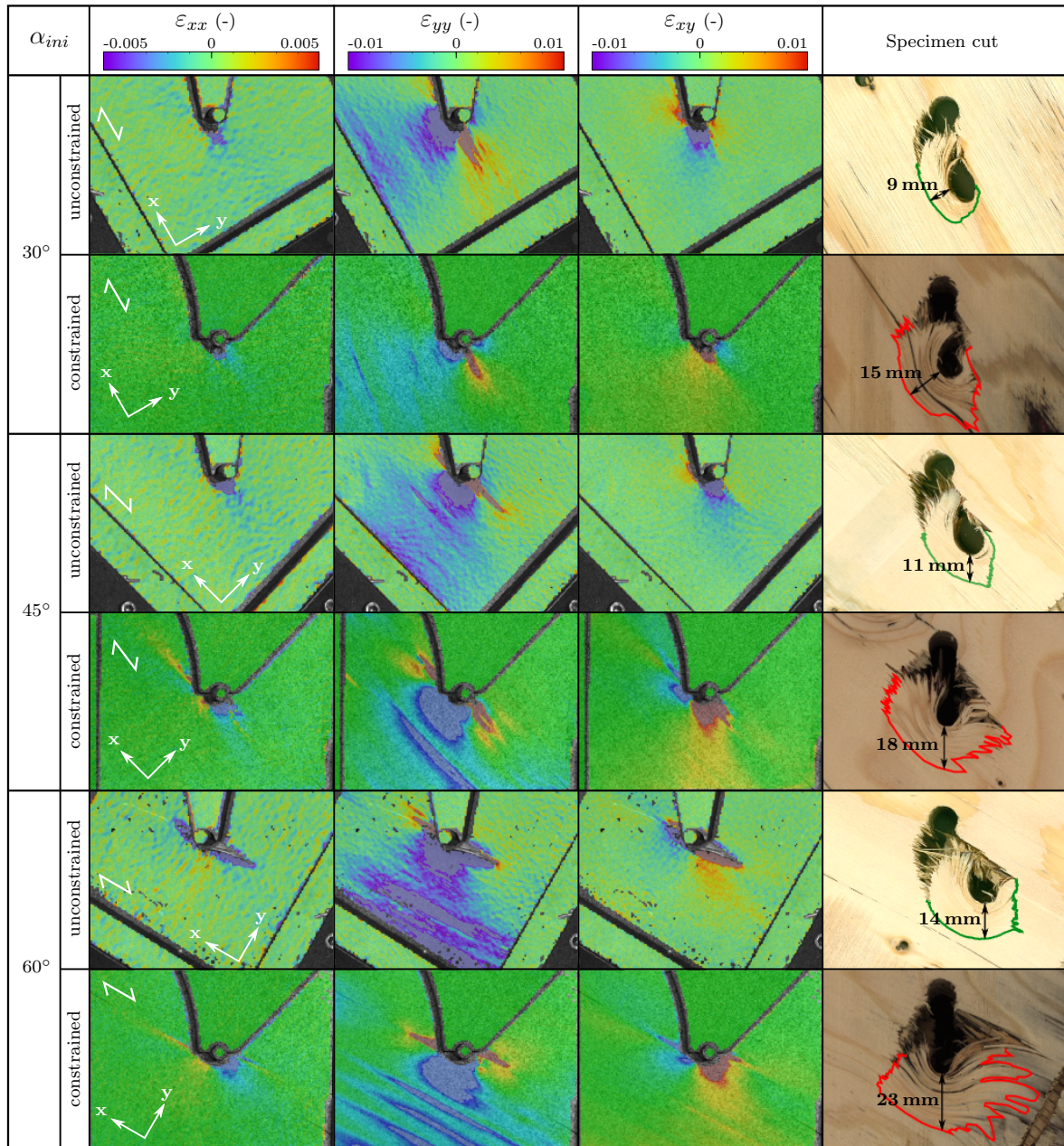


Figure 2.11: Comparison of the surface strains (DIC), expressed as engineering strains, and visual inspection for unconstrained and constrained loading conditions; (Column 1–3) Surface strains parallel to the grain ϵ_{xx} , perpendicular to the grain ϵ_{yy} and shear strains ϵ_{xy} for dowel diameter $d=12$ mm at a dowel displacement $u_{sec}=12$ mm for load-to-grain angles of 30°–60°; (Column 4) Designation of the visible plastic deformations of test specimens, cut along the center plane of the specimen, at approx. $u_{sec}=32$ mm for α_{ini} of 30°–60°.

ior on the load-to-grain angle, followed previously observed trends, also under constrained testing, namely increasing load-to-grain angle led to a decrease in the quasi-elastic limit, a decrease in the quasi-elastic loading and unloading stiffnesses, as well as a decrease in the embedment strength according to EN 383. Also, stronger displacement hardening effects for the smaller dowel diameter have been found as previously reported in literature.

For 12 mm dowels, the experimentally determined embedment strength according to EN 383 was found to be in good agreement with design equations in the Eurocode 5, while it was slightly lower for 16 mm dowels. Horizontal embedment stress of up to 20% of the vertical embedment stress were observed up to the displacement limit in EN 383. Going beyond the displacement limit used in EN 383 to define embedment strength resulted in even higher horizontal embedment stress of more than 40% of the vertical embedment stress at a dowel displacement of two times the dowel diameter.

Compared to the quasi-elastic loading stiffness, reloading and especially unloading stiffness were found to be more stable and less variable, and thus, are expected to be more reliable in the interpretation of test results and the identification of causal relationships. The variability of the stiffness along the first loading path however might be more important for stiffness properties required in the engineering design.

The comparison of constrained and previously reported unconstrained displacement controlled embedment tests led to the following conclusions. A stiffening effect in case of constrained loading became obvious for all slip curves, which became most obvious for loading under 45° and 60° to the grain, where loads resulting in up to 44% higher embedment stresses have been recorded. Consequently, higher embedment strength according to EN 383 has been measured under constrained than for unconstrained loading.

Most important, a similar trend was found for lateral displacements and lateral reaction forces as related to unconstrained and constrained displacement loading, respectively. The change of orientation of the two characteristics is thought to be related to the densification of the hollow wood cells, and consequently, to changes in the local wood properties below the dowel.

Knowledge about lateral forces or force orientation deviations is essential for the design of brittle failure modes and reinforcements of multiple dowel joints under in-plane bending moment loading. Thus, the work is expected to support the standardization process and could be used as input to analytical and numerical models of dowel joints, facilitating an advanced description of the nonlinear behavior of joints in timber structures.

Acknowledgements

The authors gratefully acknowledge the financial support of the Austrian Research Promotion Agency and the wood industry partnership Building with Wood within CEI-Bois for funding the research work within project *MechWood 2*. This work forms part of that project. The *MechWood 2* research partners are thanked for their cooperation and collaboration in this project. The financial support of the COST Action FP1402 to Michael Schweigler by means of a short term scientific mission, is thankfully acknowledged. We want to thank Michael Dorn and Bertil Enquist, Linnaeus University, for their support during testing.

Notation

d	dowel diameter
f_h	resultant embedment stress
f_{hh}	horizontal embedment stress
f_{hv}	vertical embedment stress
$f_{hv,0.02d}$	embedment strength determined by $0.02d$ offset of the quasi-elastic loading stiffness K_{elast}^{load}
$f_{hv,2d}$	embedment strength at a dowel displacement of two times the dowel diameter
$f_{hv,5mm}$	embedment strength acc. to EN 383
$f_{hv,EC5}$	embedment strength calculated acc. to Eurocode 5, Eqs. (8.31–8.33)
$f_{hv,yield}$	embedment yield strength
F_h	resultant embedment force
F_{hh}	horizontal embedment force
F_{hv}	vertical embedment force
F_{hv}^{est}	estimated quasi-elastic load limit
h	axis of the h - v coordinate system perpendicular to the vertical loading direction
K_{elast}^{load}	quasi-elastic loading stiffness
K_{plast}^{load}	elasto-plastic loading stiffness
K_{elast}^{reload}	quasi-elastic reloading stiffness
K^{unload}	unloading stiffness
K_{elast}^{unload}	quasi-elastic unloading stiffness
K_{plast}^{unload}	elasto-plastic unloading stiffness
R_a	arithmetic average of the surface roughness
u_h	horizontal dowel displacement
$u_{M,h}$	horizontal machine displacement
$u_{M,v}$	vertical machine displacement
u_{sec}	secant dowel displacement
u_v	vertical dowel displacement
$\dot{u}_{M,v}$	displacement rate
$\dot{u}_{M,v}^{load}$	displacement rate at loading
$\dot{u}_{M,v}^{unload}$	displacement rate at unloading
v	axis of the h - v coordinate system parallel to the vertical loading direction
α	current load-to-grain angle
α_{ini}	initial load-to-grain angle
γ	change of loading direction
ε_{xx}	engineering strain in grain direction
ε_{xy}	engineering shear strain
ε_{yy}	engineering strain perpendicular to the grain

An engineering modeling approach for the nonlinear load-displacement behavior of single dowel connections – parameter study (Schweigler et al., 2016a)

Authored by Michael Schweigler, Thomas K. Bader, Georg Hochreiner
& Josef Eberhardsteiner

Published in *Proceedings of the 2016 World Conference on Timber Engineering (WCTE)*

Abstract: An experimentally validated beam-on-nonlinear elastic foundation model for determination of nonlinear load-displacement behavior of single dowel connections is presented. The influence of connection properties, namely side member thickness, load-to-grain angle and dowel diameter on the connection behavior is investigated by means of a parameter study and compared to experimental findings. As a reason of the nonlinear connection behavior, strength properties and failure modes were found to depend on the displacement of the dowel. Changes in steel dowel failure modes were studied by increasing side member thickness, and corresponding transition zones could be identified. The effect of displacement hardening characteristics of the embedment behavior on overall connection properties became obvious in the study of the load-to-grain angle dependence of load-displacement curves. The development of plastic deformations in steel dowels was investigated and the onset of plastic deformations was found to be considerably lower than indicated by the first plastic hinge, thus dowels with a higher strength than used in this study should be used in practical application in order to avoid fatigue failure under serviceability load cases.

Keywords: single dowel connections, engineering modeling approach, parameter study, nonlinear slip curves

3.1 Introduction

Dowel connections are characterized by flexibility and high variability in their application for linking wood-based and steel elements. From a mechanical point of view, these connections exhibit a highly nonlinear load-displacement behavior, which originates from a nonlinear behavior of steel dowels in bending and of wood under embedment stresses. In the design of single dowel timber connections, this behavior is commonly simplified to be linear elastic and ideal plastic, as e.g. also specified in the current European timber engineering design standard Eurocode 5 (EC 5) (EN 1995-1-1, 2004). In order to overcome limitations due to these simplifications and to get access to the nonlinear behavior of dowel connections, several researchers used three-dimensional finite element method (FEM) simulations of dowel connections based on elasto-plastic and brittle material models for wood (Resch and Kaliske, 2012; Santos et al., 2009). However, the majority of these simulations were based on small strain theory, which limits the application of these models to small dowel displacements. Alternatively, beam-on-foundation models for the prediction of load-slip curves of dowel connections were introduced, as for example described by Hager (1930) or reviewed by Patton-Mallory et al. (1997). Hochreiner et al. (2013) presented an engineering, numerical modeling approach, based on beam-on-nonlinear elastic foundation principles. This modeling approach allows for consistent determination of slip curves for arbitrary connection configurations, up to large plastic dowel deformations, based on design-elements available in commercial structural analysis software. Herein, this numerical modeling approach is used for a parameter study with the aim to investigate the influence of certain parameters, affecting the nonlinear load-displacement behavior; namely the side member thickness and the load-to-grain angle as well as the dowel diameter. Among others, the influence of the aforementioned parameters on the elastic limit of dowel connections, and implications for the design of such connections will be discussed.

Influence parameters of dowel connections have been studied by various researchers. The influence of load-to-grain angle (Bléron and Duchanois, 2006) and dowel diameter (Ehlbeck and Werner, 1992) on the connection behavior was mainly studied experimentally on the dowel embedment behavior of wood. Among others, Dorn et al. (2013) investigated the single dowel connection behavior and its dependence on various parameters. The influence of the moisture content on the dowel connection behavior was experimentally studied by Sjödin et al. (2008).

The modeling approach applied herein was validated by means of comparison with experimental data (Bader et al., 2016d), which raises confidence in the model predictions of the parameter study. The paper is organized as follows: A description of the engineering model for dowel connections will be given in Section 3.2. Subsequently, experimental investigations related to connection component testing for model input as well as to connection testing for comparison purposes are reviewed in Section 3.3. Model validation with the presented dataset will be discussed in Section 3.4. In Section 3.5, results of the parameter study will be presented and discussed, before the paper is concluded in Section 3.6.

3.2 Engineering model

The basic elements of the single dowel modeling approach (Hochreiner et al., 2013) are beam elements, and translational and rotational springs with nonlinear elastic slip curves. The required input data encompass the nonlinear embedment stress-dowel displacement and dowel bending moment-bending angle relationships, respectively.

Structural elements for the steel dowel and connection members are exemplarily shown

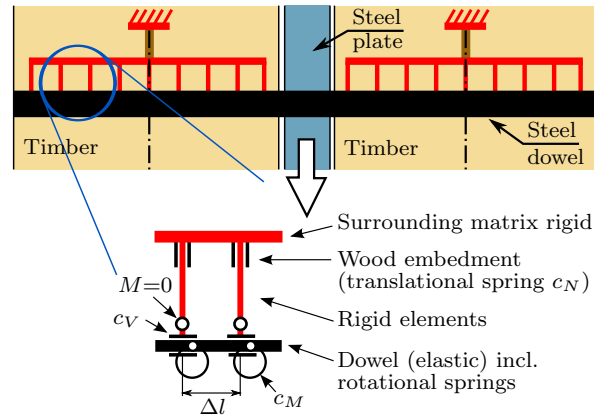


Figure 3.1: Visualization of structural elements for the single dowel model, exemplarily illustrated by means of a double shear, steel-to-timber connection.

in Figure 3.1, for a double shear steel-to-timber connection. The steel dowel is modeled by a beam chain where beam elements are connected to each other by rotational springs. The information of the elastic behavior is covered by the beam elements, while the generally nonlinear plastic behavior is considered in the rotational springs by means of nonlinear moment-rotation curves, with a rotational stiffness c_M (Figure 3.1). Beam elements representing the steel dowel are supported by rigid beam elements, which include a moment hinge close to the steel dowel. The embedment behavior is taken into account by means of nonlinear translational springs, with c_N as the translational stiffness (Figure 3.1). Reaction forces parallel to the steel dowel, present in bolted or screwed connections, could be considered by nonlinear translational springs, with c_V as the translational stiffness (Figure 3.1). Consecutively, several elements of one connection member are combined by another rigid element, which gives access to the internal forces of each connection member, further required for verification purposes.

Compilation of the loads of associated connection members results in internal forces for a specific applied displacement, e.g. at the steel plate in Figure 3.1. Incremental loading allows determining slip curves for arbitrary connection geometries.

3.3 Experiments

Experimental investigations on the connection component level, as well as on the global connection level, were carried out in order to provide input data to the above described engineering modeling approach as well as for its validation. The latter objective was tackled by comparing results from single dowel connection tests with corresponding model predictions and will be discussed in Section 3.4. As input to the model, on the connection component level, embedment tests of laminated veneer lumber (LVL) and 3-point bending tests on steel dowels were conducted to offer information on the embedment stress-displacement behavior and dowel bending moment-bending angle relationship, respectively. Load-displacement relationships of single dowel connections tested under three different load-to-grain angles are used for model validation. Experimental investigations are reviewed in the following, while detailed information can be found in Bader et al. (2016d).

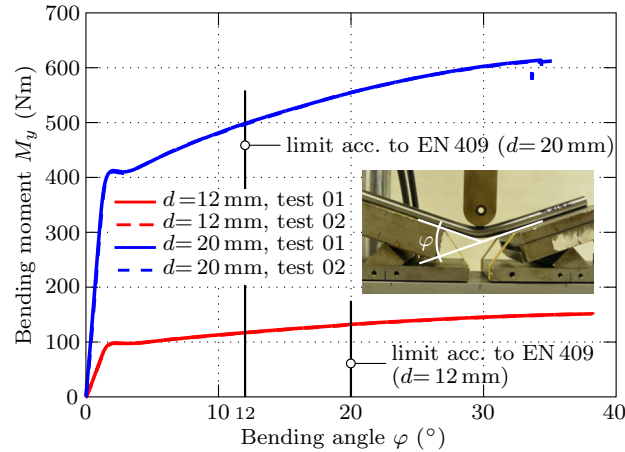


Figure 3.2: Bending moment M_y –bending angle φ relationship of heat-treated steel dowels with $d=12$ mm and $d=20$ mm (Bader et al., 2016d).

3.3.1 Bending tests on steel dowels

First, the bending moment–bending angle relationship of steel dowels was experimentally determined in a 3-point bending test setup. Dowels with two different diameters, namely 12 and 20 mm were tested. Prior to testing, a heat-treatment procedure was applied to dowels of steel quality S235 to ensure homogeneous material properties over the cross-section of the dowel, and equal conditions between different tested dowels (Bader et al., 2016d). The bending moment of the dowel, M_y , and the bending angle at mid-span, φ , were calculated from the recorded loading and displacement at mid-span of the 3-point bending test setup, respectively. The rotational stiffness c_M is then calculated as the derivative of the bending moment over the bending angle. Results are shown in Figure 3.2 by means of M_y plotted over φ . Almost identical slip-curves of two test specimens for each dowel diameter confirmed a successful heat-treatment and uniform properties of the dowels. The dowel yield moment at bending angles of 20 and 12°, as defined for 12 and 20 mm dowels according to EN 409 (2009), is given in Table 3.1.

3.3.2 Embedment tests of LVL

The embedment behavior of wood was experimentally investigated by means of full-hole embedment tests according to EN 383 (2007). Tests at three different load-to-grain angles, α , namely loading parallel to the grain (0°), at an angle of 45° to the grain and perpendicular to the grain (90°), were carried out. Similar to the loading situation of dowels in a dowel group loaded by a steel plate, a constrained loading situation for the load-to-grain angle ($\alpha=45^\circ$) deviating from the principal material directions was chosen (Bader et al., 2016d). Laminated veneer lumber (LVL), manufactured of spruce wood with parallel oriented veneers, with a total thickness of 51 mm was used. LVL was chosen for its comparably homogeneous material behavior, which allowed, in combination with reinforcement screws, for meaningful results of low variability up to large dowel displacements, even with a limited number of replications. Embedment tests were performed with dowels of high steel quality with a diameter, d , of 12 mm and 20 mm. Several LVL-elements were stored under controlled climate conditions of 20°C and 65% relative humidity, till mass equilibrium was reached. Tests were carried out displacement controlled up to a displacement of at least two times the dowel diameter.

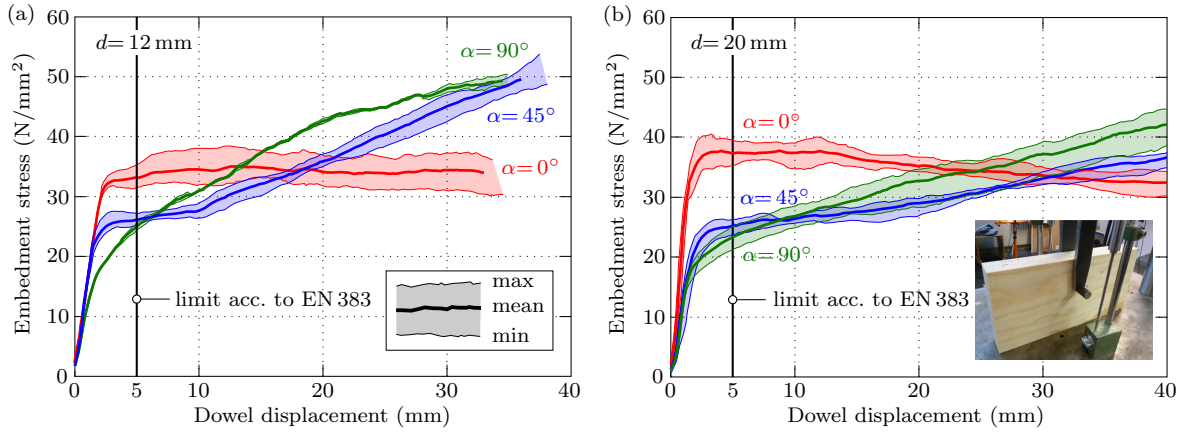


Figure 3.3: Embedment stress vs. dowel displacement of LVL for dowels loaded parallel (0°), at 45° and perpendicular to the grain (90°); (a) $d = 12$ mm; (b) $d = 20$ mm; mean values including the variability of the test data (Bader et al., 2016d).

Table 3.1: Experimentally determined connection component properties (mean values).

	$d = 12$ mm	$d = 20$ mm
Dowel yield moment acc. to EN 409, in Nm		
heat treated S235	132	500
Embedment strength acc. to EN 383, in N/mm ²		
$f_{h,0,m}$	33.1	37.7
$f_{h,45,m}$	26.1	25.2
$f_{h,90,m}$	24.9	23.3
Mean density, in kg/m ³		
LVL		495

Embedment stress-dowel displacement curves for 12 mm and 20 mm dowel diameters are presented in Figures 3.3a and 3.3b, respectively. In general, the embedment behavior can be described as quasi-linear elastic, followed by a pronounced plastic behavior. As obvious from Fig. 3.3, the quasi-elastic stiffness and stress limit decreased with increasing load-to-grain angle. In contrast, due to displacement hardening effects, the elasto-plastic stiffness increased with increasing α . Thus, embedment stresses for 45° and 90° load-to-grain angles finally exceeded the embedment stresses measured for parallel to grain loading. Results of the embedment strength determined according to EN 383 (2007), i.e. the embedment stress at a dowel displacement of 5 mm, are given in Table 3.1.

3.3.3 Single dowel connection tests

For validation purposes, single dowel tests, by means of a double shear, steel-to-LVL connection with dowel diameters d of 12 mm and 20 mm were carried out. The total width of the connection was 114 mm, consisting of two LVL-elements with 51 mm in width, separated by a 12 mm air gap covering the 10 mm steel plate for load application. As regards the

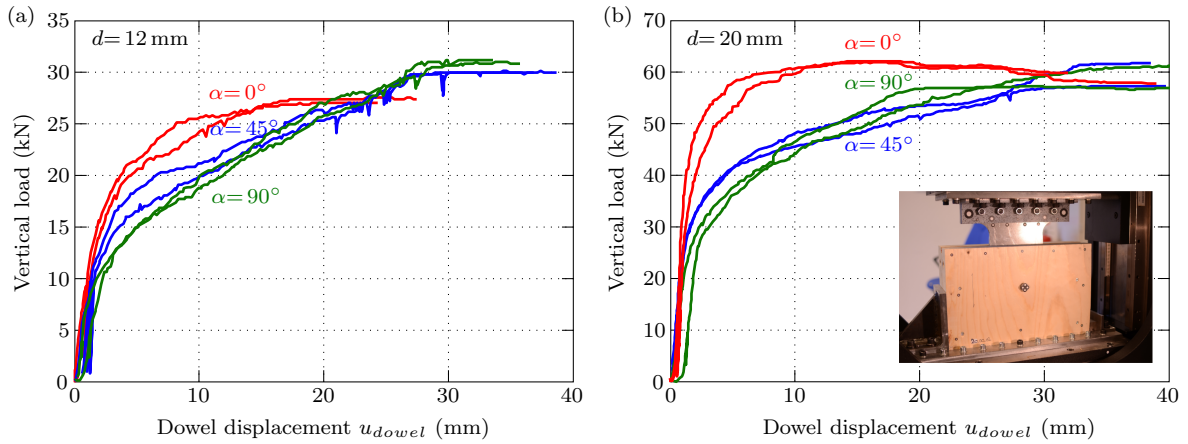


Figure 3.4: Vertical load vs. dowel displacement at the steel plate for a double shear, steel-to-LVL connection for dowels loaded parallel (0°), at 45° and perpendicular (90°) to the grain; (a) $d = 12$ mm; (b) $d = 20$ mm (Bader et al., 2016d). Please consider different scales of vertical axes (vertical load).

LVL-elements and steel dowels, same materials as for 3-point bending (Subsection 3.3.1) and embedment tests (Subsection 3.3.2) were used, in order to allow for a consistent model validation based on their experimental findings as input. The load in connection tests was applied at the same angles with respect to the grain direction, as it was done for the embedment tests, namely parallel (0°), at 45° and perpendicular (90°) to the grain. Before testing, LVL-elements were stored under controlled climate conditions of 20°C and 65% relative humidity, till mass equilibrium was reached. The load was applied displacement controlled up to a dowel displacement at the steel plate, u_{dowel} , of at least two times the dowel diameter. It should be mentioned that the steel dowels protruded approximately 10–15 mm over the LVL surface.

Figures 3.4a and b illustrate the load-displacement relationships. Only the load-component parallel to the displacement direction is considered herein. Deviations of displacement and grain direction however, cause additional reaction forces perpendicular to the displacement direction (Bader et al., 2016d). Loading parallel to the grain (0°) resulted in the stiffest elasto-plastic response with the highest reaction forces up to a dowel displacement of about 1.5 times the dowel diameter. With increasing load-to-grain angle, the loading stiffness and reaction force of the connection at small dowel displacements decreased, followed by a pronounced displacement hardening behavior of the connection. Consequently, reaction forces became even larger than for connections loaded parallel to the grain. These load direction dependent effects are well in line with the ones observed in embedment tests (cf. Figure 3.3). Pronounced bending deformation of the steel dowels were observed and quantified. This indicated the development of a plastic hinge in the center of the connection. For details, the reader is referred to Bader et al. (2016d).

3.4 Model validation

For validation purposes of the engineering beam on nonlinear elastic foundation model (see Section 3.2), the findings from single dowel tests, described in Subsection 3.3.3, are compared to the results from simulations. For the latter, experimental results from dowel bending (Subsection 3.3.1) and LVL embedment tests (Subsection 3.3.2) are used as input.

Based on the connection layout from single dowel tests, a steel-to-LVL connection in double-shear mode has been constructed. In total six different validation models have been built. Models referred to load-to-grain angles of 0° , 45° and 90° for each of the two investigated dowel diameters. Geometrical properties were identical for each of these six models. Different load-to-grain angles and dowel diameters were considered by adjustments in the corresponding nonlinear spring settings.

Referring to the single dowel experiments, the two side members in LVL had a width of $t_1 = 51$ mm each. In between a steel plate with 10 mm in width and 1 mm air gap on both sides was modeled. The steel dowel was subdivided into beam elements with a length of $\Delta l = 3$ mm. These beam elements were connected by rotational springs covering the nonlinear plastic moment-rotation behavior of the steel dowel from the corresponding experiments (see Subsection 3.3.1). The distance between the rigid support elements of the dowel, and therefore, the influence width of the nonlinear translation spring for the embedment behavior, was defined by the discretization length Δl of the steel dowel. Experimentally determined embedment stress of the corresponding force-to-grain angle, α , and dowel diameter, d , was multiplied by Δl and d , for assignment of load-displacement spring characteristics. A reduced discretization length of $\Delta l = 1.67$ mm was used in the area of the steel plate, in order to ensure a smooth transition from steel plate to the wooden side members. A linear elastic support with high embedment stiffness has been assumed at the steel plate-steel dowel interface. Frictional effects parallel to the dowel axis were neglected by setting c_V equal to zero (cf. Figure 3.1).

The commercial engineering design software package RFEM (Ing. Dlubal GmbH, Germany) was used for the simulations. Incremental loading, by means of stepwise application of a displacement at the center of the steel plate was applied. Slip curves by means of reaction force-displacement curves were determined. In addition, the incremental loading gave access to the internal forces and deformations of the steel dowel for each loading step, and thus allowed for identification of plastic deformations in the steel dowel. Calculations were carried out based on 1st order (geometrically linear) as well as 3rd order (geometrically nonlinear) theory.

In general, a good agreement between simulations and experiments was found. For higher dowel deformations, the geometrically linear model tended to overestimate reaction forces, while the geometrically nonlinear model tended to underestimate reaction forces. Up to a dowel displacement of 30 mm, larger errors were only found for 20 mm dowel connections loaded parallel to the grain, while model predictions for all other configurations closely followed experimental observations. It should be mentioned that steel dowels in connections tests protruded over the timber surface. Compared to steel dowels with a length equal to the total thickness of the connection, the test configuration allowed for maintaining the contact area even for pronounced bending deformations of the dowel. It is expected that geometrically nonlinear calculations would better represent the configuration of dowels with a length equal to the thickness of the lay-up. Results of model validation are not visualized herein; further details are given in Bader et al. (2016d). Model calculations presented in the following, are based on geometrically linear theory up to a dowel displacement of 30 mm.

The development of the modeling approach was largely motivated by the ambition to investigate individual influences of geometrical properties and material properties on the nonlinear load-displacement response of dowel connections and the development of plastic deformations in steel dowels. Such investigations will be presented and discussed next.

3.5 Parameter study

The engineering model of dowel connections (cf. Section 3.2) gives access to relationships between geometrical and material properties of the connection and its components, and the overall behavior of the connection. Such relationships will be assessed in the following parameter study by studying the influence of the dowel diameter d (12 mm and 20 mm), the load-to-grain angle α (0° , 45° and 90°), and the side member thickness t_1 (from 12 mm to 204 mm) on the nonlinear load-displacement behavior of a double shear steel-to-LVL connection. The connection lay-up described in the previous section, with a side member thickness t_1 of 51 mm and a steel plate with a thickness of 10 mm inserted in a 12 mm air gap, will be considered as a reference configuration.

In addition to the overall load-displacement behavior of the connection, descriptive parameters, namely the elastic and plastic bearing capacity, failure modes of steel dowels, and the onset and development of plastic deformations in steel dowels, i.e., the quasi-elastic limit, will be studied.

The interdependency of the above described parameters calls for a multi-dimensional evaluation, which however is difficult to present visually. A three-dimensional visualization of the global reaction force F and its dependence on the side member thickness t_1 and dowel displacement u_{dowel} , for loading parallel to the grain (0°) is given in Figure 3.5a and 3.5b for 12 mm and 20 mm dowel diameters, respectively. With exception of the load-to-grain angle dependency, these two figures cover several parameters discussed in the parameter study. In order to simplify the following discussion, specific combinations of two parameters are illustrated as cross-sections parallel to the axes of Figure 3.5. Subsequently, several results of model calculations are based on geometrically linear theory (1st order theory according to the RFEM software). Linear interpolation is applied between calculated load-displacement curves.

3.5.1 Side member thickness

In the following, the influence of the side member thickness t_1 on the single dowel connection reaction force F , together with its dependence on the dowel displacement u_{dowel} and dowel diameter d , is discussed. In addition, the influence of the side member thickness t_1 on the development of plastic deformations in the steel dowel, and therefore, on the elastic limit of the connection and the appearance of plastic hinges is shown. Furthermore, these model predictions are compared to calculations according to EC 5 (EN 1995-1-1, 2004) and DIN 1052 (2008), using component properties summarized in Table 3.1.

The reference configuration with $t_1=51$ mm is visualized by a green line in Figure 3.5. Cross-sections of the surfaces in Figure 3.5 parallel to the t_1 -axis at specific dowel displacements u_{dowel} give access to the reaction force F and its dependence on the side member thickness t_1 , for loading parallel to the grain, see Figure 3.6. The different contour lines in Figure 3.6a (for $d=12$ mm) and Figure 3.6b (for $d=20$ mm) are related to different dowel displacements u_{dowel} .

3.5.1.1 Connection strength and dowel failure modes

Figures 3.5 and 3.6 clearly depict an increase of the reaction force F with increasing side member thickness t_1 , up to a certain t_1 -limit. Further increase of t_1 beyond this limit does not change the reaction force anymore. Basically, the reaction force-side member thickness relationship can be divided into three areas. These areas are related to the three failure modes

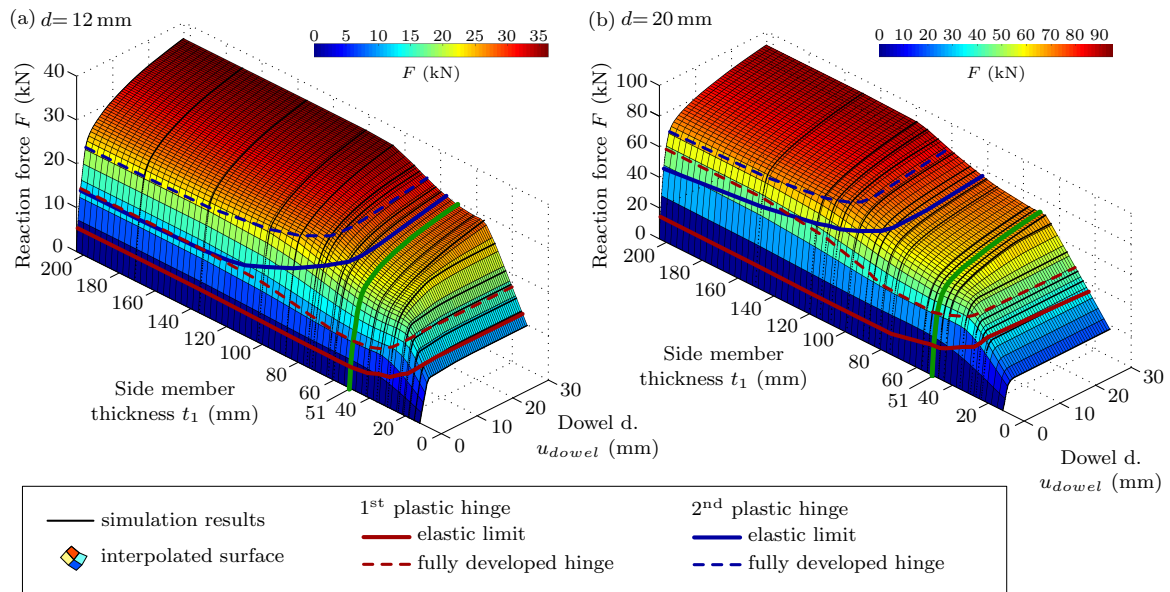


Figure 3.5: Global reaction force F of a double-shear steel-to-LVL connection plotted over the side member thickness t_1 and dowel displacement u_{dowel} for loading parallel to the grain (0°) for a dowel diameter of: (a) 12 mm, and (b) 20 mm, including elastic limits of steel dowels (red and blue lines). Please consider different scales of vertical axes (reaction force F).

according to EN 1995-1-1 (2004) for this type of connection, i.e., a more or less rigid dowel and no plastic hinge (failure mode (f) according to EN 1995-1-1 (2004)), one plastic hinge (failure mode (g) according to EN 1995-1-1 (2004)) and two plastic hinges (failure mode (h) according to EN 1995-1-1 (2004)).

For small side member thicknesses, a linear relation between F and t_1 was found, which appears as planar surface or straight lines in Figures 3.5 and 3.6, respectively. This area is related to the rigid dowel failure mode; thus embedment forces can be activated over the entire side member thickness. Further increase of t_1 leads to a nonlinear relationship between F and t_1 , where an increasing gradient on the F - t_1 curve, with increasing t_1 , was calculated. Immediately after appearance of the first plastic hinge at the steel plate, almost no increase in F was predicted. In this state, loads are transferred only in the inner parts of t_1 , while the outer parts balance in order to fulfill equilibrium conditions of the connection. At a certain t_1 the steel dowel exhibits a second plastic hinge in the side members for corresponding geometrical configurations. From this point onwards, increasing t_1 does not lead to an increase of the load-transferring zone, and thus, F stays constant, since loads are only transferred between the two outer plastic hinges in the dowel.

The calculation results not only illustrate well-known general failure modes of the steel dowel, but also predict effects of the nonlinear nature of the components behavior. In fact, calculations demonstrate that the point of transition between failure modes strongly depends on the dowel displacement u_{dowel} and the dowel diameter d , see Figures 3.5 and 3.6.

As regards the effect of the dowel diameter d , larger t_1 are necessary for 20 mm dowels compared to 12 mm dowels, to gain plastic hinges and therefore to change from one to another steel dowel failure mode. This can be explained by the stiffer behavior of the thicker steel dowel. Thus, larger contact area, and therefore larger side member thickness is required to activate embedment reaction forces suitable to create a plastic hinge in the steel dowel.

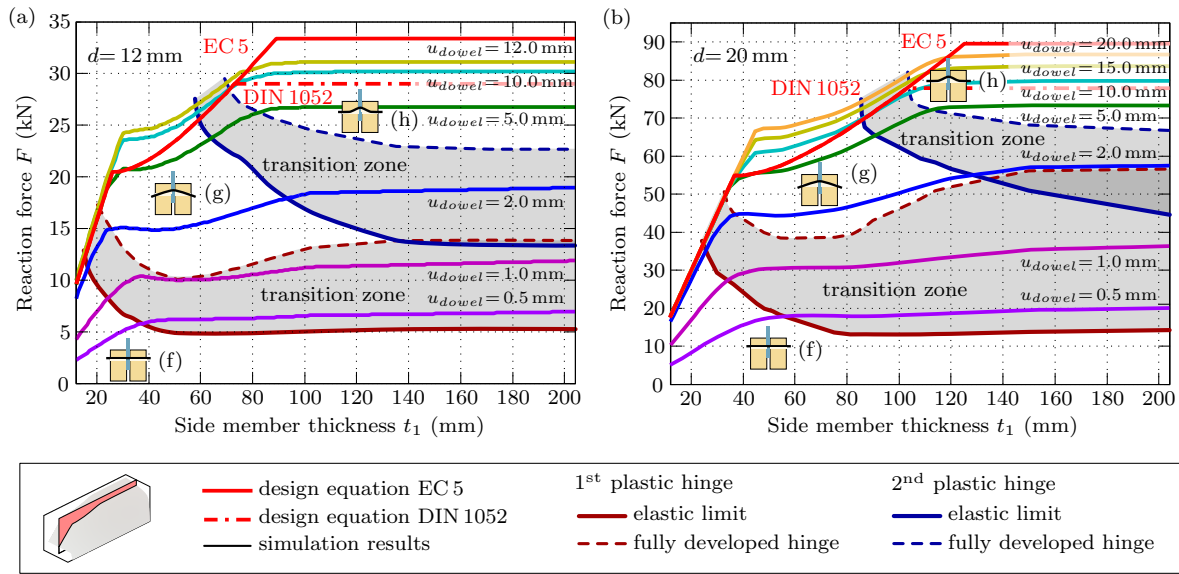


Figure 3.6: Parameter study of the influence of the side member thickness on the connection strength including possible failure modes of the double shear steel-to-timber connection, for loading parallel to the grain (0°) with a dowel diameter of: (a) $d=12$ mm, and (b) $d=20$ mm. Please consider different scales of vertical axes (reaction force F).

For example, the change between failure mode (f) and (g) at a dowel displacement of 5 mm, requires a side member thickness of approximately 27 mm and 41 mm for 12 mm and 20 mm dowels, respectively (see Figure 3.6).

A nonlinear relation between the side member thickness t_1 at the change of failure modes, and dowel displacement u_{dowel} became obvious. This is visualized by the nonlinear boundary of the planar surface in Figures 3.5a and 3.5b, as well as in the different positions of the kinks in the contour lines in Figures 3.6a and 3.6b. The dowel displacement even influences the number of developed plastic hinges. While for a 12 mm dowel at u_{dowel} larger than approximately 1 mm, up to two plastic hinges were found, only one hinge was predicted for u_{dowel} less than 1 mm (see Figure 3.6a). This is explained by smaller embedment reaction forces at small dowel displacements, not enough to cause bending stresses in the steel dowel required for the development of the second plastic hinge.

3.5.1.2 Comparison to EC 5 and DIN 1052:2008

In addition to the above discussed model predictions, the connection strength was calculated according to EN 1995-1-1 (2004) and DIN 1052 (2008), based on the experimentally determined yield moment of the steel dowel, and embedment strength (see Table 3.1). Since embedment strength and dowel yield moment are used as mean values, also the estimated strength of the connection can be considered as a mean value. The design equations of EN 1995-1-1 (2004) and DIN 1052 (2008), based on Johansens yield theory (Johansen, 1949), are identical, with only one exception. A constant partial safety factor for connections of 1.3 is used in EC 5. Consequently, a correction factor was added in design equations where steel dowel yielding is the decisive failure mode, in order to account for the lower partial safety factor for steel compared to wood. In DIN 1052 (2008) however, failure mode specific partial safety factors were used. Since partial safety factors are not considered in the calcula-

tions performed herein, EC 5 predictions overestimate load limits related to failure mode (h). Corresponding calculations are visualized in Figure 3.6.

For failure mode (f) a perfect match between model predictions, EN 1995-1-1 (2004) and DIN 1052 (2008) design equations was found. The change to failure mode (g) correlates well with the model prediction at a dowel displacement of 5 mm for both dowel diameters. With further increase of the side member thickness t_1 , estimated connection strength according to EN 1995-1-1 (2004) and DIN 1052 (2008) approaches the model prediction for a dowel displacement u_{dowel} of 10 mm, which is almost reached at the change between failure mode (g) and (h). For further increasing of t_1 , only the estimation according to DIN 1052 (2008) should be considered, since the prediction of EN 1995-1-1 (2004) is falsified by the partial safety factor correction in the corresponding design equation. Larger dowel displacement for failure mode (g) and especially for failure mode (h) in the model predictions compared to the estimations according to EN 1995-1-1 (2004) and DIN 1052 (2008), can be explained by the assumptions of the European Yield Model (EYM) (Johansen, 1949). In the EYM, fully plastic embedment behavior is assumed, which is only the case for large dowel displacements u_{dowel} . Especially the embedment zone close to the second plastic hinge does not reach the state of fully plastic embedment behavior. In order to come close to the assumptions considered in the EYM, comparable large dowel displacements up to about 10 mm are required (see Figure 3.6).

Comparison between EYM-based design equations and model predictions highlights a weak point of the EYM, which is the kinematic incompatibility of the input parameters, i.e., the yield moment of the steel dowel and the embedment strength of wood. This does not allow for consistent predictions of connection deformations. For failure mode (f), i.e., no plastic hinge, the dowel deformation can be considered equal to the underlying deformation limit of the embedment strength, i.e., 5 mm according to EN 383 (2007). As soon as a plastic hinge develops, the steel dowel deformation yields varying embedment deformations, and thus, kinematic compatibility is not fulfilled anymore.

3.5.1.3 Plastic deformations in the steel dowel

The development of plastic deformations in the steel dowel was used as indicator for the change between failure modes. The thick dark red and dark blue lines in Figures 3.5 and 3.6 indicate the elastic limit of the steel dowel for the first and second plastic hinge, respectively. In general, the elastic limit of single dowel connections should be defined either by the quasi-elastic limit of the embedment stress in timber, or by the elastic limit of the steel dowel. Herein, the elastic limit of the steel dowel is further investigated and defined by the onset of plastic strains in the outer most part of the steel dowel. The elastic limit is followed by a transition zone, where increased plastic rotation in the dowel, and consequently formation of a plastic hinge occurs. Fully developed plastic hinges, i.e., plastic deformations over the entire diameter of the steel dowel, are indicated by thin dashed dark red and dark blue lines in Figures 3.5 and 3.6. Compared to the kinks in the contour lines of Figure 3.6, indicating the transition between failure modes, considerable lower limits were found from the above definition of the fully developed plastic hinge. This finding is explained by two effects of component properties:

Firstly, the applied steel dowels do not exhibit ideal plastic behavior but encompass strain hardening (see Figure 3.2). Thus, increased plastic rotation in the plastic hinge yields additional bending capacities of the dowel, which induce additional embedment reaction forces.

Secondly, the contour lines in Figure 3.6 illustrate the sum of the embedment reaction forces over the embedment length, and therefore kinks in these lines indicate a change in the

sum of embedment reaction forces, which has not necessarily to correlate directly with the development of plastic hinges. For example, the steel dowel in failure mode (f), i.e., no plastic hinge, reacts stiff enough to fully activate embedment forces over the entire side member thickness. Therefore, the kink in the contour lines at the end of failure mode (f) indicates the side member thickness t_1 , at which full activation of embedment forces, due to dowel bending, is not possible anymore. This does not necessarily mean, that no dowel bending, or even a plastic hinge in the dowel exists up to this point.

Lines indicating the elastic limit and fully developed plastic hinge in Figures 3.5 and 3.6 show a highly nonlinear relationship with the side member thickness t_1 . The elastic limit was found to be much lower than it could be expected from the shape of the contour lines and surface in Figures 3.6 and 3.5, respectively. Thus, the elastic limit of the steel dowel was reached even before the development of the first plastic hinge affected the reaction force F .

From Figure 3.6, a strong dependency of the connection strength F and elastic limit on the side member thickness t_1 , dowel diameter d and dowel displacement u_{dowel} becomes obvious. There is however a strong interrelationship of these properties with the force-to-grain angle α , which will be discussed next.

3.5.2 Load-to-grain angle

In Figure 3.7, the reaction force predicted by the herein discussed engineering modeling approach is plotted over the dowel displacement, u_{dowel} , for three different load-to-grain angles, namely for loading parallel (0°), at 45° , and perpendicular to the grain (90°). Figures 3.7a and 3.7b, refer to $d=12$ mm and $d=20$ mm, respectively. The side member thickness has been chosen to 51 mm according to the experimentally investigated LVL thickness. Thus, the model predictions could be directly compared with the experimental findings (see Section 3.4 and Bader et al. (2016d)).

3.5.2.1 Connection slip behavior

For the slip curves in Figure 3.7, a highly nonlinear behavior becomes obvious, which partly results from the nonlinear embedment behavior (cf. Figure 3.3) and partly from the nonlinear characteristics of the steel dowel in bending (cf. Figure 3.2). A similar slip behavior for 12 mm and 20 mm dowels is predicted. Loading parallel to the grain (0°) yields the stiffest initial behavior with the highest quasi-elastic limit. Increasing load-to-grain angle leads to a decrease in initial stiffness and quasi-elastic limit. Further increase of the dowel displacement, beyond the quasi-elastic displacement limit, yields an increase of the reaction force, for all investigated load-to-grain angles. This displacement hardening effect is strongest for loading perpendicular to the grain (90°) and less pronounced parallel to the grain (0°). Also loading parallel to the grain exhibits an increase of the reaction force in the elasto-plastic state, even if no increase is considered in the corresponding embedment behavior (cf. Figure 3.3). The reason for this is found in the combination of the nonlinear characteristics of the embedment behavior and steel dowel in bending. Hence, comparable large displacements at the inner steel plate are required to fully activate embedment forces in the outer parts of the LVL side members. In addition, the slip behavior at large dowel displacements is affected by the underlying geometrically linear calculation theory (Bader et al., 2016d). For loading at 45° and 90° to the grain, the even more pronounced displacement hardening can be explained by the same effects, as discussed above, in combination with an additional increase in the corresponding embedment slip behavior (cf. Figure 3.3).

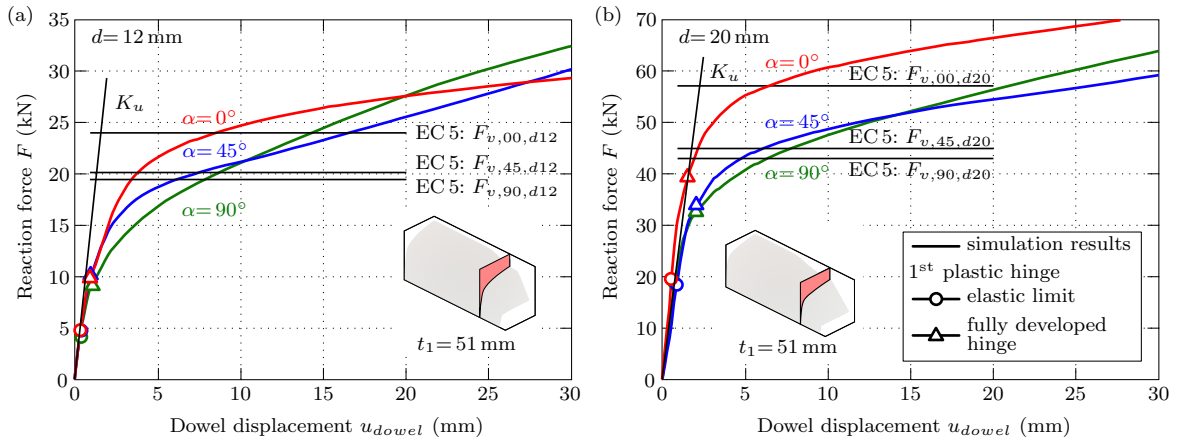


Figure 3.7: Reaction force plotted over the dowel displacement u_{dowel} for engineering model predictions of connections with dowel diameters of (a) 12 mm and (b) 20 mm, loaded parallel (0°) at 45° and perpendicular (90°) to the grain. Please consider different scales of vertical axes (reaction force F).

Table 3.2: Strength and slip modulus of single dowel connection with $t_1 = 51$ mm according to EN 1995-1-1 (2004) (mean values).

	$d = 12$ mm	$d = 20$ mm
Strength of single dowel connection, in kN		
$F_{0,m}$	23.9	57.0
$F_{45,m}$	20.2	45.1
$F_{90,m}$	19.5	43.3
Slip modulus of single dowel connection, in kN/mm		
K_u	15.3	25.5

This positive correlation between the size of displacement hardening and load-to-grain angle yields higher reaction forces for loading at 90° than 45° for a dowel displacement higher than approximately 10 mm and 15 mm for $d = 12$ mm and $d = 20$ mm, respectively. For a dowel displacement higher than approximately 20 mm and a dowel diameter of 12 mm, the reaction forces becomes even larger than for dowels loaded parallel to the grain. This fact is especially important for the load distribution in dowel groups, in the case of plastic design approaches.

3.5.2.2 Comparison to EC 5

The connection bearing strength and slip modulus K_u were calculated according to EN 1995-1-1 (2004). As stated in Subsection 3.5.1.2, these calculations are based on the experimentally determined mean values of the yield moment of the steel dowel, embedment strength and LVL density (see Table 3.1). Thus, the estimated connection strength and modulus K_u , given in Table 3.2, can also be considered as mean values. Failure mode (g) according to EC 5, i.e., one plastic hinge in the steel dowel, is predicted for all load-to-grain angles and dowel diameters.

The bearing strength according to EC 5 was found to be equal to the model prediction at a dowel displacement u_{dowel} of approximately 6 to 8 mm (see Figure 3.7). Thus, for a

dowel displacement of 20 mm, EC 5 underestimates the model prediction up to 30% and 25% for $d=12$ mm and $d=20$ mm, respectively. On the opposite, a strong overestimation of the slip modulus in the ultimate limit situation, K_u , becomes apparent. As obvious from Figure 3.7, the slip modulus strongly depends on the load-to-grain angle, as well as on other factors like the connection geometry or steel dowel quality, which are not considered in the EC 5 approach. Comparison of the connection serviceability limit strength to model predictions are not possible, since no definition for the SLS strength is given in EC 5. The nonlinear slip behavior, including a pronounced hardening in the plastic domain, makes it difficult to describe the connection slip behavior bi-linearly. Therefore, application of the nonlinear connection model is advantageous to gain a realistic connection deformation and stiffness.

3.5.2.3 Plastic deformations in the steel dowel

The engineering model was further used to study the development of plastic deformations in the steel dowel and its relation to the load-to-grain angle. For this purpose, the elastic limit and states of fully developed plastic hinges are indicated by circular and triangular markers in Figure 3.7.

Compared to connections with dowel diameters of 20 mm, connections with 12 mm dowels exhibit lower elastic limits, which can be explained by the lower stiffness and strength of the smaller circular cross section. The elastic limits for 12 mm dowels are found to be almost independent from the load-to-grain angle, and are predicted for a dowel displacement of about 0.4 mm. The corresponding reaction forces are slightly less than 5.0 kN, which is only about a sixth of the maximum reaction force. The fully developed plastic hinge is found at a displacement of about 1.0 mm, which corresponds to a reaction force of about 10 kN.

For 20 mm dowels, a dowel displacement of about 0.6–0.9 mm would be necessary to reach the elastic limit, which is considerably higher than for 12 mm dowels. The corresponding reaction force amounts to 18–20 kN, which is approximately one-third of the maximum reaction force. For the limit of the fully developed plastic hinge, considerable differences between the load-to-grain angles were revealed. The displacement limit increases from 1.5 to 2.1 mm, while the reaction forces decrease from approximately 40 kN to 33 kN, for increasing load-to-grain angle from 0° to 90° . These effects can be explained by a more uniform embedment force distribution along the dowel axis for the softer loading angles, i.e., 45° and 90° , compared to $\alpha=0^\circ$. Obviously, a softer material requires larger dowel displacements to gain reaction forces suitable to cause a plastic hinge. On the opposite, a softer embedment response yields a more uniform embedment force distribution, since the dowel bending deformation is lower, which in fact results in a larger moment arm, and thus requires a lower reaction force to reach the required bending moment to cause a plastic hinge.

Finally, the influence of the load-to-grain angle on the elastic limit, dependent on the dowel displacement u_{dowel} and side member thickness t_1 will be discussed, see Figures 3.8a and 3.8b. These figures represent a view from the top on the reaction force surfaces presented in Figure 3.5. Consistently to the previous figures, thick red and blue lines indicate the elastic limit of the first and second plastic hinge, respectively. The different line styles refer to the different investigated load-to-grain angles, i.e., loading parallel to the grain (0°), at 45° and perpendicular (90°) to the grain.

As regards the elastic limit of the first plastic hinge, only minor differences between the load-to-grain angles are predicted. This could be interpreted as the dowel bending behavior to be more decisive than the embedment behavior. However, consistently, slightly higher dowel displacements or side member thicknesses, respectively, are required with increasing

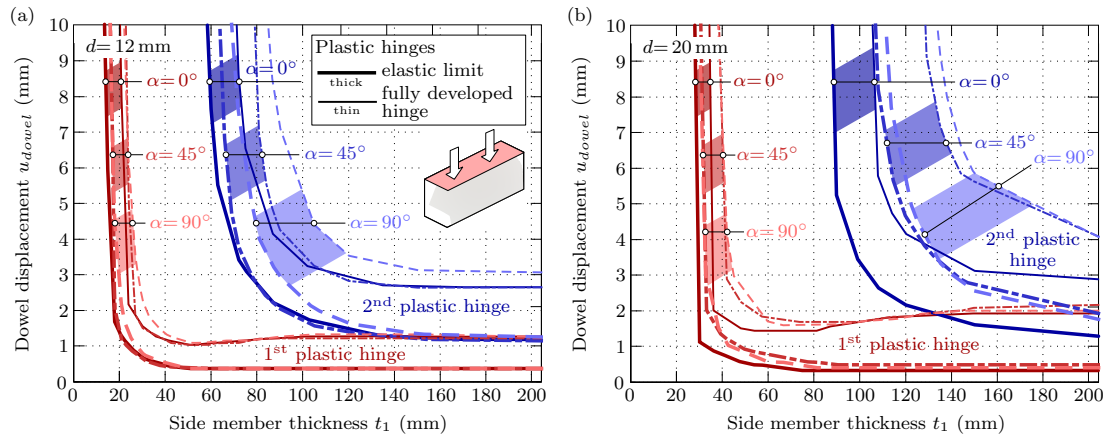


Figure 3.8: Parameter study of the influence of the load-to-grain angle on the displacement dependent development of plastic deformations in the steel dowel, for loading at 0° , 45° and 90° to the grain for dowels of (a) $d=12$ mm, and (b) $d=20$ mm. Please consider different scales of vertical axes (u_{dowel}).

load-to-grain angle to reach the first elastic limit. In addition, the size of the transition zone correlates with the size of the load-to-grain angle. Compared to $\alpha=45^\circ$ and 90° , the stiffer quasi-elastic embedment behavior at 0° yields a faster development of the plastic hinge, and thus a smaller size of the transition zone. Nevertheless, with increasing t_1 these differences in the transition zone decrease almost to zero. For the investigated connection properties, only for comparable slender connections (t_1 less than approximately 30 mm), the elastic limit of single dowel connections is governed by the quasi-elastic embedment stress limit. For larger t_1 the elastic limit of the steel dowel becomes decisive for the elastic limit of the single dowel connection. Increasing the steel quality would increase the dowel displacement related to the onset of plastic deformations in the steel dowel and thus, increase the elastic limit of the connection up to the quasi-elastic limit of the embedment behavior.

For the elastic limit of the second plastic hinge, the above discussed effects get more pronounced. For both dowel diameters, considerable differences between the load-to-grain angles of 0° and 90° are visible in Figure 3.8. While the elastic limit for $\alpha=45^\circ$ is predicted to be close to the elastic limit for $\alpha=0^\circ$ in the case of a 12 mm dowel, the corresponding elastic limit for a 20 mm dowel is found to be close to $\alpha=90^\circ$. This could possibly be explained by different experimentally determined embedment behavior between these two dowel diameters (cf. Figure 3.3). For example, the connection with 12 mm dowel, loaded at 90° to the grain, requires at a dowel displacement of 5 mm, almost 20 mm wider side members, compared to loading at 0° , in order to reach the elastic limit. Compared to the first plastic hinge, a more pronounced transition zone, and larger differences in the size of the transition zone between the different load-to-grain angles are calculated. The reason for both effects might lie in a slower development of the second plastic hinge, which is caused by back bending of the steel dowel, and therefore additionally depends on the rotational stiffness of the first plastic hinge.

The load-to-grain angle mainly influenced the development of the second plastic hinge for intermediate side member thicknesses. These findings regarding the elastic limit are expected to be of high importance. As regards the serviceability limit state (SLS), where no plastic deformations are allowed, especially in the steel elements, due to the danger of fatigue failure. Therefore, the bearing capacity for the SLS should be limited by the elastic limit of the steel dowel.

3.6 Conclusions

By means of an experimentally validated engineering modeling approach, a parameter study on a double-shear, steel-to-timber, single dowel connection was conducted. Model validation was based on a consistent experimental dataset, which encompassed connection component as well as connection tests. Good agreement of model predictions with experiments was found. Starting from the reference condition with side member thickness of 51 mm, the following influence parameters, as regards the nonlinear load-displacement behavior of connections, were investigated in this study; namely the side member thickness and the load-to-grain angle as well as the dowel diameter.

As a reason of the nonlinear connection behavior, strength properties and failure modes were found to depend on the displacement of the dowel. Increasing the side member thickness led to increased strength of the connection and a transition between different failure modes of the dowel. The transition between these failure modes was found to depend on both, the side member thickness and the dowel displacement. No distinct border but rather a transition zone between failure modes became obvious, since the connection strength is driven by nonlinear stiffness of the steel dowel and the surrounding timber matrix.

A strong influence of the load-to-grain angle on the displacement dependent connection strength was found. Pronounced displacement hardening effects in the embedment behavior for loading at 45° , and especially for loading perpendicular to the grain (90°), yielded finally higher connection strength than for loading parallel to the grain.

The causal relationship between the kinematically compatible component properties of wood and steel dowels, and the corresponding global connection response, gave also access to elastic limits and the development of plastic deformations in steel dowels. The elastic limit of the steel dowel, i.e. the onset of plastic deformations, and thus the elastic limit of the single dowel connection itself, appeared at surprisingly small dowel displacements. As a remedy, higher steel qualities of steel dowels than used in this study should be used in order to increase the serviceability limit of single dowel connections, and thus, to avoid fatigue failure. Besides side member thickness, the elastic limit was found to strongly depend on the dowel diameter and load-to-grain angle. These findings are expected to be especially important for the identification and assignment of serviceability limit states (SLS) of single dowel connections.

Compared to current design models in timber engineering design standards, the presented engineering modeling approach allows for enhanced insight into the behavior and consequently for an enhanced reliability in the design of single dowel timber connections. Its adaptability and flexibility as well as its implementation in commercial structural analysis software qualify the model suitable and valuable for practical applications.

Acknowledgement

The authors gratefully acknowledge the financial support of the Austrian Research Promotion Agency and the wood industry partnership Building with Wood within CEI-Bois for funding the research work within project *MechWood 2*. This work forms part of that project. The *MechWood 2* research partners are thanked for their cooperation and collaboration in this project. Josef Penkner is thanked for his valuable support by carrying out simulations for the parameter study.

Notation

c_M	nonlinear rotational stiffness – steel dowel in bending
c_N	nonlinear translational stiffness perpendicular to dowel axis – embedment behavior of wood
c_V	nonlinear translational stiffness parallel to dowel axis – reaction forces parallel to dowel axis
d	dowel diameter
$f_{h,\alpha,m}$	embedment strength acc. to EN 383 for loading at α (mean value)
F	reaction force of single dowel connection
$F_{v,\alpha,d}$	strength of single dowel connection with dowel diameter d , for loading at α acc. to EC 5 (based on mean value)
$F_{\alpha,m}$	strength of single dowel connection for loading at α acc. to EC 5 (based on mean values)
K_u	slip modulus for the ultimate limit state acc. to EC 5
M	bending moment
M_y	bending moment of the steel dowel
t_1	side member thickness
u_{dowel}	dowel displacement at the steel plate
α	load-to-grain angle
Δl	discretization length of beam elements
φ	bending angle at midspan of the steel dowel

Parameterization equations for the nonlinear connection slip applied to the anisotropic embedment behavior of wood (Schweigler et al., 2018b)

Authored by Michael Schweigler, Thomas K. Bader, Georg Hochreiner
& Romain Lemaître

Accepted for publication in *Composites Part B: Engineering*

Abstract: Nonlinear numerical models for the engineering design of mechanical connections in anisotropic materials require nonlinear material behavior of their components, which are essentially determined by material or structural testing. Herein, a multi-step approach for the parameterization of the nonlinear and anisotropic connection slip behavior is presented and applied to the ductile embedment behavior of steel dowels in wood. For this purpose, previously proposed regression functions for the slip behavior are reviewed, and further possible equations are discussed. Their suitability in the description of typical shapes of slip curves observed in connection testing is assessed before certain combinations are applied to an experimental dataset of embedment tests of steel dowels embedded in Laminated Veneer Lumber. The dependence of the regression parameters on the displacement range in the experimental dataset and the benefit of using parameters with a physical interpretation for being able to exploit connection test data reported in literature is highlighted.

Keywords: parameterization, wood, anisotropy, plastic deformation, analytical modeling, joints

4.1 Introduction

Increased awareness for sustainable building materials in combination with improvements and new developments in wood products and connection techniques led to a renaissance of building with timber in recent years. Breaking new ground by building complex, statically indetermined, wide-spanning and high-rising timber structures, the behavior of joints with mechanical fasteners, linking single timber elements, gets more and more important. This is particularly the case for joints made of dowel-type connections, due to their pronounced nonlinear load-deformation behavior (Bader et al., 2015, 2016c), which is a consequence of the anisotropic, nonlinear single fastener slip behavior (Bader et al., 2016d; Reynolds et al., 2016). The latter is currently strongly simplified by means of an elastic slip modulus for dowel-type connections in the European timber engineering design standard EN 1995-1-1 (2004) (Eurocode 5).

Engineering modeling of dowel-type connections (see e.g. Hochreiner et al., 2013; Bader et al., 2016d) has been shown to efficiently and realistically depict the nonlinear connection slip based on a kinematically compatible description of the embedment behavior of wood or wood-based products and steel dowel properties. In other words, numerical modeling can effectively predict causal relationships between the deformation behavior of connections and the deformation behavior of its components, avoiding the need for an experimental database on the connection level for the assignment of connection stiffness.

However, what hampers a broad application of this numerical method in engineering design is an appropriate database for material properties, reflecting not only strength but also deformation characteristics of wood and wood-based products. The complex stress state in anisotropic materials, like orthotropic composites such as wood, under embedment loading (Foust et al., 2014) makes experimental investigations of dowel-type fasteners embedded in timber indispensable. Testing standards for the embedment behavior of wood (e.g. EN 383, 2007; ASTM D5764-97a, 2002; ISO/DIS 10984-2, 2009) encompass rules for deformation measurements. However, these deformation data are rarely thoroughly reported and thus, cannot be exploited in engineering design equations. Current deformation properties according to testing standards assume linear quasi-elastic loading, unloading and reloading paths, which do not allow for a realistic nonlinear slip definition. Moreover, the embedment strength is currently defined as an ideally plastic material property, neglecting pronounced displacement hardening for loading close to perpendicular to the grain in the case of reinforced ductile connections (Schweigler et al., 2016a, 2017). Orientation dependence of connection properties is typical for composite materials in general. Anisotropic slip behavior has been reported in experiments on bolted connections in 3D woven composites in Mounien et al. (2017), as well as in glass fiber reinforced polymers in Ascione et al. (2010) and corresponding nonlinear finite-element simulation in Nerilli and Vairo (2017).

For the design of joints in timber structures, the same simplifications as for embedment testing are assumed on the connection level, where a rigid-ideally plastic limit design approach is used for the calculation of connection strength together with loading orientation independent linear elastic connection stiffness (EN 1995-1-1, 2004). This calls for a new paradigm for definition of material characteristics from testing, which allow for a nonlinear slip definition by means of parametric equations, suitable for numerical modeling of connections and structures.

Diversified shapes of slip curves from experimental investigations on connections in timber structures are illustrated in Fig. 4.1. A typical example of a continuously increasing embedment stress-displacement curve measured in embedment test of steel dowels embedded in reinforced wood specimens (Schweigler et al., 2017) is shown in Fig. 4.1a. The second type,

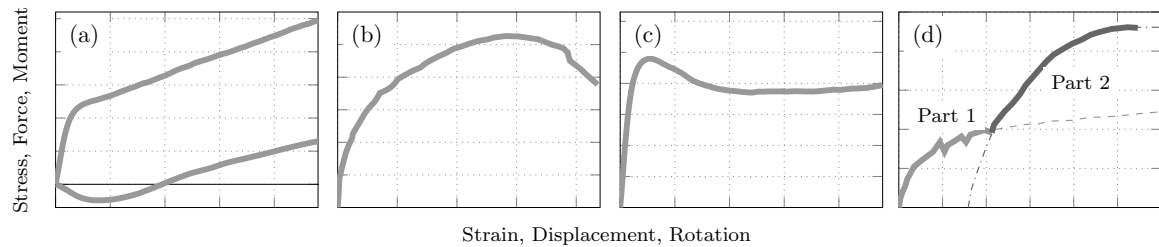


Figure 4.1: Typical slip curves from connection tests in timber structures.

illustrated in Fig. 4.1b, is more common for connection tests in ductile single dowel joints (Jorissen and Fragiacomio, 2011) or nailed joints (Yan et al., 2011) and additionally encompass softening behavior. Slip curves with a local maximum followed by a quasi yield plateau, as shown in Fig. 4.1c, can for example be found for traditional carpentry joints (Koch et al., 2013), or for modern approaches of glued-in dowels with a soft interlayer (Fauziyah et al., 2016), but might also be observed in single fastener connection tests parallel to the grain. A similar slip behavior was found for 3D woven composites as well (Mounien et al., 2017). Slip curves with two or more distinct parts, as illustrated in Fig. 4.1d, have been measured in connection tests with a change in the load-bearing mechanism during testing (Arciszewska-Kędzior et al., 2015; Shanks et al., 2008; King et al., 1996). As prime example, a multi-dowel connection loaded by a pure bending moment, which gets in contact with a stiff element after a certain rotation, could be mentioned (Bader et al., 2016c). Another example might be slip-critical connections in steel structures, or structures made of pultruded fiber reinforced polymers (PFRP). In the latter case, the first part of the joint slip is driven by friction between PFRP and steel plates, before in the second part additional bolt-bearing resistance is activated (Feo et al., 2017). For the first slip curve type (Fig. 4.1a) parametric equations able to describe curves with a linear part at the beginning and end of the curve, connected by a curved transition zone, are required. The same equations might be used for the second type (Fig. 4.1b) with the additional requirements of being able to handle a large transition zone and a negative inclination at the end of the slip curve. The third type (Fig. 4.1c) might call for different parametric equations compared to the first two types, in order to sufficiently describe the local maximum. For the last type in Fig. 4.1d, it might be suitable to analyze distinct parts of different load-bearing mechanisms separately, and subsequently combine these parts. This would allow to use the same basic parametric equations as applied for the first slip curve types in Fig. 4.1a and b.

Parametric equations for the slip behavior of connections, in order to tackle the aforementioned requirements from experimental studies, have been proposed previously. For timber joint, this goes back to the work on nailed connections of Jansson (1955) and Norén (1962). Similar definitions for connections in general, not limited to timber, have been used by Foschi (1974), Yee and Melchers (1986), as well as by Richard and Abbott (1975). These methods are based on exponential or power functions, while Biscaia et al. (2015, 2017) used a combination of a power and exponential function to describe the bond-slip of fiber reinforced polymer (FRP) laminates with concrete (Biscaia et al., 2015) and with old timber (Biscaia et al., 2017), respectively. Others like Jensen (1994) or Glos (1978) used polynomial definitions for applications in timber engineering. In addition Jensen (1994) presented an approach, which used both, exponential and polynomial functions. Sauvat (2001) presented a function to describe the foundation modulus of dowel joints in timber structures subjected to complex

cyclic loadings, and Mohamadi-Shoore and Mofid (2011) proposed and reviewed parametric equations for the moment-rotation behavior of bolted steel endplate connections. Another type of equations used in timber engineering are trigonometric functions or combinations of trigonometric functions, such as the well-known interaction criterion for compression strength at an angle to the grain proposed by Hankinson (1921), which is currently used to calculate embedment strength of wood at an angle to the grain. A similar approach, called root-mean-square (RMS), was used by Gupta and Sinha (2012) for the shear strength of Douglas-fir at an angle to the grain.

From a holistic point of view, the analytical description of the empirically determined slip behavior is a multi-dimensional problem since embedment stress or connection load depend not only on the dowel displacement but also on parameters such as load-to-grain angle, dowel diameter, wood species, density and moisture content of the wood. In this contribution, the authors aim on the description of the nonlinear slip behavior as function of the anisotropy. As a novel contribution, parametric equations for nonlinear connection slip are extended to the anisotropic behavior of wood, or anisotropic composites in general, yielding a closed mathematical expression. Parameterization of anisotropic slip substantially facilitates simplified FEM-models that use spring elements for modeling embedment behavior or connection slip. The aim of this contribution is to close the gap between experimentally determined material or connection properties, and phenomenological but nonlinear and anisotropic connection and joint models.

For describing the nonlinear slip as function of the anisotropy, the multi-dimensional problem decreases to a three-dimensional problem, which is tackled by a three-step approach. Firstly, regression analysis of the slip behavior in various directions to the grain is performed before, in a second step, a parametric equation for the regression parameters over the load-to-grain angle is derived. These two regression steps are combined in a third step. As a future effort, further steps could be added to include additional influence parameters in the slip equations.

The analysis work is based on a comprehensive experimental database established for reinforced, and thus ductile Laminated Veneer Lumber dowel connections, which includes embedment tests at constrained dowel displacement boundary conditions (Schweigler et al., 2017). Since testing was performed at various angles to the grain, the anisotropic connection behavior has been captured. Moreover, biaxial testing gave even access to lateral reaction forces, which are evoked for loading at an angle between the principal material orientations. Thus, the dataset includes typical slip curves for ductile dowel-type connections and their dependence on the anisotropy, which will form the starting point for the analysis.

The paper is organized as follows: The general parameterization strategy is outlined in Section 4.2, before previously suggested or possible regression equations are reviewed in Section 4.2. The suitability of these equations to describe typical slip curves is discussed and selected functions are applied to the experimental dataset in Section 4.3. In Section 4.4 further influences related to the parameterization strategy, such as an initial slip or the maximum displacement, as well as the effect of assumptions in the determination of parameters from experimentally gained slip curves, are discussed, before the paper is concluded in Section 4.5.

4.2 General strategy for parameterization

For the purpose of parameterization of the slip behavior of connections based on experimental data, the following three step approach has been applied in this work (see Fig. 4.2).

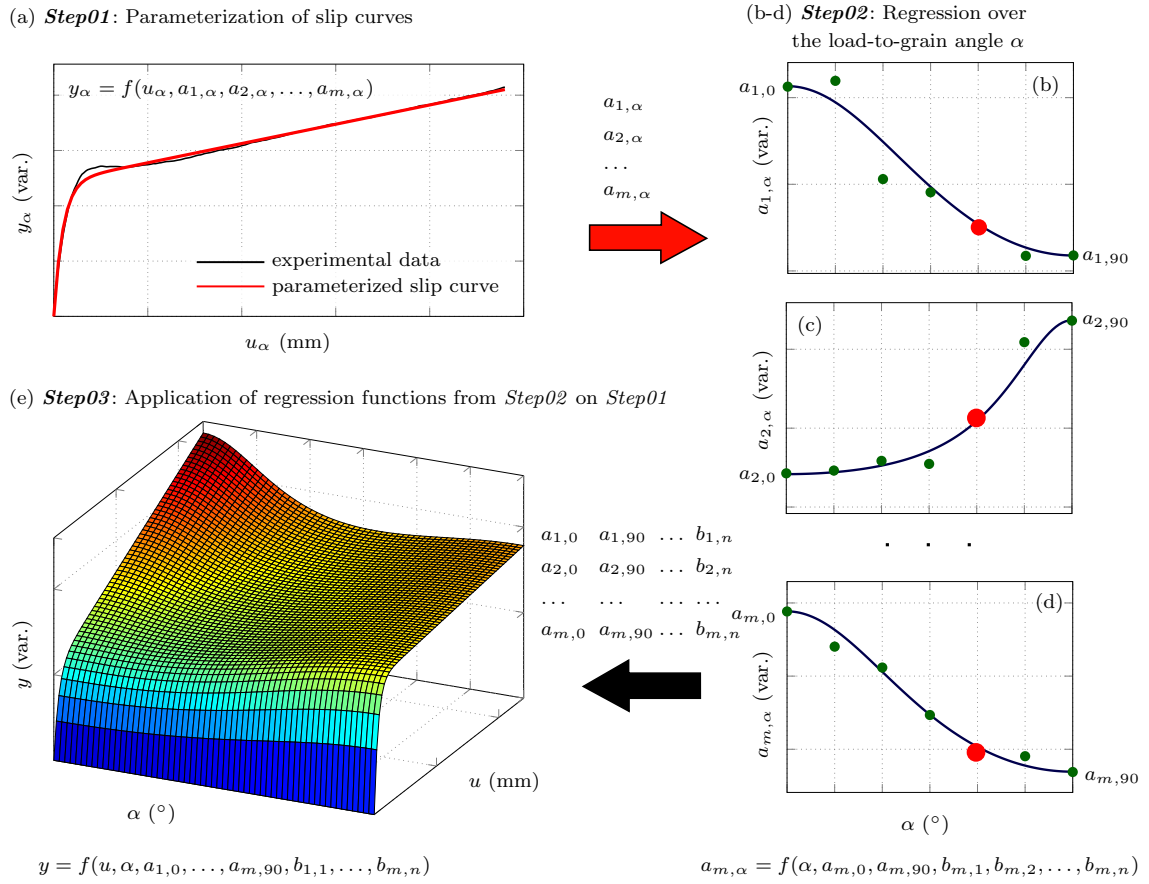


Figure 4.2: Procedure for parameterization of nonlinear, anisotropic slip curves, (a) *Step01*: regression analysis of the experimental slip curves for each experimentally measured load-to-grain angle, α , (b)–(d) *Step02*: regression of the coefficients from *Step01* over the load-to-grain angle, α , (e) *Step03*: parameterized definition as function of the load-to-grain angle, α , and dowel displacement, u .

Step01: In a first step, exponential or polynomial regression functions were used to fit the single experimentally determined slip curves for each load-to-grain angle, α_i (see Fig. 4.2a). In general, these regression functions read as

$$y_\alpha = f(u_\alpha, a_{1,\alpha}, a_{2,\alpha}, \dots, a_{m,\alpha}), \quad (4.1)$$

and give the stress or load y_α as function of the dowel displacement u_α for a specific load-to-grain angle α . The coefficients $a_{1,\alpha}$ to $a_{m,\alpha}$ in Eq. (4.1) depend in number and physical interpretation on the applied regression function. These parameters can either be determined by means of the least square method based on the information of the entire slip curve, or in the case of physical meaning of the parameters, they can be determined directly from experimental data. Applying Eq. (4.1) to each experimentally determined slip curve for the different load-to-grain angles, α , results in m coefficients for each α (see Fig. 4.2a–d).

Step02: In a second step, regression analysis was applied to each of these m coefficients to give a regression between the coefficients and the load-to-grain angle α (see Fig. 4.2b–d). In general, each of these m regression functions reads as

$$a_{1,\alpha} = f(\alpha, a_{1,0}, a_{1,90}, b_{1,1}, b_{1,2}, \dots, b_{1,n}), \quad (a)$$

$$a_{2,\alpha} = f(\alpha, a_{2,0}, a_{2,90}, b_{2,1}, b_{2,2}, \dots, b_{2,n}), \quad (b) \quad (4.2)$$

$$a_{m,\alpha} = f(\alpha, a_{m,0}, a_{m,90}, b_{m,1}, b_{m,2}, \dots, b_{m,n}). \quad (c)$$

Regression functions, $a_{m,\alpha}$, in Eq. (4.2) include for most approaches discussed herein at least two coefficients ($a_{m,0}$ and $a_{m,90}$), which are mainly related to the connection slip behavior at 0° and 90° to the grain or the maximum and minimum values of a_m , respectively. At the same time, the shape of the curve between the two limit values at 0° and 90° to the grain can be controlled by n additional coefficients $b_{m,1}$ to $b_{m,n}$. Again the least square method can be used to determine the corresponding coefficients either enforcing the boundary values of $a_{m,\alpha}$ at 0° and 90° to the grain or not.

Step03: In a third step, Eqs. (4.2a–c) are inserted into Eq. (4.1) (cf. Fig. 4.2e). Thus, applying the above described approach, connection load or embedment stress, y , depending on the dowel displacement, u , and load-to-grain angle, α , can be described by $m \cdot n$ coefficients, with an parametric equation reading as

$$y = f(u, \alpha, a_{1,0}, \dots, a_{m,90}, b_{1,1}, \dots, b_{m,n}). \quad (4.3)$$

To describe the goodness of fit of the slip curves by the parametric regression equation, the coefficient of determination (R^2) has been determined.

Description of the system response, namely embedment stress or connection load, and its dependence on the displacement state and load-to-grain angle requires mathematical expressions for the parameterization of slip curves (*Step01*) as well as for description of the regression parameters over the load-to-grain angle (*Step02*). In the following, regression equations, which might be suitable for these purposes, are presented. Since the slip behavior and the distribution of the parameters over the load-to-grain angle show different trends (see Schweigler et al. (2016a, 2017) and Fig. 4.2), suitable regression equations are discussed for the two regression steps separately in the following two subsections.

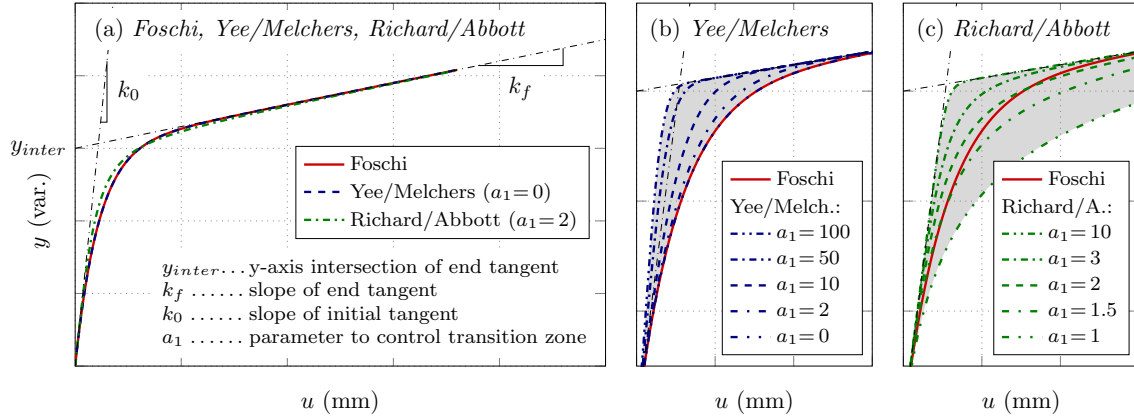


Figure 4.3: *Step01* - Parameterization of slip curves - (a) Illustration of selected regression equations (*Foschi*, *Yee/Melchers* and *Richard/Abbott*). Possible adjustment of the transition zone for the method of (b) *Yee/Melchers* and (c) *Richard/Abbott*, including comparison to the approach of *Foschi*.

4.2.1 Parameterization of slip curves (*Step01*)

The presentation of regression equations for the slip behavior of connections is restricted to approaches, which allow for a consistent description of nonlinear, continuous slip curves. Thus, sequential definitions, such as the bi-linear approach suggested by Pedersen (2002) and others are not discussed herein.

4.2.1.1 Foschi (1974)

Among others, Foschi (1974) used an exponential function to describe experimentally determined nonlinear load-slip curves of nailed connections, which in a similar manner has earlier been used by Jansson (1955) and Norén (1962). The corresponding equation gives the connection load, y , in dependence of the displacement, u , as

$$y(u) = (y_{inter} + k_f \cdot u) \left[1 - e^{-\frac{k_0 \cdot u}{y_{inter}}} \right]. \quad (4.4)$$

The coefficient k_0 describes the initial gradient and k_f the end gradient of the slip curve. The tangent of the initial gradient evolves from the origin, while the position of the end tangent is defined by the coefficient y_{inter} , which describes the intersection of the tangent with the vertical axis (see Fig. 4.3a). The transition of the slip curve between these two tangents is controlled by the interplay of the three coefficients mentioned before, and consequently, cannot be explicitly controlled.

4.2.1.2 Yee and Melchers (1986)

The definition given by Yee and Melchers (1986) could be interpreted as an extension of the one given by Foschi (1974), which adds the opportunity to control the transition of the slip curve between the initial and end tangent. This function was derived to describe the nonlinear moment-rotation curves of bolted end-plate beam-to-column connections in steel structures,

and gives the connection load as

$$y(u) = y_{inter} \left[1 - e^{-\frac{(k_0 - k_f + a_1 \cdot u) \cdot u}{y_{inter}}} \right] + k_f \cdot u, \quad (4.5)$$

with the coefficients k_0 , k_f and y_{inter} , defined in the same way as in Eq. (4.4), see Fig. 4.3a. In addition, the coefficient a_1 controls the change in the slope in the expression. Thus, compared to the previous approach, a_1 allows to steer the transition between the two tangents. As it gets obvious from Fig. 4.3b, only positive values for a_1 give meaningful results, which lead to slip curves being located higher than the ones of *Foschi*. For the limit case of $a_1=0$, the approach of *Yee/Melchers* degenerates to the approach of *Foschi*. It should be noted that large values for a_1 lead to an overestimation of the initial stiffness k_0 , see Fig. 4.3b.

4.2.1.3 Richard and Abbott (1975)

Another approach, resulting in almost the same characteristics of the described curve as for Yee and Melchers (1986), was presented by Richard and Abbott (1975). This power model approach was derived for versatile applications on stress-strain curves, and frequently used to describe the moment-rotation behavior of joints in steel frames (cf. Almusallam and Richard, 1993). The slip equation reads as

$$y(u) = \frac{(k_0 - k_f) \cdot u}{\left[1 + \left[\frac{(k_0 - k_f) \cdot u}{y_{inter}} \right]^{a_1} \right]^{\frac{1}{a_1}}} + k_f \cdot u, \quad (4.6)$$

with the coefficients k_0 , k_f and y_{inter} , defined in the same way as in Eq. (4.4), see Fig. 4.3a. The parameter a_1 controls the transition characteristic between the initial and end tangent of the curve. Compared to *Yee/Melchers*, the initial and end tangent of the slip curve represent an upper limit for the slip curve (see Fig. 4.3c). Moreover, this approach allows for slip curves being located below the one of *Foschi*.

4.2.1.4 Jensen (1994)

Jensen (1994) proposed two functions to define the load-slip behavior of dowel-type fastener connections. In a first approach, Jensen (1994) used a pure polynomial function for the description of slip curves, reading as

$$y(u) = \sum_{i=1}^6 a_i \cdot u^i, \quad (4.7)$$

with six regression coefficients a_i without obvious physical meaning. Thus, coefficients must be determined by fitting of the experimental data, for example based on the least square method.

In addition to Eq. (4.7), *Jensen* suggested to use a series of exponential functions and polynomial functions, giving the connection load as

$$y(u) = a_2(1 - e^{-a_1 \cdot u}) + e^{-a_1 \cdot u} \sum_{i=3}^8 a_i \cdot u^{i-2}. \quad (4.8)$$

Similar to the polynomial approach in Eq. (4.7), no obvious physical interpretation of the eight parameters a_i in Eq. (4.8) can be given.

4.2.1.5 Glos (1978)

Glos (1978) investigated the compressive strength of wood parallel to the grain and used the quotient of two polynomial functions to describe the nonlinear behavior, which shows similar characteristics as connection slip curves. The regression equation reads as

$$y(u) = \frac{u + a_1 \cdot u^n}{a_2 + a_3 \cdot u + a_4 \cdot u^n}, \quad (4.9)$$

where the coefficients a_{1-4} can be determined by adjusting the regression equation and its derivative to the following boundary conditions,

$$\frac{dy}{du}(u = 0) = k_0, \quad (4.10)$$

$$\frac{dy}{du}(u = u_{peak}) = k_{peak} = 0, \quad (4.11)$$

$$y(u = u_{peak}) = y_{peak}, \quad (4.12)$$

$$y(u \gg u_{peak}) = y_{max}. \quad (4.13)$$

Glos (1978) recommended to use $n=7$ for wood under compression parallel to the grain. In Eqs. (4.10–4.13), the coefficient k_0 corresponds to the initial gradient of the curve. The parameter u_{peak} represents the x-value at a local maximum of the curve with the value y_{peak} , and corresponding gradient of the curve $k_{peak}=0$. The coefficient y_{max} stands for the y-value, which is approached asymptotically for large x-values. Thus, compared to the previously described approaches, this approach allows to consider softening effects, while hardening effects cannot be described.

An extended version of the regression function from Glos (1978) was proposed by Flatscher and Schickhofer (2016) for describing the slip behavior of laterally loaded cross laminated timber (CLT) wall systems.

4.2.1.6 Sauvat (2001)

Sauvat (2001) used a combination of trigonometric functions in order to define the gradient of slip curves of dowel timber joints subjected to complex cyclic loading, instead of doing regression analysis directly on the slip curve itself. According to Sauvat (2001), the derivative of the regression equation is given as

$$y'(u) = -a_3(\arctan((u + a_4)^{a_5} + a_1) + a_2), \quad (4.14)$$

where the parameters a_{1-5} can be determined by regression analysis based on the least square method. Adaption of the equation during an industrial project (Bocquet et al., 2004), by adding an additional parameter a_6 gives

$$y'(u) = -a_3(\arctan((u \cdot a_6 + a_4)^{a_5} + a_1) + a_2), \quad (4.15)$$

with

$$\frac{d^2y}{du^2}(u = u_{peak}) = 0, \quad (4.16)$$

$$\frac{dy}{du}(u = u_{peak}) = k_0, \quad (4.17)$$

considering that $u_{peak} = -a_4/a_6$, and with

$$\lim_{u \rightarrow +\infty} \frac{dy}{du} = k_f. \quad (4.18)$$

By coupling mathematical properties of the functions, Eq. (4.16–4.18), with physical parameters of the slip behavior, i.e., the gradient of the initial and end tangent of the slip behavior (denoted as k_0 and k_f in Fig. 4.3a), it is possible to give an analytical expression of the following parameters

$$a_2 = \frac{k_0 \cdot \frac{\pi}{2} - k_f \cdot \arctan(a_1)}{k_f - k_0}, \quad (4.19)$$

$$a_3 = \frac{-k_0}{\arctan(a_1) + a_2}. \quad (4.20)$$

Thus, the parameters a_2 and a_3 , can either be determined by regression analysis based on the least square method, or be taken directly from experimental slip curves. Constant values of $a_1 = 2$ and $a_5 = 4$ are suggested for typical slip curves of timber connections. The parameter a_4 allows to consider an additional initial slip. If no initial slip is considered, a_4 is set equal to zero. The last parameter a_6 can only be set by regression based on the least square method with experimental data. The definition of k_0 according to Eqs. (4.16–4.17) means that this value is always the maximum slope of the slip curve, even in situations with an initial gap. Finally, the slip curve is derived by integration of Eq. (4.15), yielding

$$y(u) = \int_0^u y'(u) du. \quad (4.21)$$

4.2.2 Regression over the load-to-grain angle (*Step02*)

As previously shown by parameter identification from experimental testing (Schweigler et al., 2016a, 2017), strength and stiffness properties of timber connections appear in two different manners as related to the load-to-grain angle, α , namely either in an S-shaped or a bell-type relation. The latter behavior can be found for parameters which correlate with the deviation from the principal material directions. More commonly, connection parameters appear by an S-shaped relation with the load-to-grain angle, as for instance for the embedment strength, as it is currently defined in the European timber engineering design standard (Eurocode 5) (EN 1995-1-1, 2004).

Regression equations for **S-shaped** trends of connection slip parameters over the load-to-grain angle are reviewed in Subsections 4.2.2.1–4.2.2.4.

4.2.2.1 Hankinson (1921)

Strength properties of timber and their dependence on the load-to-grain angle are often described by the so-called *Hankinson formular* (Hankinson, 1921). *Hankinson* proposed this equation for the compression strength of wood under an angle to the grain (Hankinson, 1921). With the notations adapted in this paper, the *Hankinson formular* reads as

$$a(\alpha) = \frac{a_0 \cdot a_{90}}{a_0 \sin(\alpha)^{b_1} + a_{90} \cos(\alpha)^{b_1}}, \quad (4.22)$$

where a_0 and a_{90} are the parameters at the principal material directions, i.e., at the boundary of the regression curve. Compared to the original version of the *Hankinson formular*

with $b_1=2$, an adapted version is presented herein, which allows to control the shape of the curve between the principal material directions by adjusting b_1 (see Fig. 4.4a). However, in design equations, a value of two is mostly used for the parameter b_1 , see e.g. the embedment strength as a function of the load-to-grain angle, as calculated according to Eqs. 8.31–8.33 in Eurocode 5 (EN 1995-1-1, 2004). Moreover, it can be shown that the exponent of two is consistent with a coordinate transformation of the global force into the direction of the grain, in combination with a linear stress interaction criterion using the strength parallel (0°) and perpendicular to the grain (90°), while neglecting the contribution of shear stresses (Blaß and Sandhaas, 2016).

4.2.2.2 Root-mean-square (RMS) (Gupta and Sinha, 2012)

Similar to the approach of Hankinson (1921), Gupta and Sinha (2012) proposed a regression equation based on trigonometrical functions. This approach was used by the authors to describe the behavior of the shear strength at an angle to the grain. With the notations adapted in this paper, the equation reads as

$$a(\alpha) = \sqrt[b_1]{a_0^{b_1} \cos(\alpha)^{b_1} + a_{90}^{b_1} \sin(\alpha)^{b_1}}, \quad (4.23)$$

with a_0 and a_{90} as the values at the principal material directions. As in Eq. (4.22), the parameter b_1 in Eq. (4.23) controls the shape of the curve between the principal material directions (see Fig. 4.4b).

4.2.2.3 Sin-function / Cos-function for S-shaped trends

The trend of connection slip parameters with respect to the grain direction could also be described by using *sin* or *cos* functions, which would yield

$$a(\alpha) = (a_{90} - a_0) \cdot \sin(\alpha)^{b_1} + a_0, \quad (4.24)$$

or

$$a(\alpha) = (a_0 - a_{90}) \cdot \cos(\alpha)^{b_1} + a_{90}. \quad (4.25)$$

The parameters a_0 and a_{90} correspond to the values of the parameter at a load-to-grain angle of 0° and 90° , respectively. The exponent b_1 controls the shape of the curve in between the boundaries a_0 and a_{90} (see Fig. 4.4c and d).

4.2.2.4 Adapted Gompertz function

The *Gompertz function* (Gompertz, 1825) is a sigmoidal function, based on a combination of two exponential functions, which allows to describe asymmetric S-shaped distributions. The equation describes the dependence of a parameter as

$$a(\alpha) = b_1 \cdot e^{-b_2 \cdot e^{-b_3 \cdot \alpha}}, \quad (4.26)$$

with three regression parameters b_1 to b_3 . Adapting the equation to the boundary values of a_0 and a_{90} by adding the starting value of a_0 and substituting b_1 by $(a_{90} - a_0)$ yields

$$a(\alpha) = a_0 + (a_{90} - a_0) \cdot e^{-b_2 \cdot e^{-b_3 \cdot \alpha}}, \quad (4.27)$$

where a_0 and a_{90} are the values at the lower and upper boundary. The coefficients b_2 and b_3 in Eq. (4.27) control the position and inclination of the slope. The coefficient b_2 is mainly

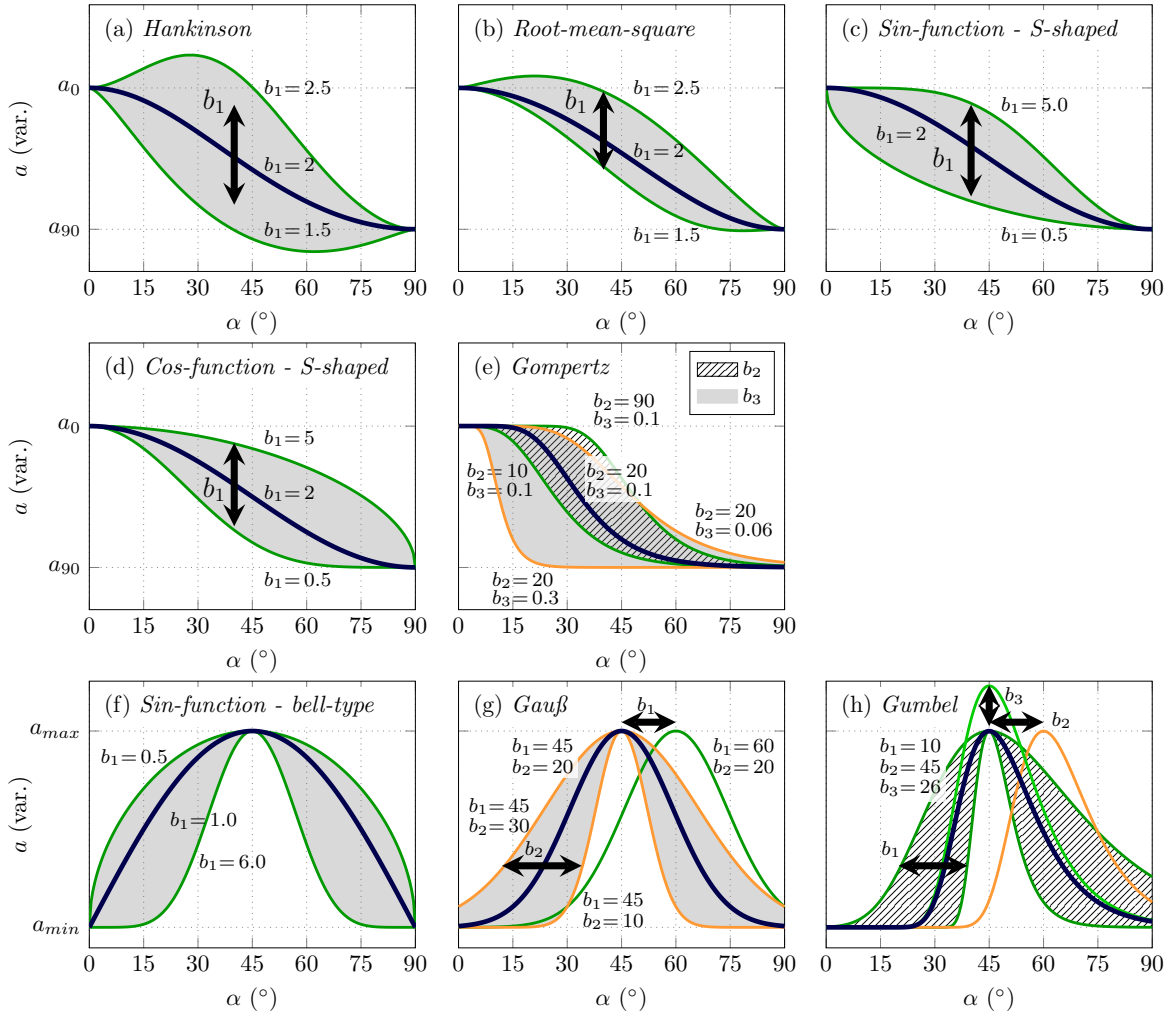


Figure 4.4: *Step02* - Methods for the regression over the load-to-grain angle, including variation of the regression curves by adjusting the fitting parameters. (a)–(e) S-shaped regression equations, (f)–(h) Bell-type regression curves.

responsible for the position of the slope (see Fig. 4.4e), while b_3 strongly influences position and inclination of the slope.

Regression equations for **Bell-type** trends of connection slip parameters over the load-to-grain angle are presented in Subsections 4.2.2.5–4.2.2.7. For this purpose, trigonometric and adapted probability density functions could be used.

4.2.2.5 Sin-function for bell-type trends

The use of a *Sin-function* is a simple way to describe symmetric distributions of parameters over the load-to-grain angle α , which is given by

$$a(\alpha) = a_{min} + (a_{max} - a_{min}) \cdot \sin(2\alpha)^{b_1}, \quad (4.28)$$

where the factor 2 in the sin-expression shifts the peak of the *sin* curve to an load-to-grain

angle of 45° . The parameters a_{min} and a_{max} relate to the minimum and maximum a -value, respectively and the factor $(a_{max} - a_{min})$ scales the *sin* function to the range between these values. Adding a_{min} moves the curve in vertical direction in order to consider values unequal to zero at the boundaries. With the exponent b_1 the shape of the curve is adjusted (see Fig. 4.4f).

4.2.2.6 Adapted Gaussian function

The adapted version of the *Gaussian density function* (Casella and Berger, 2002) is another option to describe symmetric distributions as

$$a(\alpha) = a_{min} + (a_{max} - a_{min}) \cdot e^{-\left(\frac{\alpha - b_1}{b_2}\right)^2}, \quad (4.29)$$

where a_{min} and a_{max} correspond to the minimum and maximum of the a -values, respectively. The coefficient b_1 moves the peak of the distribution along the x-axis, while the parameter b_2 controls the width of the distribution function (see Fig. 4.4g).

4.2.2.7 Adapted Gumbel function

The *Gumbel density function* (Casella and Berger, 2002) allows even to parameterize asymmetric distributions. An adapted version of the *Gumbel density function* reads as

$$a(\alpha) = a_{min} + b_3 \cdot e^{-\left(\frac{\alpha - b_2}{b_1} + e^{-\left(\frac{\alpha - b_2}{b_1}\right)}\right)}, \quad (4.30)$$

where a_{min} is the minimum value of the parameterized function. The coefficient b_1 controls the width and asymmetry of the function. The parameters b_2 and b_3 define the position and height of the peak of the distribution function, respectively (see Fig. 4.4h).

4.3 Application of parameterized regression equations to the embedment behavior of Laminated Veneer Lumber

4.3.1 Comparison of regression equations for parameterization of slip curves (*Step01*)

In the following, regression equations proposed in Subsection 4.2.1 are assessed in their suitability to describe typical shapes of slip curves observed in connection testing, before specific parameterized equations are applied to experimental datasets derived for screw-reinforced dowel connections in Laminated Veneer Lumber (Schweigler et al., 2017). More specifically, typical slip curves derived in connection testing under constrained displacement conditions are considered. Depending on the load-to-grain angle, the nonlinear slip curve might encompass softening or hardening behavior. Moreover, in the case of constrained testing, not only a load component parallel to the prescribed displacement direction, but also one perpendicular to it is evoked and these load components show different trends over the dowel displacement. Thus, three different shapes of slip curves including pronounced displacement hardening typical for loading close to perpendicular to the grain (slip curve *Type01* in Fig. 4.5a), minor softening partly observed for loading close to parallel to the grain (slip curve *Type02* in Fig. 4.5b) and a curve with change in the load direction typical for the lateral load component (slip curve

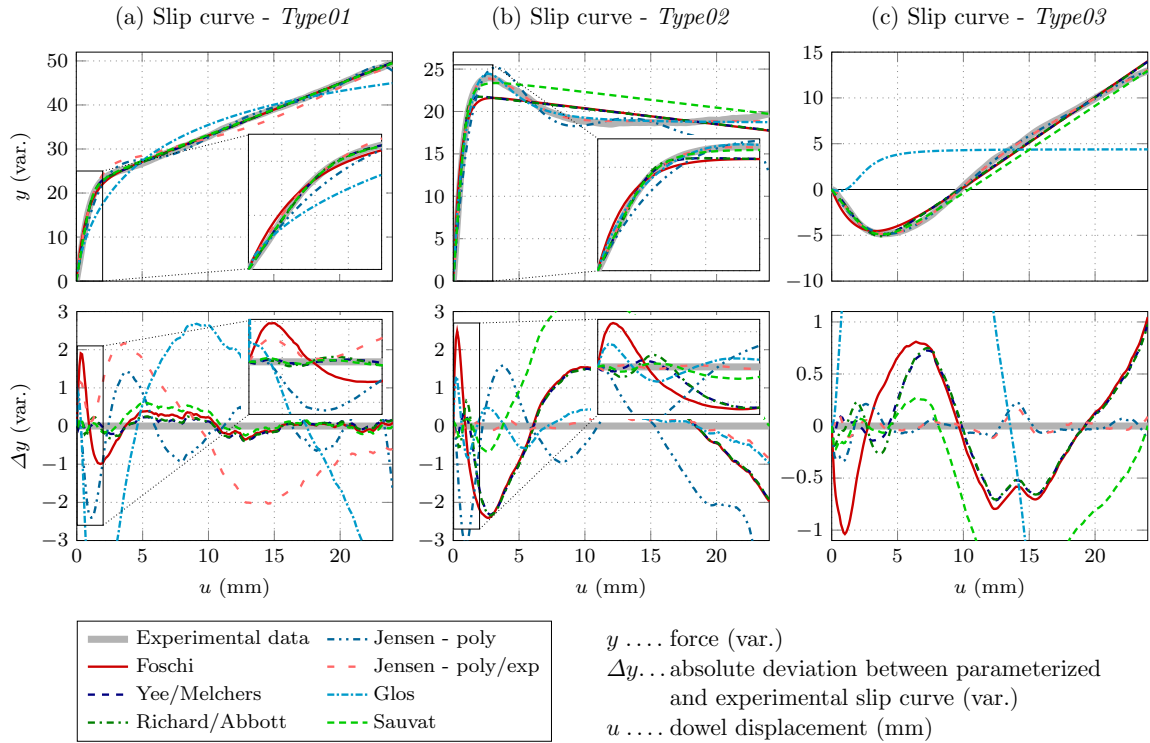


Figure 4.5: *Step01* - Parameterization of slip curves: Application of parameterization equations to different types of experimentally determined slip curves. (a) Slip curve *Type01*, (b) Slip curve *Type02* and (c) Slip curve *Type03*. Illustration of the slip curves (top), and absolute error between experimental and parameterized slip curve (bottom).

Type03 in Fig. 4.5c), are discussed in the following. In addition to the experimental data and the fitted regression equations, the absolute error of the regression with respect to the experimental data is illustrated in Fig. 4.5.

Foschi proposed a method using an exponential equation with three parameters (see Eq. (4.4) in Subsection 4.2.1.1). These parameterization equation is characterized by a linear part at the beginning and end of the slip curve, with a continuous transition in between, where the the change of the slope is controlled by the inclination of the two linear parts. Consequently, using this approach, nonlinearities in the plastic part of curve *Type02* (Fig. 4.5b), can only be linearly approximated. It should be noted that, by using the *Foschi* equation, in many cases an overestimation of the inclination of the first part of the slip curve (quasi-elastic stiffness) is necessary, to allow for a sufficient description of the transition zone between the two linear parts (see Fig. 4.5a and b). This overestimation has to be more pronounced, the larger the differences in inclination of the two linear parts are. The regression equation however has two important advantages. First, the simplicity of the approach results in a stable behavior when fitting experimentally determined slip curves. Secondly, the equation encompasses only three parameters, which even have a physical interpretation. Thus, these parameters could be taken from literature (if available) to describe nonlinear continuous slip curves, taking advantage of previously performed experiments. Furthermore, the physical meaning of the parameters facilitates the description of the parameters over the load-to-grain angle.

The regression equations proposed by *Yee/Melchers* and *Richard/Abbott* show a rather

similar behavior as compared to the one of *Foschi*, see Fig. 4.5. The same three parameters, with the same physical interpretation, are used to describe the slip curve. In addition, a fourth parameter controlling the change in the slope of the transition zone is introduced, cf. Eqs. (4.5) and (4.6). Thus, the disadvantage of the *Foschi* equation of a possible overestimation of the inclination of the first linear part, in order to sufficiently describe the transition zone is eliminated by this additional parameter. Consequently, with these two regression equations, slip curves consisting of two linear end parts, connected by a nonlinear transition zone, can almost perfectly be described (see Fig. 4.5a). However, nonlinear parts after the transition zone can only be linearly approximated.

Eqs. (4.4)–(4.6), which are based on exponential or power functions, might even be used to fit experimental data for lateral load components (cf. curve *Type03* in Fig. 4.5c). Only small differences are observed for the three different equations, which slightly differ particularly in the area of the first stress peak. As for the other slip curves, the additional parameter in the equations of *Yee/Melchers* and *Richard/Abbott* permits higher flexibility. The nonlinear path after the stress peak is however for all approaches approximated by a linear tangent.

Regression equations based on polynomial functions, *Jensen* Eqs. (4.7)–(4.8), exhibit the disadvantage of having no direct physical meaning of the regression parameters, which hinders the parameterization over the load-to-grain angle. Moreover, the use of polynomial functions might lead to a less suitable approximation of linear paths of the slip curve, cf. curve *Type01* in Fig. 4.5a, not only in the plastic, but also in the quasi-elastic part of the slip curve. The same is true even when combining the polynomial with exponential functions in Eq. (4.8). The corresponding equations can however be beneficial, if slip curves exhibit a nonlinear plastic path (curve *Type02* in Fig. 4.5b) or softening behavior in case of unreinforced connections.

The equation proposed by *Glos* (see Eqs. (4.9)–(4.13)) could be especially suitable for slip curves exhibiting a local maximum after an quasi-elastic part, which is approximated by a linear tangent and followed by a decrease in the slip curve resulting in a horizontal tangent of the curve at the peak load. Thus, this approach is particularly suitable for curve *Type02* shown in Fig. 4.5b, while the other two curve types, i.e., *Type01* (Fig. 4.5a) and *Type03* (Fig. 4.5c), cannot sufficiently be approximated by this approach, since no inclination in the slip curve (hardening or softening) after the local maximum can be considered.

Compared to the aforementioned approaches, *Sauvat* (see Eqs. (4.14)–(4.21)) proposed a regression equation for the first derivative of the slip curve. The field of application is similar to the regression equations based on exponential functions or power functions, like the approaches from *Foschi* and *Richard/Abbott*, respectively. As it gets obvious from Fig. 4.5, *Sauvat's* approach is especially suitable for a precise description of the stiffest parts of the slip curves, i.e., the elastic part in most cases, since areas of high stiffness get dominant in regression analysis based on the least square method. On the contrary, areas of low stiffness might be described less accurate, as it can be seen for slip curve *Type02* in Fig. 4.5b. Thus, similar to the equations proposed by *Yee/Melchers* and *Richard/Abbott*, *Sauvat's* equation seems to be well suited to closely follow the initial stiffness, which is decisive for an accurate prediction of the relative displacements and the load distribution in the early stage of loading.

4.3.2 Comparison of regression equations for parameterization over the load-to-grain angle (*Step02*)

Different trends of the regression parameters for slip curves over the load-to-grain angle have been found in experimental studies, and the proposed regression equations in Subsection 4.2.2 will be compared when being applied to examples. Fig. 4.6 illustrates three typical distribu-

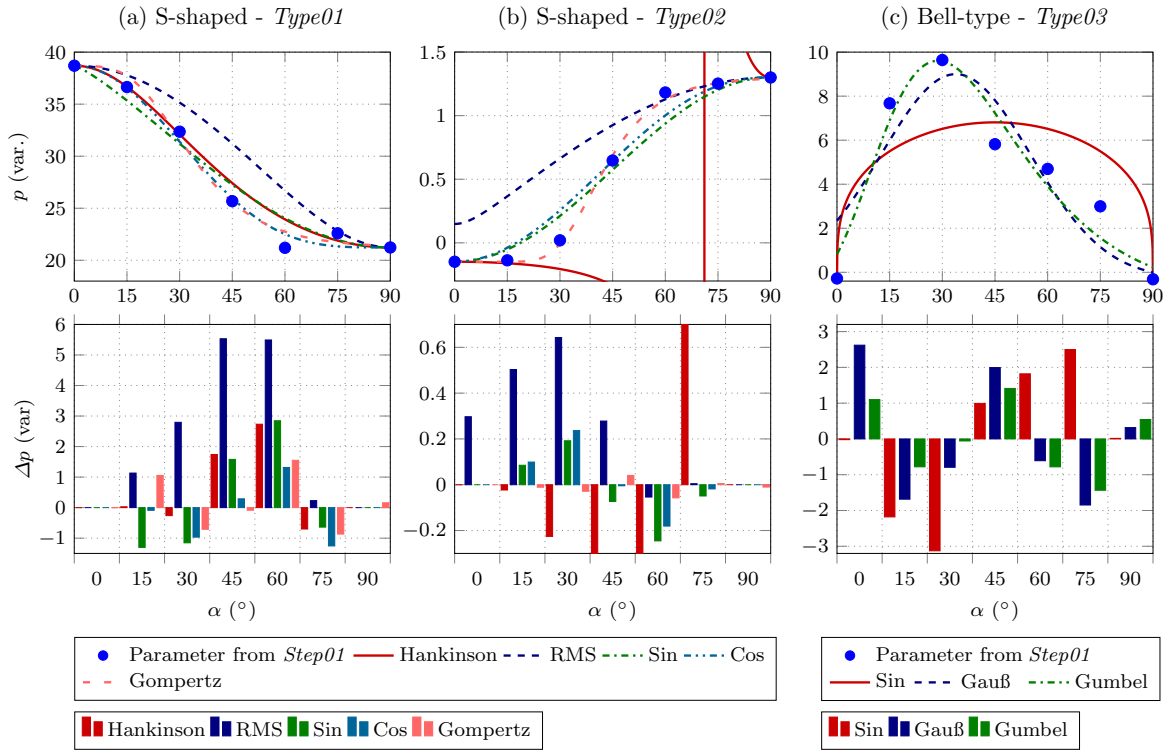


Figure 4.6: *Step02* - Parameterization of parameters over the load-to-grain angle: Application of regression equations on (a)–(b) S-shaped and (c) bell-type distributions of parameters. Illustration of the parameterized distribution functions (top), and absolute deviation between discrete parameters from *Step01* and regression functions (top).

tions of regression parameters that have been determined for seven load-to-grain angles, i.e., for a step size of 15° . The first one is typically found for strength and quasi-elastic stiffness properties that decrease with increased load angle (Fig. 4.6a) and the second one for the increase of the displacement hardening (Fig. 4.6b) with increased load-to-grain angle. Note that in case of a minor softening behavior, the parameter shown in Fig. 4.6b starts with a negative value. The third dataset depicts parameters that are zero or close to zero at the principal material orientations (Fig. 4.6c) as it was observed for lateral load components in constrained testing. Thus, the examples relate to *S-shaped* and *bell-type* courses of the parameters over the load-to-grain angle. In addition to the example data and the fitted regression equations, the absolute error of the regression with respect to the experimental data is illustrated in Fig. 4.6.

First, *S-shaped* distributions are discussed (see Fig. 4.6a and b). In these examples, the values at 0° and 90° are considered as boundary conditions of the regression curves.

The approach of *Hankinson* uses a combination of *sin* and *cos* functions to describe the behavior between 0° and 90° . The shape in between can be controlled by adjusting the exponents in the expression, cf. Eq. (4.22). However, this is only reasonable up to a certain extend, since adjusting the exponent might lead to physically meaningless distributions (cf. Fig. 3a). Therefore, the *Hankinson* expression in its originally version with the parameter $b_1=2$ is used. This approach works perfectly only for almost symmetric distributions, which follow an S-shaped decrease or increase of parameters (see Fig. 4.6a). Distributions with a

change in sign cannot be represented by this method (see Fig. 4.6b).

The *root-mean-square (RMS)* equation, Eq. (4.23), has been applied with a coefficient $b_1=2$, which seems reasonable since other coefficients would lead to values higher and lower than the limit values at the load-to-grain angle boundaries. The regression curve deviates significantly more and has a different shape than the one derived with the *Hankinson* equation, see Fig. 4.6a, which is also indicated by a larger error. Moreover, it shows the same deficiencies as the *Hankinson* equation as regards the use of negative in combination with positive boundary values (see Fig. 4.6b).

The two approaches *Sin* and *Cos* in Fig. 4.6a and b are purely based on a *sin* or *cos* function, respectively, Eqs. (4.24) and (4.25). In addition, an exponent was fitted to control the shape of the curve between the boundaries. These two methods allow for a suitable representation of increasing or decreasing trends and trends with negative values and changing sign (see Fig. 4.6a and b). These approaches are characterized by a smooth S-shaped definition of regression curves.

Compared to the other approaches, *Gompertz* uses exponential functions. Thus, this method is characterized by higher flexibility regarding the shape of the regression curve, which can be controlled by the parameters b_2 and b_3 in Eq. (4.27) (see Fig. 4.6a and b). A combination of negative and positive values, distributions with changing sign, as well as increasing and decreasing distributions can be considered by this method. For curve *Type01* in in Fig. 4.6a, the *Gompertz regression curve* closely follows the regression curve based on *Hankinson* equation. Also for curve *Type02* in in Fig. 4.6b, the *Gompertz* function shows the smallest errors compared to the example data.

A *bell-type* distribution of parameters is shown in Fig. 4.6c and the three regression equations presented in Subsection 4.2.2 are applied and compared in the following.

The use of a *Sin*-function, Eq. (4.28), would assume a symmetric distribution of the parameters, which obviously would lead to a strong simplification of the dataset. The shape of the regression curve can only be adjusted by the parameter b_1 . However, the benefit of this simple trigonometric function is that it gives a value of zero at the boundaries, i.e., at a load-to-grain angle of 0° and 90° , see Fig. 4.6c.

The approaches based on the *Gaussian* and *Gumbel* distribution, Eqs. (4.29) and (4.30), respectively, exhibit a similar behavior. Both methods use distinct parameters to control the width, height and position of the bell-type distribution function. With the *Gumbel* distribution approach it is possible to consider also asymmetric distributions. For the *Gaussian* equation, this is only possible by a shift of the curve, which however might lead to different starting values at the load-to-grain angle boundaries. The latter is also a difficulty when using the *Gumbel* equation, due to the interrelation of the parameters b_1 to b_3 in Eq. (4.30). Thus, it is not possible to enforce the regression curve to be zero at the boundaries, see Fig. 4.6c.

4.3.3 Parameterization of embedment test data for Laminated Veneer Lumber (*Step01–03*)

Based on the comparison in the previous subsections, a set of regression equations is applied to a consistent experimental dataset for embedment behavior of Laminated Veneer Lumber (LVL), see Schweigler et al. (2017). The data was established by biaxial, constrained testing of LVL (with parallel veneers, *Kerto-S* and a moisture content of about 12%) with a 12 mm steel dowel. Testing was performed for seven load-to-grain angles starting from parallel to the grain ($\alpha=0^\circ$) up to perpendicular to the grain ($\alpha=90^\circ$) with a step size of 15° . The parameterization strategy presented in Section 4.2 is now applied to this dataset by first

performing regression equations on the individual slip curves (*Step01*) before regression of the parameters over the load-to-grain angle (*Step02*). In the following, these steps are applied for both embedment stress components, the vertical f_{hv} (parallel to the prescribed displacement direction following the load-to-grain angle α) and the horizontal f_{hh} (perpendicular to the prescribed displacement direction). All slip curves are considered as mean values of at least three replications, limited with a maximum dowel displacement u of equal to 24 mm, which corresponds to two times the dowel diameter. For further details the reader is referred to Schweigler et al. (2017).

For regression analysis the least square method was applied.

4.3.3.1 Parameterized vertical embedment stress, f_{hv}

Slip curves of the dataset are illustrated in Fig. 4.7. A quasi-linear elastic, followed by an almost linear curve part gets obvious for nearly all load-to-grain angles. This calls for application of a method of the group of *exponential and power functions*, such as the approach of *Richard/Abbott*. This approach was chosen for its flexibility regarding description of the transition zone from quasi-elastic to the elasto-plastic part of the slip curve. Results are illustrated in Fig. 4.7 together with the absolute error of the regression curve with respect to the experimental data.

Parameters of the *Richard/Abbott* equation, Eq. (4.6), determined by regression analysis, as well as the coefficient of determination, R^2 , in order to describe the goodness of fit, are shown in Table 4.1. The fitting process has shown the parameter a_1 in Eq. (4.6) to be almost independent of the load-to-grain angle, for this particular dataset. Thus, the number of fitting parameters reduces from four to three parameters per load-to-grain angle, where a_1 has been chosen to be constant $a_1=3$ for all α .

The coefficient of determination, R^2 , was found to be always higher than 0.981. The absolute error between parameterized and experimentally determined slip curve, Δf_{hv} , (see Fig. 4.7) is mainly less than 1 N/mm^2 . Expressed as relative error of the parameterized with respect to the experimentally determined slip curve, the error is less than 5% for most parts of the slip curves. Only at the very beginning of the slip curve relative errors larger than 5% were found, which can be explained by sensitivity of the small absolute values to small absolute errors.

The three parameters from *Step01*, namely $f_{hv,inter}$ (denoted as y_{inter} in the previous sections), k_f and k_0 are subsequently parameterized in *Step02*. A clear S-shaped trend is found for $f_{hv,inter}$ and k_f , while an S-shaped distribution of the parameter k_0 is not obvious from the presented data. Possible reasons for this were discussed in Schweigler et al. (2017), based on which an S-shaped trend was considered in the regression analysis presented herein. Each parameter can be interpreted as mean value of at least three tests for each load-to-grain angle.

For a suitable fit of the different parameters from *Step01*, different equations have been used, namely the approaches of *Gompertz* and *Hankinson*. The approach of *Gompertz*, Eq. (4.27), emerged to best approximate the distributions of $f_{hv,inter}$ (y_{inter}) and k_f in Fig. 4.8a and b, while for k_0 in Fig. 4.8c, the approach of *Hankinson*, Eq. (4.22), was used. The related four (*Gompertz*), or two output parameters (*Hankinson*), respectively, for each regression parameter from *Step01* are given in Table 4.2 (*Step02*). The parameters at the boundaries have been enforced in the regression analysis, yielding a_0 and a_{90} in Eq. (4.27) and Eq. (4.22), respectively, to be equal to the corresponding parameters of the slip curves regression presented in Table 4.1. Thus, only the parameters b_2 and b_3 in Eq. (4.27) have been

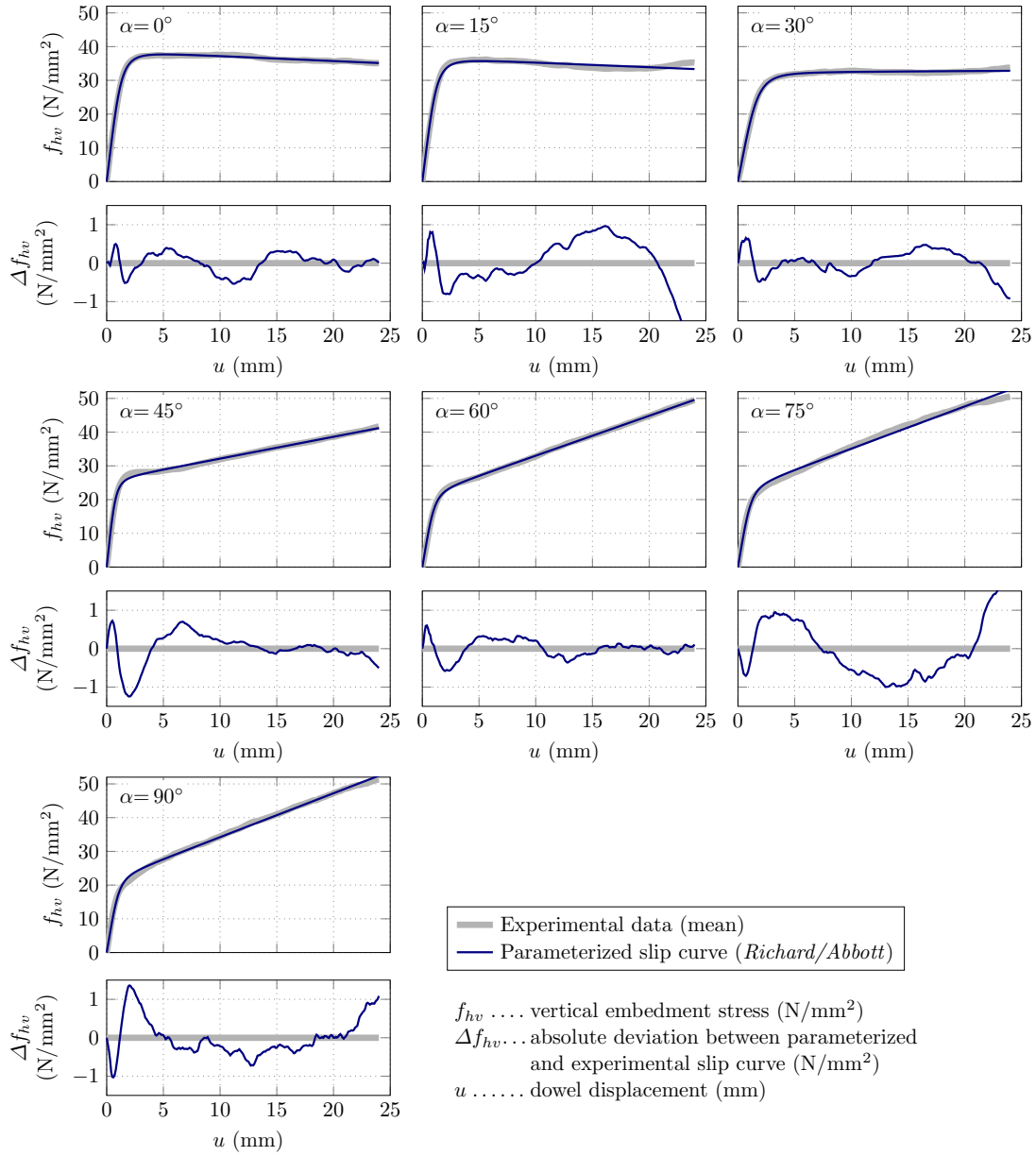


Figure 4.7: *Step01* - Regression curves for embedment slip curves f_{hv} for constrained embedment testing, $d=12$ mm, using Eq. (4.6), *Richard/Abbott*.

Table 4.1: *Step01* - Regression parameters for embedment slip curves f_{hv} using Eq. (4.6), *Richard/Abbott*.

		0°	15°	30°	45°	60°	75°	90°
$f_{hv,inter}$	(N/mm ²)	38.69	36.65	32.36	25.68	21.20	22.59	21.23
k_f	(N/mm ³)	-0.149	-0.137	0.020	0.647	1.182	1.252	1.300
k_0	(N/mm ³)	27.91	26.78	17.34	31.20	19.82	19.80	19.83
a_1	(-)	3	3	3	3	3	3	3
R^2	(-)	0.998	0.981	0.997	0.996	0.999	0.994	0.998

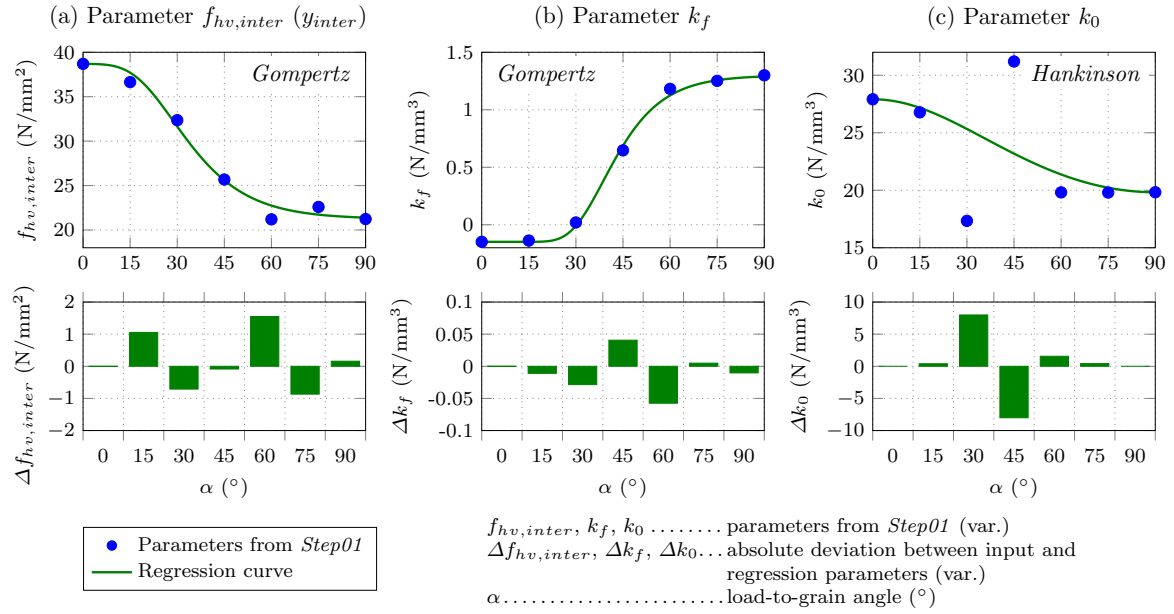


Figure 4.8: *Step02* - Regression curves for parameters $f_{hv,inter}$, k_f and k_0 from *Step01* over the load-to-grain angle for constrained embedment testing f_{hv} , $d=12$ mm (a)–(b) using Eq. (4.27) *Gompertz*, (c) using Eq. (4.22) *Hankinson*.

Table 4.2: *Step02* - Regression parameters for parameters a_i from *Step01* according to Eq. (4.6), *Richard/Abbott*, using Eq. (4.27), *Gompertz*, and Eq. (4.22), *Hankinson*, for f_{hv} .

	$f_{hv,inter}$ (N/mm ²)	k_f (N/mm ³)	k_0 (N/mm ³)
	<i>Gompertz</i>	<i>Gompertz</i>	<i>Hankinson</i>
a_0	38.69	-0.149	27.91
a_{90}	21.23	1.300	19.83
b_2	9.053	42.35	-
b_3	0.0767	0.0966	-
R^2	0.986	0.998	0.220

determined.

The goodness of fit is described by the coefficient of determination R^2 (see Table 4.2) and the absolute error between input and parameterized parameters, $\Delta f_{hv,inter}$, Δk_f and Δk_0 , in Fig. 4.8. For the parameters $f_{hv,inter}$ (y_{inter}) and k_f an almost perfect regression curve with an R^2 higher than 0.986 was found (see Fig. 4.8a and b). In contrast, the parameter k_0 exhibits two apparent outliers corrupting the S-shaped distribution of this parameter (see Fig. 4.8c). Possible reasons for that have been discussed before (cf. also discussion in Schweigler et al., 2017).

Finally, in *Step03*, the two *Gompertz* functions and the *Hankinson* function (*Step02*) are inserted into the slip curve expression of *Richard/Abbott* (*Step01*), which gives the vertical embedment stress f_{hv} as a function of the dowel displacement u and of the load-to-grain angle α . This yields an expression with 10 parameters, namely $f_{hv,inter,0}$, $f_{hv,inter,90}$, $k_{f,0}$, $k_{f,90}$, $k_{0,0}$, $k_{0,90}$ and $b_{2,f_{hv,inter}}$, $b_{3,f_{hv,inter}}$, b_{2,k_f} , and b_{3,k_f} according to Table 4.2. An illustration of the load-to-grain angle dependent slip behavior is given in Fig. 4.11a. Additionally, Fig. 4.11b shows the absolute error between parameterized and experimental data, Δf_{hv} . The goodness of the fit is additionally confirmed by an R^2 of 0.984.

4.3.3.2 Parameterized horizontal embedment stress, f_{hh}

Slip curves of the dataset are illustrated in Fig. 4.9. The slip behavior of the horizontal embedment stress component, f_{hh} , exhibits a considerable different appearance compared to the slip behavior of f_{hv} . Due to the shape of slip curves of f_{hh} , the two approaches of *Jensen*, Eqs. (4.7) and (4.8), might be most suitable for parameterization of the single slip curves (*Step01*). However, these equations have the big disadvantage of including parameters with no physical interpretation, which hinders the parameterization of these parameters over the load-to-grain angle in *Step02*. For that reason, the approach of *Foschi*, Eq. (4.4) is applied, accepting the fact of being not able to precisely describe the nonlinear behavior in the second part of the slip curve (see Fig. 4.9). The coefficients of determination R^2 were found to be larger than 0.942 with exception for α of 90° , where R^2 amounted to 0.129 (see Table 4.3). This might be explained by the definition of R^2 , which reacts sensitive to distributions of parameters close to zero, as it is the case for α of 0° and 90° . Moreover, theoretically, the lateral reaction force for loading along the principal material directions should be zero, and only small forces have been measured. Parameters from parameterization of the slip curves of f_{hh} (*Step01*) are given in Table 4.3.

In *Step02* the regression of the parameters from *Step01*, i.e., $f_{hh,inter}$, k_f and k_0 , is described. As obvious from Fig. 4.9, these parameters exhibit an almost symmetric bell-type distribution over the load-to-grain angle. Thus, the approach of *Gauß* is predestine for this dataset. The four parameters, necessary to describe the *Gaussian* distribution, Eq. (4.29), are given in Table 4.4 for each of the three parameters from *Step01*. In this equation, the minimum, a_{min} , and maximum, a_{max} , values are defined instead of the boundary values at 0° and 90° to the grain, while the parameters b_1 and b_2 control the shape in between the boundaries. The coefficient of determination R^2 amounted to values between 0.789 and 0.855 (see Table 4.4). It should be noted that deviations have especially been found at the boundaries, i.e., α of 0° and 90° , where a value close to zero should be given.

In *Step03*, combination of the interaction criteria based on *Gaussian* distribution (*Step02*) and the slip curve definitions based on the approach of *Foschi* give the horizontal embedment stress component, f_{hh} , as a function of the dowel displacement, u , and of the load-to-grain angle α (see Fig. 4.11c) while the absolute error between parameterized and experimental

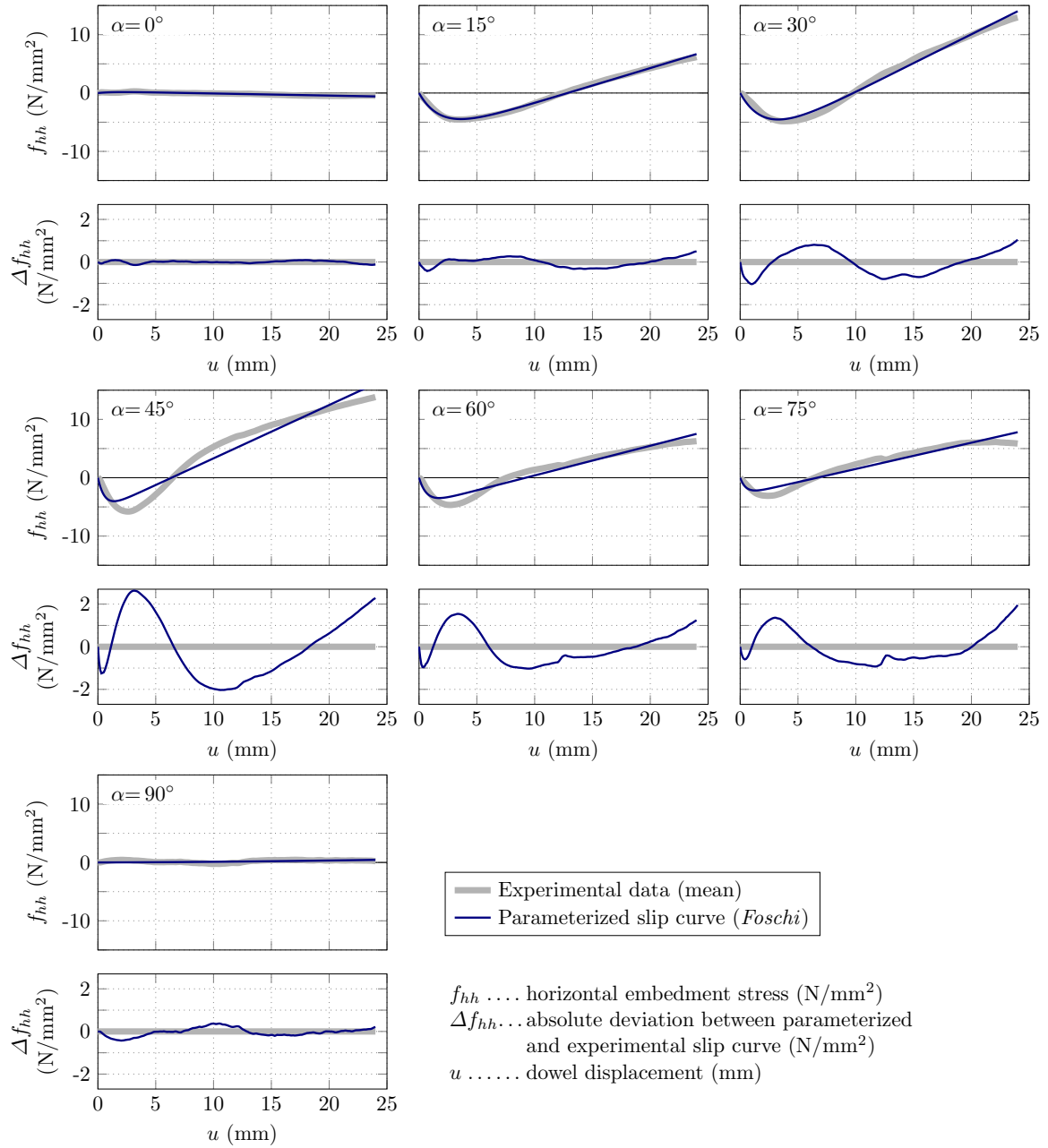


Figure 4.9: *Step01* - Regression curves for embedment slip curves f_{hh} for constrained embedment testing, $d=12$ mm, using Eq. (4.4), *Foschi*.

Table 4.3: *Step01* - Regression parameters for embedment slip curves f_{hh} using Eq. (4.4), *Foschi*.

		0°	15°	30°	45°	60°	75°	90°
$f_{hh,inter}$	(N/mm ²)	0.2812	-7.674	-9.642	-5.817	-4.695	-2.997	0.3176
k_f	(N/mm ³)	-0.0359	0.5975	0.9856	0.9140	0.5088	0.4500	0.0433
k_0	(N/mm ³)	0.1875	-3.509	-3.618	-9.020	-6.587	-5.422	0.0052
R^2	(-)	0.942	0.996	0.991	0.946	0.951	0.942	0.129

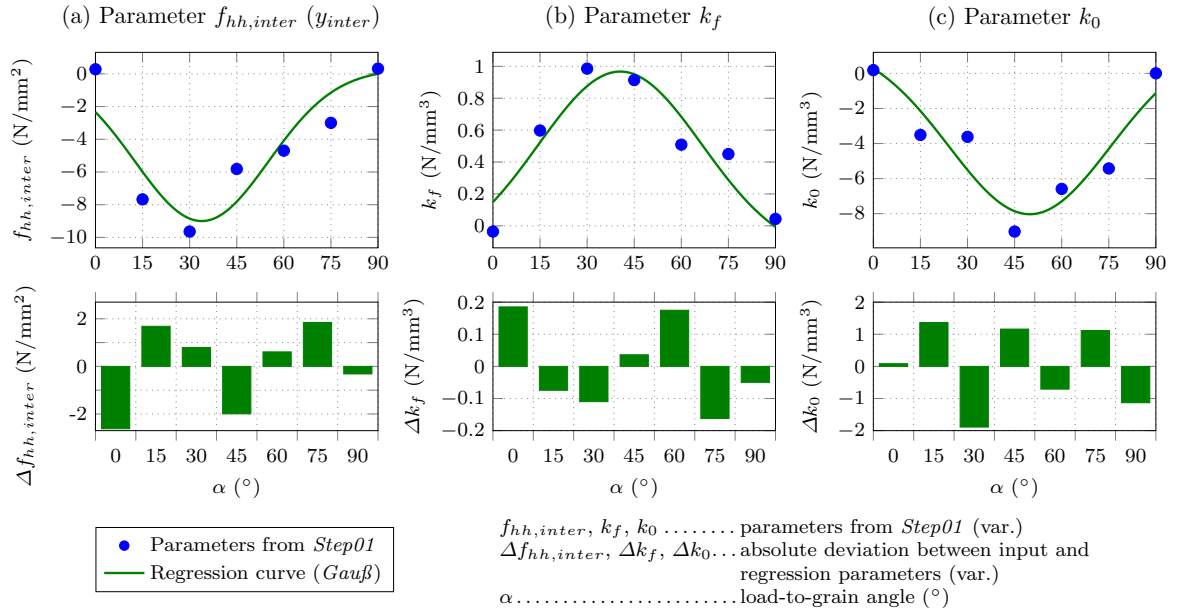


Figure 4.10: *Step02* - Regression curves for parameters $f_{hh,inter}$, k_f and k_0 from *Step01* over the load-to-grain angle for constrained embedment testing f_{hh} , $d=12$ mm, using Eq. (4.29), *Gauß*.

Table 4.4: *Step02* - Regression parameters for parameters a_i from *Step01* according to Eq. (4.4), *Foschi*, using Eq. (4.29), *Gauß*, for f_{hh} .

	$f_{hh,inter}$ (N/mm ²)	k_f (N/mm ³)	k_0 (N/mm ³)
a_{min}	0.289	-0.200	1.770
a_{max}	-9.00	0.967	-8.03
b_1	33.85	40.53	49.84
b_2	1815	2723	2646
R^2	0.789	0.877	0.855

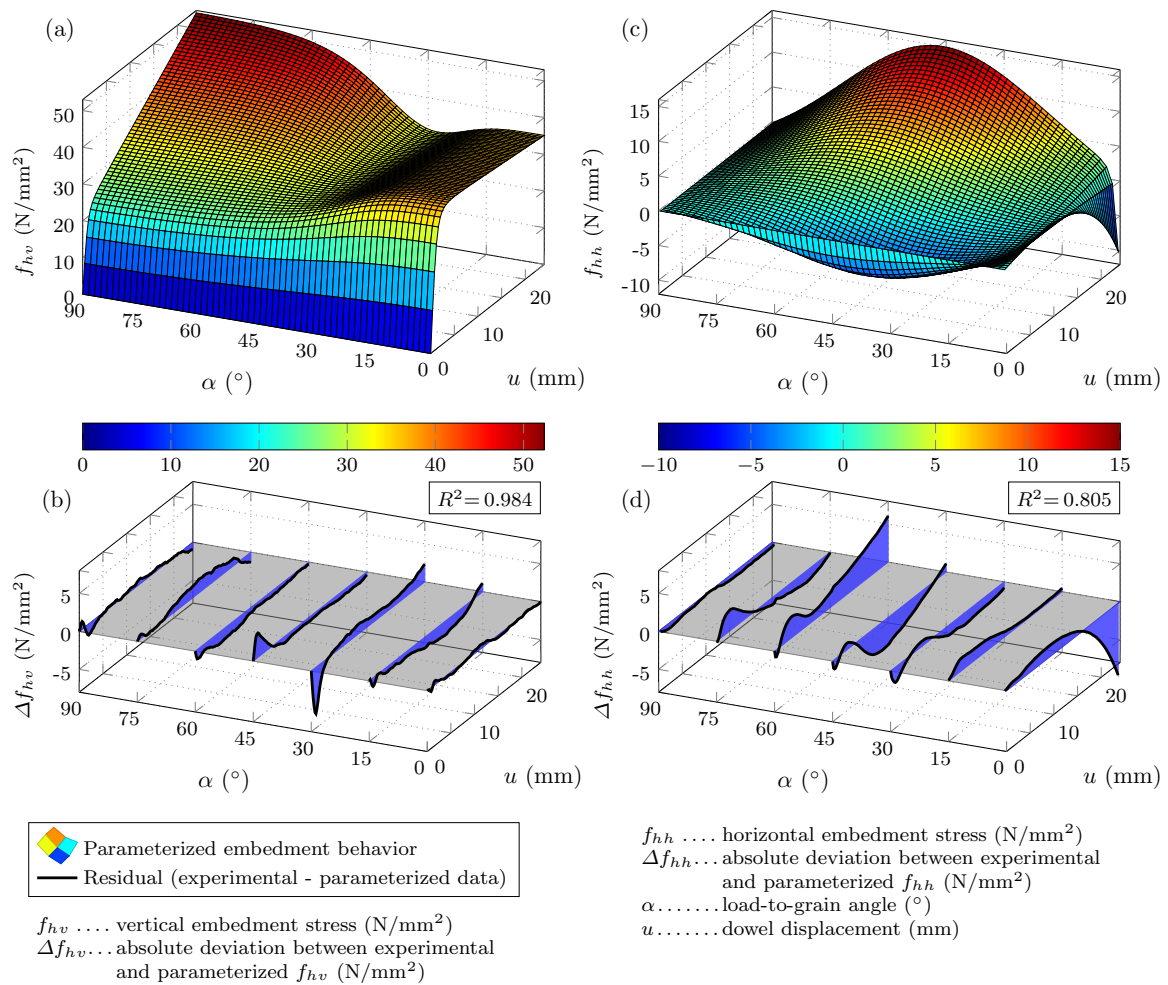


Figure 4.11: *Step03* - Parameterized definition of the embedment stress as function of the dowel displacement, u , and the load-to-grain angle, α , based on the dataset from constrained embedment tests in LVL (Schweigler et al., 2017) for a steel dowel with 12 mm in diameter. (a) parameterized vertical embedment stress component, f_{hv} , (b) absolute deviation between experimental and parameterized f_{hv} . (c) parameterized horizontal embedment stress component, f_{hh} , (d) absolute deviation between experimental and parameterized f_{hh} .

embedment behavior, Δf_{hh} , is given in Fig. 4.11d. This yields an expression with 12 parameters, namely $f_{hh,inter,min}$, $f_{hh,inter,max}$, $k_{f,min}$, $k_{f,max}$, $k_{0,min}$, $k_{0,max}$ and $b_{1,f_{hh,inter}}$, $b_{2,f_{hh,inter}}$, b_{1,k_f} , b_{2,k_f} , b_{1,k_0} , and b_{2,k_0} according to Table 4.4. Difficulties to properly describe the horizontal embedment stress, f_{hh} , at the boundaries, i.e., α of 0° and 90° , get obvious from Fig. 4.11c and d. The error particularly increases at displacements of more than 15 mm. This can be explained by the challenging task to describe slip curves with values close to zero, by a combination of multiple exponential functions, as it is the case for *Foschi* and *Gauß*.

Nevertheless, even if *Foschi* provides only an approximation of the slip curves from experiments, the general embedment behavior can be reasonably described, which is reflected by an R^2 of 0.805.

4.4 Discussion of further influences

4.4.1 Initial slip

The initial slip in embedment or connection tests is highly variable and depends on multiple factors, such as desired or undesired clearance between the dowel and borehole, the surface quality of the borehole, testing setup and size of preloading (Dorn, 2012). Thus, the weak stiffness and displacements in the initial contact between the dowel and wood could be considered as an additional effect. Mathematical expressions for pressure-contact displacement relationships have been proposed by Dorn (2012) or Iraola et al. (2016), which could be combined with a parameterized slip curve determined herein.

Thus, for parameterization of the slip curves, it might be beneficial to remove the initial slip u_{ini}^{exp} from the experimental data. In the analysis presented herein, the initial part of the embedment slip curve (u_{ini}^{exp} in Fig. 4.12a), up to an embedment stress of 10% of the embedment strength determined at 5 mm dowel displacement, $f_{h,5mm}$, was removed. Subsequently, this initial part of the measured slip curve was replaced by a linear section with an inclination equal to the quasi-elastic loading stiffness K_{elast}^{load} (see Fig. 4.12a). This stiffness is defined, following the principles of EN 383 (2007), as the inclination of the line connecting the two stress points at 10% and 40% of the embedment strength, $f_{h,5mm}$.

Alternatively, the unloading or reloading stiffness might be used for the parameterization and combined with a pressure-overclosure relationship for a nonlinear computation of connections. The latter requires a different determination of the initial slip compared to the one used herein.

The main advantage of excluding the initial slip is that causal mechanical relationships are considered separated from effects caused by the production and assembling quality. The simplest approach would be to add an initial clearance, u_{ini}^{des} , to the parameterized slip curve (see Fig. 4.12b), which should depend on predefined execution classes.

4.4.2 Influence of the displacement range of the embedment slip curve on regression parameters

So far, results of a regression analysis applying a least square fitting process on experimental slip curves up to a displacement of two times the dowel diameter has been presented. However, current test standards prescribe a maximum displacement of 5 mm. Thus, the sensitivity of the regression parameters on the underlying displacement range is discussed next.

Slip curves characterized by an almost linear tangent in the quasi-elastic and elasto-plastic part of the slip curve, as illustrated by slip curve *Type01* in Fig. 4.5a, favor parameterization equations based on exponential functions. The *Foschi* equation, Eq. (4.4), however requires

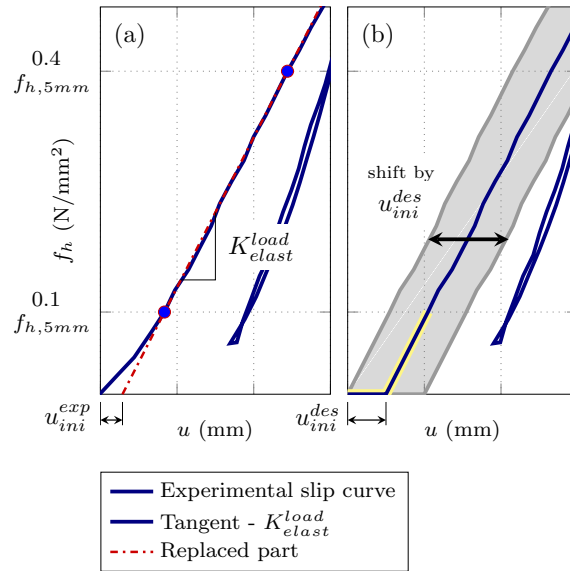


Figure 4.12: (a) Definition of the initial slip from experimental slip curves, u_{ini}^{exp} , (b) replacement of the initial slip, u_{ini}^{exp} , by an initial slip for the design of connections, u_{ini}^{des} .

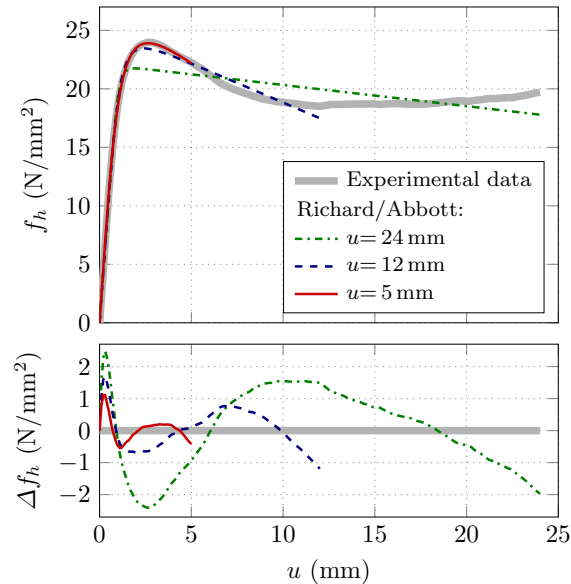


Figure 4.13: Influence of the displacement range on the global quality of the parameterized slip curve - Slip curve *type 02* - Parameterization method *Richard/Abbott*.

a strong overestimation of the initial stiffness (k_0) for a proper definition of the transition zone (see Fig. 4.5a). Reducing the underlying displacement range for fitting, reduces also overestimation of the initial stiffness, as soon as the linear elasto-plastic part of the slip curve is excluded from fitting. This goes in hand with a decrease in the parameter for the final stiffness (k_f), and increase of the parameter $f_{h,inter}$. Consequently, the transition zone can be described more precisely, while the parameter set does however not allow for extrapolation of the slip behavior to larger dowel displacements.

A second example for the influence of the displacement range on the parameterized description of slip curves is given in Fig. 4.13, which illustrates slip curve *Type02* (cf. Fig. 4.5b) described by the equation of *Richard/Abbott*. In this case, the elasto-plastic part of the slip curve exhibits a strong nonlinearity, which makes the description by means of methods based on exponential functions challenging. As it gets obvious from Fig. 4.13, the underlying displacement range significantly affects the quality of the fit for the slip curve part after the quasi-elastic zone. Reducing the displacement range leads to a reduced nonlinearity of the elasto-plastic part, which improves the quality of the fitted slip curve, which is reflected by a reduced absolute error between parameterized and experimental slip curve (see Fig. 4.13). Since, also in this case, the regression parameters depend on the considered displacement range, the extrapolation to larger dowel displacements is not possible. This is mainly related to the definition of the elasto-plastic stiffness k_f in combination with the stress or load property $f_{h,inter}$.

Consequently, the underlying displacement range should be chosen according to the purpose of the parameterized slip curve. If only the overall shape of the fitted slip curve, and not local effects like local maximums, as it can be seen in Fig. 4.13, are of interest, the full displacement range can be chosen. On the contrary, if these local discontinuities are important to be described, the displacement range should be narrowed to a slip curve range with an almost homogeneous slip curve characteristics, to be described by one of the regression equations presented in this contribution. In this case it might be beneficial to fit distinct parts of the slip curve separately, and combine them subsequently as shown in Fig. 4.1d.

4.4.3 Impact of the work on practical application

This work focused on the determination of parameters of reinforced connections, i.e., on the ductile behavior. The need for an experimental testing up to large dowel displacements was illustrated in Subsection 4.4.2, where regression parameters were found to be sensitive to the displacement range.

Instead of using regression analysis based on least square fitting principles, the definition of parameterized equations of slip curves could be based on physical parameters, namely stiffness and strength properties, directly determined in experiments. In Schweigler et al. (2017), three parameters have been determined, namely the initial stiffness, $K_{elast}^{load} = k_0$, the final stiffness, $K_{plast}^{load} = k_f$ and the strength at a dowel displacement of 5 mm, $f_{h,5mm}$. Based on these values the embedment stress at the intersection with the y-axis, $f_{h,inter}$, required for the before discussed parameterized equations, can be calculated. This was done by intersecting the y-axis by the tangent, with an inclination of k_f , evolving from the embedment stress point of the slip curve at $u = 5$ mm ($f_{h,5mm}$). The above described parameters are compared to parameters determined with regression analysis, based on least square fitting, in Tab. 4.5, for the embedment behavior of a 12 mm dowel in LVL parallel to the grain, using equations of *Foschi* Eq. (4.4), *Yee/Melchers* Eq. (4.5) and *Richard/Abbott* Eq. (4.6).

For the equations of *Yee/Melchers* and *Richard/Abbott* parameters fitted by the least

Table 4.5: Comparison of strategies to define slip curves. Exemplarily shown for the slip curve from constrained embedment test at α of 0° and a dowel with 12 mm in diameter (see Schweigler et al., 2017).

Method	based on	$f_{h,inter}$ (N/mm ²)	k_f (N/mm ³)	k_0 (N/mm ³)	a_1 (-)	R^2 (-)
<i>Foschi</i>	least square fitting	38.85	-0.158	41.0	-	0.988
	parameters from experiment	38.41	-0.122	27.6	-	0.869
	Residuum (%)	1.1	29.5	48.6		
<i>Yee/Melchers</i>	least square fitting	38.29	-0.126	29.8	10 (const)	0.996
	parameters from experiment	38.41	-0.122	27.6	10 (const)	0.994
	Residuum (%)	-0.3	3.2	8.1		
<i>Richard/Abbott</i>	least square fitting	38.69	-0.149	27.9	3 (const)	0.998
	parameters from experiment	38.41	-0.122	27.6	3 (const)	0.996
	Residuum (%)	0.7	22.1	1.1		

square method yielded almost the same values as the related parameters from experiments (see Tab. 4.5). The residuum between least square fitted and parameters directly from experiments was found to be less than 10%, with one exception; for *Richard/Abbott* the parameter for the stiffness of the elasto-plastic part a_2 (k_f) deviated by 22%, which however can be explained by the small value, which does not significantly influence the overall quality of the parameterized slip curve, which is proven by the coefficient of determination being higher than 0.994 in all cases.

In contrast, considerably different stiffness parameters were found using the *Foschi* equation. This is a consequence of a strong overestimation of k_0 , when using *least square regression analysis*. Parameters from experiments however allow for a more realistic path in the early quasi-elastic range, while underestimating the slip behavior in the transition zone. The latter leads to a lower quality of the fit with an R^2 of 0.869.

4.5 Conclusions

A three-step approach for regression analysis of the anisotropic connection slip behavior yielded suitable approximation of the experimental data by combinations of parameterized equations. The following conclusions can be drawn as regards regression equations for single slip curves:

- Slip curves with an almost linear behavior in the elastic and plastic part were found to be best approximated by regression equations based on exponential or power functions. The well-known equation of *Foschi* was found to tend to an overestimation of the initial slope of the slip curve for a sufficient description of the transition zone. Parameters of exponential and power model equations applied herein even showed a physical interpretation.
- Polynomial regression functions were found to be best suited to approximate nonlinearities in the plastic load path which is only linearly approximated by exponential functions. However, also the equations based on exponential or power functions resulted in a good approximation of this slip curve with a maximum relative error of less

than 10%.

Regression analysis between the slip curve regression parameters and the load-to-grain angle gave the following insights:

- Distributions of parameters, following closely an S-shaped trend were suitably approximated by almost all presented regression equations for this purpose. However, only the *Sin*, *Cos* and *Gompertz* approaches allowed to control reasonably well the shape of the regression curve and were even able to cope with parameters that changed sign.
- Bell-type distributions were found to be best approximated by the statistical equations of *Gauß* and *Gumbel*, due to their flexibility regarding the shape of the curve.

The study showed that a combination of regression equations gave a suitable approximation of steel dowel embedment behavior in Laminated Veneer Lumber, which even included the special case of transversal load components evoked by the anisotropic nature of the material.

For parameterized slip curves based on exponential functions it was shown that physical parameters, directly determined in experiments, could be used instead of regression analysis based on least square fitting principles. This would simplify documentation and distribution of future experimental results, and allow for exploitation of already existing experimental data for a parameterized definition of the connection slip behavior.

A parameterized definition of the empirically determined slip behavior as a function of the load-to-grain angle, is expected to support the development of numerical methods for the engineering design and standardization of connections in wood and anisotropic composites in general.

Acknowledgements

The authors gratefully acknowledge the financial support of the Austrian Research Promotion Agency and the wood industry partnership Building with Wood within CEI-Bois for funding the research work within project *MechWood 2*. This work forms part of that project. The *MechWood 2* research partners are thanked for their cooperation and collaboration in this project. The financial support of the COST Action FP1402 to Michael Schweigler by means of a short term scientific mission is thankfully acknowledged as well as fruitful discussions with Jean François Bocquet, Laurent Bléron and Carmen Sandhaas within COST Action FP1402 working group meetings.

Notation

a	coefficient from regression analysis of slip curves
a_0	coefficient from regression analysis of slip curves at $\alpha=0^\circ$
a_{90}	coefficient from regression analysis of slip curves at $\alpha=90^\circ$
a_i	coefficient i from regression analysis of slip curves
a_m	coefficient m from regression analysis of slip curves
$a_{m,\alpha}$	coefficient from regression analysis of slip curves for a specific α (<i>Step01</i>)
a_{min}	minimum value of coefficient a
a_{max}	maximum value of coefficient a

$b_{1,f_{hh,inter}}$	coefficient b_1 from regression analysis of $f_{hh,inter}$ over α
b_{1,k_0}	coefficient b_1 from regression analysis of k_0 over α
b_{1,k_f}	coefficient b_1 from regression analysis of k_f over α
$b_{2,f_{hh,inter}}$	coefficient b_2 from regression analysis of $f_{hh,inter}$ over α
$b_{2,f_{hv,inter}}$	coefficient b_2 from regression analysis of $f_{hv,inter}$ over α
b_{2,k_0}	coefficient b_2 from regression analysis of k_0 over α
b_{2,k_f}	coefficient b_2 from regression analysis of k_f over α
$b_{3,f_{hv,inter}}$	coefficient b_3 from regression analysis of $f_{hv,inter}$ over α
b_{3,k_f}	coefficient b_3 from regression analysis of k_f over α
$b_{m,n}$	coefficient n from regression analysis of a_m over the α (<i>Step02</i>)
d	dowel diameter
$f_{h,inter}$	embedment stress at intersection of the tangent from k_f with the vertical axis
f_{hh}	horizontal embedment stress
$f_{hh,inter}$	horizontal embedment stress at intersection of the tangent from k_f with the vertical axis
$f_{hh,inter,max}$	maximum value of coefficient $f_{hh,inter}$ over α
$f_{hh,inter,min}$	minimum value of coefficient $f_{hh,inter}$ over α
f_{hv}	vertical embedment stress
$f_{hv,inter}$	vertical embedment stress at intersection of the tangent from k_f with the vertical axis
$f_{hv,inter,0}$	coefficient $f_{hv,inter}$ for $\alpha=0^\circ$
$f_{hv,inter,90}$	coefficient $f_{hv,inter}$ for $\alpha=90^\circ$
$f_{h,5mm}$	embedment strength determined at 5 mm dowel displacement
k_0	initial gradient of the slip curve
$k_{0,0}$	coefficient k_0 for $\alpha=0^\circ$
$k_{0,90}$	coefficient k_0 for $\alpha=90^\circ$
$k_{0,min}$	minimum value of coefficient k_0 over α
$k_{0,max}$	maximum value of coefficient k_0 over α
k_f	end gradient of the slip curve
$k_{f,0}$	coefficient k_f for $\alpha=0^\circ$
$k_{f,90}$	coefficient k_f for $\alpha=90^\circ$
$k_{f,min}$	minimum value of coefficient k_f over α
$k_{f,max}$	maximum value of coefficient k_f over α
k_{peak}	gradient at local maximum of the slip curve
K_{elast}^{load}	quasi-elastic loading stiffness
K_{plast}^{load}	elasto-plastic loading stiffness
m	number of coefficients from regression analysis of slip curves
n	number of coefficients from regression analysis of $a_{m,\alpha}$ over α
p	parameter for regression analysis over α (<i>Step02</i>)
u	dowel displacement
u_{ini}^{des}	initial slip for the design of connections
u_{ini}^{exp}	initial slip of experimentally determined slip curve
u_{peak}	x-value at local maximum of the slip curve
u_α	dowel displacement for a specific load-to-grain angle α
y	embedment stress or connection load
y_{inter}	intersection of the tangent from k_f with the vertical axis
y_{max}	y-value at the maximum x-value of the slip curve

y_{peak}	y-value at local maximum of the slip curve
y_{α}	stress or force as function of u_{α} for a specific load-to-grain angle α
α	load-to-grain angle
α_i	load-to-grain angle of slip curve i
Δf_h	absolute deviation between parameterized and experimentally determined slip curve
Δf_{hh}	absolute deviation between parameterized and experimentally determined slip curve
$\Delta f_{hh,inter}$	absolute deviation between input and parameterized parameters of $f_{hh,inter}$
Δf_{hv}	absolute deviation between parameterized and experimentally determined slip curve
$\Delta f_{hv,inter}$	absolute deviation between input and parameterized parameters of $f_{hv,inter}$
Δk_0	absolute deviation between input and parameterized parameters of k_0
Δk_f	absolute deviation between input and parameterized parameters of k_f
Δp	absolute deviation between input and parameterized parameters of p
Δy	absolute deviation between parameterized and experimentally determined slip curve

Engineering modeling of semi-rigid joints for nonlinear analysis of timber structures (Schweigler et al., 2018a)

Authored by Michael Schweigler, Thomas K. Bader & Georg Hochreiner
Submitted to *Engineering Structures*

Abstract: Plastic analysis in engineered structures requires ductility of structural components, which in timber structures is primarily provided by joints made of dowel-type fasteners. A prerequisite for nonlinear analysis is realistic modeling of joint stiffness and load distribution in dowel-type joints. A joint model suitable for structural analysis is presented and validated in this contribution. The semi-analytical joint model is based on kinematic compatibility and equilibrium considerations. It accounts for local fastener slip by means of nonlinear elastic springs. Influences of nonlinearity and orientation dependence of fastener slip are assessed. Elastic deformations of the timber in between dowels are however neglected. The model allows for predicting global joint stiffness, as well as load distribution within the joint, taking explicitly the effect of simultaneously acting internal forces into account. Model validation builds upon an experimental database that spans from embedment testing on the material scale up to joint testing on the structural scale. Application examples demonstrate the broad applicability of the model for structural analysis. Moreover, they illustrate effects of assumptions of fastener slip on the joint and structural behavior. Limitations, as well as pros and cons of these assumptions are discussed. Special attention is drawn to load distribution within the joint, since it is important for fastener-based design, currently prescribed by the European design standard. Load distribution in joints is also important for verification against brittle failure modes. As an alternative to fastener-based design, joint-based design, by means of a framework for applying the presented model to plastic design of timber structures with ductile joints, is proposed.

Keywords: timber engineering, nonlinear structural analysis, anisotropic fastener slip, semi-rigid joints, ductility

5.1 Introduction

Plastic analysis is a well established method for the engineering design of a large number of construction materials and connections, that allow for a ductile behavior of structures. Especially for steel and also for reinforced concrete, plastic design can be applied, e.g., based on the European design standards EN 1993-1-1 (2010) and EN 1992-1-1 (2004), respectively.

General notes on ductility in timber structures, and benefits of a plastic design were given by Jorissen and Fragiacommo (2011). They emphasized that ductility in timber structures is preferably found in joints and formulated four benefits of ductile structures: (i) structural failure is announced by large deformations; (ii) stresses and forces can be redistributed within a cross-section and structure; (iii) ductile joints allow for energy dissipation under seismic loading; and (iv) that structural robustness is increased. Brühl et al. (2011) gave general requirements for ductile connections and a plastic design of joints. A capacity design method was presented, following the idea of determining an over-strength factor to avoid brittle failure of elements before plasticity is achieved. Since timber members usually fail in a brittle manner when loaded in bending or tension, ductility in timber structures is almost exclusively related to ductility in timber joints. Brittle failure in joints can be avoided by an appropriate design including reinforcement techniques (Lathuilière et al., 2015). Design rules and design methods for a kinematically compatible nonlinear plastic design of joints in timber structures are however missing in design standards. Models for the design of dowel joints will be discussed in this contribution, nevertheless the framework of the study and proposed design rules will also be valid for other types of dowel-type joints.

Plasticity is partly implicitly taken into account in the European design standard for timber structures EN 1995-1-1 (2004) (EC 5). Design equations for single-fastener connections are based on a limit state approach (Johansen, 1949), making use of a plastic embedment strength and a plastic yield moment of steel fasteners. However, only elastic stiffness of single-fastener connections is provided by means of an empirical equation, which in addition is independent of the load orientation even for large diameter dowels. Design equations for multiple-fastener joints are missing and general design rules are given only. Thus, EC 5 is primarily directed towards the behavior of single-dowels, or more generally, single-fasteners. Previous studies showed that using EC 5 equations, might lead to a strongly simplified linear elastic-ideal plastic slip curve of joints and to an underestimation of displacements at the ultimate limit state (Bader et al., 2016d,b).

Not only the global joint slip, but also load distribution among dowels in joints is essential for verification against brittle failure modes and design of reinforcement measurements, respectively. Previous studies highlighted loading direction dependence in dowel connections and elastic deformations of the timber matrix in dowel groups as main effects on load distribution, and thus, also on global joint slip (Bader et al., 2017; Jorissen, 1998). Moreover, deviation between displacement and force orientation, as a peculiarity of anisotropic materials such as timber (Bader et al., 2016d; Schweigler et al., 2017), might effect load distribution.

In order to be able to incorporate ductile joint behavior in structural analysis and engineering design, a trade-off between accuracy and calculation effort of a joint model has to be found. Previously proposed calculation models for joints have been reviewed and compared in Bader et al. (2017). The interaction of internal forces, namely axial force, transverse force and bending moment, under two-dimensional loading situations, has been emphasized. The terms *axial force* and *transverse force*, are equal to the commonly used expressions *normal force* and *shear force* in beam theory, respectively. As regards practical design, two-dimensional FEM models (Bader et al., 2017) of joints, or even a combination of beam-on-foundation model

for single-dowel connections (Bader et al., 2016d; Hirai, 1983; Hochreiner et al., 2013) and a three-dimensional discretization of the timber, might be desired since these models allow to consider effects of the deformable timber between fasteners and non-uniform stresses over the timber thickness (Jorissen, 1998; Blaß, 1995). However, computational efforts are too high for integration in structural analysis for engineering design. Strongly simplified linear and analytical models (Racher, 1995) on the contrary, fail in a realistic description of load distribution, especially when considering interaction of internal forces. This might lead to underestimation of dowel loads.

An attractive alternative related to the accuracy-calculation time trade-off, are semi-analytical joint models based on kinematic and equilibrium considerations with the assumption of rigid members and nonlinear springs for dowel slip. The only drawback of these assumptions is that non-uniform stresses over the timber thickness and elastic deformations of the timber matrix are neglected. The latter is most pronounced in the quasi-elastic loading path and for loading perpendicular to the grain (Bader et al., 2017). Corresponding models with rigid members and springs have been presented by Descamps et al. (2011) and by Jensen (1994). Jensen focused on nailed-connections and provided models for both, uncoupled and coupled description of the joint behavior, i.e., taking into account interaction of internal forces. Coupling in connection models was investigated by Vessby et al. (2010) as well. Model derivation in Jensen (1994) was either based on the joint or fastener slip, and even included elements for end-grain contact situations. In addition, concepts for implementation in structural analysis using the finite element method (FEM) were proposed and applied to calculation examples. This modeling strategy will be taken up herein, with the aim of validation and application to engineering design situations. It is expected to highlight possibilities for enhanced insight into load distribution and joint slip, including coupling of internal forces and inhomogeneous joints. Emphasis will be placed on the study of linear and nonlinear single-dowel slip models and their effect on the global joint and structural behavior. This will form the basis for joint-based nonlinear analysis of timber structures with ductile joints. To demonstrate model capabilities when integrated in structural analysis and to propose a framework for design rules are further objectives of this contribution. Herein, modeling is limited to monotonic behavior of joints subjected to in-plane loading, namely axial force, transverse force and in-plane bending moment.

The paper is organized as follows: Calculation steps of the joint model and its specialization for different dowel slip models are described in Section 5.2. In Section 5.3, the model is validated by means of comparing simulated an experimentally determined joint slip curves. Application of the model to joint design examples is investigated in Section 5.4, before strategies for model implementation in the structural analysis and example calculations are reported in Section 5.5. Finally, in Section 5.6, proposals for a joint-based design with nonlinear analysis of timber structures are presented and the paper is concluded in Section 5.7.

5.2 Joint modeling approach

5.2.1 Modeling strategy and assumptions

Starting with joint modeling from a structural engineering point of view, the relationship between relative deformations, $\Delta \mathbf{u}$, and internal forces, \mathbf{R} , can be expressed as

$$\mathbf{R} = \mathbf{K} \cdot \Delta \mathbf{u}, \quad (5.1)$$

by defining the stiffness matrix \mathbf{K} . In general, relative deformations encompass six degrees of freedom, with three relative translations and three relative rotations. The following derivation is limited to in-plane loading situations. Thus, the constitutive equation includes three relative deformations (relative axial displacement, Δu_x , relative transverse displacement, Δw_z , and relative rotation around y-axis, $\Delta \varphi_y$) and three associated internal forces (axial force, N_x , transverse force, V_z , and in-plane bending moment, M_y), and reads as (see Figure 5.1)

$$\begin{bmatrix} N_x \\ V_z \\ M_y \end{bmatrix} = \begin{bmatrix} K_{xx} & K_{xz} & K_{xy} \\ K_{zx} & K_{zz} & K_{zy} \\ K_{yx} & K_{yz} & K_{yy} \end{bmatrix} \cdot \begin{bmatrix} \Delta u_x \\ \Delta w_z \\ \Delta \varphi_y \end{bmatrix}, \quad (5.2)$$

with coefficients K_{ij} ($i, j=x, z, y$) of the stiffness matrix. In the following, components of the joint stiffness matrix will be determined based on number of dowels in a joint and their spatial distribution, taking into account their load-slip behavior.

Diagonal coefficients of the stiffness matrix \mathbf{K} , namely K_{ii} ($i=x, z, y$), describe the relationship between a relative deformation and the associated internal force component at the joint level. Loading at the *center of joint stiffness* is a necessary but not sufficient prerequisite for an uncoupled joint behavior, which is characterized by diagonal elements of \mathbf{K} being the only non-zero elements. Non-diagonal components of the stiffness matrix in Eq. (5.2), describe coupled behavior of the joint, i.e., coupling of relative displacements with the bending moment or relative rotation with axial or transverse force.

In the general case of an arbitrary joint layout with orientation dependent and nonlinear dowel slip, it is difficult to choose the reference point for loading being equal to the *center of joint stiffness*, since the center of joint stiffness is a function of the single-dowel connection stiffness, and might change during loading. Thus, internal forces become a function of all relative deformations at the joint, i.e., Δu_x , Δw_z and $\Delta \varphi_y$. Coupling of internal forces and relative deformations is also a consequence of interaction of internal forces and their effect on load distribution within the joint. Thus, coupling of internal forces affects diagonal and non-diagonal components of the stiffness matrix, \mathbf{K} . In addition, non-diagonal components might be *unsymmetric* with respect to the diagonal of \mathbf{K} , as a reason of (i) interaction between internal forces; (ii) anisotropic nonlinear dowel slip; as well as of (iii) loading at a reference point different from the *center of joint stiffness*.

The joint model, presented herein, rests on kinematic compatibility and equilibrium of forces, and is based on the following *assumptions*:

- Timber is assumed to be rigid, which means that elastic deformations of wood between single dowels are neglected.
- Steel plates are assumed to be rigid, which implies that the position of the single dowels does not change during loading. Thus, dowel displacements can be directly related to relative joint deformations. The same can be assumed for timber-to-timber joints, which is a stronger simplification, since timber exhibits a comparable soft and anisotropic material behavior that might lead to changes in position between single dowels during loading.
- The displacement directions of single dowels, $\hat{\alpha}_i$, are assumed to be constant during a load increment, and thus, are equal to the secant displacement direction calculated from deformed to undeformed dowel position.

- Orientations of dowel forces, $\bar{\alpha}_i$, are assumed to be equal to displacement directions of the dowels, $\hat{\alpha}_i$, which is a simplification for constrained loading situations (Bader et al., 2016d).
- It is assumed that the slip behavior of dowels is not affected by adjacent dowels, i.e., dowels do not influence each other.
- Nonlinear (or linear) elastic dowel slip is assumed, i.e., unloading follows the loading path. Consequently, for nonlinear elastic dowel slip, joint forces are path independent, while the work carried out by the joint is path dependent.

5.2.2 Calculation procedure

In the following, derivation of the joint behavior as a consequence of the number of dowels, geometry of the joint and dowel slip, is described. The calculation is performed in five steps, which are illustrated by means of a flow chart in Figure 5.1.

Step01: Model input

Joint geometry, including the number of dowels and their position, together with definition of the dowel slip, is required. The right-handed rectangular coordinate system follows the orientations of the connected members, with x parallel to the beam axis and y - z defining the cross-sectional plane (see Fig. 5.1). The grain orientation in timber might deviate to the beam axis by an angle β .

In the first step, a set of relative deformations at an arbitrary point of the joint, subsequently called *reference point*, is prescribed. It includes a relative displacement in axial direction, Δu_x , a relative displacement in transverse direction, Δw_z , and a relative rotation around the out-of-plane axis, $\Delta \varphi_y$. Advantageous is definition of the *reference point* at the beam axis, perpendicular to the geometrical center of the joint. In many design situations, this is a point close to the *center of joint stiffness*, and thus keeps the dominance of possibly unsymmetric non-diagonal elements of \mathbf{K} to a minimum.

Step02: Dowel displacement and displacement-to-grain angle

As a consequence of the assumption of rigid timber and steel matrix, each dowel i experiences the same axial, μ_i , and transverse displacement, ω_i , as a result of relative joint displacements Δu_x and Δw_z . Thus, μ_i and ω_i are given by

$$\mu_i = \Delta u_x, \quad \text{and} \quad \omega_i = \Delta w_z. \quad (5.3)$$

Size and direction of the dowel displacement, caused by a relative rotation, $\Delta \varphi_y$, of the joint around a reference point is linearly related to the distance of the dowels to that point. Direction of the displacement is assumed to be perpendicular to the line connecting dowel i and the reference point (r_i in Figure 5.1). A linearization of the circular displacement path is considered herein. Displacement components parallel, $\delta_{\varphi,i,x}$, and transverse to the beam axis, $\delta_{\varphi,i,z}$, consequently read as

$$\delta_{\varphi,i,x} = \tan(\Delta \varphi_y) \cdot z_i, \quad (5.4)$$

$$\delta_{\varphi,i,z} = \tan(\Delta \varphi_y) \cdot x_i, \quad (5.5)$$

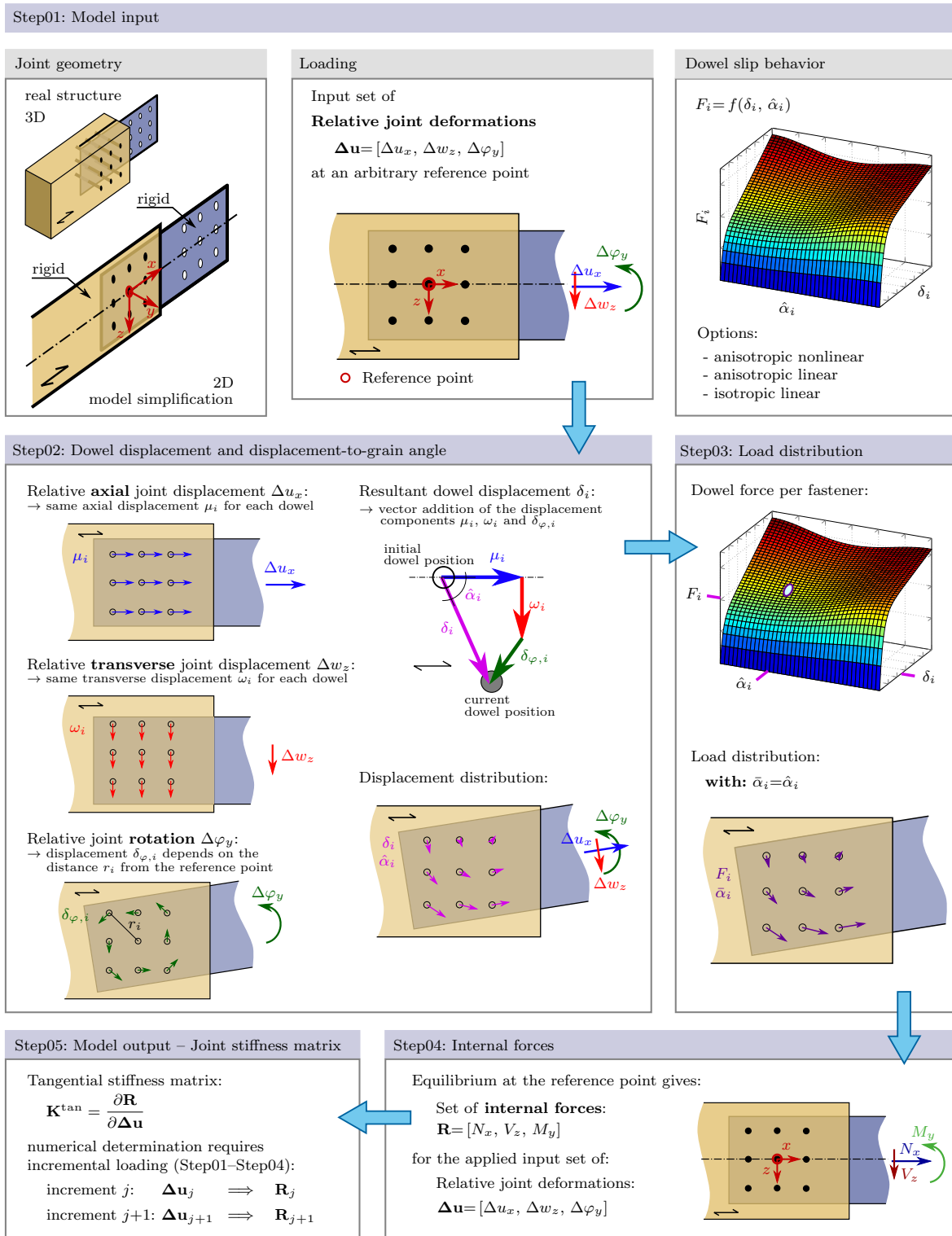


Figure 5.1: Flow chart – Joint model – Calculation procedure.

where the parameters x_i and z_i refer to the axial and transverse coordinates of dowel i . A further simplification could be done by replacing $\tan(\Delta\varphi_y)$ by $\Delta\varphi_y$ in radians, which is true for small $\Delta\varphi_y$.

Resultant dowel displacement components parallel, $\delta_{i,x}$, and transverse to the beam axis, $\delta_{i,z}$, are then determined as follows

$$\delta_{i,x} = \mu_i + \delta_{\varphi,i,x}, \quad (5.6)$$

$$\delta_{i,z} = \omega_i - \delta_{\varphi,i,z}. \quad (5.7)$$

Finally, resultant dowel displacement, δ_i , is calculated by

$$\delta_i = \sqrt{\delta_{i,x}^2 + \delta_{i,z}^2}, \quad (5.8)$$

and the displacement-to-grain angle, $\hat{\alpha}_i$, of dowel i is determined by

$$\hat{\alpha}_i = \arctan\left(\frac{\delta_{i,z}}{\delta_{i,x}}\right) + \beta, \quad (5.9)$$

with β as the angle between the beam axis, x , and the grain direction. β is defined positive in the positive rotational direction of the y -axis.

Step03: Load distribution

Having at hand the size, δ_i , and orientation with respect to the grain, $\hat{\alpha}_i$, of the dowel displacement, the loading of the single dowels can be calculated. Therefore, δ_i and $\hat{\alpha}_i$ are taken as input to predefined dowel slip curves. Herein, a parameterized definition of the single-dowel connection behavior, i.e., an analytic function for F_i is used, reading as

$$F_i = f(\delta_i, \hat{\alpha}_i). \quad (5.10)$$

A deviation of the load and displacement orientation, as a consequence of constrained displacement loading (Bader et al., 2016d; Schweigler et al., 2018a), could be considered in this relationship. In the following, we however assume $\bar{\alpha}_i$ to be equal to $\hat{\alpha}_i$. The dowel force components $F_{i,x}$ and $F_{i,z}$ can then be determined as

$$F_{i,x} = F_i \cdot |\cos(\bar{\alpha}_i)| \cdot \frac{\delta_{i,x}}{|\delta_{i,x}|}, \quad (5.11)$$

$$F_{i,z} = F_i \cdot |\sin(\bar{\alpha}_i)| \cdot \frac{\delta_{i,z}}{|\delta_{i,z}|}. \quad (5.12)$$

Ratios of the dowel displacement components with respect to their absolute value are used to assign the correct force component orientation.

Step04: Internal forces

Finally, internal forces (N_x , V_z , M_y) are determined by applying equilibrium of forces at the reference point, yielding

$$N_x = \sum_{i=1}^n F_{i,x}, \quad V_z = \sum_{i=1}^n F_{i,z}, \quad (5.13)$$

$$M_y = \sum_{i=1}^n F_{i,x} \cdot z_i - \sum_{i=1}^n F_{i,z} \cdot x_i, \quad (5.14)$$

with n as the number of dowels in the joint. By this calculation step, we established a relationship between the set of relative joint deformations $(\Delta u_x, \Delta w_z, \Delta \varphi_y)$ and the internal forces (N_x, V_z, M_y) .

Step05: Model output – Joint stiffness matrix

The joint stiffness matrix \mathbf{K} acc. to Eq. (5.2) can be expressed as tangential stiffness matrix \mathbf{K}^{tan} , reading as

$$\mathbf{K}^{\text{tan}} = \frac{\partial \mathbf{R}}{\partial \Delta \mathbf{u}} = \frac{\partial (N_x, V_z, M_y)}{\partial (\Delta u_x, \Delta w_z, \Delta \varphi_y)} = \begin{bmatrix} \frac{\partial N_x}{\partial \Delta u_x} & \frac{\partial N_x}{\partial \Delta w_z} & \frac{\partial N_x}{\partial \Delta \varphi_y} \\ \frac{\partial V_z}{\partial \Delta u_x} & \frac{\partial V_z}{\partial \Delta w_z} & \frac{\partial V_z}{\partial \Delta \varphi_y} \\ \frac{\partial M_y}{\partial \Delta u_x} & \frac{\partial M_y}{\partial \Delta w_z} & \frac{\partial M_y}{\partial \Delta \varphi_y} \end{bmatrix}, \quad (5.15)$$

using a numerical differentiation, \mathbf{K}^{tan} is determined by

$$\mathbf{K}^{\text{tan}} = \begin{bmatrix} \frac{N_{x,j+1} - N_{x,j}}{\Delta u_{x,j+1} - \Delta u_{x,j}} & \frac{N_{x,j+1} - N_{x,j}}{\Delta w_{z,j+1} - \Delta w_{z,j}} & \frac{N_{x,j+1} - N_{x,j}}{\Delta \varphi_{y,j+1} - \Delta \varphi_{y,j}} \\ \frac{V_{z,j+1} - V_{z,j}}{\Delta u_{x,j+1} - \Delta u_{x,j}} & \frac{V_{z,j+1} - V_{z,j}}{\Delta w_{z,j+1} - \Delta w_{z,j}} & \frac{V_{z,j+1} - N_{x,j}}{\Delta \varphi_{y,j+1} - \Delta \varphi_{y,j}} \\ \frac{M_{y,j+1} - M_{y,j}}{\Delta u_{x,j+1} - \Delta u_{x,j}} & \frac{M_{y,j+1} - M_{y,j}}{\Delta w_{z,j+1} - \Delta w_{z,j}} & \frac{M_{y,j+1} - M_{y,j}}{\Delta \varphi_{y,j+1} - \Delta \varphi_{y,j}} \end{bmatrix}. \quad (5.16)$$

Thus, for numerical determination of \mathbf{K}^{tan} , *incremental loading* is necessary, which means that *Step01–Step04* of the above presented calculation procedure are repeated j -times, with j as the number of increments. At the beginning of each incremental loading procedure an initial set of relative joint deformations, $\Delta \mathbf{u}_{j,in}$, has to be chosen, reading as

$$\Delta \mathbf{u}_j = \Delta \mathbf{u}_{j,in} = [\Delta u_x, \Delta w_z, \Delta \varphi_y]. \quad (5.17)$$

Its application to Eqs. (5.3)–(5.14) yields an initial set of internal forces

$$\mathbf{R}_j = [N_{x,j}, V_{z,j}, M_{y,j}]. \quad (5.18)$$

Incremental change, $d\Delta \mathbf{u}$, of the relative joint deformations, $\Delta \mathbf{u}_j$, gives a new set of relative joint deformations, reading as

$$\Delta \mathbf{u}_{j+1} = \Delta \mathbf{u}_j + d\Delta \mathbf{u}, \quad (5.19)$$

with

$$d\Delta \mathbf{u} = [d\Delta u_x, d\Delta w_z, d\Delta \varphi_y]. \quad (5.20)$$

Using $\Delta \mathbf{u}_{j+1}$ in Eqs. (5.3)–(5.14), yields

$$\mathbf{R}_{j+1} = [N_{x,j+1}, V_{z,j+1}, M_{y,j+1}]. \quad (5.21)$$

5.2.3 Material models for single-dowel connection and joint behavior

Load-deformation behavior of dowels is an essential input to the joint model and governs the global response. Assumptions applied herein will be discussed next, starting with an anisotropic, i.e., orientation dependent, nonlinear elastic formulation. Joint modeling could be simplified by assuming linear elastic slip curves of dowels, with or without an orientation dependence. This finally yields analytic equations for the load distribution and joint stiffness (Racher, 1995), which are derived based on the model description in the following.

5.2.3.1 Anisotropic nonlinear elastic joint model

The anisotropic nonlinear elastic joint model requires information of the dowel force, F_i , as a function of the displacement-to-grain angle, $\hat{\alpha}_i$, and dowel displacement, δ_i . Thus, for determination of F_i , the analytic definition given in Eq. (5.10) is used (Schweigler et al., 2018a). Alternatively, F_i could be defined pointwise for specific δ_i and $\hat{\alpha}_i$. However, analytic definition of the dowel slip is highly recommended since it substantially speeds up the calculation process. Parameterized dowel slip behavior can be based on results from single-dowel connection experiments or numerical simulations. For the latter beam-on-foundation models as presented in Bader et al. (2016d); Hirai (1983); Hochreiner et al. (2013) might be used.

In calculations presented herein, a parameterized dowel slip based on numerical results from beam-on-nonlinear elastic foundation modeling is exploited. In order to end up with a parameterized equation for F_i the stepwise procedure proposed in Schweigler et al. (2018a) is used. The exponential regression function proposed by Foschi (1974) is applied to single-dowel connection slip curves, and reads as

$$F_i(\delta_i) = (F_{inter}^{non} + k_f^{non} \cdot \delta_i) \left[1 - e^{-\frac{k_{ini}^{non} \cdot \delta_i}{F_{inter}^{non}}} \right]. \quad (5.22)$$

The coefficient k_{ini}^{non} describes the initial gradient and k_f^{non} the end gradient of the slip curve. The tangent of the initial gradient, k_{ini}^{non} , evolves from the origin, while the position of k_f^{non} is defined by the coefficient F_{inter}^{non} , which describes the intersection of k_f^{non} with the vertical axis. In addition, a regression function is applied to each of these three coefficients, namely k_{ini}^{non} , k_f^{non} and F_{inter}^{non} , to give a regression between the coefficients and the displacement-to-grain angle $\hat{\alpha}_i$. For this purpose, the so-called *Hankinson formular* (Hankinson, 1921) is used, which reads as

$$F_{inter}^{non}(\hat{\alpha}_i) = \frac{F_{inter,0}^{non} \cdot F_{inter,90}^{non}}{F_{inter,0}^{non} \sin^2(\hat{\alpha}_i) + F_{inter,90}^{non} \cos^2(\hat{\alpha}_i)}, \quad (5.23)$$

$$k_f^{non}(\hat{\alpha}_i) = \frac{k_{f,0}^{non} \cdot k_{f,90}^{non}}{k_{f,0}^{non} \sin^2(\hat{\alpha}_i) + k_{f,90}^{non} \cos^2(\hat{\alpha}_i)}, \quad (5.24)$$

$$k_{ini}^{non}(\hat{\alpha}_i) = \frac{k_{ini,0}^{non} \cdot k_{ini,90}^{non}}{k_{ini,0}^{non} \sin^2(\hat{\alpha}_i) + k_{ini,90}^{non} \cos^2(\hat{\alpha}_i)}, \quad (5.25)$$

with $F_{inter,0}^{non}$, $k_{f,0}^{non}$, $k_{ini,0}^{non}$ and $F_{inter,90}^{non}$, $k_{f,90}^{non}$, $k_{ini,90}^{non}$ as the parameters parallel (0) and perpendicular (90) to the grain, respectively. Finally, Eqs. (5.23)–(5.25) are inserted into Eq. (5.22). Thus, single-dowel connection load, F_i , is calculated based on six parameters, namely $F_{inter,0}^{non}$, $k_{f,0}^{non}$, $k_{ini,0}^{non}$ and $F_{inter,90}^{non}$, $k_{f,90}^{non}$, $k_{ini,90}^{non}$, and reads as

$$F_i = f(\delta_i, \hat{\alpha}_i, F_{inter,0}^{non}, k_{f,0}^{non}, k_{ini,0}^{non}, F_{inter,90}^{non}, k_{f,90}^{non}, k_{ini,90}^{non}). \quad (5.26)$$

Joint stiffness matrix

Internal forces, as a consequence of relative deformations of a joint, can be calculated using Eqs. (5.3)–(5.14). This gives access to a tangential stiffness matrix according to Eq. (5.16).

Load distribution

Calculating load distribution in a multiple-dowel joint for a given set of *internal forces*, however, requires an iterative calculation procedure, which is described in the following.

In a first step, three uncoupled slip curves for the joint, namely the relations between $N_x - \Delta u_x$, $V_z - \Delta w_z$, and $M_y - \Delta \varphi_y$ are determined, using Eqs. (5.3)–(5.14). For this purpose, the incremental procedure described by Eqs. (5.17)–(5.21) is applied, in order to account for the nonlinearity in dowel slip. In a second step, these three uncoupled, nonlinear slip curves of the internal forces are applied to calculate in a *trial step*, associated relative joint deformations for the given set of internal forces. Deformations can then be used to calculate internal forces by using Eqs. (5.3)–(5.14). Due to coupling between the internal forces, estimated forces will however be unequal to the prescribed forces, under non-uniform loading situations. Thus, an iteration procedure, by means of the *Newton-Raphson method*, is applied, with a stepwise correction of the relative deformation of the joint. Having at hand relative deformations of the joint, displacements of the dowels can be calculated using Eqs. (5.3)–(5.9), and the corresponding load distribution by using Eqs. (5.10)–(5.12).

5.2.3.2 Anisotropic linear elastic joint model

Simplification by assuming linear elastic single-dowel connection slip, naturally reduces modeling efforts.

Single-dowel stiffness, $k_{\hat{\alpha},i}^{ani}$, between the principal material directions, i.e., parallel and perpendicular to the grain, is calculated by using the approach of *Hankinson*, as defined in Eq. (5.24) or (5.25). Thus, the orientation dependent linear elastic single-dowel connection stiffness reads as

$$k_{\hat{\alpha},i}^{ani}(\hat{\alpha}_i) = \frac{k_0^{ani} \cdot k_{90}^{ani}}{k_0^{ani} \sin(\hat{\alpha}_i)^2 + k_{90}^{ani} \cos(\hat{\alpha}_i)^2}, \quad (5.27)$$

with k_0^{ani} and k_{90}^{ani} as the quasi-elastic stiffness parallel and perpendicular to the grain. Those are determined as secant stiffness between the points at the slip curve acc. to Eq. (5.22), defined by the dowel force at 10% and 40% of the bearing capacity of the single-dowel connection, $F_{i,limit}$. $F_{i,limit}$ is calculated as the force at δ_i equal to 15 mm. Definition of $F_{i,limit}$ as well as the position of the points for stiffness determination follow the recommendations of the testing standard for single-fastener connections EN 26 891 (1991). Thus, the nonlinear slip reduces to an anisotropic linear slip.

Joint stiffness matrix

The tangential stiffness matrix of the joint is calculated according to Eq. (5.16). For anisotropic linear elastic dowel slip, the *calculation procedure* given by Eqs. (5.3)–(5.14) simplifies. Thus, dowel force components $F_{i,x}^{ani}$ and $F_{i,z}^{ani}$ can directly be calculated from the dowel displacement components and thus Eqs. (5.11)–(5.12) reduce to

$$F_{i,x}^{ani} = k_{\hat{\alpha},i}^{ani} \cdot \delta_{i,x}, \quad (5.28)$$

$$F_{i,z}^{ani} = k_{\hat{\alpha},i}^{ani} \cdot \delta_{i,z}, \quad (5.29)$$

with the anisotropic linear single-dowel connection stiffness, $k_{\hat{\alpha},i}^{ani}$, according to Eq. (5.27).

Alternatively to incremental determination, *diagonal elements* of the joint stiffness matrix, \mathbf{K} , can be calculated analytically. For loading by axial and transverse force, the stiffness component $K_{N_x}^{ani}$ and $K_{V_z}^{ani}$ are equal to K_{xx} and K_{zz} in Eq. (5.2), respectively, reading as

$$K_{N_x}^{ani} = \sum_{i=1}^n k_{\hat{\alpha},i}^{ani} \quad \text{with} \quad \hat{\alpha} = 0^\circ + \beta, \quad (5.30)$$

$$K_{V_z}^{ani} = \sum_{i=1}^n k_{\hat{\alpha},i}^{ani} \quad \text{with} \quad \hat{\alpha} = 90^\circ - \beta. \quad (5.31)$$

The rotational joint stiffness $K_{M_y}^{ani}$, which is equal to K_{yy} in Eq. (5.2) is calculated as

$$K_{M_y}^{ani} = \sum_{i=1}^n k_{\hat{\alpha},i}^{ani} \cdot r_i^2, \quad (5.32)$$

with r_i as the distance of the dowel to the center of rotation. For determination of $K_{M_y}^{ani}$ the reference point has to be chosen equal to the center of rotation of the joint. However, coupling between the diagonal elements of \mathbf{K} , as it is the case for loading by a combination of N_x and/or V_z with M_y , is not accounted for in the above-mentioned equations.

Load distribution

Load distribution in the joint, based on a set of *internal forces*, can be determined analytically. Dowel force components parallel to the beam axis $F_{M_y,i,x}^{ani}$, and transverse to the beam axis $F_{M_y,i,z}^{ani}$ due to an in-plane bending moment M_y are then given by

$$F_{M_y,i,x}^{ani} = \frac{k_{\hat{\alpha},i}^{ani} \cdot M_y}{K_{M_y}^{ani}} \cdot z_i, \quad (5.33)$$

$$F_{M_y,i,z}^{ani} = \frac{k_{\hat{\alpha},i}^{ani} \cdot M_y}{K_{M_y}^{ani}} \cdot x_i. \quad (5.34)$$

In the case of loading by an axial force, N_x , and/or transverse force, V_z , the internal forces are distributed uniformly over the single dowels of the joint. Thus, the force components $F_{N_x,i}^{ani}$ and $F_{V_z,i}^{ani}$ read as

$$F_{N_x,i}^{ani} = \frac{N_x}{n}, \quad F_{V_z,i}^{ani} = \frac{V_z}{n}. \quad (5.35)$$

For a combination of N_x and/or V_z with M_y , an iterative procedure, as described for the anisotropic nonlinear elastic joint model in Subsection 5.2.3.1, would be required. Neglecting the interaction, caused by combined loading including M_y , the resultant force of dowel i could be calculated by vectorial summation of the load components given by Eqs. (5.33)–(5.35), yielding

$$F_i^{ani} = \sqrt{\left(F_{M_y,i,x}^{ani} + F_{N_x,i}^{ani}\right)^2 + \left(F_{M_y,i,z}^{ani} + F_{V_z,i}^{ani}\right)^2}. \quad (5.36)$$

5.2.3.3 Isotropic linear elastic joint model

Further simplification of the dowel slip behavior, by means of a loading direction independent single-dowel connection stiffness k_i^{iso} , leads to an isotropic linear elastic joint modeling approach. As a consequence of the isotropic linear dowel stiffness, an uncoupled joint behavior is given. Herein, we determine the isotropic single-dowel connection stiffness k_i^{iso} by

$$k_i^{iso} = \frac{k_0^{ani} + k_{90}^{ani}}{2}, \quad (5.37)$$

with k_0^{ani} and k_{90}^{ani} according to Subsection 5.2.3.2. Thus, the nonlinear slip curve reduces to a single linear slip curve.

Joint stiffness matrix

Stiffness matrix components are independent from applied loading, when assuming isotropic linear dowel slip. Thus, tangential stiffness matrix is equivalent to secant stiffness matrix. The *calculation procedure* given by Eqs. (5.3)–(5.14) simplifies and, dowel force components $F_{i,x}^{iso}$ and $F_{i,z}^{iso}$ are calculated directly from the dowel displacement components. Thus, Eqs. (5.11)–(5.12) reduce to

$$F_{i,x}^{iso} = k_i^{iso} \cdot \delta_{i,x}, \quad (5.38)$$

$$F_{i,z}^{iso} = k_i^{iso} \cdot \delta_{i,z}, \quad (5.39)$$

with k_i^{iso} according to Eq. (5.37).

Alternatively, *diagonal elements* of the joint stiffness matrix \mathbf{K} can be calculated as follows. Axial and transverse stiffness components, K_{Nx}^{iso} and K_{Vz}^{iso} , referring to K_{xx} and K_{zz} in Eq. (5.2), respectively, are of equal size and are given by

$$K_{Nx}^{iso} = K_{Vz}^{iso} = \sum_{i=1}^n k_i^{iso}. \quad (5.40)$$

The rotational joint stiffness K_{My}^{iso} , which is equal to K_{yy} in Eq. (5.2), is calculated as

$$K_{My}^{iso} = k_i^{iso} \cdot I_p, \quad (5.41)$$

with I_p as the so-called polar moment of inertia, defined as the sum of squares of polar radii r_i , which are the radial distances of each dowel to the center of rotation. For determination of K_{My}^{iso} the reference point has to be chosen equal to the center of rotation of the joint.

Load distribution

Load distribution in the joint, based on a set of internal forces, can be determined analytically. Force components $F_{x,i}^{iso}$ and $F_{z,i}^{iso}$ of a single dowel due to a combination of in-plane bending moment, axial force and transverse force, are calculated as (Racher, 1995)

$$F_{x,i}^{iso} = \frac{M_y}{I_P} \cdot z_i + \frac{N_x}{n}, \quad (5.42)$$

$$F_{z,i}^{iso} = \frac{M_y}{I_P} \cdot x_i - \frac{V_z}{n}. \quad (5.43)$$

The parameters x_i and z_i are the axial and transverse distance of the dowel to the center of rotation, respectively. Thus, the size of the dowel force components and consequently dowel forces F_i^{iso} depends only on the position of the dowel with respect to the center of rotation. The resultant force of dowel i is then calculated by vectorial summation of the load components $F_{x,i}^{iso}$ and $F_{z,i}^{iso}$.

5.2.3.4 Other types of fastener behavior including contact

Slip curves discussed in the previous subsections are typical for laterally loaded dowel-type fasteners. Their behavior can be different within a joint, e.g., when combining dowels with different diameters. This is even more important when combining different types of fasteners within a joint, in order to fulfill compatibility requirements. Another type of kinematic constrained in a joint might be given by contact situations, which can be evoked as a consequence of a relative translation or a relative rotation. The possible contact area can be discretized by contact elements with a corresponding (nonlinear) slip behavior. Similar to dowel-type fasteners, a quasi-elastic loading path as well as a yield plateau, with or without displacement hardening, could be determined for timber-to-timber, or timber-to-steel contact situations that cause compressive stresses parallel or perpendicular to the grain in timber, respectively. A bi-linear slip curve could be a suitable simplification of the nonlinear behavior, with the yield limit, F_i^{con} , reading as

$$F_i^{con} = A_{con,i} \cdot f_{c,y,timber}, \quad (5.44)$$

with the compressive strength of timber, $f_{c,y,timber}$, and the contact area, $A_{con,i}$ of the contact element i . The model allows taking into account variations in the contact area as well as in the compressive strength over the height of the cross-section.

Incremental changes of an initial relative joint deformation state gives access to the stiffness of the joint with a contact situation according to Eq. (5.16). Thus, the model gives also access to load distribution, including contact forces, which allows calculating contact stresses.

5.3 Joint model validation

5.3.1 Single-dowel connection slip for validation

Before applying the engineering joint model to design situations, a comparison of model predictions with experimental observations is performed for validating the suitability of the model. Input data for model validation are illustrated in Fig. 5.2. Experimental investigations of laminated veneer lumber (LVL)-to-steel single-dowel and multiple-dowel joints have been presented in Bader et al. (2016d); Schweigler et al. (2017); Bader et al. (2015). Using the same materials (LVL with parallel veneer layers), as well as double shear connection with a slotted-in steel plate, throughout experiments allowed to build up a consistent database from material properties to joint behavior, which will be exploited in numerical simulations in the following.

Load-relative displacement behavior of the LVL-to-steel single-dowel connection is a crucial input to the joint model. Thus, its derivation will be discussed first. Model validation will be limited to 12 mm steel dowel connections and slip curves have been derived by means of a beam-on-nonlinear foundation model, similar to the approach presented in Bader et al. (2016d); Hochreiner et al. (2013), using the finite element software ABAQUS, with a geometrically nonlinear calculation. Material properties of LVL, by means of the embedment

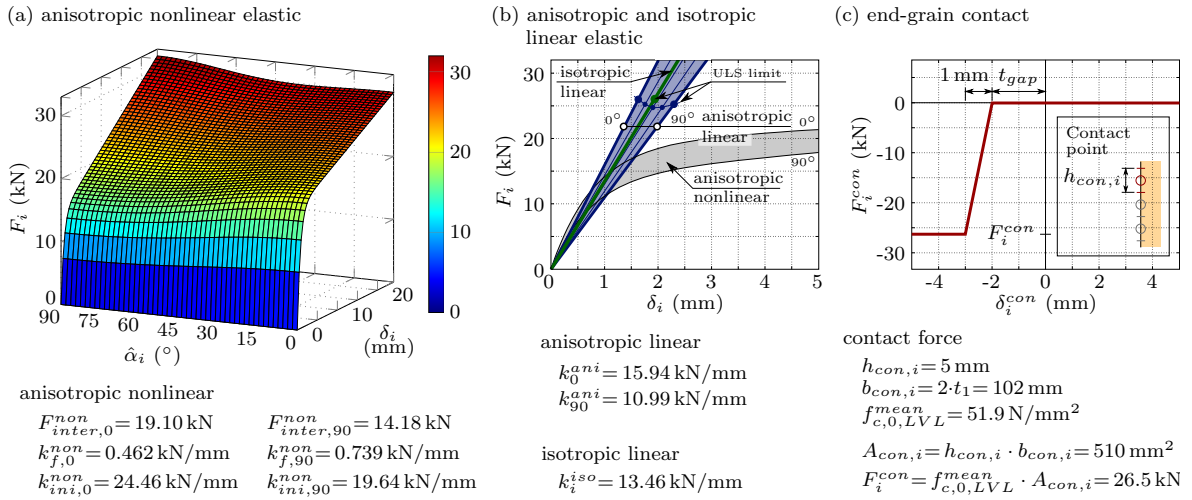


Figure 5.2: Single-dowel connection and contact slip curves for validation and application examples ($d=12 \text{ mm}$): (a) anisotropic nonlinear elastic slip, (b) anisotropic and isotropic linear elastic slip, and (c) end-grain contact slip.

behavior, were reported in Schweigler et al. (2016a). Regression analysis with parameterized Eqs. (5.22)–(5.26) was applied on the experimentally determined embedment slip. Steel dowel properties were given in Bader et al. (2016d). Additionally, an axial resistance between LVL and steel was considered by a penalty friction model, applying a friction coefficient of 0.3. This assumption is well in line with wood-to-steel friction coefficients reported in McKenzie and Karpovich (1968). Regression analysis has been performed on calculation results from the beam-on-nonlinear foundation model, using parameterized Eqs. (5.22)–(5.26). Corresponding parameters for the dowel slip are given in Fig. 5.2a. Single-dowel connection slip predicted by this model are slightly stiffer compared to a previous model presented in Bader et al. (2016d), where frictional effects were neglected, but still corresponds well to experimental data presented in Bader et al. (2016b).

In addition to nonlinear dowel slip (Fig. 5.2a), anisotropic and isotropic linear elastic slip (Fig. 5.2b) were used as well. These linear models were determined as described in Eq. (5.27), and Eq. (5.37), respectively. The corresponding slip curves and stiffness parameters are given in Fig. 5.2b.

5.3.2 Dowel joint under moment loading

The joint model is validated by two different dowel groups loaded by a pure bending moment (Bader et al., 2015). Joint experiments were carried out as 4-point bending tests with a symmetric dowel group at midspan of the test setup. Two different joint layouts, i.e., squared and circular arrangement of 9 dowels with 12 mm in diameter were tested (Bader et al., 2015). This combination of test set-up and joint layout allowed for a direct relation of the measured loading, and subsequently calculated bending moment, with the measured relative rotation at the joint. The loading situation of pure bending moment, and pure relative rotation at the joint was proven by the fact of the center of rotation being equal to the geometrical center of the joint over the entire loading procedure. Further details on the joint experiments can be taken from Bader et al. (2015).

For simulation of the joint slip behavior, namely the $M_y - \Delta\varphi_y$ relationship, the incremental

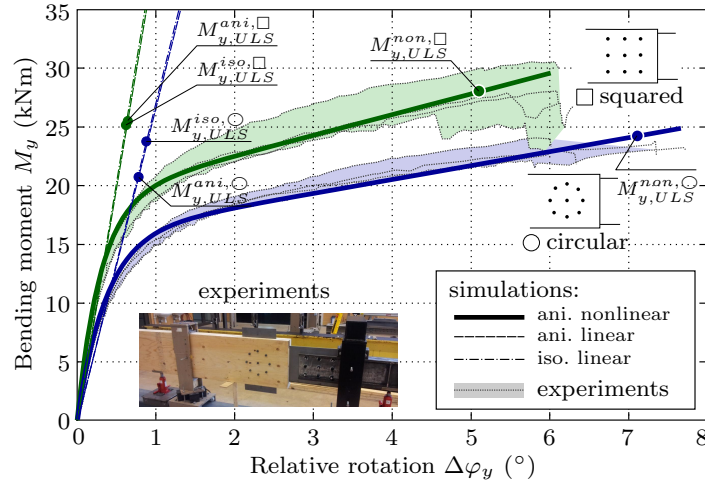


Figure 5.3: Model validation: M_y – $\Delta\varphi_y$ relationship of joints with 9 dowels, $d=12$ mm, in circular and squared arrangement; comparison between experimental and simulation results, including the fastener-based ULS limit, i.e., joint bearing capacity.

procedure shown in Eqs. (5.17)–(5.21) was applied. As initial set of relative joint deformations, $\Delta\mathbf{u}_j$ was set equal to zero (cf. Eq. (5.17)). For the second and all further load steps, a multiple of $d\Delta\mathbf{u}$ was added to $\Delta\mathbf{u}_j$, according to Eq. (5.19). $d\Delta\varphi_y$ was the only non-zero component of $d\Delta\mathbf{u}$ (cf. Eq. (5.20)). For each relative rotation, $\Delta\varphi_y$, a bending moment, M_y , was calculated using Eqs. (5.3)–(5.14), based on anisotropic nonlinear (Eqs. (5.22)–(5.26) and Fig. 5.2a), anisotropic linear (Eq. (5.27) and Fig. 5.2b), and isotropic linear dowel slip (Eq. (5.37) and Fig. 5.2b).

Comparison of simulation with experimental results showed that simulation results from nonlinear connection model were clearly within the range of variability of the experimental data for both joint layouts, i.e., squared and circular (Fig. 5.3). For the initial, quasi-elastic part of the slip curve, simulation results were found to lie at the upper end of the experimental results, while for relative rotations of approximately 1.5° to 5° the simulation gave a bending moment at the lower limit of the experiments. It needs to be emphasized that the model neglects elastic deformations in timber in between the dowels, which might be a reason for a slight overestimation of the quasi-elastic stiffness (Bader et al., 2017). Since the global response of the joint strongly depends on the single-dowel connection slip, there might be an indication that even higher friction forces could be achieved in the nonlinear transition path ($\Delta\varphi_y$ of 1.5° to 5°). However, for even larger relative rotations, simulations tended to overestimate experimental data, since cracking, and the possible change from static to sliding friction along the dowel axis, as well as secondary effects caused by pronounced bending deformations of dowels were not explicitly accounted for in the model.

Linear models (dashed and dash-dotted lines in Fig. 5.3) showed only for the initial, i.e., quasi-elastic part of the joint slip a good agreement with experimental results. For loading close to joint bearing capacity (ULS limit), indicated by circular markers in Fig. 5.3, a pronounced overestimation of experimentally determined joint slip was seen. For linear models, the joint bearing capacity was limited by the single-dowel bearing capacity, $F_{i,limit}$, which was determined at a dowel displacement, δ_i , of 15 mm (cf. Subsection 5.2.3.2 and 5.2.3.3). Similar joint stiffness was seen for anisotropic and isotropic linear model, for both joint layouts, while considerable differences in joint bearing capacity for circular arrangement was seen. This can

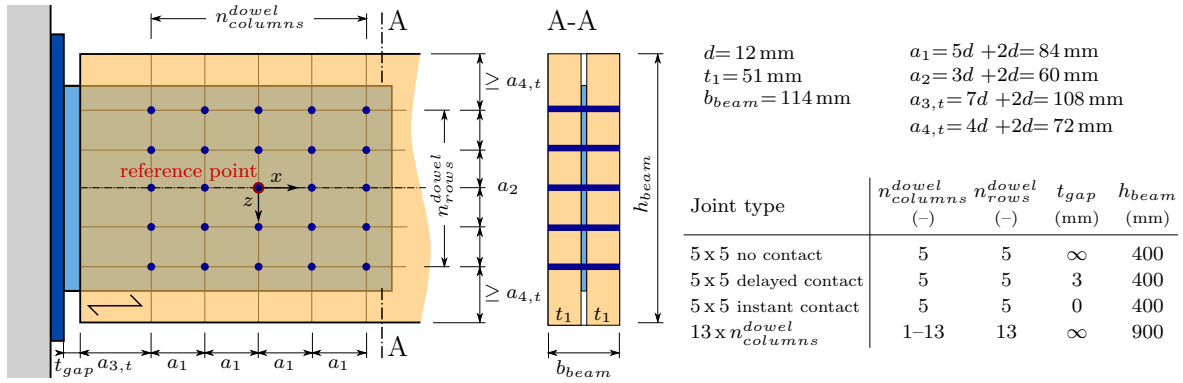


Figure 5.4: Joint geometry for application examples, including geometrical joint properties and specification of applied *Joint types*.

Table 5.1: Stiffness properties of Kerto-S[®], Metsä, Finland, from (Z-9.1-100, 2011), and (Kohlhauser and Hellmich, 2012).

$E_L = 13800 \text{ MPa}$	$E_R = 300 \text{ MPa}$	$E_T = 300 \text{ MPa}$
$G_{LR} = 500 \text{ MPa}$	$G_{LT} = 500 \text{ MPa}$	$G_{RT} = 50 \text{ MPa}$
$\nu_{RL} = 0.394$	$\nu_{TL} = 0.394$	$\nu_{TR} = 0.516$

be explained by a strongly simplified load distribution when considering isotropic, i.e., direction independent dowel slip. In comparison with nonlinear modeling, joint bearing capacity for linear models was found to be lower, which is an effect of load redistribution, and thus additional activation of dowel forces in the case of nonlinear modeling.

5.4 Model applications for studying joint behavior

Simulation results showed good correlation with results from joint experiments, which raises confidence in the model. In the following, the model will be applied to different joint design situations. First, slip curves of joints related to internal forces and using different connection models (presented in Subsections 5.2.3.1–5.2.3.3) will be discussed, before limit surfaces of joints, as related to an interaction of internal forces, will be illustrated. Finally, the influence of connection models on load distribution within joints will be presented.

5.4.1 Input data for calculation examples

Geometrical input data for application examples are illustrated in Fig. 5.4, and builds upon the single-dowel slip applied for model validation (Fig. 5.2). Furthermore, calculation examples with end-grain contact situations will be presented. For modeling purposes, compressive strength of LVL, $f_{c,0,LVL}^{mean}$, was measured on samples with a dimension of 50 x 50 x 50 mm. Mean density at standard climate amounted to 491 g/cm³ and a mean value of $f_{c,0,LVL}^{mean}$ of 51.92 N/mm² (stdv= 1.17 N/mm²) was measured. Together with a discretization length of 5 mm and a width of LVL of two times 51 mm, A_{con} and F_i^{con} , according to Eq. (5.44), were calculated and a slip of 1 mm was assumed, see (Fig. 5.2c).

Double-shear steel-to-LVL joints with a cross-section according to Fig. 5.4 will be investigated. Stiffness properties in Table 5.1 were taken as mean values from the technical approval

of Kerto-S (Z-9.1-100, 2011), and from literature (Kohlhauser and Hellmich, 2012). Poisson's ratios are given for the sake of completeness only, since for presented example calculations they do not affect the joint or structural behavior. The first index of Poisson's ratios refers to the strain and the second index refers to the stress direction. In this contribution we assumed $\nu_{TL} = \nu_{RL}$. In Fig. 5.4 joint geometry is exemplary shown for the *Joint type - 5x5 no contact*. The number of dowel columns, $n_{columns}^{dowel}$, and dowel rows, n_{rows}^{dowel} , for the other joint geometries used in this contribution, are given in Fig. 5.4 as well. The reference point for load application, by means of Δu_x , Δw_z and $\Delta \varphi_y$, was always chosen to be equal to the geometrical center of the joint. Compared to the minimum distances of EC 5 (EN 1995-1-1, 2004), the distances between the dowels, as well as the edge distances, were increased by two times the dowel diameter, in order to account for possible plastic deformations, expressed in terms of relative displacements, in plastic analysis.

5.4.2 Joint slip

Joint slip can be illustrated by internal force–relative displacement/rotation relationships. In case of an uncoupled description, a single internal force is considered to be the only non-zero component of the internal force matrix. Stiffness is then interpreted as the corresponding diagonal component of the stiffness matrix \mathbf{K} . In case of joints with a double-symmetric layout, regarding geometric and mechanical properties, and the reference point in the geometrical center of the joint, non-diagonal elements of \mathbf{K} , become equal to zero. Otherwise, a so-called coupled behavior, i.e., non-diagonal components of the stiffness matrix are not equal to zero, is given. Moreover, the coupling between internal loads (or relative deformations) can affect also diagonal components of \mathbf{K} . Thus, combination of internal forces influences the joint slip.

In Fig. 5.5 uncoupled slip, namely N_x – Δu_x , V_z – Δw_z and M_y – $\Delta \varphi$ relationships, and in Fig. 5.6 coupled slip will be discussed for joints presented in Fig. 5.4.

Calculation procedure

In both cases, *uncoupled* and *coupled* description, an incremental procedure shown by Eqs. (5.17)–(5.21) in Subsection 5.2.2 has to be used for determining joint slip curves.

For *uncoupled description* three different uniform situations with prescribed global relative deformations Δu_x , Δw_z , or $\Delta \varphi_y$, respectively, yield three internal forces for each of them. Only the associated internal force is considered in the case of uncoupled description, while additional relative displacements are neglected. For double-symmetric joints, only the associated diagonal component of \mathbf{K} is non-zero and each increment gives access to a point on the slip curve.

In the case of a *coupled description* of the slip behavior, also non-diagonal components are considered. This is, e.g., the case for asymmetric joint layouts. Moreover, the combination of internal forces introduces coupling, in the case of modeling based on anisotropic and/or nonlinear dowel slip. Thus, the joint slip is described by a tangential stiffness matrix according to Eq. (5.16), which is determined by applying a set of incremental relative joint deformations from an initial deformation state.

Application example

In Figure 5.5, joint slip for an *uncoupled loading situation* is presented. Joint type "5x5 no contact" according to Fig. 5.4 was chosen.

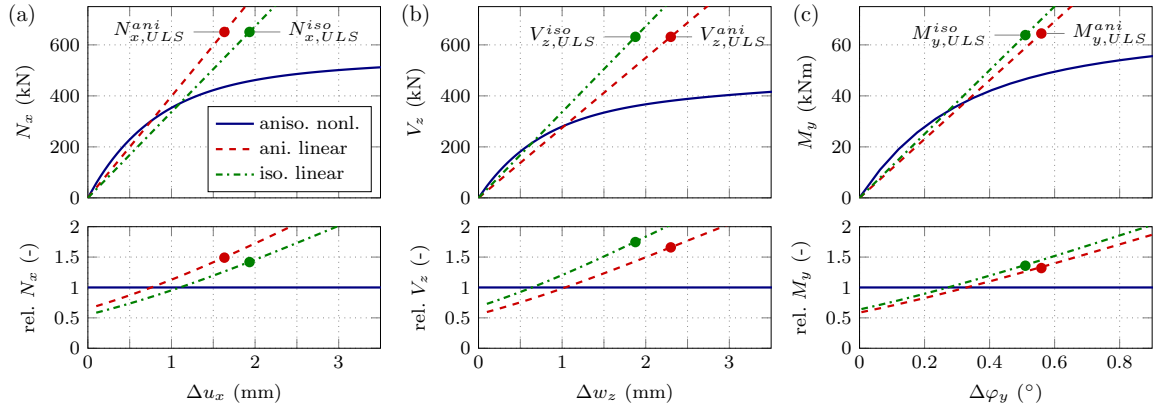


Figure 5.5: Uncoupled joint slip behavior: Comparison of anisotropic nonlinear, anisotropic linear, and isotropic linear joint model; (a) axial force, N_x , vs. relative axial displacement, Δu_x , (b) transverse force, V_z , vs. relative transverse displacement, Δw_z , and (c) bending moment, M_y , vs. relative rotation, $\Delta \varphi_y$, including the fastener-based ULS limit, i.e., joint bearing capacity, for the linear models, indicated by circular markers (e.g. $N_{x,ULS}^{ani}$).

In the following, the influence of different material models for connection behavior, namely *anisotropic nonlinear elastic* (cf. Subsection 5.2.3.1 and Fig. 5.2a), *anisotropic linear elastic* (cf. Subsection 5.2.3.2 and Fig. 5.2b), and *isotropic linear elastic* (cf. Subsection 5.2.3.3 and Fig. 5.2b), on the joint slip is assessed. Joint slip is expressed by absolute values (upper part of Fig. 5.5), and relative values (lower part of Fig. 5.5) of internal forces \mathbf{R} , plotted over corresponding $\Delta \mathbf{u}$. Relative values for load increment j are defined by

$$\text{rel. } N_{x,j} = \frac{N_{x,j}}{N_{x,j}^{non}}, \quad \text{rel. } V_{z,j} = \frac{V_{z,j}}{V_{z,j}^{non}}, \quad \text{rel. } M_{y,j} = \frac{M_{y,j}}{M_{y,j}^{non}}, \quad (5.45)$$

with $N_{x,j}^{non}$, $V_{z,j}^{non}$, and $M_{y,j}^{non}$ as internal forces based on anisotropic nonlinear dowel slip for load increment j .

Bearing capacity of the single-dowel connection, $F_{i,limit}$, was determined at a relative displacement equal to 15 mm. The joint bearing capacity, for axial, $N_{x,ULS}$, and transverse loading, $V_{z,ULS}$, at Δu_x and Δw_z equal to 15 mm, respectively, was the same for the nonlinear and linear joint models. This is due to the fact that dowel displacement components μ_i and ω_i are equally distributed over the dowels, when neglecting elastic deformations of the timber matrix. For the bending moment, a maximum relative displacement δ_i equal to 15 mm, yielded a global relative rotation $\Delta \varphi_y$ equal to 4.8° . M_y of the nonlinear model at this rotation was considered as strength, $M_{y,ULS}^{non}$, and compared to linear models. Linear models yielded about 18% lower strength than the nonlinear, since the latter allowed for load redistribution within the joint.

As regards relative joint deformations at joint bearing capacity, substantial differences between linear and nonlinear model got obvious. For the nonlinear model, up to almost 10-times higher joint deformations were required to reach the bearing capacity. Thus, with linear models joint stiffness was considerably overestimated in the ultimate limit state (ULS), even if stiffness was reduced by two-thirds according to EC 5. This indicates the joint bearing capacity to be incompatible with joint deformations for linear models. Internal forces at ULS of the linear models, namely $N_{x,ULS}^{ani}$, $N_{x,ULS}^{iso}$, $V_{z,ULS}^{ani}$, $V_{z,ULS}^{iso}$, showed an overestimation of about

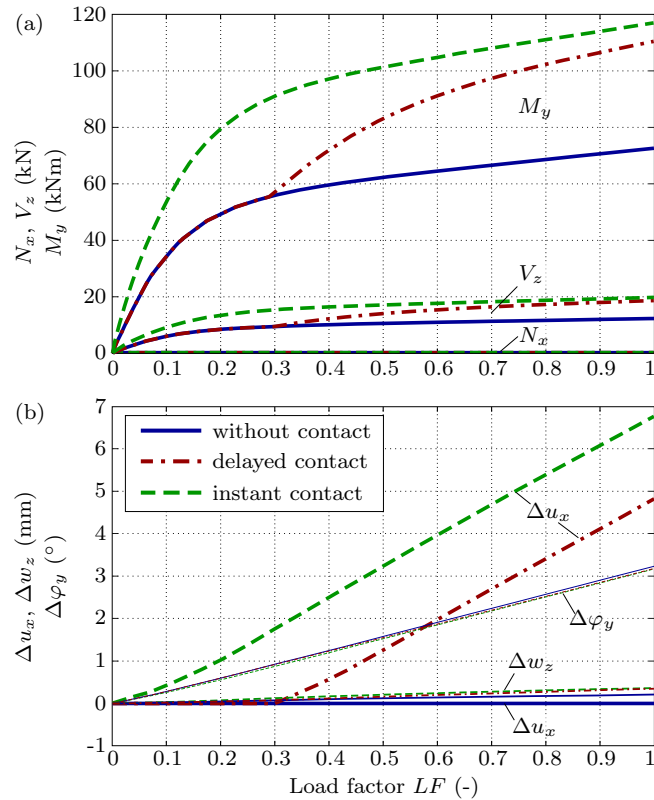


Figure 5.6: Nonlinear coupled joint behavior, (a) internal forces of a joint (5x5 dowels) without contact, with delayed contact and instant contact of the beam end, (b) corresponding relative deformations, i.e., relative axial and transverse displacement, Δu_x and Δw_z , and relative rotation, $\Delta \varphi_y$, at the center point of the joint.

50% (Fig. 5.5a and b), and $M_{y,ULS}^{ani}$ and $M_{y,ULS}^{iso}$ of more than 30% (Fig. 5.5c), compared to the nonlinear model. For internal forces, up to approximately 50% of the bearing capacity, which corresponded to Δu_x and Δw_z of about 1 mm and $\Delta \varphi_y$ of about 0.3° , only small differences in joint stiffness between linear and nonlinear models were found (see Fig. 5.5). Directional dependence of joint stiffness becomes obvious in Figs. 5.5a–b, where for the anisotropic linear model the stiffness for transverse force loading, K_{zz} , was found to be 45% lower than for axial force loading, K_{xx} . The isotropic linear elastic model does not consider this difference at all, i.e., K_{zz} is equal to K_{xx} . For moment loading, differences in joint stiffness, K_{yy} , between anisotropic and isotropic model were less pronounced, which is a result of smeared load distribution, and thus homogenization in the case of moment loading.

For the anisotropic nonlinear model, loading beyond dowel displacements of 15 mm might be considered. Thus, increasing δ_i from 15 mm to 24 mm, for the nonlinear model, increased the difference in strength to about 45% for M_y , compared to the linear models. Corresponding difference for N_x - and V_z -loading were about 16% and 26%, respectively.

The example shows that linear models are a suitable simplification for uncoupled joint slip and small relative deformations only, while the nonlinear model even captures the transition from quasi-elastic to plastic behavior.

Joint slip as discussed before, is a consequence of the number and arrangement of dowels. In a next step the influence of an *inhomogeneous joint layout* on the joint slip will be demon-

strated. For this purpose, joint type "5x5 no contact" was extended by possible contact elements at the beam end, resulting in joint type "5x5 delayed contact" and "5x5 instant contact" as defined in Fig. 5.4. Load–relative displacement relationship for contact behavior is given in Fig. 5.2c. Introducing contact elements requires a *coupled* description, since the stiffness conditions within the dowel group substantially change during loading. Consequently, contact not only affects the M_y – $\Delta\varphi_y$ relationship, but also leads to additional relative displacements, i.e., Δu_x and Δw_z , at the reference point of the joint (Fig. 5.6b). Loading is described by the load factor LF , with $LF=1$ for $\Delta\varphi_y$ equal to 3.2° . Only *anisotropic nonlinear* dowel slip (cf. Subsection 5.2.3.1 and Fig. 5.2a) was applied.

Instead of load–relative displacement relationships, internal forces are plotted over the load factor in Figure 5.6, for illustration of joint slip. The applied loading caused a dominant M_y and a small V_z at the joint, while resultant N_x was equal to zero. Thus, a loading situation with two simultaneously acting internal forces was caused (cf. experimental tests in Bader et al., 2016c).

Without contact, joint slip corresponded to the M_y curve shown by the continuous line in Fig. 5.6a. Instantaneous contact led to considerably higher bending moments, as a result of a substantial increase in the rotational stiffness K_{yy} and the additionally activated stiffness term K_{yx} . The joint with delayed contact followed the M_y curve without contact until relative displacement at the beam end was equal to the clearance t_{gap} . Contact loads, caused a change in the load distribution within the joint, and thus a change in the joint slip behavior, namely the rotational stiffness of the joint increased substantially. With increasing loading, the slip curve for delayed contact converged to the slip curve of the joint with instantaneous contact. A similar behavior was seen for V_z . The plot of relative joint deformations over the load factor shows that the joint experienced considerable relative axial displacement in case of contact (Fig. 5.6b). This indicates, that the center of rotation of the joint was different from the reference point. In this case, coupled description of the joint behavior is indispensable.

Results from this application example were well in line with observations from experiments on multiple-dowel joints, including end-grain contact (Bader et al., 2016c). However, modeling of the contact situation in this experiments would require taking into account that contact forces were applied by a pendulum. Thus, contact stiffness and contact loading direction in experiments changed during loading, which is different from the herein applied rigid contact situation.

5.4.3 Joint limit surface – interaction of internal forces

Influence of interaction of relative deformations on internal forces of joints is further illustrated by means of limit surfaces. They allow for a direct assessment of the joint including the interaction between the internal forces. Thus, a coupled description of the joint needs to be considered. A displacement limit, $\delta_{i,max}$, i.e., limiting the maximum relative displacement of the dowels, was considered. Limit state was reached when the maximum dowel displacement was equal to the limit displacement, reading as

$$f(\delta) = \frac{\max(\delta_i)}{\delta_{i,max}} = 1. \quad (5.46)$$

Limit surfaces could be used for verification of joints, independent from the verification of the timber structure itself. However, it should be mentioned that brittle failure is not accounted for in the definition of limit surfaces.

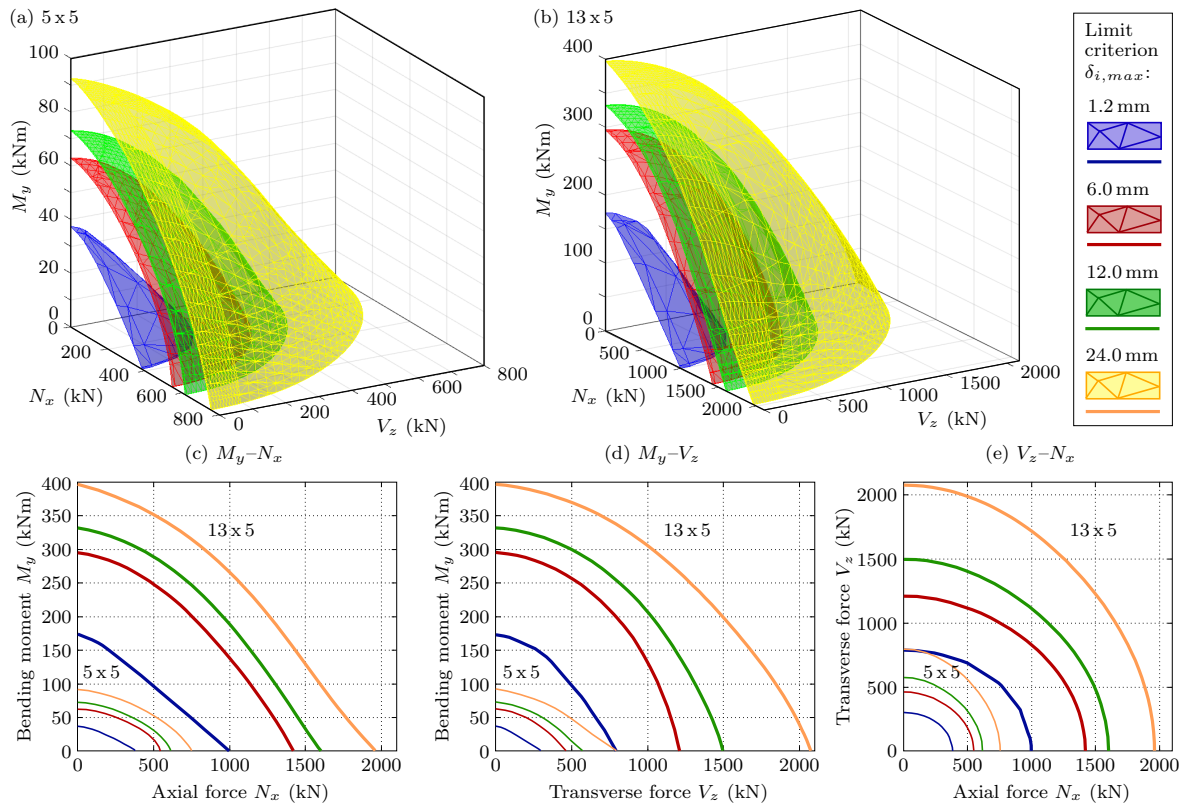


Figure 5.7: Joint limit surface: Interaction of internal forces for joints with 5x5 and 13x5 dowels according to Fig. 5.4a; (a)–(b) interaction of N_x , V_z and M_y , and (c)–(e) interaction for pairs of internal forces.

Calculation procedure

To create a limit surface of a certain joint layout, the full set of relative joint deformations is applied simultaneously to the calculation procedure given by Eqs. (5.3)–(5.14). A 3-dimensional grid of relative joint deformations with $m \cdot n \cdot o$ elements, representing the number of increments for the relative joint deformations, is created as input to the model. Therefore, the incremental procedure given by Eqs. (5.17)–(5.21) is applied. Each set of relative joint deformations gives a set of internal forces, and additionally a number indicating if the limit state according to Eq. (5.46) is reached or not. Linear interpolation is used between the calculated points of the 3D grid, for drawing the corresponding limit surface.

Application example

Limit surfaces for two different joint layouts, namely a *small* joint with 5x5 dowels and a *large* joint with 13x5 dowels (cf. Fig. 5.4) were calculated. Anisotropic nonlinear dowel slip (see Subsection 5.2.3.1 and Fig. 5.2a) was applied only. $\delta_{i,max}$ was set equal to 1.2 mm, 6 mm, 12 mm and 24 mm. These values represent the end of the quasi-elastic path up to two times the dowel diameter, which was considered an upper limit of dowel slip herein. Limit surfaces for interaction of the full set of internal forces, namely N_x , V_z and M_y , are given in Fig. 5.7a and b, for the 5x5 and 13x5 joint, respectively. In Figure 5.7c–e, limit curves for pairs of internal forces, i.e., 2D sections of the limit surface, are shown.

Pronounced nonlinear interaction between internal forces becomes obvious in Fig. 5.7. Figures 5.7c–e show that the order of nonlinearity depends on the interacting internal forces, joint layout, and size of dowel displacement. While limit curves for V_z-N_x interaction exhibited an almost circular shape, an almost linear interaction was seen for the M_y-N_x interaction for the 13x5 joint with the limit criterion $\delta_{i,max}=1.2$ mm. The latter was an effect of the joint geometry in combination with loading by N_x and M_y . Loading by N_x caused evenly distributed dowel displacements parallel to the grain direction (cf. Eq. 5.3), which accumulated with almost grain parallel displacements of the outermost dowels due to M_y .

Comparing limit curves for different $\delta_{i,max}$ showed the hardening behavior of multiple-dowel joints, which was a result of displacement hardening of the single-dowel connections and load redistribution in the case of moment loading. The bearing capacity more than doubled when dowel displacement of 24 mm instead of 1.2 mm was considered. Stronger joint hardening was seen for loading by pure V_z compared to pure N_x (see Fig. 5.7e), since stronger displacement hardening occurred perpendicular than parallel to the grain (cf. Fig. 5.2a).

In addition differences between the two investigated joint layouts get obvious, especially from Fig. 5.7d. A higher bending moment bearing capacity related to the transverse force bearing capacity was seen for the 13x5 joint compared to the 5x5 joint. This can be explained by the higher number of dowels being located further away from the center of rotation. Thus a higher number of dowels was fully, or almost fully activated in the case of bending moment loading.

5.4.4 Load distribution and load redistribution

Load distribution within the joint, and thus the force per dowel, is an essential input for the assessment of brittle failure modes of joints in the case of plastic analysis, as well as for verification in the case of fastener-based joint design. Besides load distribution, also load redistribution among dowels within the joint can be investigated by the herein presented model. Load redistribution is caused by incremental change of relative joint deformations in combination with the anisotropic nonlinear dowel slip.

Calculation procedure

For assessment of load distribution for a certain set of joint deformations the calculation procedure given by Eqs. (5.3)–(5.12) is followed. This allows to directly relate joint deformation with size and direction of dowel displacements, and thus consequently with dowel forces, i.e., the load distribution.

In case of internal forces as input for assessment of the load distribution within the joint, an iterative procedure as described in Subsection 5.2.3.1 is required. For the simplified cases of anisotropic and isotropic linear dowel slip behavior, Eqs. (5.33)–(5.36) and Eqs. (5.42)–(5.43), respectively, can be used.

For investigating load redistribution, an incremental procedure as shown in Eqs. (5.17)–(5.21) with at least two load increments are needed. The load redistribution gets visible by changes in load-to-grain angle, $\bar{\alpha}_i$ and in the size of dowel forces, F_i , between loading increments.

Application example

The effect of different approaches for the dowel slip, as well as the size of loading on the load distribution and redistribution is illustrated in Fig. 5.8. A dowel group with 5x5 dowels

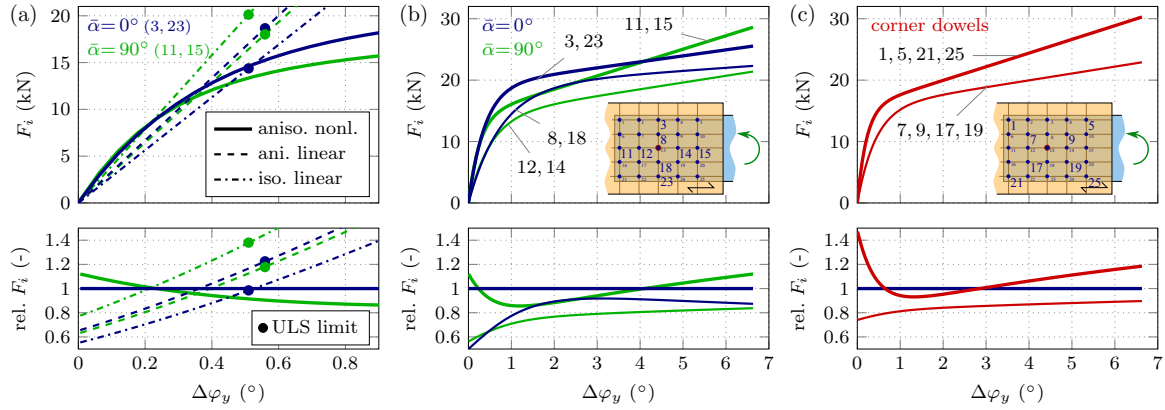


Figure 5.8: Load distribution within a joint (5 x 5 dowels): Dowel forces, F_i , vs. relative joint rotation, $\Delta\varphi_y$, for pure in-plane bending moment, including illustration of relative dowel forces $rel. F_i$ according to Eq. (5.47). (a) Comparison of joint models including the fastener-based ULS limit for the linear models, (b) dowels loaded parallel and perpendicular to the grain based on anisotropic nonlinear slip, and (c) corner dowels based on anisotropic nonlinear slip.

(without contact) according to Fig. 5.4 was exemplarily investigated. Three different (linear and nonlinear) dowel slip models were applied and compared. The joint was loaded by a pure in-plane bending moment. Global joint slip is illustrated in Fig. 5.5c, while the related dowel forces, F_i , plotted over the relative joint rotation, $\Delta\varphi_y$, are presented in Figs. 5.8a–c (upper part). The lower part illustrates relative dowel forces calculated by

$$rel. F_{i,j} = \frac{F_{i,j}}{F_{3,j}^{non}}, \quad (5.47)$$

with $F_{i,j}$ as the dowel force for load increment j of dowel i . $F_{3,j}^{non}$ represents the dowels force of dowel 3 from anisotropic nonlinear dowel slip model, which corresponds to one of the outer dowels loaded parallel to the grain ($\bar{\alpha}=0^\circ$). Related numbering of dowels is given in Figs. 5.8b and 5.9a.

From Figure 5.8 it gets obvious that nonlinear anisotropic dowel slip strongly affected load distribution. Assuming *isotropic linear elastic dowel slip*, a load distribution linearly related to the distance from the center of rotation was given. Thus, the dowel furthest away from the center of rotation got the highest load. For the given joint layout these were the corner dowels. The dowels loaded perpendicular to the grain (dowels 11, 15 in Fig. 5.8a) were loaded by 40% higher forces than the dowels loaded parallel to the grain (dowels 3, 23 in Fig. 5.8a). This was in contradiction to the *anisotropic linear* and *nonlinear model*, where dowels loaded parallel and perpendicular to the grain got almost the same forces in the initial loading part (see Fig. 5.8a). This was a result of the stiffer behavior parallel to the grain in combination with a smaller distance to the center of rotation, compared to the dowels loaded perpendicular to the grain. Thus, isotropic linear dowel slip led to an underestimation of dowel forces directed parallel or almost parallel to the grain.

It gets also obvious from Fig. 5.8a that for anisotropic and isotropic linear models, loading at ULS (indicated by circular markers in Fig. 5.8a) was overestimated for outer dowels (e.g. dowels 3 and 11 in Fig. 5.8a), when comparing with the *anisotropic nonlinear model*. At the same time, loading for the inner dowels was underestimated. This was a result of arising load redistribution from the outer to the inner dowels, when loading in the plastic regime.

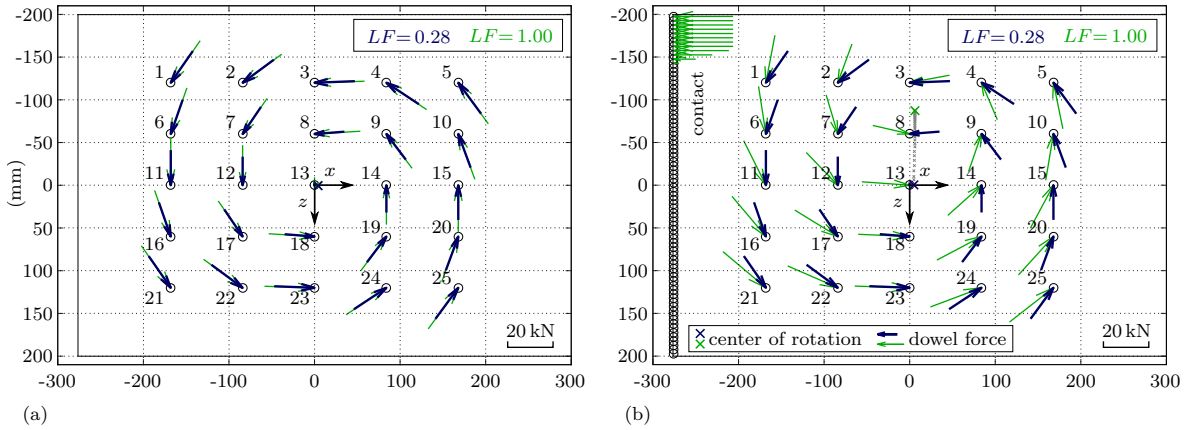


Figure 5.9: Load distribution within a joint (5x5 dowels): Illustration of dowel forces, F_i , and the center of rotation (COR) for two *load factors*, LF , and two joint layouts, namely (a) without contact, (b) with delayed contact at the beam end, for loading according to Fig. 5.6.

Load redistribution from the outer to the inner dowels gets also visible in Fig. 5.8b and c, where, with increased loading, forces of inner dowels (e.g. dowels 7, 8 and 12 in Fig. 5.8b and c) increased relative to outer dowels (e.g. dowels 1, 3 and 11 in Fig. 5.8b and c). Thus, for loading of $\Delta\varphi_y$ between 1 to 2.5° dowel forces of the inner dowels were only about 10% smaller than for the outer dowels (see Fig. 5.8b and c). However it got also obvious, that with consecutive loading, loads were back-redistributed to the outer dowels. This was caused by displacement hardening of the dowels, which had an stronger effect on outer dowels than on inner dowels.

A second reason for load redistribution between dowels is the *anisotropic* nonlinear slip of dowels. Load orientation dependent single-dowel connection slip caused load redistribution between dowels with similar distances from the center of rotation. This became obvious when comparing forces of dowels loaded parallel and perpendicular to the grain (e.g. dowel 3 and 11 in Fig. 5.8b, respectively). Initially softer behavior of dowels loaded perpendicular to the grain (rel. $F_{11}=86\%$ at $\Delta\varphi_y=1.0^\circ$), compared with a strong hardening in the plastic regime, finally resulted in higher forces than for loading parallel to the grain (rel. $F_{11}=112\%$ at $\Delta\varphi_y=6.6^\circ$).

In Figure 5.9, the influence of a possible contact behavior at the beam end on load distribution is illustrated by extending dowel group with 5 x 5 dowels (cf. Fig. 5.4) with contact elements at the beam end. t_{gap} was set equal to 3 mm, i.e., delayed contact was considered. The joint was loaded by the set of relative joint deformations according to Fig. 5.6b. Load distribution for two loading steps, namely for a *load factor*, LF , of equal to 0.28 and 1.00, is illustrated in Fig. 5.9a and b.

For the joint *without contact* (Fig. 5.9a), load redistribution between dowels was observed. The distribution of the dowel forces indicated a loading situation by almost pure relative rotation. However, the position of the center of rotation was situated slightly right from the geometrical center. Hence, loading of the joint led to a small transverse relative displacement. Comparing dowel forces at a load factor of $LF=0.28$, showed the highest loads for dowels loaded parallel to the grain (dowels 3 & 23 in Fig. 5.9a). For $LF=1.00$ the highest loaded dowel moved to the corner dowels, i.e., dowel 1 & 21 in Fig. 5.9a. Load redistribution from outer to inner dowels was seen when comparing forces of inner dowels loaded parallel to the grain (dowel 8) between the two load steps. For $LF=0.28$ and $LF=1.00$, this dowel experienced a

force of 74% and 89% of highest loaded dowel, respectively.

Figure 5.9b shows a substantial change in load distribution, namely in size and orientation of dowel forces, as soon as contact is activated. This led to a change of the center of rotation (COR), which moved in vertical direction towards the activated contact points. Thus, forces of lower dowels, i.e., further away from the COR, substantially increased, and forces close to the COR even changed sign of loading direction (see Fig. 5.9b).

5.5 Application in engineering design

For statically indetermined structures, joint stiffness affects load distribution within and deformation of the structure. At the same time, relative deformations of the joint depend on the global loading of the joint, which is again a function of stiffness of the joints and the timber members in the timber structure. Thus, in these structures it is important to consider the interaction between joints and structural members. Uncoupled stiffness could serve as input to structural analysis. Application of a coupled and possibly nonlinear joint model in structural analysis can be realized in two ways; either (i) the nonlinear joint behavior is calculated for a set of $m \cdot n \cdot o$ relative deformation states and subsequently considered as input to the structural analysis; or (ii) the description of the joint behavior given by *calculation procedure* in Eqs. (5.3)–(5.14) is directly implemented in the structural analysis software. In the latter case, joint stiffness is calculated in each load increment and directly considered in assembling of the stiffness matrix for the structural analysis. A two-step approach with pre-assembled joint stiffness was followed herein.

Modeling procedure

Considering joint stiffness as input to the structural analysis can be done either by uncoupled or by coupled nonlinear springs. Coupled springs can however only rarely be found in commercial structural analysis software. For this reason, both opportunities will be discussed and compared. Modeling of structures was realized in the software package *ABAQUS*, where so-called *connector elements* describe displacements and rotations between two nodes in 3D space, which in our case were parts of structural members. In the calculation example, joint deformations were considered relative to the timber member.

The behavior of the connector element (CONN3D2 in ABAQUS/CAE 2016, Simulia, USA) is specified by load–displacement and moment–rotation relationships, which in case of coupling yields internal forces that depend on three relative deformations each (cf. Fig. 5.10a). The procedure for definition of the input to the connector element is similar to the procedure for joint limit surfaces (Subsection 5.4.3), where the full set of relative joint deformations is applied simultaneously to the joint model given by Eqs. (5.3)–(5.14) using the incremental procedure given by Eqs. (5.17)–(5.21) to build a 3-dimensional grid, representing the joint stiffness. The input to these three coupled springs is exemplarily shown in Fig. 5.10a. Slices parallel to relative joint deformations equal to zero, allow for illustration of coupling between two relative joint deformations, which gets obvious from Fig. 5.10a. During structural analysis the software accesses the predefined joint stiffness for assembling of the global stiffness matrix of the timber structure. Points between predefined grid points of the joint stiffness are determined by linear interpolation.

For uncoupled springs, three uncoupled slip curves, i.e., the diagonal elements of the stiffness matrix \mathbf{K} , determined as described in Subsection 5.4.2, are necessary in order to specify the behavior of two translational and one rotational springs.

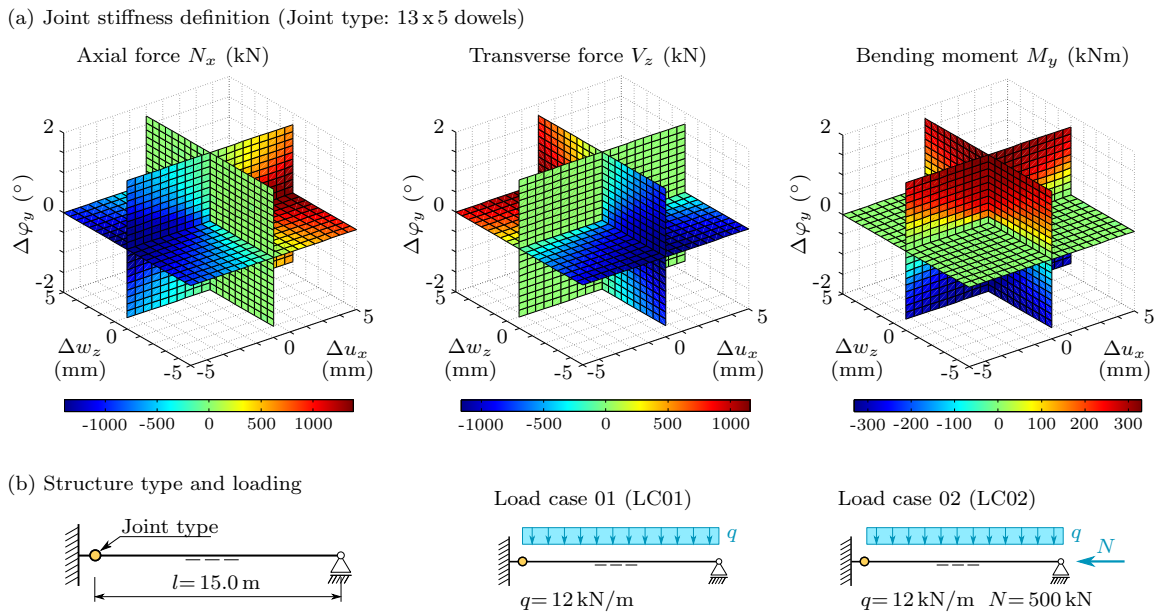


Figure 5.10: Input to structural analysis example. (a) Input to the *connector element* (CONN3D2, ABAQUS): Predefined joint stiffness by means of three coupled nonlinear springs, exemplarily shown for a joint with 13x5 dowels (cf. Fig. 5.4a); axial forces, N_x , transverse force, V_z , and bending moment, M_y , depending on axial and transverse relative displacement, Δu_x and Δw_z , and relative rotation, $\Delta \varphi_y$. (b) Definition of structural and loading properties, including dimensions of the structure and size of loading.

Application example

The influence of joint stiffness on load distribution within and deformation of the timber structure is illustrated by a simple beam model, shown in Figure 5.11. A single-span beam with clamped support at the left beam end, and a roller bearing on the right beam end, was used (see Fig. 5.10b). Attached to the clamped end (which was modeled with a rigid beam element), a joint with predefined slip was introduced (Fig. 5.10a). Thus, the rigid element represented the steel plate in the timber-to-steel dowel joint. The span between the joint and the roller bearing on the right hand side amounted to 15.0m. Dimensions of the beam cross-section are given in Fig. 5.4a. An orthotropic, elastic material model, with mechanical properties defined in Tab. 5.1, was used for the timber beam, modeled by a beam element including shear-elastic behavior. The size of loading was constant for all investigated joints. Two different loading situations, i.e., loading by a uniformly distributed load q (left column in Fig. 5.11), and loading by a combination of a uniformly distributed load and axial force $q + N$ (right column in Fig. 5.11), are discussed in the following. q amounted to 12 kN/m and N to 500 kN. Calculations were based on geometrically nonlinear theory.

In order to investigate the influence of the joint stiffness on the structural behavior, the size of the multiple-dowel joints was adjusted. The number of dowel rows, n_{rows}^{dowel} , was kept constant by 13 dowels, while the number of dowel columns, $n_{columns}^{dowel}$, was varied between 1–13. Thus, the size of the joint ranged from 13 to 169 dowels. Nonlinear and linear material models for the single-dowel and joint behavior were applied and compared. For the linear models, only the uncoupled behavior is illustrated in Fig. 5.11, while for the nonlinear model coupled and uncoupled behavior was investigated. In addition to joint stiffness, the two limit

cases of a rigid and hinged joint were investigated as well.

In Fig. 5.11a and b, a considerable influence of joint stiffness on the bending moment distribution gets obvious. With increasing number of dowels, joint stiffness increased, which led to an increase of the bending moment at the joint and simultaneously to a decrease of the field moment. For load case LC01 (q), the moment at the joint increased by a factor of more than six between the smallest and largest investigated dowel group (see Fig. 5.11a). Simultaneously, the field moment decreased by more than 35%. Similar numbers were found for the load case LC02 ($q + N$), illustrated in Fig. 5.11b. It can also be seen, that the limits of perfectly-hinged and fully-rigid joints could not be reached, even when considering a comparably small joint and comparably large joints, respectively. Thus, neglecting joint stiffness in structural analysis might lead to internal forces on the unsafe side, as it was the case for the bending moment at the joint, when considering a comparably small dowel group. From Fig. 5.11c and d, an increase of transverse force at the joint with increasing joint stiffness by about 20% can be observed. The opposite trend got obvious for the maximum deflection of the beam, which decreased substantially with increasing joint stiffness, from about 1/150 to 1/300 of the beam span (Fig. 5.11e and f). From calculations presented in Fig. 5.11, one could conclude that load distribution and bending deformation reacted more sensitive to joint stiffness for smaller dowel groups. However, the limit of a rigid joint can hardly be reached even for comparably large joints.

In addition to the load distribution and bending deformation for structures with a coupled joint model (continuous lines in Fig. 5.11), results are also given for uncoupled springs (dashed lines in Fig. 5.11). Both results are based on anisotropic nonlinear elastic dowel slip. For LC01, hardly any differences between those two approaches was seen. This was a result of the symmetric joint geometry in combination with only one dominant internal force acting at the joint, namely the bending moment. The comparably small transverse force hardly influenced the load distribution, which led to an almost uncoupled joint behavior. However, for LC02, a considerable difference between coupled and uncoupled description was seen, especially for smaller joints. In this case, the axial force strongly influenced the load distribution within the joint, which effected its stiffness. As it gets obvious from Fig. 5.11b, d and f, uncoupled description led to a stiffer joint behavior, and thus to a higher bending moment and transverse force at the joint, and to a lower maximum deflection and field moment. The stiffer behavior for uncoupled description can be explained when going back to the load distribution within the joint, i.e., dowel forces. Considering the loading separately, i.e., uncoupled, dowel forces might be still in the quasi-linear elastic part of the slip curve. In contrast, considering load interaction, i.e., coupled, leads to larger dowel displacements. Thus, the resultant dowel displacement might already be in the nonlinear elastic part, which leads to a loss in stiffness. In addition, displacement direction might change, which effects the global joint stiffness as well. In the case of LC02, with a dowel group with $n_{columns}^{dowel} = 2$, the uncoupled description gave more than twice of the moment at joint compared to the coupled description, while the field moment was underestimated by about 10%. With increased joint stiffness, difference between coupled and uncoupled description decreased. This might be explained by the dowel behavior being still in the quasi-linear elastic range for both descriptions, since the loading per dowel becomes smaller with increased number of dowels.

Results from the anisotropic and isotropic linear model for uncoupled description are illustrated by dash-dotted and dotted lines in Fig. 5.11, respectively. Linear models are typically related to fastener-based design. Thus, joint strength is limited by the bearing capacity of the single-dowel, indicated as ULS limit in Fig. 5.11. Loading per dowel increased with decreasing joint size when exposed to constant loading. Thus, ULS limit was reached for joints of

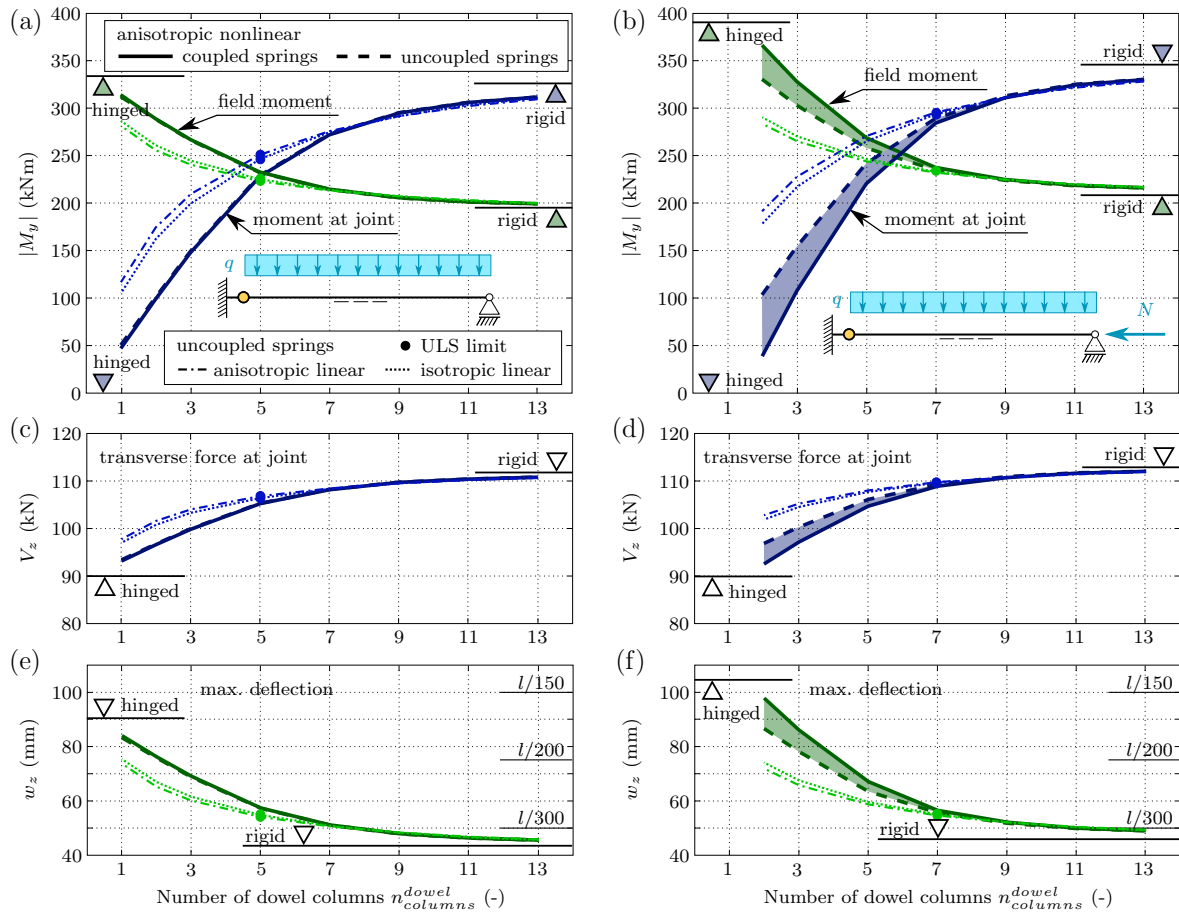


Figure 5.11: Load distribution within and deformation of the structure, dependent on the joint stiffness expressed by the number of dowel columns, $n_{columns}^{dowel}$, for a joint with 13 dowel rows. Comparison of coupled and uncoupled joint description based on anisotropic nonlinear, as well as anisotropic and isotropic linear dowel slip, including the fastener-based ULS limit, i.e., joint bearing capacity, for load cases LC01 q (left column), and LC02 $q + N$ (right column). Following parameters are plotted over $n_{columns}^{dowel}$: (a)–(b) absolute value of the joint and field bending moment, $|M_y|$, (c)–(d) transverse force at the joint, V_z , (e)–(f) maximum beam deflection, w_z .

13x5 and 13x7 dowels for LC01 and LC02, respectively. However, in most practical design calculations, structural analysis is carried out independent from verification of the joint bearing capacity. The calculation example showed that for small joints the moment at joint was overestimated by up to 140%, while the field moment was underestimated at the same time (see Fig. 5.11a and b). This was a result of the stiffer definition of the dowel slip at the upper limit of the elastic range in the linear models compared to the nonlinear model (cf. Fig. 5.2b). With increased size of the joint, difference in internal forces decreased, since also difference in dowel stiffness decreased. For large dowel joints, overestimation even reversed to a minor underestimation. The same applied for the transverse force and maximum deflection of the beam.

5.6 Joint-based design of semi-rigid joints with nonlinear structural analysis

European timber engineering design standard EC 5 is currently focusing on a fastener-based design of joints, resting on internal forces derived by an elastic structural analysis. Characteristic material properties, namely embedment strength and yield moment are applied for calculating characteristic single-fastener strength (and consequently of joint strength) based on a limit state approach, while mean values of linear single-fastener stiffness are specified. EC 5 does not provide rules for modeling of multiple-fastener joints, but an isotropic linear elastic load distribution model is commonly applied in practice.

The joint model applied in this contribution could be used according to the current design philosophy with elastic structural analysis in combination with a linear elastic joint stiffness predicted by the model. Verification would then be based on characteristic strength values as input to the joint model, which would yield a lower strength limit. This concept might be a suitable design strategy for the prediction of lower limits of brittle joints and to cover model uncertainties, while the potential of ductile joints cannot be fully exploited.

It can be demonstrated, that the joint model and its integration in global structural analysis, as presented in this paper, is capable to fulfill all principles in EC 5 related to the design of connections. It especially can be applied for nonlinear (elasto-plastic) calculations of structures (see also EN 1990, 2002, (EC 0)) able to redistribute internal forces via ductile joints, according to 5.1(3) in EC 5.

Ductile joints exhibit substantially reduced variability, which is supported by experimental observations that highlighted

- comparable low variability of test results with impact of ductility (probably as a consequence of reinforcement) at the stage of larger displacements in comparison to elastic tests (Schweigler et al., 2016a),
- comparable low variability of wood-based products in opposition to specimens made of solid timber (Thelandersson and Larsen, 2003a,b; Blaß and Sandhaas, 2017),
- significantly reduced variability due to large volumes/cross-sections and numerous fasteners within a joint, which is valid for both elastic and plastic domain (Kandler and Füssl, 2017; Källsner and Girhammar, 2009),
- homogenization for structural members consisting of various structural constituents like joints or whole systems (Kirkegaard et al., 2011; Vessby, 2011).

This motivates a joint-based design of ductile (and reinforced) connections in structural analysis, in combination with an appropriate global partial safety factor in verification. It should be mentioned that according to EC0, partial safety factors for materials are subdivided into a material-specific part and a part related to the accuracy of the structural modeling. Due to complex relationships not only in joints, the structural part of partial safety factors has been excluded from code calibration (Baravalle et al., 2017; Köhler and Fink, 2012), making it today impossible to benefit from more accurate structural modeling in terms of reduced partial safety factors.

Determination of internal forces at joints with structural analysis of the applied joint model could be realized by setting extreme values of stiffness and/or strength or by using mean values of stiffness and/or strength. This applies to both, linear and nonlinear modeling. Stiffness properties depend on various factors and upper and lower limits of stiffness can considerably affect load distribution within structures, and thus, loads at joints (cf. Fig. 5.11). It is impossible in practice to catch all possible combinations of extreme values of stiffness parameters already when using linear elastic stiffness, and it becomes even more complicated for nonlinear calculations. Main disadvantage in using single limit values (upper or lower) of stiffness is that load distribution is affected, and that partial safety factors would have to be increased due to increased modeling uncertainties.

In order to compensate unrealistic internal forces as a consequence of elastic structural analysis, the concept of the over-strength factor has been introduced in the field of earthquake design (Fragiacomo et al., 2011). This design method is however not implemented for ultimate limit state design of joints under quasi-static loading. The basic idea behind it is that ductility is guaranteed by overdesigning structural members that might fail in brittle manner, taking into account their variability. The design is based on a linear elastic structural analysis with linear elastic joint slip and takes into account overestimation of forces at joints and underestimation of internal forces of structural members.

Realistic nonlinear joint stiffness modeling with adequate and guaranteed ductility opens up alternative design strategies using mean values for nonlinear structural analysis. This yields the most likely load distribution in the structure (as well as in multiple-fastener joints) and its deformation. As quasi trade-off for the use of slip curves implemented at the level of 50% fractile for stiffness and load carrying capacity, a guarantee against premature brittle failure of such dowel-type joints must be established, e.g., by reinforcing the surrounding timber matrix by full threaded screws. Verification against brittle group failure modes needs to be performed using characteristic material properties with adequate partial safety factors. A realistic load distribution within joints that accounts for stiffness variations (including anisotropy) in dowel fasteners is a prerequisite for these verifications. Partial safety factors should account for higher quality of structural and joint modeling.

In the light of above presented aspects, more innovative and effective design concepts for the design of ductile joints, within a revised version of EC5, are suggested as follows. Failure criteria and partial safety factors for joints and structures should be related to the type and quality of structural analysis and joint model used for both, structural analysis and verification. This could, e.g., be realized in a similar way as commonly used for steel structures, see Tab. 5.2.

In addition to a simplified design using load level dependent secant moduli (cf. K_{ser} and K_u in EC5), design with nonlinear joint slip curves and reduced partial safety factors should be made possible in a revised version of EC5. Mean values of stiffness should be used for both members and joints in order to end up with most probable system displacements and distribution of internal forces as source for local or global failure, minimizing the distance to

Table 5.2: Design concepts for timber structures.

Type of structural analysis	Type of resistance	Type of failure criterion
linear elastic	elastic	local, fastener strength
linear elastic	nonlinear (elasto-plastic)	local, fastener strength
nonlinear	nonlinear (elasto-plastic)	global, joint strength

extreme and therefore less probable distributions by unrealistic setting of material parameters or inadequate structural modeling. Verification against brittle group failure modes needs to be performed using characteristic material properties with appropriate partial safety factors.

The joint model should in future studies be used for stochastic modeling, i.e., for predicting uncertainties of joint stiffness and strength based on single-fastener or material variations.

5.7 Conclusion

The semi-analytical joint model with nonlinear elastic single-dowel slip curves (validated in a previous study) realistically reproduced the ductile, nonlinear joint slip of multiple-dowel joints tested under moment loading. It was demonstrated that material models are decisive for predictions of global joint properties. Linear models, even when using load direction dependence, were limited to the quasi-elastic domain, and in combination with ideal-plastic material models, would yield a strong simplification of the nonlinear joint slip.

Application of the model to different joints gave insight into their slip behavior and load distribution within multiple-dowel joints, under uniform and even under simultaneously acting internal forces. Limit surfaces highlighted the importance of coupled modeling when it comes to the interaction of internal forces. The influence of inhomogeneous joint layout on global slip and load distribution was demonstrated by adding a possible end-grain contact point. Load distribution is strongly affected by the assumed single-dowel slip behavior. Nonlinear single-dowel slip accounts for load redistribution, which is not possible in linear models. Neglecting load orientation dependence and using the so-called polar moment of inertia approach, load distribution strongly simplifies, which might lead to underestimation of single-dowel forces. Load distribution is decisive for verification of ductile and brittle failure modes of joints in the ultimate limit state design, for which the nonlinear model will give more realistic results.

Compatibility of the joint model with structural analysis was demonstrated by implementation into a simple structure with one semi-rigid connection. It was shown, that the limit of fully-rigid joint behavior cannot be reached by practical joints. Larger multiple-dowel joints are needed when designed by linear joint models compared to design approaches based on nonlinear models. The latter allows for taking advantage of plastic resources of dowels when going beyond the elastic limit of linear joint models. The influence of coupling between internal forces on joint stiffness got visible by the distribution of bending moment and beam deflection, when the joint was loaded by more than one dominant internal force, and dowel displacements exceeded the quasi-elastic regime.

Fastener-based joint design, as it is currently prescribed by the European design code for timber structures (EC 5), rely on a realistic distribution of dowel forces within the joint,

since joint bearing capacity is based on verification of single-fastener strength. This can only be ensured by models considering the anisotropic nonlinear nature of the single-dowel slip, especially when loading beyond the quasi-elastic regime. For design situations in the quasi-elastic regime, anisotropic linear models might be suitable as well.

In nonlinear joint-based design, joint bearing capacity is considered instead of bearing capacity of the single-dowel. However, load distribution is still of major importance, since it is fundamental for verification against brittle failure modes, limiting the ductile behavior of the joint. Moreover, in nonlinear models, joint stiffness is essential for load distribution within the structure. This is why the use of mean values of stiffness in structural analysis with nonlinear joints is proposed, which yields the most likely load distribution within the structure. Ductility must be ensured by appropriate reinforcement and verification against brittle failure modes with appropriate partial safety factors.

Acknowledgements

The authors gratefully acknowledge the financial support of the Austrian Research Promotion Agency and the wood industry partnership Building with Wood within CEI-Bois for funding the research work within project *MechWood 2*. This work forms part of that project. The *MechWood 2* research partners are thanked for their cooperation and collaboration in this project. The WG3 members of COST Action FP1402 are thanked for the fruitful discussions and for their valuable input within working group meetings. Melanie Schwaiger is thanked for her support in preparing calculation examples.

Notation

a_1	distance between dowels in grain direction
a_2	distance between dowels perpendicular to the grain
$a_{3,t}$	distance between dowel and free beam end – in grain direction
$a_{4,t}$	distance between dowel and free beam end – perpendicular to the grain
$A_{con,i}$	contact area of contact point i
b_{beam}	width of the timber beam
$b_{con,i}$	width of contact area of contact point i
d	dowel diameter
$d\Delta\mathbf{u}$	incremental change of relative joint deformations
E_L	Young's modulus in longitudinal direction
E_R	Young's modulus in radial direction
E_T	Young's modulus in tangential direction
$f_{c,0,LVL}^{mean}$	compressive strength of LVL parallel to the grain (mean value)
$f_{c,y,timber}$	compressive strength of timber
$f(\delta)$	indicator for displacement limit
F_i	single-dowel force
$F_{i,j}$	single-dowel force of dowel i for load increment j
$F_{i,limit}$	bearing capacity of the single-dowel connection, calculated as the force at δ_i equal to 15 mm
$F_{i,x}$	single-dowel force component of dowel i in x-direction
$F_{i,z}$	single-dowel force component of dowel i in z-direction

F_i^{ani}	single-dowel force based on anisotropic linear elastic model
$F_{i,x}^{ani}$	single-dowel force component F_i^{ani} in x-axis
$F_{i,z}^{ani}$	single-dowel force component F_i^{ani} in z-axis
$F_{M_y,i}^{ani}$	single-dowel force component based on anisotropic linear elastic model, caused by M_y -loading
$F_{M_y,i,x}^{ani}$	single-dowel force component $F_{M_y,i}^{ani}$ in x-axis
$F_{M_y,i,z}^{ani}$	single-dowel force component $F_{M_y,i}^{ani}$ in z-axis
$F_{N_x,i}^{ani}$	single-dowel force component based on anisotropic linear elastic model, caused by N_x -loading
$F_{V_z,i}^{ani}$	single-dowel force component based on anisotropic linear elastic model, caused by V_z -loading
F_i^{con}	contact force yield limit of contact point i
F_i^{iso}	single-dowel force based on isotropic linear elastic model
$F_{i,x}^{iso}$	single-dowel force component F_i^{iso} in x-axis
$F_{i,z}^{iso}$	single-dowel force component F_i^{iso} in z-axis
$F_{x,i}^{iso}$	single-dowel force in x-axis, caused by a combination of M_y and N_x , based on isotropic linear elastic model
$F_{z,i}^{iso}$	single-dowel force in z-axis, caused by a combination of M_y and V_z , based on isotropic linear elastic model
$F_{3,j}^{non}$	single-dowel force of dowel 3 (loading parallel to the grain) for load increment j , based on anisotropic nonlinear elastic model
F_{inter}^{non}	single-dowel force at intersection of k_f^{non} with the vertical axis, based on anisotropic nonlinear elastic model
$F_{inter,0}^{non}$	F_{inter}^{non} for loading parallel to the grain
$F_{inter,90}^{non}$	F_{inter}^{non} for loading perpendicular to the grain
G_{LR}	shear modulus in LR-plane
G_{LT}	shear modulus in LT-plane
G_{RT}	shear modulus in RT-plane
h_{beam}	height of the timber beam
$h_{con,i}$	height of contact area of contact point i
i	index of single-dowel
I_p	polar moment of inertia
j	number of load increments
k_0^{ani}	quasi-elastic single-dowel stiffness parallel to the grain
k_{90}^{ani}	quasi-elastic single-dowel stiffness perpendicular to the grain
$k_{\alpha,i}^{ani}$	single-dowel stiffness for the anisotropic linear elastic model
k_i^{iso}	quasi-elastic, isotropic single-dowel stiffness
k_{ini}^{non}	initial gradient of the nonlinear slip curve, based on anisotropic nonlinear elastic model
$k_{ini,0}^{non}$	k_{ini}^{non} for loading parallel to the grain
$k_{ini,90}^{non}$	k_{ini}^{non} for loading perpendicular to the grain
k_f^{non}	end gradient of the nonlinear slip curve, based on anisotropic nonlinear elastic model
$k_{f,0}^{non}$	k_f^{non} for loading parallel to the grain
$k_{f,90}^{non}$	k_f^{non} for loading perpendicular to the grain
\mathbf{K}	stiffness matrix of the joint
K_{ij}	coefficients of the stiffness matrix

K_{ser}	slip modulus of the single-dowel in the serviceability limit state acc. to EC 5
K_u	slip modulus of the single-dowel in the ultimate limit state acc. to EC 5
K_{Nx}^{ani}	axial joint stiffness for the anisotropic linear elastic model
K_{Vz}^{ani}	transverse joint stiffness for the anisotropic linear elastic model
K_{My}^{ani}	rotational joint stiffness for the anisotropic linear elastic model
K_{Nx}^{iso}	axial joint stiffness for the isotropic linear elastic model
K_{My}^{iso}	rotational joint stiffness for the isotropic linear elastic model
K_{Vz}^{iso}	transverse joint stiffness for the isotropic linear elastic model
\mathbf{K}^{tan}	tangential stiffness matrix of the joint
LF	load factor
M_y	in-plane bending moment
$M_{y,j}$	in-plane bending moment at the joint for load increment j
$M_{y,ULS}$	fastener-based ULS limit for the bending moment of the joint
$M_{y,ULS}^{ani}$	$M_{y,ULS}$ based on anisotropic linear elastic model
$M_{y,ULS}^{iso}$	$M_{y,ULS}$ based on isotropic linear elastic model
$M_{y,j}^{non}$	$M_{y,j}$ based on anisotropic nonlinear elastic model
$M_{y,ULS}^{non}$	$M_{y,ULS}$ based on anisotropic nonlinear elastic model
$M_{y,ULS}^{non,\bigcirc}$	fastener-based ULS limit for the bending moment of the joint with circular layout based on anisotropic nonlinear elastic model
$M_{y,ULS}^{non,\square}$	fastener-based ULS limit for the bending moment of the joint with squared layout based on anisotropic nonlinear elastic model
n	number of dowels
$n_{columns}^{dowel}$	number of dowel columns
n_{rows}^{dowel}	number of dowel rows
N	axial external loading
N_x	axial force
$N_{x,j}$	axial force at the joint for load increment j
$N_{x,ULS}$	fastener-based ULS limit for the axial force of the joint
$N_{x,ULS}^{ani}$	$N_{x,ULS}$ based on anisotropic linear elastic model
$N_{x,ULS}^{iso}$	$N_{x,ULS}$ based on isotropic linear elastic model
$N_{x,j}^{non}$	$N_{x,j}$ based on anisotropic nonlinear elastic model
$N_{x,ULS}^{non}$	$N_{x,ULS}$ based on anisotropic nonlinear elastic model
q	uniformly distributed external load
r_i	distance between dowel i and reference point
rel. $F_{i,j}$	relative value of the single-dowel force of dowel i for load increment j
rel. $N_{x,j}$	relative value of the axial force at the joint for load increment j
\mathbf{R}	internal forces at the joint
\mathbf{R}_j	internal forces at the joint for load increment j
t_1	side member thickness of the timber beam
t_{gap}	clearance at beam end
V_z	transverse force
$V_{z,j}$	transverse force at the joint for load increment j
$V_{z,ULS}$	fastener-based ULS limit for the transverse force of the joint
$V_{z,ULS}^{ani}$	$V_{z,ULS}$ based on anisotropic linear elastic model
$V_{z,ULS}^{iso}$	$V_{z,ULS}$ based on isotropic linear elastic model
$V_{z,j}^{non}$	$V_{z,j}$ based on anisotropic nonlinear elastic model
$V_{z,ULS}^{non}$	$V_{z,ULS}$ based on anisotropic nonlinear elastic model

w_z	maximum beam deflection
x	orientation parallel to the beam axis
x_i	axial coordinate of dowel i
y	out-of-plane orientation
z	orientation perpendicular to the beam axis
z_i	transverse coordinate of dowel i
$\hat{\alpha}_i$	displacement-to-grain angle
$\bar{\alpha}_i$	load-to-grain angle
β	angle between grain orientation and beam axis
δ_i	resultant displacement of dowel i
$\delta_{i,max}$	limit displacement of single-dowels
$\delta_{i,x}$	displacement component of dowel i in x-direction
$\delta_{i,z}$	displacement component of dowel i in z-direction
$\delta_{\varphi,i}$	displacement of dowel i caused by $\Delta\varphi_y$
$\delta_{\varphi,i,x}$	displacement component of dowel i in x-direction, caused by $\Delta\varphi_y$
$\delta_{\varphi,i,z}$	displacement component of dowel i in z-direction, caused by $\Delta\varphi_y$
$\Delta\mathbf{u}$	relative deformations at the joint
$\Delta\mathbf{u}_j$	set of relative joint deformations for increment j
$\Delta\mathbf{u}_{j,in}$	initial set of relative joint deformations
Δu_x	relative axial displacement
Δw_z	relative transverse displacement
$\Delta\varphi_y$	relative rotation around y-axis
μ_i	axial displacement of dowel i
ν_{RL}	Poisson's ratio in RT-plane
ν_{TL}	Poisson's ratio in TL-plane
ν_{TR}	Poisson's ratio in TR-plane
ω_i	transverse displacement of dowel i

Conclusions and outlook

Summary of the combined experimental and computational study

This work follows the philosophy of a multiscale approach. Therefore, a bottom-up strategy is applied to describe the mechanical behavior of joints based on the load-deformation characteristics of their components. Accordingly, a combination of experimental and computational methods – in a multiscale manner – was used to get insight into the joint level regarding the global load-deformation behavior, addressed to the joint stiffness and strength, as well as into local load distribution within the joint. The latter gives access to dowel forces for verification of ductile failure modes in single-dowel-based design approaches, as well as brittle failure modes of the timber matrix in the joint area. Global load-deformation behavior of joints can be used in nonlinear analysis of timber structures, and thus, facilitates joint-based design methods. Up to the implementation in structural analysis, four scales of observation were defined, as follows:

- At the lowest scale, load-deformation characteristics of connection components, namely under wood embedment stress and steel dowel bending moments were considered. Studies on the embedment behavior were based on experimental methods, while mechanical properties of the steel dowel were investigated numerically and experimentally.
- At the scale of single-dowel connections, load-displacement characteristics were investigated numerically by a beam-on-nonlinear elastic foundation model, which was in addition validated by comparison with single-dowel connection experiments.
- At the scale of multiple-dowels constituting a joint, a semi-analytical model was developed for prediction of global joint slip and local load distribution within semi-rigid joints. Validity of the model was proven by comparison with experimental results.
- At the highest scale – the timber structure – load-deformation behavior of joints was considered in nonlinear analysis, to study their influence on load distribution and member deformations in timber structures.

Throughout all scales of observation, the principles of mechanical description of the load-deformation behavior up to large displacements, including loading situations with load application in between the principal material directions, and thus, accounting for the direction dependent behavior of wood was followed. At the wood embedment scale, only experimental studies were used. Tests were carried out on full-hole LVL specimens, for two different dowel diameters, seven different load-to-grain angles, for unconstrained and constrained lateral displacement boundary conditions. For the moment-rotation behavior of steel dowels in bending, 3-point bending tests as well as tensile test were conducted. Information on the latter were applied in numerical simulation of the dowel bending in a 3-dimensional FEM model.

At the next higher length scale – single-dowel connection – information from the previous scale were taken as input to numerical modeling by means of a beam-on-nonlinear foundation model. The steel dowel was represented by a beam chain, consisting of beam elements connected by rotational springs, covering the information on the nonlinear moment-rotation behavior of the steel dowel from 3-point bending tests or simulations, respectively. This beam chain rests on nonlinear elastic, translational springs, representing the wood embedment slip from embedment test. Integration of the embedment spring forces over the timber thickness, for specific displacement loading, gives a resulting force, and by using an incremental calculation procedure, it gives access to the slip curve of the single-dowel connection. This model allowed for prediction of the nonlinear, direction dependent dowel slip, giving access to study influence parameters thereon. Furthermore, the model allowed for definition of the serviceability limit state (SLS) as a result of plastic deformations in the steel dowel. A multi-dimensional parameterization technique was developed, which allows for mathematical description of slip curves as a function of the load-to-grain angle, based on pointwise defined slip data. The applicability was assessed for typical slip curves in timber connections, and consequently applied to experimental and numerical results from embedment and single-dowel slip. Information from the single-dowel connection model was used at joint level to consider the nonlinear load-displacement characteristics of single-dowels in the assembly of a joint. A semi-analytical model was developed, by assuming rigid connection members with nonlinear, direction dependent springs, representing the single-dowel slip. Thereby, different design situations, including contact situations, were studied, as regards their local load distribution, and global load-deformation behavior. Beside single-dowel forces as a result of joint loading, and slip curves of the joint, limit surfaces, allowing direct verification of joints, were determined. Joint slip was implemented by means of coupled springs in analysis of timber structures, giving access to load distribution and deformation of timber members in structures as a result of the nonlinear coupled joint behavior.

Research contribution and main findings

The presented combined experimental and computational study on dowel connections substantially contributes to the knowledge in timber engineering science and engineering design of joints in timber structures in four ways:

- Novel testing procedures at the embedment and single-dowel level gave detailed insight into the mechanical behavior of these connection components, which could not be fully exploited by pure numerical methods yet.
- Numerical modeling based on beam-on-nonlinear foundation method proved to be a useful tool to identify nonlinear single-dowel slip, which gives access to single-dowel connection stiffness and strength for arbitrary connection layouts.
- Parameterized equation for the loading direction dependent, nonlinear slip of connection components, based on the developed multi-dimensional parameterization technique, is expected to facilitate the use of nonlinear numerical methods in timber engineering practice.
- The semi-analytical joint model proved to be an attractive alternative to strongly simplified analytical models, and advanced scientific 3D FEM calculations. It gives valuable

insights into local load distribution, and global joint slip, which opens the door to joint-based design and nonlinear structural analysis in engineering design of joints, as well as to enhanced single-dowel-based design strategies.

Main findings related to the above-mentioned research contributions are summarized in the following according to the five publications.

In **Publications 1 and 2** steel dowels embedded in screw-reinforced LVL, with unconstrained and constrained lateral dowel displacement conditions, respectively, yielded pronounced ductile embedment behavior of LVL. This was proven by a steady loading path, without obvious load drops, as well as surface strain images from DIC, which did not show distinct cracking. Slip curves, by means of embedment stress–dowel displacement relationships, were characterized by an almost linear path in the quasi-elastic, as well as in the elasto-plastic region, with a nonlinear transition zone in between. As regards stiffness, results from unloading paths were found to be less variable, and amounted to about twice of the stiffness from loading path in the quasi-elastic region. This is an indicator that plastic deformations already appear in the quasi-elastic loading path. Comparable results were found for unconstrained and constrained loading, as well as for both dowel diameters. With increasing load-to-grain angle, quasi-elastic unloading stiffness decreased by more than 50% when loaded perpendicular to the grain compared to parallel to the grain. In contrast, elasto-plastic loading stiffness substantially increased with increasing load-to-grain angle, in terms of pronounced displacement hardening when loading at an angle of more than 45° to the grain. This is a result of densification of the hollow wood cells in combination with the rope effect in wood fibers. For constrained loading, pronounced displacement hardening was found already for load-to-grain angles larger than 30°, as a reason of stiffening effects. This got also obvious from the embedment strength, calculated at a dowel displacement of twice the dowel diameter, which resulted in up to 44% higher embedment stresses for loading at 45° and 60° in constrained compared to unconstrained loading. At this displacement limit, embedment strength for large load-to-grain angles was found to be considerably, i.e., up to 90% higher than the strength predicted by EC 5. These EC 5 predicted values, however, correlated well with experimental embedment strength at a displacement limit of 5 mm, as it is defined in EN 383. For unconstrained dowel displacement condition, loading at an angle different from the principal material directions caused lateral movement of the dowel, which even changed orientation with consecutive loading. This is well in line with lateral reaction forces caused in constrained loading conditions, which changed sign as well. Lateral, i.e., horizontal embedment stresses, up to 20% for the 5 mm displacement limit, and even up to 40% of the vertical embedment stress, for a displacement limit of two-times the dowel diameter were found. Lateral stresses are important for verification against brittle failure modes and design of reinforcement measures. Information on the nonlinear, direction dependent embedment slip, is expected to be a valuable input to numerical models of single-dowel connections. Furthermore, loading up to large dowel displacements highlighted the remarkable plastic resources in embedment strength, when loaded beyond the 5 mm limit of the corresponding testing (EN 383) and design standard (EC 5).

In **Publication 3**, numerical modeling, by means of a beam-on-nonlinear elastic foundation model, allowed to predict nonlinear, loading direction dependent load-displacement behavior of single-dowel connections. The global response is a consequence of the nonlinear, loading direction dependent embedment behavior, in combination with the nonlinear moment-rotation slip of steel dowels in bending. Parameter study demonstrated that ductile failure modes of a single-dowel connection do not only depend on the side member thickness and dowel diameter, but also on the dowel displacement. From the development of plastic

hinges in the steel dowel, characterizing the failure modes, it became obvious that no distinct border, but kind of a transition zone between failure modes exists. This is again a result of nonlinear steel dowel and wood embedment behavior. Similar to embedment behavior, higher single-dowel connection strength was found for load-to-grain angles of 45° and 90° than for 0°, when allowing for large dowel displacements. Surprisingly low elastic limits of the investigated single-dowel connections were found. Considering the elastic limit of the steel dowel as elastic limit of the connection, i.e., the onset of plastic deformations in the dowel, elastic dowel displacement limits of 0.4–0.9 mm were found. This corresponds to a single-dowel connection strength of only 15%–30% of the ultimate strength. The ultimate connection strength, calculated by EC 5-based limit state analysis, required a dowel displacement of 6–8 mm, in order to match results from beam-on-nonlinear elastic foundation simulations, which violates the 5 mm displacement limit at which the embedment strength is defined, and thus, highlights kinematical incompatibility of the EC 5 design concept. Furthermore, simulated quasi-elastic single-dowel connection stiffness was found to considerably depend on the loading direction. This is however not accounted for in EC 5. Furthermore, quasi-elastic stiffness was found to be overestimated by EC 5 for the investigated connections. By this parameter study, flexibility and reliability of the numerical model was proven. Allowing for a detailed insight in the single-dowel connection behavior, as well as for implementation in commercial structural analysis software, it is expected to be an attractive alternative to currently used design models in engineering practice.

In **Publication 4** numerous regression equations from literature were identified to be suitable for description of connection slip curves. Equations with exponential or power functions, such as the well-known equation by *Foschi*, proved to be ideally suited for curves with linear behavior in the elastic and plastic part. For curves with nonlinearities in the plastic range, equations based on polynomial functions were found to be most reasonable. As regards interaction curves, two prevalent curve types were identified from timber engineering applications. These are bell-type and S-shaped curves. The latter, were sufficiently described by combination of exponential functions or trigonometric functions, such as the *Hankinson* equation. Bell-type curves were approximated by equations from statistics, such as equations from *Gauß* or *Gumbel*. Combination of regression functions for slip curves and interaction curves, yielded a three-step approach for mathematical description of the connection slip as a function of the load-to-grain angle. Application of this approach to the experimental dataset from constrained embedment tests (**Publication 2**) proved the suitability for a parameterized definition of nonlinear loading direction dependent slip behavior. This is confirmed by a coefficient of determination R^2 of equal to 0.984 and 0.805 for the vertical and horizontal embedment stress component, respectively. Furthermore, it was shown that some regression equations allow for physical interpretation of their parameters, which gives direct access to a mathematical slip behavior description based on experimentally determined parameters without the need of regression analysis. Parameterized definition of slip curves, as a function of the load-to-grain angle, is expected to substantially support the development and dissemination of numerical methods in the engineering design of timber connections.

In **Publication 5** the semi-analytical joint model has proven to realistically predict the global joint slip, as well as local load distribution within the joint. It was demonstrated, that the challenging issues of interaction between internal forces, including bending moments, as well as contact situations can be sufficiently addressed. The importance of the underlying material model, by means of linear or nonlinear, loading direction dependent or independent single-dowel slip behavior was shown. From application examples, it got obvious that global

joint slip predicted by linear models is limited to small joint displacements and rotation, and thus limited to the quasi-elastic range. Limit surfaces for joint strength, using coupled description, highlighted the importance of considering interaction between internal forces, as well as the remarkable plastic resources of ductile joints. It was shown that load distribution can only be sufficiently predicted by nonlinear, loading direction dependent models. Linear models lead to a simplified load distribution, which might lead to single-dowel forces on the unsafe side. Implementation of joint stiffness in structural analysis highlighted the influence on load distribution between joint and structural members and the effect on member deformation. It was shown that the limit cases of rigid interaction cannot be reached for joints in engineering practice. Furthermore, a considerable difference in load distribution within the structure, between coupled and uncoupled joint models was seen, when loading by more than one dominant internal force beyond the quasi-elastic range. Uncoupled modeling of the joint, as well as models based on linear single-dowel slip, led to overestimation of the joint stiffness, and thus, to overestimation of joint forces, while member forces were underestimated. Thus, for nonlinear analysis with semi-rigid joints it is suggested to use mean values of stiffness to gain the most likely load distribution. Modeling of joint behavior, based on nonlinear loading direction dependent single-dowel slip, was found to be important for both, i.e. *single-dowel-based* design methods, which rely on realistic load distribution within the joint, and *joint-based* design approaches, which rely on realistic joint stiffness prediction, and load distribution for verification against brittle failure modes.

Proposals for the next generation of design and test standards

In the current version of the *European engineering design standard* for timber structures, EC 5 (EN 1995-1-1, 2004), the design of dowel connections is addressed by a single-dowel-based design method. Single-dowel connection strength is calculated by a limit-state approach going back to the work of Johansen (1949), and stiffness is determined separately by empirical equations. However, no information on how to distribute loads within the joint, especially when loaded by a bending moment is given. In engineering practice, mainly the strongly simplified isotropic linear approach, based on the so-called polar moment of inertial, is used to distribute loads, since it gets along with information provided by EC 5. In this work, it was shown that one of the general principles, i.e., *kinematical compatibility*, is in general violated by this approach. Furthermore, load distribution was found to be strongly simplified, when using linear elastic, direction independent single-dowel slip definition. On the other hand, the current design concept is characterized by its simplicity in application.

Thus, it might be reasonable to introduce in addition to the current simple design concept, a more advanced design concept, which overcomes the drawbacks of the current regulations. However, clear application limits for the simplified design concept have to be given. This could either be done by limitation to defined design situations, or by restriction to certain *consequence classes* according to EN 1990 (2002). As an intermediate design concept, between simple and advanced design concept, an improved version of the current simple design concept could be introduced. This concept would still rely on linear elastic single-dowel behavior, however, with the extension of loading direction dependent stiffness. In combination with the beam-on-nonlinear foundation model for prediction of single-dowel connection stiffness at an angle to the grain, it would yield more realistic load distributions for loading in the quasi-elastic range, as it was shown in this work. This design concept would require revision of the EC 5, by including information on the loading direction dependent embedment slip, as input to the beam-on-nonlinear foundation model.

As regards the advanced design concept, general requirements for joint models, like, e.g., the joint model presented in Publication 5, should be given in EC 5. These requirements should be addressed to accuracy of the model predictions, as well as their applicability. With nonlinear joint models, a *joint-based* design could be introduced as well. Of special importance is definition of an appropriate stochastic framework, when taking advantage of ductile semi-rigid joint behavior in nonlinear structural analysis, since joint slip has system character regarding its stiffness (see Publication 5). Furthermore, input parameters for nonlinear joint models would have to be included in EC 5 and related product standards, respectively. This is mainly related to stiffness and strength parameters of the nonlinear, loading direction dependent wood embedment and steel dowel bending behavior, in order to allow for prediction of the nonlinear, loading direction dependent single-dowel behavior, based on numerical single-dowel connection models as it was for example presented in Publication 3.

To allow for numerical modeling of dowel joints and their components, related *testing standards* have to be revised as well. In the European testing standard for embedment strength of dowel type fasteners, EN 383 (2007), regulations should be extended to loading at angles between the principal material directions. In this sense, statements regarding the lateral dowel displacement condition should be included as well (cf. Publications 1 and 2). Furthermore, the displacement limit should be increased from 5 mm to a relative limit of, e.g., two times the dowel diameter, or a combination of relative and absolute limit, like two times the dowel diameter or 20 mm. Testing up to large dowel displacements should be performed on reinforced test specimens, in order to avoid premature brittle failure of the wood matrix. Regulations for the strength and position of the reinforcement have to be given. In addition, documentation of the load-displacement curve should be recommended, since it is a valuable information for nonlinear numerical modeling. Furthermore, stiffness and strength embedment parameters should be introduced, to allow for parametric reconstruction of the embedment slip curve (cf. Publication 4).

These proposals for adjustment of EN 383, could also be applied to the general test standard for joints with mechanical fasteners, EN 26 891 (1991). As regards the testing standard for determination of the yield moment of dowel-type fasteners in bending, EN 409 (2009), general principles given above for EN 383 should be followed as well. This is especially related to documentation of the moment-rotation curve. The maximum bending angle at testing should be adjusted to the expected bending angles in joints, when applying elasto-plastic design. Absolute testing limits instead of dowel diameter dependent limits should be used, since also dowels of large diameter can be exposed to large bending angles in ductile connections.

Perspectives and future research studies

In this work a thorough mechanical study from dowel connection components, i.e., wood embedment characteristics and the behavior of steel dowels in bending, over the single-dowel connection, up to the local and global joint behavior, with final implementation of joint characteristics in nonlinear structural analysis, was presented.

However, the complex mechanical nature of wood, as well as the huge variety of wood products, connection techniques, as well as application cases in engineering design, did not allow to cover all possible variations in this study. Thus, in a first step, it might be interesting to apply the herein presented experimental program at the connection component level to other wood products and to other dowel-type fasteners. Of special interest would be application of the proposed embedment test procedure to solid timber, for studying the influence of wood defects like knots. This, would broaden the experimental database, which could be exploit

in numerical models at the next higher connection levels. Furthermore, reliable predictions of the variability of experimental embedment data, in particular for loading in the plastic regime, could be given.

As another field of future studies, the numerical beam-on-nonlinear elastic foundation model could be extended to three-dimensional loading situations. In consequence, this would require three-dimensional definition of the embedment characteristics as well, which could be tackled by coupled springs in three-dimensional space. Mathematical definition by parameterized embedment test data, as presented herein, is expected to facilitate the development of these modeling tool. Furthermore, thorough investigations on the frictional behavior between wood and steel dowel surface along the dowel axis, would enhance modeling at large single-dowel deformations. This would allow to consider the so-called rope effect that leads to increased lateral strength of connections.

The semi-analytical joint model could be extended as well. Using mathematically described load-displacement relationships for the single-dowels might allow for analytic joint stiffness determination, which would improve the applicability in nonlinear structural analysis. In addition, the joint model could be extended to three-dimensional loading situations, which indeed, requires information on the three-dimensional single-dowel connection behavior. Based on load distribution within the joint, concepts for verification against brittle failure modes should be developed, which might use models from fracture mechanics.

In order to transfer the semi-analytical joint model into a design concept for joint-based verification of dowel connections in nonlinear analysis, additional effort on the stochastic framework has to be invested. For the challenging task of coupling between joint stiffness and strength in nonlinear analysis, a suitable way has to be found to predict realistic joint stiffness, and joint strength satisfying the safety requirements of EC 0. This stochastic concept should be addressed to joint-failure, accounting for (i) homogenization effects in large multiple-dowel joints, (ii) the influence of the deformation level on the variability, as well as (iii) accuracy of the applied joint model.

Implementation of rules for the use of computational modeling in EC 5, would be expected to facilitate the development and engineering application of nonlinear joint models, which in turn would allow for new ways in timber engineering design, and thus, for more reliable and economic design of dowel connections.

Bibliography

- Almusallam, T. and Richard, R. (1993). Steel frame analysis with flexible joints exhibiting a strain-softening behavior. *Computers & Structures*, 46(1):55–65.
- Arciszewska-Kędzior, A., Kunecký, J., Hasníková, H., and Sebera, V. (2015). Lapped scarf joint with inclined faces and wooden dowels: experimental and numerical analysis. *Engineering Structures*, 94:1–8.
- Ascione, F., Feo, L., and Maceri, F. (2010). On the pin-bearing failure load of gfrp bolted laminates: an experimental analysis on the influence of bolt diameter. *Composites Part B: Engineering*, 41(6):482–490.
- ASTMD5764-97a (2002). Standard Test Method for Evaluating Dowel-Bearing Strength of Wood and Wood-Based Products. *ASTM International*.
- Avez, C., Lefèvre, C., Crocetti, R., and Descamps, T. (2017). Large-diameter single dowel joint: finite element modelling of a reinforced joint. *International Wood Products Journal*, pages 1–7.
- Awaludin, A., Smittakorn, W., Hirai, T., and Hayashikawa, T. (2007). Bearing properties of shorea obtusa beneath a laterally loaded bolt. *Journal of Wood Science*, 53(3):204–210.
- Bader, T. K., Bocquet, J.-F., Schweigler, M., and Lemaitre, R. (2017). Numerical modeling of the load distribution in multiple fastener joints. In *International Conference on Connections in Timber Engineering – From Research to Standards*, pages 136–152.
- Bader, T. K., Dastoorian, F., Ebrahimi, G., Unger, G., Lahayne, O., Hellmich, C., and Pichler, B. (2016a). Combined ultrasonic-mechanical characterization of orthotropic elastic properties of an unrefined bagasse fiber-polypropylene composite. *Composites Part B: Engineering*, 95:96–104.
- Bader, T. K., Schweigler, M., Hochreiner, G., and Eberhardsteiner, J. (2016b). Load distribution in multi-dowel timber connections under moment loading—integrative evaluation of multiscale experiments. In *World Conference on Timber Engineering (WCTE 2016), August 22–25, 2016, Vienna, Austria*. Vienna University of Technology, Austria.
- Bader, T. K., Schweigler, M., Hochreiner, G., Enquist, B., Dorn, M., and Serrano, E. (2016c). Experimental characterization of the global and local behavior of multi-dowel LVL-connections under complex loading. *Materials and Structures*, 49(6):2407–2424.
- Bader, T. K., Schweigler, M., Hochreiner, G., Serrano, E., Enquist, B., and Dorn, M. (2015). Dowel deformations in multi-dowel LVL-connections under moment loading. *Wood Material Science & Engineering*, 10(3):216–231.

- Bader, T. K., Schweigler, M., Serrano, E., Dorn, M., Enquist, B., and Hochreiner, G. (2016d). Integrative experimental characterization and engineering modeling of single-dowel connections in LVL. *Construction and Building Materials*, 107:235–246.
- Baravalle, M., Mikoschek, M., Colling, F., and Köhler, J. (2017). Calibration of simplified safety formats for structural timber design. *Construction and Building Materials*, 152:1051–1058.
- Berardi, U. (2017). A cross-country comparison of the building energy consumptions and their trends. *Resources, Conservation and Recycling*, 123:230–241.
- Biscaia, H. C., Chastre, C., Cruz, D., and Viegas, A. (2017). Prediction of the interfacial performance of CFRP laminates and old timber bonded joints with different strengthening techniques. *Composites Part B: Engineering*, 108:1–17.
- Biscaia, H. C., Chastre, C., and Silva, M. A. (2015). Bond-slip model for FRP-to-concrete bonded joints under external compression. *Composites Part B: Engineering*, 80:246–259.
- Blaß, H. J. (1995). Multiple fastener joints. *Proceedings of Timber Engineering STEP I C*, 15.
- Blaß, H. J. and Sandhaas, C. (2016). *Ingenieurholzbau - Grundlagen der Bemessung*. KIT Scientific Publishing, Karlsruhe. In German.
- Blaß, H. J. and Sandhaas, C. (2017). *Timber Engineering – Principles for design*, chapter Chapter B6: Wood products, pages 99–132. KIT Scientific Publishing.
- Bléron, L. and Duchanois, G. (2006). Angle to the grain embedding strength concerning dowel type fasteners. *Forest Products Journal*, 56(3):44–50.
- Bocquet, J. F., Sauvat, N., and Racher, P. (2004). Fiabilité et compétitivité des assemblages de structures bois : mécanismes de ruine associés aux assemblages à plans multiples. Technical report, Centre Technique du Bois et de l’Ameublement. In French.
- Bouchaïr, A., Racher, P., and Bocquet, J. (2007). Analysis of dowelled timber to timber moment-resisting joints. *Materials and Structures*, 40(10):1127–1141.
- Brühl, F., Kuhlmann, U., and Jorissen, A. (2011). Consideration of plasticity within the design of timber structures due to connection ductility. *Engineering Structures*, 33(11):3007–3017.
- Casella, G. and Berger, R. L. (2002). *Statistical inference*, volume 2. Duxbury Pacific Grove, CA.
- Descamps, T., Van Parys, L., and Datoussaïd, S. (2011). Development of a specific finite element for timber joint modeling. *International Journal for Computational Methods in Engineering Science and Mechanics*, 12(1):1–13.
- Dias, A. M. P. G., Van de Kuilen, J. W., Cruz, H. M. P., and Lopes, S. M. R. (2010). Numerical modeling of the load-deformation behavior of doweled softwood and hardwood joints. *Wood and Fiber Science*, 42(4):480–489.
- DIN 1052 (2008). Entwurf, Berechnung und Bemessung von Holzbauwerken – Allgemeine Bemessungsregeln und Bemessungsregeln für den Hochbau (Design of timber structures – General rules and rules for buildings). *Deutsches Institut für Normung, Berlin, Germany*. In German.

- Dorn, M. (2012). *Investigations on the serviceability limit state of dowel-type timber connections*. PhD thesis, Vienna University of Technology, Austria.
- Dorn, M., de Borst, K., and Eberhardsteiner, J. (2013). Experiments on dowel-type timber connections. *Engineering Structures*, 47:67–80.
- Ehlbeck, J. and Werner, H. (1992). Softwood and hardwood embedding strength for dowel-type fasteners. In *CIB-W18 Meeting 25-7-2, Aahus, Sweden*.
- EN 14592 (2012). Timber structures – Dowel-type fasteners – Requirements. *European Committee for Standardization (CEN), Brussels, Belgium*.
- EN 1990 (2002). Eurocode 0: Basis of structural design. *European Committee for Standardization (CEN), Brussels, Belgium*.
- EN 1992-1-1 (2004). Eurocode 2: Design of concrete structures – Part 1-1: General rules and rules for buildings. *European Committee for Standardization (CEN), Brussels, Belgium*.
- EN 1993-1-1 (2010). Eurocode 3: Design of steel structures – Part 1-1: General rules and rules for buildings. *European Committee for Standardization (CEN), Brussels, Belgium*.
- EN 1995-1-1 (2004). Eurocode 5: Design of timber structures – Part 1-1: General – Common rules and rules for buildings. *European Committee for Standardization (CEN), Brussels, Belgium*.
- EN 26 891 (1991). Timber structures; Joints made with mechanical fasteners; General principles for the determination of strength and deformation characteristics. *European Committee for Standardization (CEN), Brussels, Belgium*.
- EN 383 (2007). Timber structures – Test method – Determination of embedment strength and foundation values for dowel type fasteners. *European Committee for Standardization (CEN), Brussels, Belgium*.
- EN 409 (2009). Timber structures – Test methods – Determination of the yield moment of dowel type fasteners. *European Committee for Standardization (CEN), Brussels, Belgium*.
- EN ISO 4288 (1997). Geometrical product specifications (GPS) – Surface texture: Profile method – Rules and procedures for the assessment of surface texture. *European Committee for Standardization (CEN), Brussels, Belgium*.
- Fauziyah, S., Soesilohadi, R., Retnoaji, B., and Alam, P. (2016). Dragonfly wing venous cross-joints inspire the design of higher-performance bolted timber truss joints. *Composites Part B: Engineering*, 87:274–280.
- Feo, L., Latour, M., Penna, R., and Rizzano, G. (2017). Pilot study on the experimental behavior of GFRP-steel slip-critical connections. *Composites Part B: Engineering*, 115:209–222. Composite lattices and multiscale innovative materials and structures.
- Flatscher, G. and Schickhofer, G. (2016). Displacement-based determination of laterally loaded cross laminated timber (CLT) wall systems. In *Proceedings of INTER / 49-12-1, Graz, Austria*.
- Foschi, R. O. (1974). Load-slip characteristics of nails. *Wood Science*, 7(1):69–76.

- Foust, B., Lesniak, J., and Rowlands, R. (2014). Stress analysis of a pinned wood joint by grey-field photoelasticity. *Composites Part B: Engineering*, 61:291–299.
- Fragiacomo, M., Dujic, B., and Sustersic, I. (2011). Elastic and ductile design of multi-storey crosslam massive wooden buildings under seismic actions. *Engineering Structures*, 33(11):3043–3053.
- Franke, B. and Quenneville, P. (2011). Numerical modeling of the failure behavior of dowel connections in wood. *Journal of Engineering Mechanics*, 137(3):186–195.
- Franke, S. and Magnière, N. (2014). The embedment failure of european beech compared to spruce wood and standards. In *Materials and Joints in Timber Structures*, pages 221–229. Springer.
- Franke, S. and Quenneville, P. (2010). Embedding behaviour of LVL and radiata pine lumber. In *Proceedings of 11th World Conference on Timber Engineering, Italy*.
- Fueyo, J. G., Dominguez, M., Cabezas, J., and Rubio, M. (2009). Design of connections with metal dowel-type fasteners in double shear. *Materials and Structures*, 42(3):385–397.
- Gerner, M. (2000). *Entwicklung der Holzverbindungen: Forschungs- und Untersuchungsergebnisse*. Fraunhofer IRB-Verlag. In German.
- Glos, P. (1978). Zur Bestimmung des Festigkeitsverhaltens von Brettschichtholz bei Druckbeanspruchung aus Werkstoff- und Einwirkungskenngrößen. Technical report, Laboratorium für den Konstruktiven Ingenieurbau (LKI), Technische Universität München, Deutschland. In German.
- Gompertz, B. (1825). On the nature of the function expressive of the law of human mortality, and on a new mode of determining the value of life contingencies. *Philosophical transactions of the Royal Society of London*, 115:513–583.
- Gupta, R. and Sinha, A. (2012). Effect of grain angle on shear strength of douglas-fir wood. *Holzforschung*, 66:655–658.
- Hager, K. (1930). Der Lochleibungsdruck bei Holzverbindungen. *Der Bauingenieur*, 11(50):865–866. In German.
- Hankinson, R. L. (1921). Investigation of crushing strength of spruce at various angles of grain. *Air Force Information Circular*, 3(259).
- Hirai, T. (1983). Nonlinear load-slip relationship of bolted wood-joints with steel side-members II. Application of the generalized theory of a beam on an elastic foundation. *Mokuzai Gakkaishi*, 29:839–844.
- Hochreiner, G., Bader, T., de Borst, K., and Eberhardsteiner, J. (2013). Stiftförmige Verbindungsmittel im EC5 und baustatische Modellbildung mittels kommerzieller Statiksoftware. *Bauingenieur*, 88:275–289. In German.
- Hübner, U., Bogensberger, T., and Schickhofer, G. (2008). Embedding strength of european hardwoods. *Proceedings of CIB-W18, Paper*, pages 41–7.
- Hwang, K. and Komatsu, K. (2002). Bearing properties of engineered wood products I: effects of dowel diameter and loading direction. *Journal of Wood Science*, 48(4):295–301.

- Iraola, B., Cabrero, J. M., and Gil, B. (2016). Pressure-overclosure law for the simulation of contact in spruce joints. In *World Conference on Timber Engineering (WCTE 2016), August 22–25, 2016, Vienna, Austria*.
- ISO/DIS 10984-2 (2009). Timber structures – Dowel type fasteners – Part 2: Determination of embedding strength and foundation values. *International Organization for Standardization*.
- Jansson, G. B. I. (1955). Effect of nail characteristics on the load-carrying capacity of a nailed joint. Master's thesis, Iowa State College.
- Jensen, J. L. (1994). *Dowel-type fastener connections in timber structures subjected to short-term loading*. PhD thesis, Technical University of Denmark (DTU).
- Johansen, K. W. (1949). Theory of timber connections. *Int Assoc Bridge Struct Eng.*, 9:249–262.
- Jorissen, A. and Fragiacomio, M. (2011). General notes on ductility in timber structures. *Engineering structures*, 33(11):2987–2997.
- Jorissen, A. J. M. (1998). *Double shear timber connections with dowel type fasteners*. Delft University Press Delft, The Netherlands.
- Källsner, B. and Girhammar, U. A. (2009). Plastic models for analysis of fully anchored light-frame timber shear walls. *Engineering Structures*, 31(9):2171 – 2181.
- Kandler, G. and Füssl, J. (2017). A probabilistic approach for the linear behaviour of glued laminated timber. *Engineering Structures*, 148:673–685.
- Karagiannis, V., Málaga-Chuquitaype, C., and Elghazouli, A. (2016). Modified foundation modelling of dowel embedment in glulam connections. *Construction and Building Materials*, 102:1168–1179.
- King, W., Yen, J. R., and Yen, Y. A. (1996). Joint characteristics of traditional chinese wooden frames. *Engineering Structures*, 18(8):635–644.
- Kirkegaard, P. H., Sørensen, J. D., Čizmar, D., and Rajčić, V. (2011). System reliability of timber structures with ductile behaviour. *Engineering Structures*, 33(11):3093–3098. *Modelling the Performance of Timber Structures*.
- Koch, H., Eisenhut, L., and Seim, W. (2013). Multi-mode failure of form-fitting timber connections – Experimental and numerical studies on the tapered tenon joint. *Engineering Structures*, 48:727–738.
- Köhler, J. and Fink, G. (2012). Reliability based code calibration of a typical Eurocode 5 design equations. In *World Conference on Timber Engineering (WCTE 2012), July 15–19, 2012, Auckland, Australia*, volume 4, pages 99–103.
- Kohlhauser, C. and Hellmich, C. (2012). Determination of poisson's ratios in isotropic, transversely isotropic, and orthotropic materials by means of combined ultrasonic-mechanical testing of normal stiffnesses: Application to metals and wood. *European Journal of Mechanics-A/Solids*, 33:82–98.
- Lathuillière, D., Bléron, L., Descamps, T., and Bocquet, J.-F. (2015). Reinforcement of dowel type connections. *Construction and Building Materials*, 97:48–54.

- Lederer, W., Bader, T. K., Muszyński, L., and Eberhardsteiner, J. (2016). Exploring a multi-modal experimental approach to investigation of local embedment behaviour of wood under steel dowels. *Strain*, 52(6):531–547.
- Liřner, K. and Rug, W. (2013). *Holzbausanierung: Grundlagen und Praxis der sicheren Ausföhrung*. Springer-Verlag. In German.
- McKenzie, W. and Karpovich, H. (1968). The frictional behaviour of wood. *Wood Science and Technology*, 2(2):139–152.
- Meyer, A. (1957). Die Tragföhigkeit von Nagelverbindungen bei statischer Belastung. *Holz als Roh- und Werkstoff*, 15(2):96–109. In German.
- Mohamadi-Shoore, M. and Mofid, M. (2011). New modeling for moment–rotation behavior of bolted endplate connections. *Scientia Iranica*, 18(4):827–834.
- Möller, T. (1950). En ny metod för beräkning av spikförband. Technical Report 117, Chalmers Tekniska Högskolan Handlingar. In Swedish.
- Mounien, R., Fagiano, C., Paulmier, P., Tranquart, B., and Irisarri, F.-X. (2017). Experimental characterization of the bearing behavior of 3D woven composites. *Composites Part B: Engineering*, 116:369–376.
- Nerilli, F. and Vairo, G. (2017). Progressive damage in composite bolted joints via a computational micromechanical approach. *Composites Part B: Engineering*, 111:357–371.
- Norén, B. (1962). Nailed joints – A contribution to the theoretical analysis of yield and strength. *Swedish For. Prod. Res. Laboratory Report*, (123B).
- Ormarsson, S. and Blond, M. (2012). An improved method for calculating force distributions in moment-stiff timber connections. In *Proceedings of the World conference on Timber Engineering (WCTE 2012), 15–19 July 2012, Auckland, New Zealand*.
- Patton-Mallory, M., Pellicane, P. J., and Smith, F. W. (1997). Modeling bolted connections in wood. *Journal of structural engineering*, 123(8):1054–1062.
- Pedersen, M. U. (2002). *Dowel Type Timber Connections - Strength modelling*. PhD thesis, Department of Structural Engineering and Materials (BKM), Technical University of Denmark (DTU).
- Racher, P. (1995). Moment resisting connections. *Proceedings of Timber Engineering STEP I C*, 16.
- Resch, E. and Kaliske, M. (2010). Three-dimensional numerical analyses of load-bearing behavior and failure of multiple double-shear dowel-type connections in timber engineering. *Computers & Structures*, 88(3):165–177.
- Resch, E. and Kaliske, M. (2012). Numerical analysis and design of double-shear dowel-type connections of wood. *Engineering Structures*, 41:234–241.
- Reynolds, T., Harris, R., and Chang, W.-S. (2013). Viscoelastic embedment behaviour of dowels and screws in timber under in-service vibration. *European Journal of Wood and Wood Products*, 71(5):623–634.

- Reynolds, T., Sharma, B., Harries, K., and Ramage, M. (2016). Dowelled structural connections in laminated bamboo and timber. *Composites Part B: Engineering*, 90:232–240.
- Richard, R. M. and Abbott, B. J. (1975). Versatile elastic-plastic stress-strain formula. *Journal of the Engineering Mechanics Division*, 101(4):511–515.
- Rodd, P. (1973). *The Analysis of Timber Joints Made with Circular Dowel Connectors*. PhD thesis, University of Sussex, Brighton, U.K.
- Sandhaas, C., Ravenshorst, G., Blass, H., and van de Kuilen, J. (2013). Embedment tests parallel-to-grain and ductility aspects using various wood species. *European Journal of Wood and Wood Products*, 71(5):599–608.
- Sandhaas, C. and van de Kuilen, J. W. G. (2017). Strength and stiffness of timber joints with very high strength steel dowels. *Engineering Structures*, 131:394–404.
- Santos, C., De Jesus, A., Morais, J., and Lousada, J. (2010). A comparison between the EN 383 and ASTM D5764 test methods for dowel-bearing strength assessment of wood: Experimental and numerical investigations. *Strain*, 46(2):159–174.
- Santos, C. L., de Jesus, A. M., Morais, J. J., and Fontoura, B. F. (2013). An experimental comparison of strengthening solutions for dowel-type wood connections. *Construction and Building Materials*, 46:114–127.
- Santos, C. L., De Jesus, A. M., Morais, J. J., and Lousada, J. L. (2009). Quasi-static mechanical behaviour of a double-shear single dowel wood connection. *Construction and Building Materials*, 23(1):171–182.
- Sauvat, N. (2001). *Résistance d’assemblages de type tige en structure bois sous chargements cycliques complexes*. PhD thesis, LERMES / CUST, Université Blaise Pascal-Clermont II, France. In French.
- Sawata, K. and Yasumura, M. (2002). Determination of embedding strength of wood for dowel-type fasteners. *Journal of Wood Science*, 48(2):138–146.
- Schoenmakers, J., Jorissen, A., and Leijten, A. (2010). Evaluation and modelling of perpendicular to grain embedment strength. *Wood Science and Technology*, 44(4):579–595.
- Schoenmakers, J. and Svensson, S. (2011). Embedment tests perpendicular to the grain – Optical measurements of deformation fields. *European Journal of Wood and Wood Products*, 69(1):133–142.
- Schweigler, M., Bader, T. K., and Hochreiner, G. (2018a). Engineering modeling of semi-rigid joints for nonlinear analysis of timber structures. *Submitted to Engineering Structures*.
- Schweigler, M., Bader, T. K., Hochreiner, G., and Eberhardsteiner, J. (2016a). An engineering modeling approach for the non-linear load-displacement behavior of single-dowel connections – parameter study. In *World Conference on Timber Engineering (WCTE 2016), August 22–25, 2016, Vienna, Austria*. Vienna University of Technology, Austria.
- Schweigler, M., Bader, T. K., Hochreiner, G., and Lemaître, R. (2018b). Parameterization equations for the nonlinear connection slip applied to the anisotropic embedment behavior of wood. *Accepted for publication in Composites Part B: Engineering*.

- Schweigler, M., Bader, T. K., Hochreiner, G., Unger, G., and Eberhardsteiner, J. (2016b). Load-to-grain angle dependence of the embedment behavior of dowel-type fasteners in laminated veneer lumber. *Construction and Building Materials*, 126:1020–1033.
- Schweigler, M., Bader, T. K., Vessby, J., and Eberhardsteiner, J. (2017). Constrained displacement boundary conditions in embedment testing of dowel-type fasteners in LVL. *Strain*, 53(6):e12238, pp. 17. DOI: 10.1111/str.12238.
- Shanks, J. D., Chang, W.-S., and Komatsu, K. (2008). Experimental study on mechanical performance of all-softwood pegged mortice and tenon connections. *Biosystems Engineering*, 100(4):562–570.
- Sjödin, J., Enquist, B., and Serrano, E. (2006). Contact-free measurements and numerical analyses of the strain distribution in the joint area of steel-to-timber dowel joints. *Holz als Roh- und Werkstoff*, 64(6):497–506.
- Sjödin, J., Serrano, E., and Enquist, B. (2008). An experimental and numerical study of the effect of friction in single dowel joints. *Holz als Roh- und Werkstoff*, 66(5):363–372.
- Stamato, G. C. and Calil Jr, C. (2000). Plywood embedment stiffness. In *Proceedings of the WCTE 2000*.
- Stelmokas, J. W., Zink, A. G., and Loferski, J. R. (1997). Image correlation analysis of multiple-bolt wood connections. *Wood and Fiber Science*, 29(3):210–227.
- Thelandersson, S. and Larsen, H. J. (2003a). *Timber Engineering*, chapter 4: Structural timber – Variability and statistical modeling, pages 45–66. John Wiley & Sons.
- Thelandersson, S. and Larsen, H. J. (2003b). *Timber Engineering*, chapter 11: Reliability of structures with timber and wood-based products, pages 177–200. John Wiley & Sons.
- Vessby, J. (2011). *Analysis of shear walls for multi-storey timber buildings*. PhD thesis, Linnaeus University.
- Vessby, J., Serrano, E., and Olsson, A. (2010). Coupled and uncoupled nonlinear elastic finite element models for monotonically loaded sheathing-to-framing joints in timber based shear walls. *Engineering Structures*, 32(11):3433–3442.
- Whale, L. and Smith, I. (1986). The derivation of design clauses for nailed and bolted joints in Eurocode 5. In *CIB-W18 Meeting 19-7-6, Florence, Italy*.
- Yan, L., Zou, X. J., and She, C. G. (2011). Performance of the nail joints on wood frame shear walls. In *Advanced Materials Research*, volume 255, pages 350–354. Trans Tech Publ.
- Yee, Y. L. and Melchers, R. E. (1986). Moment-rotation curves for bolted connections. *ASCE Journal of Structural Engineering*, 112(3):615–635.
- Z-9.1-100 (2011). Allgemeine bauaufsichtliche Zulassung – Furnierschichtholz "Kerto S" und "Kerto Q". *Zulassungsstelle für Bauprodukte und Bauarten - Bautechnisches Prüfamts*. In German.

Personal information

Curriculum Vitae

Personal Data

Name:	Michael Schweigler
Academic Degree:	Dipl.-Ing.
Date of Birth:	6th May 1988
Place of Birth:	St. Pölten, Austria
Nationality:	Austrian
Current address:	Horngasse 5, 3140 Pottenbrunn, Austria

Education

07/2013 – 01/2018	Doctoral studies in Civil Engineering at Vienna University of Technology (TU-Wien), Vienna, Austria
02/2011 – 06/2013	Master's studies in Civil Engineering at TU-Wien
01/2011 – 06/2011	Master's studies in Civil Engineering at the Royal Institute of Technology (KTH Stockholm), Stockholm, Sweden
03/2008 – 01/2011	Bachelor's studies in Civil Engineering at TU-Wien
09/2002 – 06/2007	Technical High School for Civil Engineering, Krems/Donau, Austria

Work Experience

07/2017 – 12/2017	Project Assistant, Institute for Mechanics of Materials and Structures, Vienna University of Technology
07/2013 – 06/2017	University Assistant, Institute for Mechanics of Materials and Structures, Vienna University of Technology
09/2011, 09/2010, 08/2009 – 09/2009	Construction Designer at "Zieritz & Partner ZT GmbH", St. Pölten, Austria, Internship
08/2008 – 09/2008, 02/2008	Assistant for Construction Management at "Strabag AG", Hausleiten, Austria, Internship

Teaching

03/2014 – 12/2017	Timber Engineering
10/2013 – 01/2017	Timber Engineering 2
10/2013 – 12/2016	Strength of Materials – Laboratory exercises

Activities Abroad

- 05/2016 Short Term Scientific Mission on “Experimental characterization and parameterization of the load-to-grain angle dependent embedment behavior of dowel-type fasteners in laminated veneer lumber (LVL)”, Linnæus University, Växjö, Sweden
- 12/2013 COST FP1101 Training School on “Assessment and Reinforcement of Timber Elements”, University of Mons, Mons, Belgium

Awards

- 2016 Award to Young Researcher, granted by the Danubia Adria Society for Advances in Experimental Methods
- 2012 Award for excellent performance as a student, granted by the “Windhag-Stipendienstiftung für Niederösterreich”
- 2009, 2010, 2012, 2013 Award for excellent performance as a student, granted by the Faculty of Civil Engineering, Vienna University of Technology

Scientific Dissemination

Monographs

M. Schweigler. A numerical model for slip curves of dowel connections and its application to timber structures. *Master's Thesis*, Vienna University of Technology, Vienna, Austria, 2013.

Publications in Scientific Journals (peer-reviewed)

M. Schweigler, T.K. Bader, G. Hochreiner, G. Unger, and J. Eberhardsteiner. Load-to-grain angle dependence of the embedment behavior of dowel-type fasteners in laminated veneer lumber. *Construction and Building Materials*, 126:1020–1033, 2016b.

M. Schweigler, T.K. Bader, J. Vessby, and J. Eberhardsteiner. Constrained displacement boundary conditions in embedment testing of dowel-type fasteners in LVL. *Strain*, 53(6):e12238, pp. 17, DOI: 10.1111/str.12238, 2017.

M. Schweigler, T.K. Bader, G. Hochreiner, and R. Lemaître. Parameterization equations for the nonlinear connection slip applied to the anisotropic embedment behavior of wood. *Accepted for publication in Composites Part B: Engineering*, 2018b.

M. Schweigler, T.K. Bader, and G. Hochreiner. Engineering modeling of semi-rigid joints for nonlinear analysis of timber structures. *Submitted to Engineering Structures*, 2018a.

T.K. Bader, M. Schweigler, G. Hochreiner, E. Serrano, B. Enquist, and M. Dorn. Dowel deformations in multi-dowel LVL-connections under moment loading. *Wood Material Science and Engineering*, 10(3):216–231, 2015.

T.K. Bader, M. Schweigler, G. Hochreiner, B. Enquist, M. Dorn, and E. Serrano. Experimental characterization of the global and local behavior of multi-dowel LVL-connections under complex loading. *Materials and Structures*, 6:2407–2424, 2016c.

T.K. Bader, M. Schweigler, E. Serrano, M. Dorn, B. Enquist, and G. Hochreiner. Integrative experimental characterization and engineering modeling of single-dowel connections in LVL. *Construction and Building Materials*, 107:235–246, 2016d.

T.K. Bader, M. Schweigler, G. Hochreiner, and J. Eberhardsteiner. Ingenieurmodelle für die Strukturmodellierung und Nachweisführung von stiftförmigen Verbindungen im Holzbau (in German). *Österreichische Ingenieur- und Architekten-Zeitschrift*, Heft 1–12/2017, 2017.

G. Hochreiner, T.K. Bader, M. Schweigler, and J. Eberhardsteiner. Structural behavior and design of dowel groups – Experimental and numerical identification of stress states and failure mechanisms of the surrounding timber matrix. *Engineering Structures*, 131:421–437, 2017.

T. Schlappal, M. Schweigler, S. Gmainer, M. Peyerl, and B. Pichler. Creep and cracking of concrete hinges: insight from centric and eccentric compression experiments. *Materials and Structures*, 50(244), 2017.

Conference Papers (peer-reviewed)

- M. Schweigler, T.K. Bader, G. Hochreiner, and J. Eberhardsteiner. An engineering modeling approach for the nonlinear load-displacement behavior of single dowel connections – parameter study. In J. Eberhardsteiner, W. Winter, A. Fadai, and M. Pöll, editors, *CD-ROM Proceedings of the World Conference on Timber Engineering (WCTE 2016)*, Vienna University of Technology, Grafisches Zentrum HTU GmbH, Vienna, Austria, 2016a. Paper 755, 10 pages.
- T.K. Bader, J.F. Bocquet, M. Schweigler, and R. Lemaitre. Numerical modeling of the load distribution in multiple fastener joints. In *Proceedings of the International Conference on Connections in Timber Engineering – From Research to Standards; in the framework of COST FP1402*, TU Graz, Austria, pages 136–152, 2017.
- T.K. Bader, M. Schweigler, G. Hochreiner, and J. Eberhardsteiner. Load distribution in multi-dowel timber connections under moment loading - integrative evaluation of multiscale experiments. In J. Eberhardsteiner, W. Winter, A. Fadai, and M. Pöll, editors, *CD-ROM Proceedings of the World Conference on Timber Engineering (WCTE 2016)*, Vienna University of Technology, Grafisches Zentrum HTU GmbH, Vienna, Austria, 2016b. Paper 156, 9 pages.
- G. Hochreiner, C. Riedl, M. Schweigler, T.K. Bader, and J. Eberhardsteiner. Matrix failure of multi-dowel type connections – engineering modelling and parameter study. In J. Eberhardsteiner, W. Winter, A. Fadai, and M. Pöll, editors, *CD-ROM Proceedings of the World Conference on Timber Engineering (WCTE 2016)*, Vienna University of Technology, Grafisches Zentrum HTU GmbH, Vienna, Austria, 2016. Paper 795, 10 pages.
- G. Hochreiner, T.K. Bader, M. Schweigler, G. Esser, S. Hagmann, and B. Glatz. The Historic Roof Structure of the Spanish Riding School in Vienna Structural Assessment In *Proceedings of the International Conference on Structural Health Assessment of Timber Structures (SHATIS'15)*, DWE Poland, pages 248–259, 2015.

Conference Papers (not peer-reviewed)

- M. Schweigler, T.K. Bader, G. Hochreiner, and J. Eberhardsteiner. Ein baustatischer Modellierungsansatz für das Last-Verformungsverhalten von Stabdübelgruppen im Ingenieurholzbau (in German). In *Berichte des Doktorandenkolloquium Holzbau Forschung + Praxis*, Universität Stuttgart, Germany, pages 157-164, 2014.
- T.K. Bader, M. Schweigler, G. Hochreiner, and J. Eberhardsteiner. Berechnungsmodell für das Last-Verformungsverhalten von Stabdübelgruppen im Ingenieurholzbau (in German). In *Berichte der Fachtagung Baustatik-Baupraxis 12*, TU München, Germany, pages 113–121, 2014.

Conference Presentations and Posters

- M. Schweigler, T.K. Bader, G. Hochreiner, and J. Eberhardsteiner. Berechnungsmodell für das Last-Verformungsverhalten von Stabdübelgruppen im Ingenieurholzbau (in German). Oral presentation at the “Fachtagung Baustatik-Baupraxis, München, Germany, 2014.

- M. Schweigler, T.K. Bader, G. Hochreiner, and J. Eberhardsteiner. Ein baustatischer Modellierungsansatz für das Last-Verformungsverhalten von Stabdübelgruppen im Ingenieurholzbau (in German). Oral presentation at the “Doktorandenkolloquium Holzbau Forschung + Praxis”, Stuttgart, Germany, 2014.
- M. Schweigler, T.K. Bader, and J. Eberhardsteiner. Load direction dependency of the embedment behaviour of dowel-type fasteners in laminated veneer lumber. Oral presentation at the “16th International Conference on Experimental Mechanics (ICEM 16)”, Cambridge, United Kingdom, 2014.
- M. Schweigler, T.K. Bader, G. Hochreiner, and J. Eberhardsteiner. Load-deformation behavior of single dowel connections in timber structures. Poster presentation at the “1st Vienna Young Scientists Symposium”, Vienna, Austria, 2015.
- M. Schweigler, T.K. Bader, G. Hochreiner, and J. Eberhardsteiner. Experimental characterization of dowel connections beyond the elastic domain. Poster presentation at the “32nd Danubia-Adria Symposium (DAS 32)”, Zilina, Slovakia, 2015.
- M. Schweigler, T.K. Bader, G. Hochreiner, and J. Eberhardsteiner. A novel approach for the load-displacement behavior of single-dowel connections in laminated veneer lumber. Oral presentation at the “17th International Conference on Experimental Mechanics (ICEM 17)”, Rhodes, Greece, 2016.
- M. Schweigler, T.K. Bader, G. Hochreiner, and J. Eberhardsteiner. An engineering modeling approach for the nonlinear load-displacement behavior of single dowel connections – Parameter study. Oral presentation at the “World Conference on Timber Engineering (WCTE 2016)”, Vienna, Austria, 2016.
- M. Schweigler, T.K. Bader, and J. Eberhardsteiner. The influence of displacement boundary conditions on the embedment behavior of dowel-type fasteners. Poster presentation at the “33rd Danubia-Adria Symposium on Advances in Experimental Mechanics (DAS 33)”, Portorož, Slovenia, 2016.
- M. Schweigler, T.K. Bader, and J. Vessby. Experimental characterization and parameterization of the load-to-grain angle dependent embedment behavior of dowel-type fasteners in LVL. Oral presentation at the “5th Workshop of COST Action FP1402”, Mons, Belgium, 2016.
- M. Schweigler, T.K. Bader, and J. Eberhardsteiner. An engineering modeling approach for the load-deformation behavior of multi-dowel connections in timber structures. Oral presentation at the “2017 Engineering Mechanics Conference (EMI 2017)”, San Diego, USA, 2017.

Scientific Reports

- M. Schweigler. Short Term Scientific Mission (STSM) Report – Experimental characterization and parameterization of the load-to-grain angle dependent embedment behavior of dowel-Type fasteners in laminated veneer lumber (LVL). Report for *COST Action FP1402 “Basis of Structural Timber Design” – from research to standards*, Mons, Belgium, 2016. 19 pages.